

# Temporal and spatial organisation of RhoA during cytokinesis

---

Dissertation zur Erlangung des Doktorgrades der  
Naturwissenschaften Doctor rerum naturalium (Dr. rer. nat.)

**Jennifer Leonie Bellessem**

München 2023



Ludwig-Maximilians-Universität München  
Fakultät für Biologie

Diese Dissertation wurde angefertigt  
unter der Leitung von Prof. Dr. Esther Zanin  
am Lehrstuhl für Zell- und Entwicklungsbiologie  
an der Ludwig-Maximilians-Universität München.

Erstgutachterin: Prof. Dr. Esther Zanin

Zweitgutachter: Prof. Dr. Christof Osman

Tag der Abgabe: 21.07.2023

Tag der mündlichen Prüfung: 26.01.2024

## **ERKLÄRUNG**

Ich versichere hiermit an Eides statt, dass meine Dissertation selbständig und ohne unerlaubte Hilfsmittel angefertigt worden ist.

Die vorliegende Dissertation wurde weder ganz, noch teilweise bei einer anderen Prüfungskommission vorgelegt.

Ich habe noch zu keinem früheren Zeitpunkt versucht eine Dissertation einzureichen oder an einer Doktorprüfung teilzunehmen.

München, den 21.07.2023

Jennifer Bellessem

# Table of Contents

List of Figures.....	1
List of Tables.....	4
List of Formulas .....	5
List of Abbreviations.....	6
Abstract.....	10
Zusammenfassung .....	12
1 Introduction.....	14
1.1 Mitosis in animal cells .....	14
1.2 Cytokinesis in animal cells .....	16
1.2.1 RhoA maturation and regulation during cytokinesis.....	17
1.2.2 Formation of the contractile ring.....	20
1.2.2.1 Contractile forces and F-actin alignment during cytokinesis .....	24
1.2.3 Positioning of the division plane .....	28
1.2.4 The formation of a narrow RhoA activity zone at the equatorial cortex.....	30
1.2.5 Maintenance of a narrow RhoA zone at the equatorial cortex .....	31
1.3 Cortical excitability.....	35
1.4 Strategies to visualize RhoA <i>in vivo</i> .....	37
1.5 <i>C. elegans</i> as model organism to study cytokinesis.....	39
1.5.1 <i>C. elegans</i> life cycle.....	39
1.5.2 Cell division of the <i>C. elegans</i> one-cell embryo .....	40
1.6 Aims of the thesis .....	42
2 Material and Methods.....	44
2.1 Material.....	44
2.2 Methods .....	52
2.2.1 <i>C. elegans</i> maintenance .....	52
2.2.2 Worm freezing.....	54

2.2.3	Worm lysis and genotyping.....	54
2.2.4	Worm crosses .....	54
2.2.5	Plasmid generation .....	55
2.2.5.1	PCR amplification.....	57
2.2.5.2	Gibson Assembly <sup>®</sup> cloning.....	59
2.2.5.3	Transformation.....	60
2.2.5.4	Colony-PCR, plasmid purification and sequencing.....	60
2.2.6	Mos1-mediated single-copy insertion (MosSCI) .....	61
2.2.7	Generation of dsRNA .....	62
2.2.8	Microinjection of dsRNA .....	63
2.2.9	Embryonic lethality assay.....	65
2.2.10	Antibody generation against RHO-1 .....	65
2.2.10.1	Antigen expression and purification .....	65
2.2.10.2	Bradford assay.....	67
2.2.10.3	RHO-1 antibody purification .....	67
2.2.11	Nanobody generation against active, GTP loaded RHO-1 .....	69
2.2.11.1	Antigen expression and purification for immunization and biopanning .....	70
2.2.11.2	Cloning of V <sub>H</sub> H sequences.....	72
2.2.11.2.1	Transient transfection of HeLa cells to test V <sub>H</sub> H sequences <i>in vivo</i> .....	73
2.2.11.2.2	Microinjections to test V <sub>H</sub> H sequences in <i>C. elegans</i> .....	73
2.2.12	Western Blot analysis .....	73
2.2.13	Live-cell imaging using spinning disk confocal microscopy .....	74
2.2.13.1	Central- and cortical plane imaging .....	75
2.2.13.2	High-time resolution imaging (cortical plane only).....	75
2.2.14	Image analysis .....	76
2.2.14.1	Image representation .....	76
2.2.14.2	Cytokinesis timing analysis.....	77
2.2.14.3	Line-scan and zone width analysis.....	77

2.2.14.4	Co-localization analysis of equatorial foci.....	78
2.2.14.5	Structure analysis of equatorial foci.....	79
2.2.14.6	PIV analysis.....	80
2.2.14.6.1	Velocity distribution assay.....	81
2.2.14.6.2	Velocity correlation assay.....	81
2.2.14.6.3	Orientation correlation assay.....	81
2.2.14.7	Alignment assay.....	82
2.2.14.8	FRAP experiments.....	83
2.2.14.8.1	FRAP analysis.....	84
2.2.14.8.1.1	Lateral Diffusion analysis.....	85
2.2.14.9	Statistical analysis.....	85
3	Results.....	86
3.1	Generation of fluorescently-labeled RHO-1 to study its localization and dynamics in <i>C. elegans</i> one-cell embryos.....	86
3.1.1	Generation of a genetic replacement system to monitor GFP::RHO-1 in early <i>C. elegans</i> embryos by live-cell imaging.....	87
3.1.1.1	N-terminal tagging of RHO-1 impairs RHO-1 function during embryonic development but not during first cell division.....	90
3.1.2	CRISPR/Cas9 as an approach to tag <i>rho-1</i> at the endogenous locus.....	92
3.1.2.1	Three different approaches of endogenous <i>rho-1</i> tagging with a fluorophore using CRISPR/Cas9 resulted in homozygous sterile animals.....	92
3.1.3	Generation of a RHO-1 nanobody to specifically monitor active RHO-1 <i>in vivo</i> .....	95
3.1.3.1	Antigen preparation and verification of GDP and GTP loaded state.....	96
3.1.3.2	<i>In vivo</i> tests of GFP-tagged nanobody sequences showed no specificity for RhoA in HeLa cells and RHO-1 in <i>C. elegans</i> .....	99
3.2	Generation of a RHO-1 antibody to test endogenous- and transgenic RHO-1 expression levels.....	100

3.3	How is active RHO-1 maintained in a narrow zone at the equatorial membrane during cytokinesis? .....	102
3.3.1	GFP::RHO-1 is present in two distinct pools at the plasma membrane during cell division of the one-cell <i>C. elegans</i> embryo .....	102
3.3.1.1	The dense RHO-1 meshwork at the equatorial membrane is not an artifact of the GFP-tag.....	105
3.3.2	How does RHO-1 regulation by GAPs and GEF contribute to the localization of RHO-1 in the two observed membrane pools? .....	107
3.3.2.1	The equatorial RHO-1 zone but not anterior foci are ECT-2 dependent... ..	107
3.3.2.2	GFP::RHO-1 localization into PH-positive anterior foci and into the equatorial RHO-1 zone is independent of RGA-3/4 .....	109
3.3.2.3	'RhoA flux' mediated by RGA-3/4 regulates cytokinesis timing .....	110
3.3.2.4	Restricting RHO-1 into a narrow zone depends on RGA-3/4 .....	112
3.3.3	How do the two PM-targeting motifs of RHO-1 contribute to its localization in the two observed membrane pools? .....	114
3.3.3.1	The PBS and CAAX-motif localize RHO-1 to the PM representing a prerequisite for cytokinesis.....	114
3.3.3.2	The PBS and CAAX-motif together are sufficient to localize RHO-1 to the PM .....	117
3.3.3.3	The PBS and CAAX-motif are not sufficient to specifically accumulate RHO-1 at the equator.....	120
3.3.4	Does the actin cytoskeleton act as a physical barrier that restricts RhoA into a narrow zone at the equatorial membrane?.....	121
3.3.4.1	Equatorial RHO-1 zone formation is independent of linear and branched F-actin .....	122
3.3.4.2	Equatorial RHO-1 meshwork formation requires formin-induced F-actin polymerization.....	125
3.3.4.3	Equatorial RHO-1 foci in <i>cyk-1(RNAi)</i> embryos represent active RHO-1 .....	126
3.3.4.4	Formation of GFP::RHO-1 filamentous foci at the equator is dependent on anillin .....	128

3.3.4.5	Myosin II and ring constriction are not required for dense RHO-1 meshwork formation at the equator.....	130
3.3.4.6	Are GFP::RHO-1 filamentous-like structures at the equatorial membrane a consequence of a dense F-actin meshwork?.....	132
3.3.4.6.1	FRAP experiments to test whether F-actin restricts RHO-1 mobility at the equatorial cortex.....	132
3.3.4.6.2	RHO-1 velocities are reduced at the equatorial cortex, a region of high F-actin density.....	135
3.3.4.7	Reduced RHO-1 velocities at the equator are driven by formin-induced F-actin polymerization.....	138
3.3.4.8	Reduced RHO-1 velocities at the equator are independent of myosin II and ring constriction.....	139
3.3.4.9	Equatorial F-actin and RHO-1 partially co-localize .....	141
3.3.4.10	RHO-1 circumferentially aligns around the equatorial membrane following F-actin alignment .....	142
4	Discussion .....	145
5	References .....	161
6	Appendix .....	183
6.1	Semi-automated macros used for image processing of cortical plane live-cell microscopy images. ....	183
	Acknowledgement.....	185
	Curriculum Vitae .....	187

## List of Figures

Figure 1:	Mitosis in animal cells. ....	17
Figure 2:	RhoA maturation and regulation.....	19
Figure 3:	Formation of the contractile ring. ....	23
Figure 4:	F-actin alignment during cytokinesis.....	28
Figure 5:	Positioning of the division plane. ....	30
Figure 6:	The ‘membrane-skeleton picket fence model’.....	33
Figure 7:	The ‘RhoA flux model’.....	35
Figure 8:	<i>C. elegans</i> life cycle.....	40
Figure 9:	First cell division of the <i>C. elegans</i> one-cell embryo. ....	41
Figure 10:	Image processing for representation of the cortical plane. ....	77
Figure 11:	FRAP image acquisition and analysis. ....	85
Figure 12:	Generation of a genetic replacement system, where a GFP-tagged <i>rho-1</i> transgene is integrated into <i>C. elegans</i> genome and endogenous RHO-1 can be depleted by dsRNA injection. ....	88
Figure 13:	GFP::RHO-1 can replace endogenous RHO-1 during first cell division of the one-cell <i>C. elegans</i> embryo. ....	89
Figure 14:	N-terminal tagging of RHO-1 impairs its function during embryonic development but not during first cell division. ....	91
Figure 15:	Approaches to tag endogenous RHO-1 using CRISPR/Cas9.....	94
Figure 16:	Generation of a RHO-1 Nanobody to specifically monitor active RHO-1 <i>in vivo</i> .....	96
Figure 17:	Antigen preparation and verification of GDP and GTP loaded state. ....	97
Figure 18:	<i>In vivo</i> tests of GFP-tagged nanobodies showed no specific plasma membrane enrichment.....	100
Figure 19:	Generation and validation of a RHO-1 antibody. ....	101
Figure 20:	GFP::RHO-1 localizes into two distinct pools during cytokinesis.....	104
Figure 21:	RHO-1 tagged with mCherry also forms a dense meshwork at the equatorial membrane.....	105
Figure 22:	Internally-tagged RHO-1 localizes into a narrow RHO-1 zone at the equatorial membrane.....	106
Figure 23:	The equatorial GFP::RHO-1 zone but not anterior foci are ECT-2 dependent. ....	108



Figure 24:	GFP::RHO-1 localization into PH-positive anterior foci and into the equatorial RHO-1 zone is independent of RGA-3/4.....	110
Figure 25:	‘RhoA flux’ mediated by RGA-3/4 regulates cytokinesis timing. ....	111
Figure 26:	Narrow GFP::RHO-1 zone width is restricted by RGA-3/4.....	113
Figure 27:	The PBS and CAAX-motif mediate RHO-1 PM binding, which represents a prerequisite for cytokinesis.....	116
Figure 28:	The PBS and CAAX-motif together are sufficient to localize RHO-1 to the PM.....	119
Figure 29:	The PBS and CAAX-motif are not sufficient to specifically accumulate RHO-1 at the equator.....	121
Figure 30:	Equatorial GFP::RHO-1 zone formation is independent of linear and branched F-actin. ....	124
Figure 31:	Equatorial GFP::RHO-1 meshwork formation requires formin-induced F-actin polymerization.....	126
Figure 32:	Equatorial GFP::RHO-1 foci in <i>cyk-1(RNAi)</i> embryos represent active RHO-1.....	128
Figure 33:	Depletion of anillin reduces GFP::RHO-1 filamentous-like structures at the equator and embryos fail first division. ....	130
Figure 34:	Myosin II and ring constriction are not required for dense GFP::RHO-1 meshwork formation at the equator. ....	131
Figure 35:	FRAP experiments to test the influence of F-actin on GFP::RHO-1 mobility.. ..	134
Figure 36:	GFP::RHO-1 and F-actin dynamics are reduced at the equatorial cortex. ..	136
Figure 37:	Movement of GFP::RHO-1 and F-actin occur in similar directions with low correlation in velocity. ....	137
Figure 38:	Reduced GFP::RHO-1 velocity at the equator is dependent on formin-induced F-actin polymerization. ....	138
Figure 39:	Reduced GFP::RHO-1 velocity at the equator is independent of NMY-2 and ring constriction. ....	140
Figure 40:	Equatorial F-actin and GFP::RHO-1 only partially co-localize. ....	142
Figure 41:	GFP::RHO-1 circumferentially aligns around the equatorial cortex following F-actin alignment. ....	144
Figure 42:	GFP::RHO-1 is present in two distinct membrane associated pools during cell division.....	151

Figure 43: The ‘RhoA flux’ contributes to a narrow GFP::RHO-1 zone..... 152

Figure 44: During anaphase the dense F-actin mesh at the cell equator acts as a physical barrier that slows down GFP::RHO-1 mobility..... 157

Figure 45: During anaphase onset GFP::RHO-1 follows F-actin alignment along the equator. .... 159

Figure 46: Model of equatorial narrow RHO-1 zone formation and maintenance during cytokinesis. .... 160

## List of Tables

Table 1:	Chemicals and Reagents .....	44
Table 2:	Solutions and Buffers.....	45
Table 3:	Enzymes.....	48
Table 4:	Kits.....	48
Table 5:	Antibodies.....	48
Table 6:	Equipment.....	49
Table 7:	Bacterial strains.....	50
Table 8:	Softwares .....	50
Table 9:	Worm strains used and generated for this study .....	52
Table 10:	Plasmids used and generated in this study.....	56
Table 11:	PCR setup for standard reaction using <i>Taq</i> -DNA polymerase .....	58
Table 12:	Thermocycler conditions for <i>Taq</i> -DNA polymerase.....	58
Table 13:	PCR setup for standard reaction using Phusion <sup>®</sup> DNA polymerase.....	58
Table 14:	Thermocycler conditions for Phusion <sup>®</sup> DNA polymerase.....	59
Table 15:	Gibson Assembly Protocol .....	60
Table 16:	Composition of MosSCI injection mix.....	62
Table 17:	Composition of in vitro transcription reaction.....	63
Table 18:	RNAi experiments .....	64
Table 19:	Buffers used for Affinity Chromatography .....	67
Table 20:	Standard curve Bradford Assay .....	67
Table 21:	Buffers used for cross linking of proteins to SulfoLink <sup>™</sup> Coupling Resin ..	68
Table 22:	Binding buffer used for GST and RHO-1 antibody purification.....	69
Table 23:	Buffers used for affinity purification .....	71
Table 24:	Dialysis Buffer .....	72
Table 25:	Buffer for size-exclusion .....	72
Table 26:	Composition of SDS-gel for SDS-gel electrophoresis .....	74
Table 27:	V <sub>H</sub> H sequences received from ChromoTek.....	98

**List of Formulas**

Formula 1:	Calculation for total amount of fragments to be used for Gibson Assembly.	60
Formula 2:	Calculation of circularity in Fiji.....	80
Formula 3:	Conversion of magnitude into velocity.....	81
Formula 4:	Calculation of the angle between two vectors .....	82
Formula 5:	Normalization of recovery curves.....	84

## List of Abbreviations

AA	Amino acid
AH	Anillin homology domain
APC	Anaphase promoting complex
APS	Ammonium persulfate
Arp2/3	Actin Related Protein 2/3
ATP	Adenosine triphosphate
<i>B. malayi</i>	<i>Brugia malayi</i>
bp	Base pair
BSA	Bovine serum albumin
<i>C. elegans</i>	<i>Caenorhabditis elegans</i>
<i>C. remanei</i>	<i>Caenorhabditis remanei</i>
CAAX	(C=cysteine, A=aliphatic amino acid, X=any AA)
Carb	Carbenicillin
CDK1	Cyclin-Dependent Kinase 1
cDNA	Complementary DNA
CPC	Chromosomal passenger complex
C-terminus	Carboxy-terminus
ddH <sub>2</sub> O	Double distilled water
DIC	Differential interference contrast
DMEM	Dulbecco's modified Eagle's medium
DNA	Deoxyribonucleic acid
dNTP	Deoxyribonucleoside triphosphate
dsRNA	Double stranded ribonucleic acid
<i>E. coli</i>	<i>Escherichia coli</i>
Ect2	Epithelial Cell Transforming 2
EDTA	Ethylenediaminetetraacetic acid
ELC	Essential light chain
ELISA	Enzyme-linked Immunosorbent Assay
ER	Endoplasmic reticulum
EtOH	Ethanol

F-actin	Filamentous actin
FBS	Fetal bovine serum
FH1/2	Formin homology domain 1/2
FR	Fluorescence recovery
FRAP	Fluorescence recovery after photobleaching
GAM	Goat anti-Mouse
GAP	GTPase activating protein
GAR	Goat anti-Rabbit
GDP	Guanosine diphosphate
GEF	Guanine nucleotide exchange factor
GFP	Green fluorescent protein
GMP	Guanosine monophosphate
GST	Glutathione-S-transferase
GTP	Guanosine triphosphate
GTPase	Guanosine Triphosphate-binding protein
h	Hours
<i>H. sapiens</i>	<i>Homo sapiens</i>
H <sub>2</sub> O	Water
HPLC	High performance liquid chromatography
INCENP	Inner Centromere Protein
IPTG	Isopropyl-β-D-thiogalactopyranosid
IT	Internal-tagged
kDa	Kilo Dalton
mCh	mCherry
2-MEA	2-Mercaptoethylamine-HCl
MgcRacGAP	Male Germ Cell RacGAP
min	Minutes
MKLP1	Mitotic Kinesin-like Protein 1
MLC	Myosin light chain
MosSCI	Mos1-mediated single-copy insertion
MP-GAP	Mitotic-Phase-GAP
mRNA	Messenger RNA
MT	Microtubule
NEBD	Nuclear envelope breakdown

NGM	Nematode growth medium
NMY-2	Non-muscle myosin II
N-terminus	Amino-terminus
Pbl	Pebble
PBS	Poly-Basic-Sequence
PCR	Polymerase chain reaction
PH	Pleckstrin homology
PIP <sub>2</sub>	Phosphatidylinositol-4,5-bisphosphat
PIV	Particle image velocimetry
Plk1	Polo-like Kinase 1
PM	Plasma membrane
PMSF	Phenylmethylsulfonyl fluoride
PRC1	Protein Regulator of Cytokinesis 1
RBD	RhoA binding domain
RFP	Red fluorescent protein
RhoA	Ras homolog family member A
RhoGDI	Rho guanine dissociation inhibitor
RLC	Regulatory light chain
RNA	Ribonucleic acid
RNAi	RNA interference
ROCK	Rho kinase
ROI	Region of interest
Rpm	Rounds per minute
RT	Room temperature
RT-PCR	Reverse transcription polymerase chain reaction
s	Seconds
<i>S. cerevisiae</i>	<i>Saccharomyces cerevisiae</i>
SD	Standard deviation
SDS	Sodium dodecyl sulfate
SEM	Standard error of the mean
sfGFP	Super folder-GFP
TCA	Trichloroacetic acid
TEMED	Tetramethylethylenediamine
ts	Temperature sensitive

UTR	Untranslated region
Vs.	Versus
WASP	Wiskott-Aldrich Syndrome protein
WAVE	WASP family verprolin homologous protein
<i>X. laevis</i>	<i>Xenopus laevis</i>



## Abstract

Cell division is a fundamental process that is required for life. Cell division ensures correct inheritance of genetic material that needs to be passed on from a mother cell to the daughter cells. Cell division is required for reproduction, growth and repair mechanisms throughout life of an organism. An essential step of cell division is termed cytokinesis and represents the formation and physical separation of the two daughter cells. By distributing the genetic and cytoplasmic contents, cell division ensures genetic inheritance from generation to generation. Cytokinesis is initiated after chromosome segregation and is tightly regulated in time and space by recruitment of essential proteins into a narrow equatorial zone, forming the contractile ring. The contractile ring is an actomyosin based structure, which generates forces to change the shape of the mother cell. The initiation of contractile ring assembly is driven by the small Guanosine Triphosphate-binding protein (GTPase) Ras homolog family member A (RhoA) that is locally activated at the equator by signals from the mitotic spindle, a microtubule (MT) based structure. RhoA cycles between an active and an inactive state, driven by a guanine nucleotide exchange factor (GEF) and a GTPase activating protein (GAP). During cytokinesis active RhoA is confined within a narrow zone at the equator. How this narrow zone of RhoA is formed and maintained is an important question in the field of cell division. RhoA is a peripheral membrane protein that is anchored to the plasma membrane (PM) by a lipid moiety. Therefore, active RhoA is thought to be able to diffuse within the PM. Free diffusion, without restrictions, would result in the displacement from the site of activation.

The present study investigated molecular mechanisms that contribute to the confinement of a narrow zone of active RhoA during cytokinesis. To address this question, our laboratory established a RhoA probe, which is functional during cytokinesis, to study RhoA dynamics in the *Caenorhabditis elegans* (*C. elegans*) one-cell embryo. The tool was designed by introducing N-terminal Green fluorescent protein (GFP)-tagged RHO-1 (*C. elegans* homolog of RhoA) into the genome and endogenous RHO-1 was depleted by RNAi (RNA interference). To address how the RhoA zone forms, genetic perturbations were combined with dynamics studies using the GFP::RHO-1 reporter during cytokinesis in the *C. elegans* one-cell embryo.

Live-cell imaging revealed that GFP::RHO-1 was present in two distinct pools during cell division. An anterior pool of GFP::RHO-1 patches and an equatorial pool of GFP::RHO-1 filamentous-like structures, arranged in a narrow GFP::RHO-1 zone. While localization of the anterior pool was driven by the two RHO-1 PM-targeting motifs (Poly-Basic-Sequence (PBS) and CAAX-motif), the equatorial pool was dependent on the activation of RHO-1 by the GEF Epithelial Cell Transforming 2 (ECT-2 in *C. elegans*). Restricting GFP::RHO-1 within a narrow zone required the two main GAPs, Rho GTPase Activating protein (RGA)-3 and RGA-4. The formation of equatorial GFP::RHO-1 filamentous-like structures was driven by formin-induced F-actin.

Based on the literature and my data I am proposing a model where (1) active RHO-1 is confined into a narrow zone by accelerated 'RhoA flux' mediated by the two main GAPs RGA-3 and RGA-4 and (2) corralling of RHO-1, by formin-induced F-actin, maintains RHO-1 at the site of activation to increase availability for efficient RHO-1 reactivation and subsequent activation of downstream effectors required for ring ingression.

## Zusammenfassung

Die Zellteilung ist fundamental für jedes Individuum und repräsentiert die Basis für das Leben von Organismen. Mittels Zellteilung wird die Weitergabe des genetischen Materials sichergestellt. Zellteilung ist wichtig für die Reproduktion, das Wachstum und Reparaturmechanismen aller Organismen. Die Zytokinese ist der letzte Schritt der Zellteilung und beschreibt die physische Trennung zweier Tochterzellen, bei dem das genetische sowie zytoplasmatische Material auf die beiden Tochterzellen aufgeteilt wird. Die Zytokinese wird nach der Auftrennung der Chromosomen eingeleitet und unterliegt einer strikten zeitlichen und räumlichen Regulierung. Diese Regulierung führt dazu, dass sich essentielle Proteine für die Zytokinese am Zelläquator in einer schmalen Zone anreichern, um dort den kontraktilen Ring zu formen. Filamentöses Aktin und Myosin bilden das Grundgerüst des kontraktilen Rings und führen zur Kontraktilität der Zelle. Damit erfolgen die Einschnürung und die physische Teilung der Mutterzelle. Die Bildung des kontraktilen Rings wird durch die kleine GTPase RhoA eingeleitet, welche zuvor durch Signale der mitotischen Spindel lokal am Zelläquator aktiviert wird. RhoA durchläuft Zyklen aus aktiver und inaktiver Form ('RhoA flux'). Die aktive Form wird durch Nukleotid Austauschfaktoren (GEF) und die inaktive Form durch GTPase aktivierende Proteine (GAP) katalysiert. Während der Zytokinese reichert sich aktives RhoA in einer schmalen Zone am Zelläquator an. Die molekularen Mechanismen, die RhoA in einer schmalen Zone halten, sind jedoch nicht bekannt. RhoA ist ein membrangebundenes Protein, welches über einen Lipid-Anker verfügt und daher die Eigenschaft besitzt frei in der Plasma Membran (PM) zu diffundieren. Bei ungehemmter Diffusion würde sich aktives RhoA jedoch entlang der PM von der Stelle der Aktivierung entfernen, womit die lokale Bildung des kontraktilen Rings nicht mehr gewährleistet wäre.

Die vorliegende Dissertation beschäftigt sich mit den molekularen Mechanismen, die zu einer schmalen Begrenzung der RhoA Zone während der Zytokinese beitragen. Um diese Fragestellung zu bearbeiten, wurde zunächst ein funktionaler RhoA Reporter für den Modellorganismus *C. elegans* in unserem Labor entwickelt, der für Studien im Einzellembryo verwendet werden kann. N-terminal mit GFP markiertes RHO-1 (*C. elegans* Homolog von RhoA) wurde in das Genom integriert und endogenes RHO-1 wurde mittels RNAi stark herunterreguliert. Unter Verwendung des GFP::RHO-1

Reporters wurde die Dynamik von GFP::RHO-1 während der Zytokinese im Einzelembryo in Echtzeit, mit verschiedenen Konditionen, verfolgt.

Mikroskopische Echtzeitanalysen haben ergeben, dass sich GFP::RHO-1 während der Zellteilung in zwei verschiedenen Regionen anreichert. Eine anteriore Anreicherung, hervorgerufen durch zwei RHO-1 Domänen (Poly-basische Sequenz (PBS) und CAAX-Domäne), die für den Transport des Proteins zur PM verantwortlich sind. Für die zweite, äquatoriale Anreicherung, ist die Aktivierung von RHO-1 durch den Nukleotid Austauschfaktor ECT-2 erforderlich. In diesem Bereich erschien aktives GFP::RHO-1 in Form filamentöser Strukturen, welche eine schmale Zone bildeten. Um eine schmale Zone zu gewährleisten, werden die beiden GAPs RGA-3/4 benötigt. Filamentöse GFP::RHO-1 Strukturen waren nur sichtbar, in Anwesenheit des Formins CYK-1, welches zur Ausbildung von F-actin am Zelläquator benötigt wird.

Aufgrund der erhobenen Daten und der zugrunde liegenden Literatur wurde folgendes Modell aufgestellt: (1) beschleunigte Zyklen aus Aktivierung und Inaktivierung von RHO-1 (erhöhter 'RhoA flux') führt zu einer Begrenzung von RHO-1 in eine schmale Zone am Zelläquator, und (2) das von RHO-1 induzierte F-aktin Gerüst am Zelläquator bildet ein enges Netzwerk unterhalb der PM, welches RHO-1 lokal am Zelläquator stabilisiert, was wiederum zur schnellen Reaktivierung von RHO-1 und nachfolgend zur lokalen Aktivierung von nachgeschalteten Effektoren führt und somit einen Beitrag zur räumlichen Regulierung leistet.

# 1 Introduction

The existence of all organisms is based on cell division. Cell division is required for reproduction in unicellular as well as in multicellular organisms. The latter further depends on multiple rounds of divisions during development, to increase cell number and to induce growth. Over time cells that die or get damaged need replacement, which is provided by cell division, showing the importance of the process not only during early development, but during the entire lifespan. The cell itself is the smallest unit of a living organism and harbors the genome that carries all information to form a multitude of different cell types. Cellular processes, for instance cell division, are controlled by gene expression and signaling and need tight regulation (Uzbekov and Prigent, 2022). The discovery of different cell cycle stages and cell division goes back to 1882 where Walther Flemming was able to stain cells and visualize subcellular structures (Flemming, 1882). Mutations in genes that regulate cell division can cause cancer and other human diseases by abnormal temporal and spatial organization of the proteins involved (Lacroix and Maddox, 2012). The division of a mother cell results in the formation of two daughter cells, where each cell contains a complement of genetic and cytoplasmic material. To ensure genetic inheritance, first deoxyribonucleic acid (DNA) needs to be duplicated, followed by the partitioning of the chromosomes and cellular components, finalized by the division of the cytoplasm termed cytokinesis (Glotzer, 2005; Green et al., 2012; D'Avino et al., 2005). These events are tightly regulated by the cell cycle machinery, including several checkpoints that guarantee completion of one process and subsequent continuation of the next (Budirahardja and Gonczy, 2009). This thesis investigates the molecular mechanisms that control cell division in time and space, and thereby contributes to the basic understanding of this complex, precisely regulated and life essential process.

## 1.1 Mitosis in animal cells

Mitosis in animal cells is characterized by a defined sequence of steps, which ensures the successful genetic inheritance from one generation to the next one. During interphase, cells grow and get prepared for cell division. Interphase includes the synthesis phase, where DNA replication takes place to double the set of chromosomes. Interphase is followed by mitosis, where the replicated chromosomes are separated and the mother cell is divided into two daughter cells (Uzbekov and Prigent, 2022). Crucial for mitosis is the highly

organized and dynamic bipolar microtubule (MT) structure, termed mitotic spindle (Figure 1). The organizing centers for the MT network are the centrosomes, building the poles of the mitotic spindle. Astral MTs emanate from the centrosomes towards the cell periphery and interpolar MTs form antiparallel bundles that overlap at the center of the cell between the segregating chromosomes (Glotzer, 2009; Sandquist et al., 2011). A protein complex, termed kinetochore, which associates with the sister chromatids during mitosis, is required for chromosomal movement. Kinetochores serve as a binding site for kinetochore MTs that are attached to the centrosomes (Figure 1 B) (Glotzer, 2009; Musacchio and Desai, 2017).

Mitosis is subdivided into the following phases: prophase, prometaphase, metaphase, anaphase and telophase (Figure 1 A). In prophase the chromosomes begin to condense and the duplicated centrosomes, membraneless organelles associated with the nucleus, begin to move apart to form the poles of the mitotic spindle. In prometaphase the event of Nuclear Envelope Breakdown (NEBD) occurs, and the chromosomes become attached to the kinetochore MTs that emanate from the spindle poles. Metaphase is reached once all chromosomes are attached to MTs. At this time point, the mitotic spindle is fully formed and the cell is prepared for the physical division. The chromosomes are aligned along the equator, between the two spindle poles, representing the metaphase plate. During early anaphase, the sister chromatids get separated by the attached MTs that move towards the opposing poles. The central spindle forms during anaphase onset, consisting of overlapping MT bundles, in between the segregating chromosomes (Green et al., 2012; D'Avino et al., 2005). Central spindle assembly requires three main components/complexes: (1) the microtubule bundling protein, termed Protein Regulator of Cytokinesis 1 (PRC1; SPD-1 in *Caenorhabditis elegans* (*C. elegans*)), (2) the centralspindlin complex consisting of the kinesin motor protein Mitotic Kinesin-like Protein 1 (MKLP1; ZEN-4 in *C. elegans*) and the Male Germ Cell RacGAP (MgcRacGAP; CYK-4 in *C. elegans*) and (3) the Chromosomal Passenger Complex (CPC) composed of Aurora B kinase, Inner Centromere Protein (INCENP), Survivin and Borealin (D'Avino and Giansanti, 2015). All of these three key components are regulated by Cyclin-Dependent Kinase 1 (CDK1) (Neef et al., 2007; Niiya et al., 2005; Menant and Karess, 2012). During metaphase to anaphase transition CDK1 activity declines, dependent on the Anaphase Promoting Complex (APC), ensuring correct temporal regulation. The APC induces sister chromatid separation as well as the degradation of Cyclin B, which is a coactivator of CDK1, therefore leading to its inactivation and initiation of mitotic exit (Pines, 2011). During anaphase, when the sister

chromatids become separated, the spindle poles move apart and a cleavage furrow forms. The cleavage furrow is a deep invagination of the plasma membrane (PM), whose formation is caused by the contraction of the underlying actin cortex. During telophase, the cleavage furrow ingresses and the nuclear envelope within the daughter cells reassemble. The chromosomes decondense and the physical separation of the two daughter cells is finalized by abscission (Green et al., 2012).

## 1.2 Cytokinesis in animal cells

The division of the cytoplasm is termed cytokinesis and describes the time point of cell division, from the initiation of the cleavage furrow till the abscission of the two daughter cells from each other (Figure 1 A). The process is precisely regulated in time and space by the cell cycle machinery and the mitotic spindle, respectively (Mishima, 2016; D'Avino et al., 2005). During anaphase onset, a contractile ring assembles underneath the PM, at the equator of the cell, consisting of several proteins required for furrow formation and ingression (Figure 1 A, Figure 3). The key initiator of the contractile ring is the small Guanosine Triphosphate-binding Protein (GTPase) Ras homolog family member A (RhoA) that itself is activated by the guanine nucleotide exchange factor (GEF) Epithelial Cell Transforming 2 (Ect2; ECT-2 in *C. elegans*) during anaphase (Basant and Glotzer, 2018). The prerequisite for cytokinesis is the formation of a narrow zone of active RhoA at the cell equator, which induces the formation of the contractile ring. Along with active RhoA, actin, myosin II, anillin and septins form the contractile ring (Figure 3) (Piekny et al., 2005). During telophase, the contractile ring ingresses followed by the final step, termed abscission, reflecting the physical separation of the two daughter cells (Figure 1) (Mierzwa and Gerlich, 2014; Pollard and O'Shaughnessy, 2019).

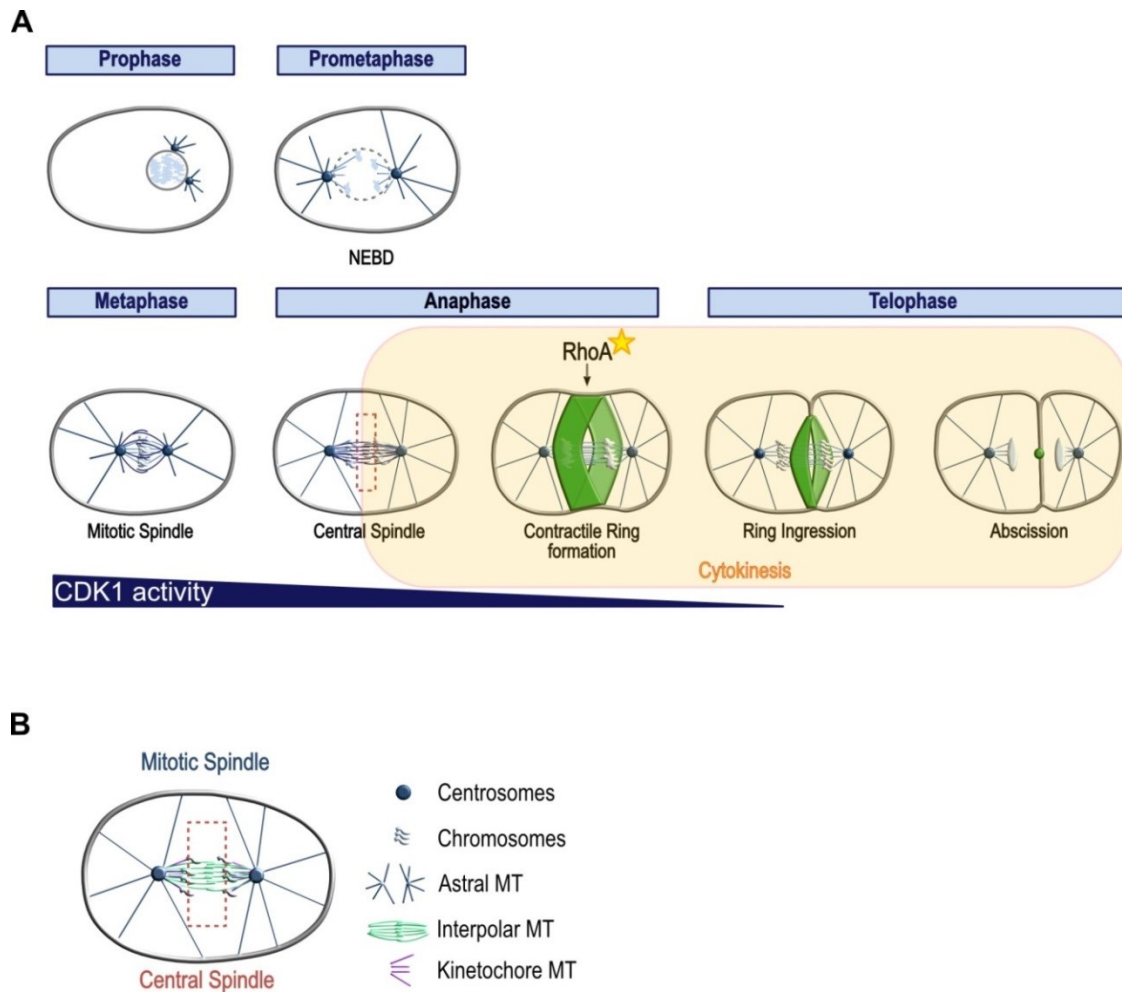


**Figure 1: Mitosis in animal cells. (A)** Schematic showing the division of a mother cell into two daughter cells from prophase to telophase. During prometaphase, the nuclear envelope breaks down (NEBD) and the chromosomes become attached to kinetochore MTs. The mitotic spindle forms and regulates cytokinesis in a spatial manner. The central spindle (Anaphase; red box) is built out of microtubule bundles in between the spindle poles and the segregating chromosomes. A contractile ring (green), initiated by active RhoA, assembles during anaphase that constricts and divides the cell into two. Cytokinesis (orange box) represents the physical separation of the daughter cells starting from furrow initiation until abscission. With decreasing CDK-1 activity, cytokinesis is initiated representing temporal regulation. Adopted from (Green et al., 2012) **(B)** Schematic of an anaphase cell where the mitotic spindle is set. The spindle consists of astral-, inter-polar- and kinetochore MTs. The MT network arises from the centrosomes, building the two poles of the spindle. During anaphase onset, the central spindle (red box) forms in between the segregating chromosomes.

### 1.2.1 RhoA maturation and regulation during cytokinesis

RhoA is a Guanosine triphosphate (GTP)-binding protein that is required for diverse cellular processes. Influencing the organization of the actomyosin and microtubule network, RhoA plays a role in cell shape regulation, locomotion and polarity (Jaffe and Hall, 2005). In particular, RhoA is essential for cell cycle regulation and cytokinesis.



During cytokinesis RhoA activates downstream effectors such as Rho kinase (ROCK) and Diaphanous-related formins which drive contractile ring formation (Pollard and O'Shaughnessy, 2019; D'Avino et al., 2005). Further, RhoA is indispensable for development for example for neurite outgrowth, dorsal closure and myogenesis (Rodríguez, 2021). Due to its diverse roles in cellular processes, loss of function of RhoA is embryonically lethal in mice and *C. elegans* (Konstantinidis et al., 2015; Motegi and Sugimoto, 2006).

The common characteristic of GTPases is to act as molecular switches that cycle between an active and inactive state (Figure 2 A). Due to a GTP binding domain, GTPases undergo conformational changes dependent on binding of GTP or guanosine diphosphate (GDP). In the active GTP-bound form RhoA interacts with downstream effectors, however when bound to GDP the protein is inactive (Hodge and Ridley, 2016). The cycle of activation and inactivation is supported by GEFs and GTPase activating proteins (GAPs), respectively (Jordan and Canman, 2012; Rossman et al., 2005; Tcherkezian and Lamarche-Vane, 2007).

RhoA is synthesized in the cytosol and undergoes post-translational modification at the endoplasmic reticulum (ER). The protein harbors two PM-targeting motifs at its carboxy-terminus (C-terminus): (1) a Poly-Basic-Sequence (PBS) and (2) a CAAX-motif (C=cysteine, A=aliphatic amino acid (AA), X=any AA) (Michaelson et al., 2001) (Figure 2 B). The latter is the signaling motif for the post-translational modification, which is a three-step enzymatic process where RhoA is equipped with a lipid anchor. First, a lipid moiety is attached to the cysteine (prenylation), followed by the cleavage of the three last AAs (AAX; proteolysis). In the final step the cysteine is methylated (Clarke, 1992). The last two enzymatic steps (proteolysis and methylation) occur at the ER (Choy et al., 1999) (Figure 2 B). After prenylation, RhoA is functional and occurs in the GDP-bound inactive and GTP-bound active form in the cell. During cytokinesis the GEF for RhoA is Ect2 (Yüce et al., 2005; Dechant and Glotzer, 2003), while Mitotic-Phase-GAP (MP-GAP) acts as the GAP in humans (Zanin et al., 2013) and the two Rho GTPase Activating proteins RGA-3 and RGA-4 in *C. elegans* (Zanin et al., 2013; Mangal et al., 2018; Schmutz et al., 2007; Schonegg and Constantinescu, 2007). The GAP catalyses the intrinsically low hydrolysis rate of 0.02 per min (Zhang and Zheng, 1998b). In the active GTP loaded state, RhoA activates downstream effectors leading to the initiation of the contractile ring (Figure 3). In the absence of active RhoA, contractile ring components fail to accumulate

at the equator and subsequently the cell fails to divide (Jantsch, 2000; Drechsel et al., 1997). After prenylation, RhoA harbors a lipid moiety at its C-terminus that can be inserted into the PM, which functions as a membrane anchor, yet the protein is present in the cytoplasm and PM-associated (Tnimov et al., 2012) (Figure 2 B). Rho guanine dissociation inhibitors (RhoGDI) can bind GDP- and GTP loaded RhoA *in vitro* (Hart et al., 1992; Hancock and Hall, 1993; Tnimov et al., 2012) and have been discussed in being able to recruit and release RhoA to and off the PM, respectively (Golding et al., 2019; Tnimov et al., 2012; Garcia, 2011). RhoGDIs form a binding pocket around the lipid moiety of RhoA and are therefore able to sequester prenylated RhoA in the cytoplasm (DerMardirossian and Bokoch, 2005; Moon and Zheng, 2003) (Figure 2 B). The PBS and CAAX-motif have been shown to be sufficient for PM localization by transient expression of the two motifs in human cells (Michaelson et al., 2001). The canonical model predicts that, during cytokinesis, Ect2 activates RhoA at the PM (Wagner and Glotzer, 2016; Su et al., 2011; Kotýnková et al., 2016; Yüce et al., 2005; D'Avino et al., 2005).

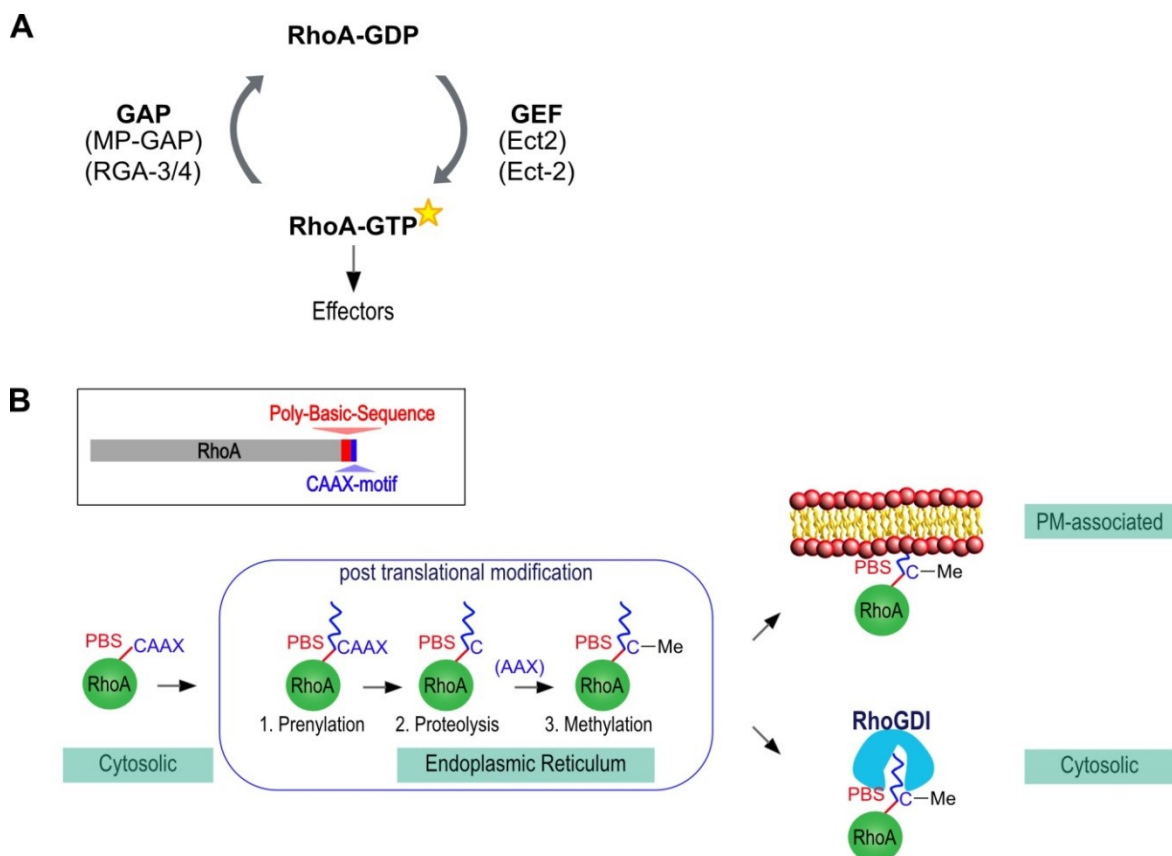


**Figure 2: RhoA maturation and regulation.** (A) RhoA cycles between an inactive GDP-bound and an active GTP-bound state. The activation is mediated by the GEF Ect2 (ECT-2 in *C. elegans*) and the intrinsically low hydrolysis rate is accelerated by the GAP MP-GAP in humans and RGA-3/4 in *C. elegans*. RhoA-GTP activates downstream effectors that lead to the formation of the contractile ring. (B) RhoA harbors two PM-targeting motifs at its C-terminus: (1) a Poly-Basic-Sequence (PBS; red) and (2) a CAAX-motif (blue). RhoA is post-translationally

modified, at the CAAX-motif, by a three step enzymatic process: (1) prenylation, (2) proteolysis and (3) methylation. The two latter steps occur at the ER. Post translational modified RhoA occurs in the cytosol and PM-associated. RhoGDI can bind GDP and GTP bound prenylated RhoA *in vitro* and sequesters the lipid moiety of RhoA within a binding pocket.

### 1.2.2 Formation of the contractile ring

The centralspindlin complex is a heterotetramer, composed of a dimer of the kinesin MKLP1 and a dimer of MgcRacGAP, which is involved in central spindle assembly. During anaphase, the polo-like kinase 1 (Plk1) phosphorylates MgcRacGAP, which in turn leads to a binding site for the GEF Ect2. Subsequently, Ect2 is recruited to the spindle midzone (Nishimura and Yonemura, 2006; Yüce et al., 2005; Somers and Saint, 2003). For human and *Drosophila* cells it was shown that Ect2 localizes to the spindle midzone as well as to the equatorial membrane during anaphase onset (Chalamalasetty et al., 2006; Su et al., 2011; Prokopenko et al., 1999). However, in *C. elegans* ECT-2 is only present at the PM but not at the spindle midzone (Motegi and Sugimoto, 2006). To test the requirement of Ect2 to be localized to the spindle midzone by the centralspindlin complex, experiments were performed inhibiting Plk1 or using phosphodeficient mutants of MgcRacGAP in human cells. Both approaches showed that indeed phosphorylation of MgcRacGAP by Plk1 is required for Ect2 localization to the spindle midzone, which in turn leads to the translocation to the equatorial membrane and is a prerequisite for cytokinesis (Petronczki et al., 2007; Burkard et al., 2009). Depletion of MgcRacGAP impedes RhoA activation in most cell types, however *C. elegans* is one exception (White and Glotzer, 2012). In the absence of MgcRacGAP the cytokinetic furrow of the one-cell embryo ingresses, but the ring regresses and cytokinesis eventually fails (Jantsch, 2000). Interestingly, *C. elegans* shows a unique parallel pathway that leads to the activation of RhoA in the early embryo. Early contractility events (described in detail in 1.5.2) such as polarity establishment and pseudocleavage formation, which are independent of centralspindlin, require the protein NOP-1. For cytokinesis NOP-1 is dispensable and only leads to a slight delay in RhoA activation. However, in the absence of both NOP-1 and MgcRacGAP the activation of RhoA is completely abolished (Tse et al., 2012). Collectively, Ect2 binding to MgcRacGAP is a prerequisite for RhoA activation at the equatorial membrane in most organisms. For *C. elegans* there is an exception, where a parallel pathway, in addition, leads to the activation of RhoA that is sufficient for furrow ingression. Using an optogenetic tool, where RhoA was locally activated by a GEF at the PM, revealed that the

PM localization of the GEF is sufficient to activate RhoA and to induce furrow formation (Wagner and Glotzer, 2016). Of note, for this study another GEF than Ect2 was used to activate RhoA. In line with these findings, Kotýnková *et al.* supported the model of PM-associated Ect2 being essential and sufficient for cytokinesis using chemical genetics studies. Targeting transgenic Ect2 to the PM during anaphase onset, in the absence of endogenous Ect2, revealed that PM-associated Ect2 is sufficient for furrow formation and ingression (Kotýnková *et al.*, 2016). Therefore, the canonical model predicts that PM-associated Ect2 activates the small GTPase RhoA, which in turn accumulates within an equatorial band, referred to as RhoA zone, where downstream effectors are activated and subsequently the contractile ring assembles to ingress a furrow.

The contractile ring is an actomyosin based structure consisting of long unbranched formin-induced filamentous actin (F-actin), active nonmuscle myosin II (hereafter referred to as myosin) and the cross-linking proteins anillin, septins, plastin and  $\alpha$ -actinin (Figure 3) (Leite *et al.*, 2019). The contractile ring is linked to the PM and by ingression bisects the mother cell (Green *et al.*, 2012). The existence of the contractile ring was first hypothesized back in 1954 (Marsland and Landau, 1954) and was verified 14 years later by electron microscopy of jellyfish eggs (Schroeder, 1968). Contractile ring assembly is initiated by active RhoA by: (1) the polymerization of F-actin and (2) the activation of myosin (Bement *et al.*, 2006; Piekny *et al.*, 2005) (Figure 3). In its active PM-associated state RhoA binds and activates formins by changing their conformation, thereby releasing their autoinhibition and inducing the polymerization of F-actin (Severson *et al.*, 2002; Watanabe *et al.*, 2008; Otomo *et al.*, 2005). Formins are highly conserved proteins that upon activation form dimers, leading to the initiation of actin filament assembly. Their ability to stay associated with the barbed ends of F-actin facilitates rapid elongation and polymerization. Formin-nucleated F-actin, that forms parallel bundles due to cross-linkers, is proposed to be the main F-actin architecture present in the contractile ring (Severson *et al.*, 2002; Davies *et al.*, 2014). Cytokinesis formins belong to the Diaphanous-related formin homology protein family. For *C. elegans* the formin crucial for cytokinesis was shown to be CYK-1 (diaphanous in *Drosophila*; mDia2 in vertebrates) (Castrillon and Wasserman, 1994; Watanabe *et al.*, 2008; Swan *et al.*, 1998).

In parallel, active RhoA activates ROCK leading to the phosphorylation of the regulatory light chain of myosin (Matsumura, 2005; Kimura *et al.*, 1996). Myosin consists of a dimer of two myosin heavy chains and two pairs each of myosin light chains (MLCs): the

regulatory light chains (RLCs) and the essential light chains (ELCs). The heavy chain is composed of a head and a tail, of which the head (N-terminus) contains the motor activity region with an actin- and ATP binding domain. While the motor domain is conserved, there is a variety of tail regions specifying different myosins and their subcellular localization. The MLCs are located at the neck. Myosins are activated by phosphorylation of the RLC, which releases the interaction of the head and the tail and leads to an interaction of the tail regions in an antiparallel manner (Brito and Sousa, 2020). This formation subsequently results in bipolar filaments, of an average 30 myosin molecules, which work together in cross-linking F-actin as well as sliding F-actin along each other (Billington et al., 2013). The latter is induced by ATP hydrolysis, leading to conformational changes, allowing myosin to move towards the barbed end of F-actin (Osório et al., 2019). In the absence of myosin cells fail cytokinesis (Matsumura et al., 2011; Mabuchi and Okuno, 1977; Schroeder, 1972; Poteryaev et al., 2005).

Another core component of the contractile ring is the scaffolding protein anillin, which links the contractile ring to the PM (Piekny and Maddox, 2010). Anillin contains several binding domains at its C-terminus that are capable of binding active RhoA (RhoA binding domain (RBD)), lipids (C2 domain), septins (pleckstrin homology (PH) domain) and microtubules (Oegema et al., 2000; Piekny and Glotzer, 2008; Sun et al., 2015; van Oostende Triplet et al., 2014; Field et al., 2005a). With the N-terminus anillin can further bind myosin, F-actin and formins (Oegema et al., 2000; Field and Alberts, 1995; Straight et al., 2005). Anillin's function rather lies in the stability and maintenance of the contractile ring than in the assembly. It has been shown for *Drosophila* and human cells that the formation of the contractile ring can occur in the absence of anillin, however cells start to oscillate when the ring tries to ingress and subsequently fail cytokinesis (Somma et al., 2002; Oegema et al., 2000; Straight et al., 2005). *C. elegans* harbors three anillin homologs, of which ANI-1 is required for cortical contractility events in the early embryo and shows the most conservation with human and *Drosophila* anillin (Maddox et al., 2005). In *C. elegans* *ani-1 RNA interference (RNAi)* results in embryonic lethality, however cytokinesis in the one-cell embryo does complete. In the fertilized *C. elegans* oocyte a number of cortical contractility events occur that are described in detail in 1.5.2. In brief, the female nucleus undergoes two rounds of meiotic divisions both resulting in the extrusion of a polar body. At the same time, the membrane builds invaginations over the entire embryo (termed ruffling) that become restricted to the anterior when polarity is established (Chalmers et al., 2012). The female pronucleus migrates towards the male

pronucleus, while a transient furrow (termed pseudocleavage furrow) ingresses and regresses. The pronuclei meet and the nuclear envelope breaks down, followed by spindle assembly and cytokinesis (Figure 9). While cytokinesis was not affected in the absence of ANI-1, polar body extrusion was abnormal or failed and ruffling as well as pseudocleavage furrow formation was absent indicating a role of ANI-1 in early contractility events (Maddox et al., 2005). It was further shown that contractile ring ingression of the first cell division became symmetric compared to asymmetric ingression in wild-type (Maddox et al., 2007). Conserved in several organisms is the equatorial cortex localization of anillin during anaphase, which follows RhoA localization (Maddox et al., 2005; Oegema et al., 2000; Straight et al., 2005).

Besides myosin and anillin, the cytokinetic actin ring is further cross-linked by  $\alpha$ -actinin, septins and plastrin (Descovich et al., 2018). Septins are filament forming GTPases and act as a scaffold, within the contractile ring, by cross-linking F-actin into curved, tightly packed arrays (Mavrakis and Azou, 2014). Septins and anillin have been reported to act as a linker for the contractile ring with the PM (Hickson and O'Farrell, 2008). Plastrins cross-link F-actin into parallel or antiparallel bundles. There is only one homolog of plastrin found in *C. elegans* (PLST-1), however there are three in humans (Ding et al., 2017).

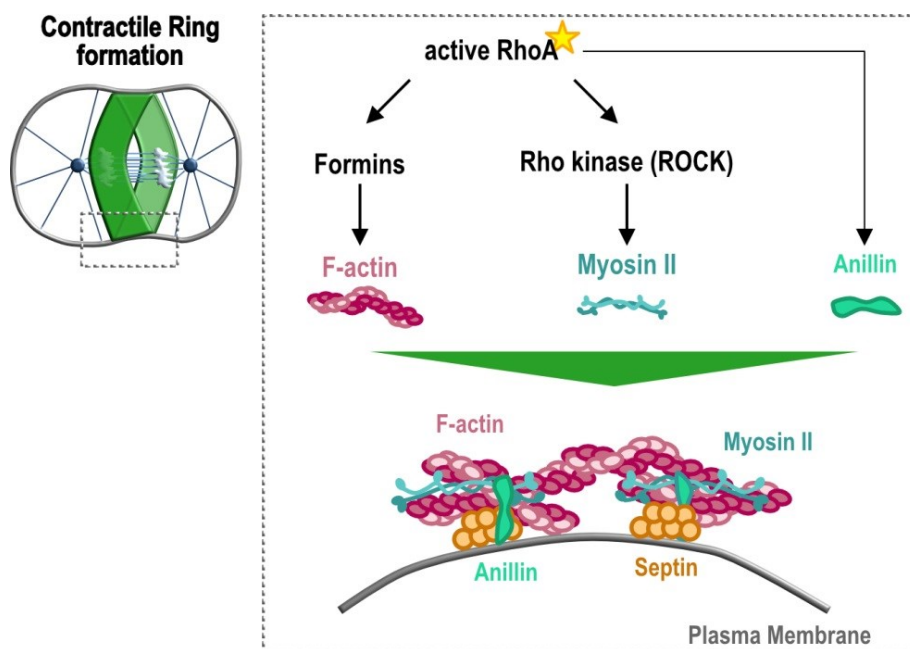


**Figure 3: Formation of the contractile ring.** During anaphase a contractile ring is formed at the equator beneath the PM. Core components of the contractile ring are F-actin (red), non-muscle myosin II (blue; NMY-2 in *C. elegans*), the scaffold protein anillin (green; ANI-1 in *C. elegans*) and septins (orange; UNC-59 and UNC-61 in *C. elegans*). Locally activated RhoA (RHO-1 in *C. elegans*) at the equator activates formins (CYK-1 in *C. elegans*) and ROCK, leading to the

polymerization of F-actin and activation of myosin. Active RhoA further recruits anillin to the equatorial zone.

### 1.2.2.1 Contractile forces and F-actin alignment during cytokinesis

For the constriction of the ring, cytoskeleton rearrangements are essential to generate forces that drive the inward pulling of the PM. The canonical model predicts the following three contributions to allow ring constriction: (1) treadmilling of F-actin; the polymerization and disassembly of F-actin, (2) actomyosin filament sliding and (3) cytoskeleton cross-linking (Pinto et al., 2013).

#### *Induction of different F-actin networks by Rho GTPases*

A balance of assembly and disassembly of F-actin was described to be important for ring ingression supporting force generation (Pinto et al., 2013; Miller, 2011; Zumdieck et al., 2007). Actin networks arise from single monomeric actin proteins with a size of 42 kDa. Actin filament assembly initially starts with a step called nucleation that forms actin dimers and trimers. Actin trimers are the basic unit for rapid filament elongation, limited by the amount of actin monomers present. Actin filaments are double stranded helical polar polymers. The two ends are called barbed- and pointed ends that differ in elongation dynamics. The latter elongates 10 times slower compared to the fast elongating barbed ends (Blanchoin and Boujemaa, 2014). After incorporation of monomeric ATP-bound actin at the barbed end, ATP is hydrolyzed in the filament and ADP-bound actin dissociates from the pointed end (McCullagh and Saunders, 2014). The initial nucleation step is thermodynamically unfavorable and can be supported by the actin monomer binding protein profilin (PFN-1 in *C. elegans*). The complex of actin monomers and profilin is subsequently used for *de novo* actin assembly by nucleation factors, including Actin Related Protein 2/3 complex (Arp2/3) and formins. F-actin is found in different architectures within the cell that show different mechanical properties, namely bundles of parallel and antiparallel actin filaments as well as cross-linked- and branched actin networks. Branched actin networks are initiated by the nucleation factor Arp2/3 complex that interacts with a preexisting actin filament. Arp2/3 needs to be activated by the Wiskott-Aldrich Syndrome protein (WASP) or WASP family verprolin homologous protein (WAVE), to induce actin filament nucleation. Branched networks of F-actin induce cell movement in a myosin-independent manner. By the formation of F-actin branches, the cell membrane is pushed leading to cell movement. However, to induce forces capping

proteins are required to block growth at barbed ends and to terminate actin polymerization. The second important nucleators of F-actin are formins, containing a formin homology 1 and 2 domain (FH1/FH2). The FH1 domain is required to capture actin-profilin complexes and the FH2 domain interacts with barbed ends of F-actin. During polymerization formins stay attached to the barbed ends (Blanchoin and Boujemaa, 2014). While polymerization of linear actin filaments, nucleated by formins, is essential for cytokinesis, Arp2/3-mediated actin nucleation plays an indirect role for cytokinesis by preventing an excess of monomeric actin. Although Arp2/3 nucleated F-actin networks are not enriched in the contractile ring, the complex is required for correct temporal formation of the ring (Chan et al., 2019). It was further proposed that Arp2/3 nucleated F-actin disturbs cytokinesis and therefore is restricted to the cell poles. This would be mediated by inactivating the small GTPase Rac at the cell equator by MgcRacGAP (Canman et al., 2008). In sum, formins are essential for cytokinesis, while the Arp2/3 complex plays a minor role. The actin cytoskeleton is a highly dynamic network that needs to adapt to the environment, which requires the ability of fast reorganization. Therefore, also disassembly of F-actin plays an important role in actin architectures. F-actin disassembly is catalyzed by cofilin or can be induced by myosin contractility. Cofilin decorates F-actin at the ADP subunits leading to fragmentation of the filaments and subsequent disassembly. Myosins are able to bring F-actin bundles into an antiparallel orientation and induce contraction, which can also lead to filament buckling and subsequent fragmentation (Blanchoin and Boujemaa, 2014).

Members of the Rho family of GTPases are regulators of the actin cytoskeleton, including Rho, Rac and Cdc42 (Hall, 1998; Kimura et al., 1996; Bishop and Hall, 2000). While all three proteins are able to induce transient contractile F-actin arrays, that can rapidly assemble and disassemble (Bement et al., 2006), only Rho induces contractile ring formation (Chircop, 2014). Rho, Rac and CDC42 promote actin assembly via different pathways and effectors to generate different cellular structures (Davidson and Wood, 2016). Common to those different pathways is the rapid polymerization and depolymerization of F-actin, ensuring fast reaction upon stimuli (D'Avino, 2009; Zumdieck et al., 2007). The different pathways of F-actin polymerization are postulated to be limited and dependent on each other by the total amount of monomeric actin present in a cell (Rotty and Bear, 2015). Rac and Cdc42 activate the WAVE complex or WASP, respectively (Soderling and Scott, 2006; Miki and Takenawa, 2003), resulting in Arp2/3 complex nucleated branched actin networks. However, Rho activates formins leading to



the polymerization of linear F-actin required for contractile ring formation (Otomo et al., 2005; Bohnert et al., 2013).

#### *Actomyosin filament sliding*

The two core components, F-actin and non-muscle myosin II, are required for force generation to induce contractility. Studies using electron microscopy revealed that linear actin filament bundles align at the equator, parallel to the ring circumference during cytokinesis (Maupin and Pollard, 1986; Henson et al., 2017; Schroeder, 1972). Therefore, it was proposed that during ring ingression forces could be generated by an antiparallel filament sliding mechanism mediated by myosin, similar to the described mechanism for sarcomeres in muscles (Pinto et al., 2013; Schroeder, 1975; Zumdieck et al., 2007). This goes in line with myosin being present within the contractile ring in an array of aligned filaments parallel to actin filaments (Henson et al., 2017). The bipolar myosin filaments walk along F-actin towards their plus ends. Since actin filaments are arranged in an antiparallel manner, this movement of myosin induces the reduction of the ring diameter (Schwayer et al., 2016). In addition, *in vitro* experiments showed that also random and disorganized actin networks could generate contractile forces with the help of myosin (Zumdieck et al., 2007; Ennomani et al., 2016; Pollard, 1976; Janson et al., 1991). Further, it was shown that the thickness of the contractile ring remains constant during constriction (Carvalho et al., 2009). This implies that F-actin needs to be disassembled to remain the thickness of the ring, while the circumference decreases. The exact mechanism of myosin dependent contractility of the contractile ring remains an open question in the field. Myosin is capable to act as an F-actin cross-linker and is also able to slide F-actin filaments. Both characteristics can contribute to contractility of the actomyosin network. It was long questioned, whether myosin motor activity is required for contractility. A study in *C. elegans* using NMY-2 motor mutants (one of two *C. elegans* myosins, of which only NMY-2 is essential for cytokinesis) showed that indeed the motor activity represents the driving force and determines the pace of constriction (Osório et al., 2019).

#### *Cytoskeleton cross-linking in the contractile ring*

F-actin forms bundles and networks with the help of actin cross-linkers, which are postulated to be required for contractility induction (Schwayer et al., 2016). Cross-linking networks are made of already existing F-actin polymers (mainly nucleated by formins) that are connected by cross-linking proteins, which bundle F-actin into parallel, antiparallel or mixed polarity structures. Dependent on the cross-linker, bundles can either be packed in a

dense manner or rather loose allowing F-actin sliding. While parallel bundles are found for example in filopodia and microvilli, antiparallel bundles are found in the contractile ring during cytokinesis. Known actin cross-linkers for cytokinesis are myosin, anillin, septins, plastin and  $\alpha$ -actinin (Descovich et al., 2018).

In summary, contractile forces can be induced by a filament sliding mechanism, by network ingression that requires treadmilling of F-actin and actin cross-linkers or most likely a combination of the mentioned (Pinto et al., 2013; Zumdieck et al., 2007).

#### *F-actin alignment during cytokinesis*

Several studies addressed the question of contractile ring filament alignment. However, visualization of filament orientation is not trivial. Using fluorescence polarization microscopy Fishkind and co-workers showed in mammalian cells that actin filament alignment was increased during late cytokinesis (Fishkind and Wang, 1993). Another study showed random oriented actin filaments when furrow ingression was initiated, while a partial alignment occurs later during cytokinesis mediated by myosin and ring constriction (Spira and Cuylen, 2017). Filament alignment could be an active mechanism that might be supported by myosin pulling forces or could be the consequence of mechanical forces induced by cortical actomyosin flow as proposed by White and Borisy (White and Borisy, 1983). A recent study in *C. elegans* proposes a model of “filament-guided filament assembly” (Li and Munro, 2021). The authors tracked formin-induced actin filament formation and found that newly formed filaments orient along existing F-actin, representing an additional mechanism of filament alignment during cytokinesis. Another study in *C. elegans* revealed that compression by actomyosin cortical flow leads to ring formation, while active alignment enhances ring formation (Reymann et al., 2016). In the same study it was shown that, prior to cytokinesis, actin filaments are randomly organized and upon cleavage furrow initiation F-actin aligns circumferentially around the equator (Figure 4), supporting the findings from 1993 and 2017 (Spira and Cuylen, 2017; Fishkind and Wang, 1993).

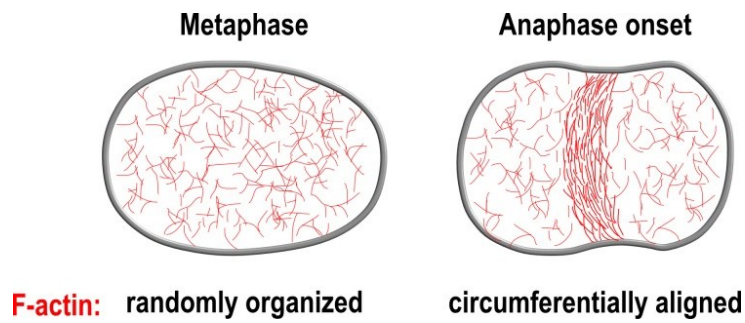


**Figure 4: F-actin alignment during cytokinesis.** The canonical model predicts that F-actin circumferentially aligns at the equatorial cortex during anaphase onset. At earlier stages F-actin is randomly organized. Adapted from (Spira and Cuylen, 2017; Leite et al., 2019).

### 1.2.3 Positioning of the division plane

To properly divide the cytoplasmic and genetic content of the mother cell into the two daughter cells, the contractile ring needs precise positioning at the cell equator during cytokinesis. Pioneering work from 1961 showed that the spatial position of the division plane is defined by cues derived from the mitotic spindle. With physical perturbation experiments Rappaport *et al.* showed that an additional spindle, in a common cytoplasm, induced two division planes (Rappaport, 1961) and relocating a spindle during anaphase induced several furrows (Rappaport, 1985). These findings indicated that the division plane is determined by the mitotic spindle in between the opposing asters, yet the mechanisms behind remained elusive. Supporting Rappaport's findings, Bement *et al.* showed that active RhoA zones in sea urchin embryos were sensitive to and dependent on the mitotic spindle using physical perturbation experiments (Bement and Benink, 2005). The present understanding of the signaling cues that position the division plane is a combination of positive and negative stimuli. The central spindle contributes to the positioning of the contractile ring via centralspindlin, which activates and then localizes Ect2 to the division site leading to the activation of RhoA (D'Avino and Giansanti, 2015; Green et al., 2012; Mishima, 2016). This positive stimulus accumulates active RhoA, which induces the formation of the contractile ring at the equatorial membrane (Figure 5). Interestingly, *C. elegans* embryos deficient in central spindle formation, due to a mutation in SPD-1, which is required for MT bundling, showed normal first divisions, however failed in subsequent cell divisions (Verbrugghe and White, 2004). This indicates that signals from the central spindle cannot be the sole source for positioning. These findings were supported by a recent study in *C. elegans*, showing that in the absence of the central

spindle astral MTs are sufficient to form a midbody and to complete cytokinesis (Hirsch et al., 2022). An additional signal arises from the astral MTs contributing to the positioning of the division plane. Initially, two opposing theories about the contribution of astral MTs were thought to play a role: (1) Astral MT build a scaffold for a positive stimulus that is transported along astral MTs. The stimulus arises from both asters, therefore a high density zone at the equatorial cortex is built, which induces contractility. (2) Astral MT show higher density at the polar region, leading to a stiffer polar cortex compared to the equatorial zone. Therefore, contractility is favored at the equator, representing a negative stimulus (D'Avino et al., 2005; Glotzer, 2004) (Figure 5). Even though the two astral MT theories first sounded controversial, it is now accepted that both models can coexist. Recently, our research group identified a molecular mechanism of an inhibitory signal arising from astral MTs in *C. elegans* (Mangal et al., 2018). Using molecular perturbation assay in combination with live-cell imaging of the one-cell embryo, we found that the activation of Aurora A kinase by TPXL-1 on astral MTs is required for polar clearing of contractile ring components. The term polar clearing refers to the removal of contractile ring components at the poles during anaphase onset. Here we used anillin as a marker for contractile ring components, which mimics RhoA localization. While an initial PM-localized pool of anillin at the anterior cortex is removed during anaphase onset, the pool of PM-localized anillin at the equator increases. We showed that contractile ring components are restricted to the equatorial membrane in an Aurora A kinase dependent manner (Mangal et al., 2018). The described signal represents a negative aster-based stimulus contributing to the positioning of the division plane (Figure 5). In summary, the combination of different positive and negative stimuli is required to localize the contractile ring at the correct position during cytokinesis.

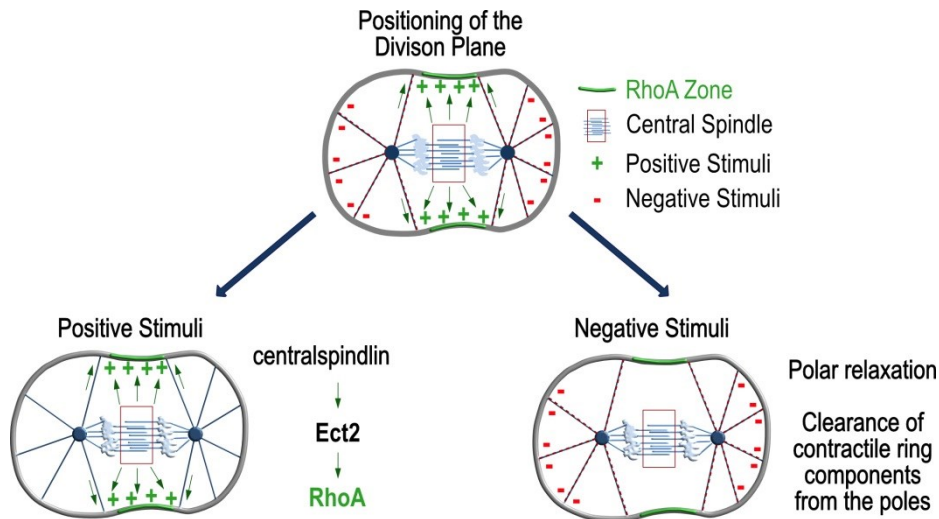


**Figure 5: Positioning of the division plane.** The canonical model predicts that signals from the central spindle MTs (positive stimuli) and the astral MTs (negative stimuli) contribute to division plane positioning.

#### 1.2.4 The formation of a narrow RhoA activity zone at the equatorial cortex

Small GTPases form dynamic activity zones at the site of action to induce contractility, of which two well studied mechanisms are wound healing and cytokinesis (Bement and Benink, 2005; Kamijo et al., 2006; Yüce et al., 2005; Yonemura and Hirao, 2004). The common characteristic of the activity zone of small GTPases is a constrained semi-stable enrichment of the protein at the PM (Bement et al., 2006). During cytokinesis active RhoA assembles into a narrow zone that is highly organized in time and space. Active RhoA assembly ensures the correct positioning of the contractile ring, followed by ingression and abscission, to give rise to two daughter cells each containing the genetic and cytoplasmic content of the mother cell.

To study active RhoA zone formation different approaches have been used to visualize RhoA during cytokinesis. In fixed tissue cells endogenous RhoA was visualized by immunofluorescence with an antibody against RhoA. Using this approach RhoA was shown to localize into a narrow zone at the equatorial membrane (Yonemura and Hirao, 2004; Takaishi et al., 1995; Yüce et al., 2005). In human cells a stable cell line was established that overexpressed *C. elegans* RHO-1 fused to YFP (YFP::RHO-1), to test the function of the Ect2 centralspindlin complex on RhoA. Localization of YFP::RHO-1 to the equatorial PM was verified by simultaneous staining against endogenous RhoA. Using this

approach the authors showed that YFP::RHO-1 localized into a narrow zone at the equatorial membrane during anaphase in live-cell imaging, in the presence of endogenous RhoA (Yüce et al., 2005). A study in *C. elegans* was performed using a fusion protein of Green fluorescent protein (GFP)-tagged RHO-1 under the *pie-1* promoter that was integrated into the genome, in addition to endogenous RHO-1. Following its localization, using live-cell imaging, the authors showed that GFP::RHO-1 localized to the equatorial cortex before and during ring ingression, where RHO-1 appeared in filamentous structures and small dots localized into a narrow zone. In *ect-2(RNAi)* embryos GFP::RHO-1 was no longer visible at the equatorial cortex. The protein appeared in the same region as a marker for F-actin (Motegi et al., 2006). Another approach was used by Benink *et al.*, who performed experiments using *Xenopus* oocytes to address spatial segregation of active Rho GTPases during wound healing. To follow active RhoA and Cdc42 they used the RhoA binding domain of mouse rhotekin (rGBD) fused to eGFP and the Cdc42 binding domain of N-WASP fused to eGFP or mRFP. The constructs were microinjected in oocytes and were subsequently imaged either in fixed or live samples (Benink and Bement, 2005). The same probe (eGFP-rGBD) was used to follow active RhoA during cytokinesis in sea urchin embryos. It was shown that equatorial active RhoA forms a narrow zone that remains constant over time in respect to cell ingression (Bement and Benink, 2005), indicating that the activation and inactivation of RhoA might occur rather simultaneously than sequentially. In the same study the authors showed that the RhoA zone shows a quick response, in disassembly and assembly, when the spindle was physically manipulated. In summary, using different approaches in a variety of organisms it was shown that RhoA localizes into a narrow activity zone at the equatorial cortex.

### **1.2.5 Maintenance of a narrow RhoA zone at the equatorial cortex**

The question how a narrow zone of RhoA is maintained in between the segregating chromosomes still remains an open question in the field. A constant recruitment of active RhoA to the PM without inactivation would result in an increase and broadening of the RhoA zone, which was not detected by imaging using the mentioned approaches in 1.2.4. Due to the low intrinsic hydrolysis rate of RhoA, constant recruitment and activation of RhoA at the PM would lead to spreading along the PM, considering the membrane as a medium allowing free lateral diffusion (Bement et al., 2006).

The plasma membrane provides a barrier between the cytoplasm of a cell and its surrounding environment. The separation of the two aqueous milieus is ensured by a

phospholipid bilayer. Besides phospholipids also proteins are fundamental components of the PM that are important to quickly respond to intra- and extracellular stimuli. Proteins in the PM occur as transmembrane- or peripheral proteins (Singer, 2004). The latter is true for the small GTPase RhoA, which can be transiently anchored within the PM by covalently attached lipids. The basic model for biological membranes was proposed in 1972 by Jonathan Singer and Garth Nicolson and was termed the ‘fluid mosaic model’ (Singer and Nicolson, 1972). New insights on membrane organization have extended this model over the past 48 years, yet the basic concept of a flexible structure, where both phospholipids and proteins can diffuse laterally (in a restricted manner) within the membrane, is still up to date (Akhunzada et al., 2019). The PM is covered by the cortical actin-cytoskeleton and the pericellular matrix at the inner and outer surface of the cell, respectively. These structures peripheral to the membrane as well as the interaction between lipids and intramembrane proteins are involved in restricting the mobility of membrane components and therefore the diffusion within the PM (Vereb et al., 2003). Considering a two dimensional fluid, as it was first described by Singer and Nicolson, free lateral diffusion is expected (Saffman and Delbrück, 1975). However, performing diffusion experiments within artificial membranes that were based on the theory of the ‘fluid mosaic model’, showed higher diffusion coefficients in artificial membranes compared to the ones obtained from plasma membrane experiments (Ritchie et al., 2003). The second inconsistency that was puzzling was the fact that oligomers or protein complexes showed a drastic drop in diffusion coefficients compared to monomers (Kusumi et al., 2005). However, considering the ‘fluid mosaic model’ and Brownian motion within the PM, protein size should not show any effect on the diffusion coefficient (Saffman and Delbrück, 1975). Using fluorescence recovery after photobleaching (FRAP) experiments and single molecule tracking, scientists in the field proposed that the actin cytoskeleton acts as a fence beneath the PM (Sheetz et al., 1980; Sheetz, 1983; Edidin et al., 1991). Further, transmembrane proteins that link the actin cytoskeleton with phospholipids at the outer leaflet of the membrane could act as pickets (Sheetz, 1993; Lee et al., 1993). The actin cytoskeleton together with transmembrane proteins was described as the ‘membrane-skeleton picket fence model’ (Morone et al., 2006; Sheetz, 1983) (Figure 6 A). The ‘membrane-skeleton picket fence model’ is an extension to the ‘fluid-mosaic model’. The model explains the discrepancy between a theoretical free diffusion within the PM and the observed slower diffusion coefficients found for components in the PM. Due to the actin network the PM is compartmentalized and free diffusion can only occur within

compartments (Figure 6 B). However, it was shown that proteins are able to hop onto an adjacent compartment termed as ‘hop diffusion’ (Sako and Kusumi, 1994; Kusumi et al., 1993; Saxton, 1995). This model further explains the discrepancy between diffusion coefficients found for monomers and oligomers. Spatial hindrance by the actin cytoskeleton shows stronger impact by increased particle size, due to oligomerization or protein complex formation. It was further postulated that larger protein complexes could even be immobilized by the actin fence by a corralling mechanism (Kusumi et al., 2005) (Figure 6 B; c).

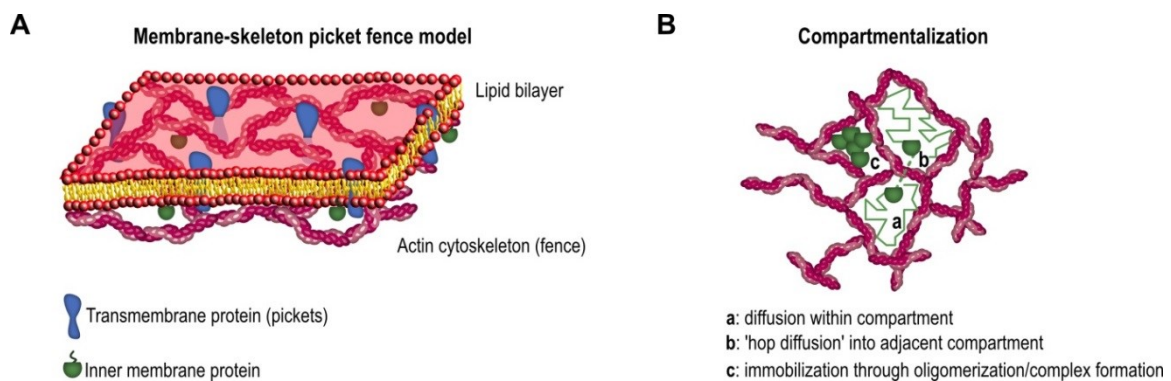


**Figure 6: The ‘membrane-skeleton picket fence model’.** (A) Schematic showing the lipid bilayer and the adjacent actin cytoskeleton on the inner membrane. The actin network beneath the PM forms a fence-like structure that is connected to the PM. Transmembrane proteins (blue) connect the cytoskeleton with the outer leaflet of the membrane and act as pickets of the fence. Inner membrane proteins (green) are able to diffuse within the PM, however restricted by the actin fence and pickets. (B) Due to the actin cytoskeleton the PM was shown to be compartmentalized. Inner membrane proteins and lipids are restricted in diffusion by the fence structure. (a) Within one compartment proteins are able to freely diffuse. (b) Proteins can further hop into an adjacent compartment, termed ‘hop diffusion’. (c) Oligomerization or protein complex formation within one compartment can lead to immobilization. Adapted from (Ritchie et al., 2003).

Restricting RhoA into a narrow activity zone was postulated concerning the phenomenon of a corralling mechanism (Bement et al., 2006). Corralling could be achieved by different means: (1) the actomyosin cortex, (2) anchorage within the PM, (3) effector binding, or a combination of the three possibilities.

Considering the ‘membrane-skeleton picket fence model’, Heinemann *et al.* addressed the question, whether indeed the actin cytoskeleton is able to reduce the mobility of proteins and lipids within the PM. Interestingly, the diffusion coefficient of both lipids and proteins was shown to be reduced proportional to an increase of actin densities in an artificial system. Lipids were less affected compared to proteins, which is likely to be the case because of particle size. Diffusion coefficients were reduced from  $9.9 \pm 0.6 \mu\text{m}^2/\text{s}$  and



$5.9 \pm 0.9 \mu\text{m}^2/\text{s}$  in an actin-free medium to  $4.8 \pm 0.4 \mu\text{m}^2/\text{s}$  and  $0.7 \pm 0.1 \mu\text{m}^2/\text{s}$  in the presence of actin for a lipid (DOPE) and a membrane binding protein (CtxB), respectively (Heinemann et al., 2013). The experiment indicated that indeed an actin meshwork beneath the PM can restrict the mobility of lipids and proteins within the PM. However, regarding RhoA during cytokinesis there is evidence that corralling by the actomyosin cortex cannot be the sole restricting mechanism towards RhoA zone. Studies using actin drugs that prevent actin assembly showed that in the absence of F-actin, a RhoA zone still forms (Bement and Benink, 2005; Hickson and O'Farrell, 2008). However, following RhoA zone after anaphase onset revealed that the maintenance at the equator was lost and RhoA moved inward toward the spindle poles (Bement and Benink, 2005). Although F-actin was shown to not be required for RhoA zone formation, the corralling of RhoA and its regulators within the contractile ring underneath the PM could still be a mechanism contributing to the maintenance of the RhoA zone during anaphase onset, redundantly with other mechanisms.

Another possible explanation of RhoA restriction within a narrow zone is based on the postulated 'RhoA flux model' (Bement et al., 2006; Miller and Bement, 2009). This model describes fast cycles of activation and inactivation of the small GTPase by GEF and GAP regulation, respectively. The model predicts that reducing flux by lacking GAP activity would broaden the RhoA zone (Figure 7). Initially, it was postulated that the Ect2-MgcRacGAP complex, that is required for activating RhoA at the equatorial membrane (Nishimura and Yonemura, 2006; Kamijo et al., 2006; Yüce et al., 2005; Zhao and Fang, 2005; Somers and Saint, 2003), leads to a fast cycling of RhoA during cytokinesis (Miller and Bement, 2009). Ect2, as a GEF, activates RhoA. MgcRacGAP contains a GAP domain that is able to inactivate Rho family GTPases such as RhoA, Cdc42 and Rac. Since RhoA is essential for cytokinesis, it was first postulated that the MgcRacGAP inactivates RhoA during this process. Alternatively, it was thought that RhoA is inactivated by MgcRacGAP during late stages of cytokinesis in an Aurora B dependent manner (Minoshima et al., 2003). Although it was shown that the GAP activity of MgcRacGAP is required for cytokinesis (Canman et al., 2008; Somers and Saint, 2003), its GAP activity is rather specific for Rac than RhoA (Canman et al., 2008). Canman *et al.* specifically disrupted the GAP activity of MgcRacGAP (CYK-4 in *C. elegans*) and tested its function towards RhoA. They showed that (1) the GAP activity was required for cytokinesis and (2) the cytokinesis defects could be rescued by depletion of Rac, indicating that MgcRacGAP rather inactivates Rac not RhoA. The authors postulated that the

inactivation of Rac and its downstream effectors Arp2/3 is required for cytokinesis to successfully complete (Canman et al., 2008). The two GAPs RGA-3 and RGA-4 were first shown to be required to inactivate RhoA during polarity establishment (Schmutz et al., 2007; Schonegg and Constantinescu, 2007) and later it was shown that also during cytokinesis RGA-3/4 are the two main GAPs essential for inactivating RhoA in *C. elegans* (Zanin et al., 2013). Zanin *et al.* showed in *C. elegans*, by using catalytically-defective GAP point mutations of MgcRacGAP and RGA-3, that RGA-3 resulted in hypercontractility, while MgcRacGAP rather showed decreased contractility. Increased contractility was used as readout for active RhoA. Therefore, the two functionally redundant RhoA GAP homologous, RGA-3 and RGA-4, and not MgcRacGAP inactivate RhoA during cytokinesis in *C. elegans*.

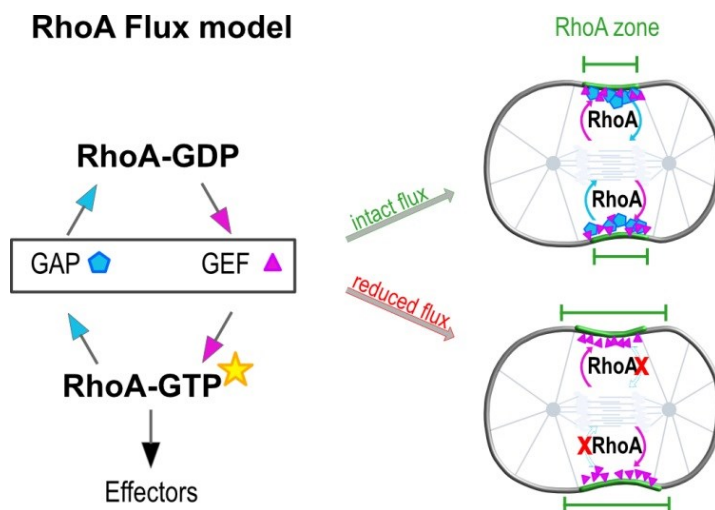


**Figure 7: The ‘RhoA flux model’.** The ‘RhoA flux model’ describes the accelerated cycling of RhoA through the activation and inactivation by GEF and GAPs, respectively. A fast cycling of RhoA supports the restriction of RhoA into a narrow zone (intact flux), while a reduced flux, due to the lack of GAP activity, results in a broader RhoA zone.

### 1.3 Cortical excitability

The actin cytoskeleton forms a powerful network underneath the PM, termed the cell cortex, which is able to induce rapid changes in cell morphology, important for cell movement and contractility events such as cytokinesis (Pollard and Cooper, 2009; Blanchoin and Boujema, 2014). The actin cortex is anchored to the PM by linker proteins (Clark et al., 2014). The cortical network is a highly dynamic structure that supports the PM and determines cell shape by tension created by myosin-generated forces. There is increasing evidence that the cortex acts as an excitable medium, which upon a local

stimulus transitions from a low activity state into an excited high activity state with the ability of spreading the excited state within the medium, subsequently resulting in a travelling wave. This phenomenon was termed cortical excitability and was first described in *Dictyostelium discoideum* (Vicker, 2000). The requirement for an excitable medium is the fast activation and slow negative feedback for inactivation of a component resulting in bistable front propagation. If a local pulse of activation occurs, this amplitude will be spread over the entire system and tend to spread away from the source driven by diffusion, resulting in a travelling wave (Iglesias and Devreotes, 2012; Priya et al., 2017). This activator-inhibitor mechanism has been described for cytokinesis in frog and echinoderm embryos, where RhoA acts as the activator while F-actin acts as the inhibitor (Bement et al., 2015). The authors showed the existence of traveling waves of RhoA and F-actin, where F-actin with a slight delay followed RhoA. They propose a model, where autoactivation of RhoA induces traveling waves, while the delayed inhibition of RhoA by F-actin leads to the shift in wavefronts (Bement et al., 2015). From these experiments the question arises how a static cytokinetic ring can ingress, where RhoA and F-actin coexist at the same location, when RhoA and F-actin act in an activator-inhibitor-manner. It was proposed by mathematical modeling that the increase of Ect2 at the equatorial membrane leads to a changed threshold and stable steady state, losing the requirement to propagate the activity within a traveling wave. Therefore, RhoA and F-actin are postulated to be able to coexist even though the activator-inhibitor mechanism retains its functionality (Goryachev et al., 2016). A similar question was addressed for RhoA activity zones at the epithelial zonula adherens, where an activator-inhibitor mechanism was described for RhoA and myosin (Priya et al., 2017). The authors used mathematical modeling to reveal how a static contractility zone can occur in an excitable medium, prone of propagating active signals with delocalization of the activity away from a zone of activation. They postulate that the bistable feedback is counteracted by an inward advection derived from contractility driven by myosin (Priya et al., 2017). Therefore, there are two critical characteristics of the cortex that make a stable RhoA activity zone possible: (1) behavior as an excitable medium and (2) the ability to generate contractile forces. Further evidence for an activator-inhibitor mechanism was shown by a study in the *C. elegans* early embryo using genetic perturbation and quantitative imaging (Michaux et al., 2018). The authors showed the presence of pulsed contractions in two-cell stage embryos, which consist of local RhoA, F-actin and myosin. Consistent to earlier findings in echinoderm eggs (Bement et al., 2015), RhoA activation and inactivation peak ahead of F-actin and myosin.

The authors postulate an autoactivation of RhoA and a delayed negative feedback by the GAPs RGA-3/4, which they claim are recruited by F-actin. They further show that pulse activity is independent of myosin, therefore postulating a mechanism that does not require myosin force generation (Michaux et al., 2018). In conclusion, several studies have shown evidence for an activator-inhibitor mechanism for different cellular events that require contractility (Priya et al., 2017; Graessl et al., 2017; Michaux et al., 2018; Michaud et al., 2021; Segal et al., 2018; Bement et al., 2015; Goryachev et al., 2016). They all share the common pathway of RhoA activity zones, activating actomyosin networks. The canonical model predicts an autoactivation of RhoA, which leads to an excited state above the threshold of the excitable medium, leading to a spreading of activity throughout the system. The RhoA peak is subsequently inhibited by delayed feedback via the actomyosin network, of which the favorable idea is that RhoA is negatively regulated by F-actin, which has been shown to recruit the GAP for RhoA (Michaux et al., 2018; Bement et al., 2015).

#### **1.4 Strategies to visualize RhoA *in vivo***

To gain insights into molecular mechanisms and pathways on a protein level *in vivo*, visualization of target proteins is an indispensable tool. Immunofluorescence staining of fixed samples has the disadvantage that dynamic processes cannot be studied well, since this method is restricted in its temporal resolution. For dynamic processes, such as cytokinesis, live-cell imaging is a favorable method of choice to dissect its spatiotemporal dynamics. The prerequisite to follow a specific protein of interest, using fluorescence microscopy, is labelling the protein in a manner that the protein is not affected and remains its physiological function. This can be achieved by different means: (1) labelling the protein of interest with a fluorophore or (2) using a specific dye or biosensor to monitor the protein of interest.

Tagging the small GTPase RhoA with a fluorophore is not trivial and was shown to impair correct localization and function of RhoA (Yonemura and Hirao, 2004). Therefore, most studies investigating RhoA dynamics were performed in the presence of endogenous RhoA, where functionality of the transgene was not tested (Budnar et al., 2019; Michaelson et al., 2001; Abreu, 2014; Motegi and Sugimoto, 2006; Nakayama et al., 2009; Schonegg and Constantinescu, 2007; Yoshida et al., 2009). As an alternative, domains of proteins with binding capacity for active RhoA were successfully used as biosensors to monitor active RhoA (Bement and Benink, 2005; Piekny and Glotzer, 2008). Using the binding domain of rhotekin (Bement and Benink, 2005) or anillin (Piekny and Glotzer,

2008) fused to a fluorophore, the authors showed that these biosensors localized to the equatorial membrane as previously shown for RhoA by immunostainings (Yonemura and Hirao, 2004; Takaishi et al., 1995; Yüce et al., 2005). In contrast to labelling the full-length protein, where active and inactive RhoA can be followed, biosensors that are downstream effectors of RhoA specifically monitor active RhoA. However, one caveat of those sensors is that they might occupy active RhoA and therefore alter RhoA signaling.

RhoA consists of a C-terminal CAAX-motif, which due to prenylation is cleaved off during post-translational modification (1.2.1). Therefore, tagging RhoA at the C-terminus is not an option. Yoshida *et al.* generated a GFP-RhoA fusion protein in budding yeast that was expressed from the native promoter with endogenous levels in a *rho1* null strain (Yoshida et al., 2009). The localization of GFP-tagged RhoA was consistent with endogenous RhoA, determined by immunofluorescence, representing the first fusion transgene able to complement for endogenous protein. Bendezú *et al.* established an internal-tagged fusion protein of the small GTPase Cdc42 in fission yeast. The authors chose a solvent-exposed poorly conserved external loop that was distant from effector binding sites. A construct was generated where GFP or mCherry with a linker sequence were integrated within the Cdc42 coding sequence. The fusion protein was expressed from a plasmid, which was shown to complement a Cdc42 temperature sensitive (ts) mutant. Next, strains were engineered that expressed the construct under the endogenous promoter, in the absence of endogenous protein. Strains expressing the internal-tagged protein showed no difference in cell growth and division compared to control, indicating that indeed internal-tagging of Cdc42 can complement for endogenous Cdc42 in fission yeast (Bendezú et al., 2015). During the course of my study, the internal-tagging strategy was also employed for RhoA and Cdc42 in *X. laevis* embryos, where the probes were injected and expressed as exogenous GTPases in addition to endogenous RhoA and Cdc42, respectively (Golding et al., 2019). Fluorescently internal-tagged RhoA localized to the equatorial furrow region during cytokinesis in the presence of endogenous RhoA. To also test whether the internal-tagged protein can complement for endogenous RhoA, they generated an internal-tagged RhoA mutated for the C3 ribosylation site to make the protein resistant for C3 exotransferase, which is a RhoA specific toxin. Applying the C3 exotransferase inhibited endogenous RhoA, while the mutant was not affected and showed a specific Rho zone around wounds that closed with similar kinetics as control (Golding et al., 2019). This approach was the first showing a functional GFP-fusion protein for RhoA in animal cells that was used for experiments regarding wound repair.

## 1.5 *C. elegans* as model organism to study cytokinesis

*C. elegans* is a nematode with a size of 1 mm that can easily be cultivated on petri dishes in the laboratory using *E. coli* as food source. The organism is an ideal candidate for cell developmental and cell biological research, due to transparency and a rapid life cycle. Especially the one-cell embryo, with a size of 30  $\mu\text{m}$  x 50  $\mu\text{m}$ , has been used for studies regarding cell division. The embryo is well suited as model organism since its divisions are stereotypical and temporally invariant and molecular perturbation studies can be conducted using RNAi. By microinjections of dsRNA into the syncytial gonad, the target mRNA is degraded while pre-existing protein present within the gonad is diminished over time being packed into early oocytes. Therefore, oocytes produced about 36 h post injection are reproducibly depleted of the targeted gene product (Oegema and Hyman, 2006).

### 1.5.1 *C. elegans* life cycle

The reproductive life cycle of *C. elegans* is three days, which slightly varies depending on the cultivation temperature. The favorable temperature is between 12°C and 25°C (Corsi et al., 2015). The majority of the populations are self-fertilizing hermaphrodites and only less than 0.2 % arises as male. The mature self-fertilized hermaphrodite produces about 300 progeny, mating with male increases the number up to 1400. Hermaphrodites produce oocytes for approximately 4 days. After this fertile period the adult can live for further 15 days. The life cycle of *C. elegans* is shown in Figure 8. At 22°C the *in utero* development takes about 150 min, of which the first division of the zygote occurs about 40 min post-fertilization. The eggs are laid at gastrula stage, when the embryo harbors ~30 cells. *Ex utero* development lasts for about 9 hours. Afterwards, the animals hatch as larvae with a size of 250  $\mu\text{m}$ . The first larval stage is termed L1, followed by three more larval stages L2-L4. In case of environmental changes as high temperature, no food source or crowding the L1 larvae change to a resting stage, termed dauer larvae, where the animal can survive under unfavorable environmental conditions for up to 4 month (Golden and Riddle, 1984). When dauer larvae are back on favorable conditions they enter the life cycle as L4 larvae and become mature adults. The time an animal develops from one larval stage to the next takes between 8 to 12 hours (at 22°C) as indicated in Figure 8.

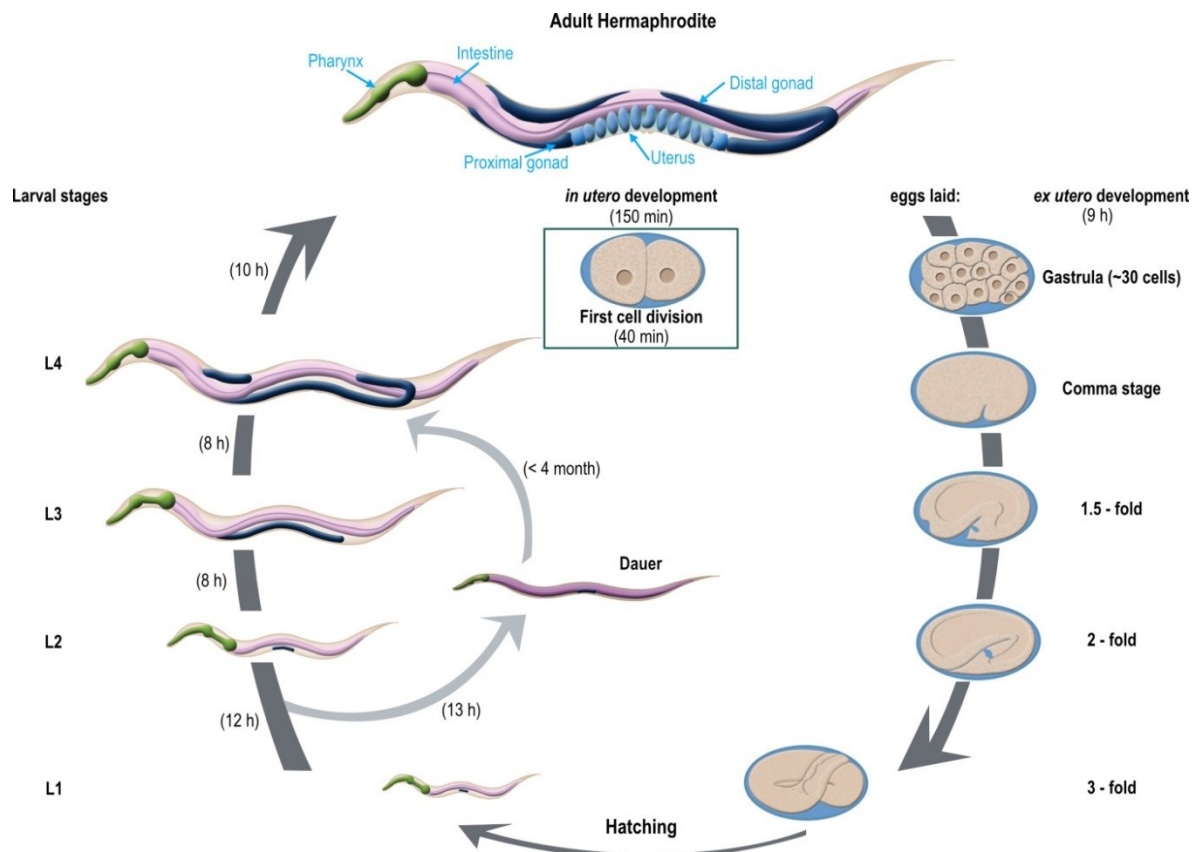


**Figure 8: *C. elegans* life cycle.** The *in utero* development of a *C. elegans* embryo takes around 150 min. Afterwards the eggs are laid in gastrula stage and the *ex utero* development of the eggs is accomplished after 9 hours when the animal hatches as L1 larva. Until reaching adulthood the worm passes three more larval stages, L2-L4. The time in brackets indicates the duration of development between the different stages. Adapted from (Hall and Altun, 2009).

### 1.5.2 Cell division of the *C. elegans* one-cell embryo

Fertilization takes place in the spermathecal, where mature oocytes are arrested in meiotic prophase. When the sperm enters the oocyte, the zygote is moved into the uterus and female meiosis is completed. During meiosis two polar bodies get extracted (Albertson and Thomson, 1993). At the same time the entire cortex begins to form invaginations, an event termed ruffling (Figure 9). Sperm entry defines the posterior of the zygote (Goldstein and Hird, 1996) and the sperm harbors two centrioles. The maternal centrioles are removed during oogenesis (Mikeladze, 2012). When the oocyte is fertilized the two pronuclei are positioned at the opposing poles of the zygote. During pronuclear migration the two nuclei move towards each other, while the anterior cortex still forms ruffles and a transient furrow, that ingresses and regresses, forms at the center, termed pseudocleavage (Figure 9). Once the two pronuclei meet, they move together into the center of the cell where rotation

and centration takes place. The centrosomes become oriented towards the anterior and posterior pole of the cell, forming the poles of the mitotic spindle. Next, the nuclear envelope breaks down and the chromosomes get attached to MTs. During metaphase, when all chromosomes are aligned in between the two spindle poles, the mitotic spindle is set and the cell is prepared for cytokinesis. During anaphase the contractile ring forms at the equatorial cortex, which leads to furrow formation and ring ingression, followed by telophase and abscission to finalize cell division (Oegema and Hyman, 2006).

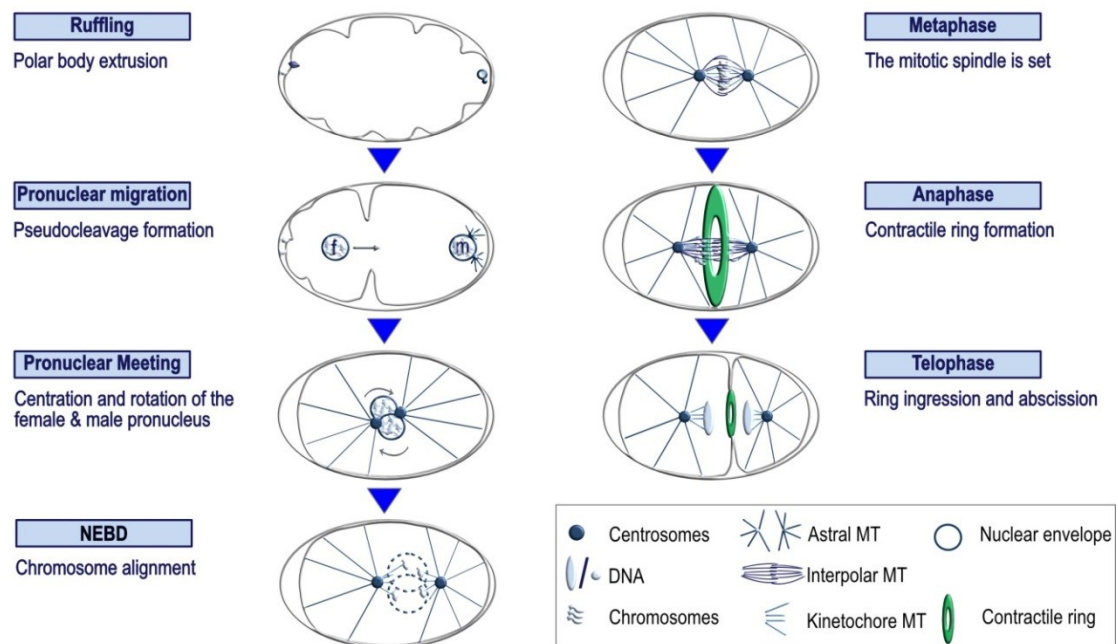


**Figure 9: First cell division of the *C. elegans* one-cell embryo.** The fertilized oocyte harbors the female (f) and male (m) pronucleus. Only the male pronucleus is attached with centrioles. When the sperm enters the oocyte, the cortex starts to ruffle and the female meiotic divisions are finalized with the extrusion of two polar bodies. During pronuclear migration the female and male pronuclei start to migrate towards each other. A transient invagination forms at the equator that ingresses and regresses (pseudocleavage). When the two pronuclei meet, they move towards the center and start to rotate and finally orient the centrosomes towards the two opposing poles. The centrosomes form the poles of the mitotic spindle. While the nuclear envelope breaks down (NEBD), the chromosomes get attached to MTs, emanating from the centrosomes, and the mitotic spindle forms and is positioned in the center. The mitotic spindle consists of astral-, kinetochores- and interpolar MTs. During anaphase a contractile ring is initiated at the equatorial cortex, leading to furrow formation and subsequently ingresses to divide the cell into two. Adapted from (Oegema and Hyman, 2006).



## 1.6 Aims of the thesis

The canonical model predicts that, during metaphase to anaphase transition, the local activation of RhoA by Ect2 specifies the division plane by signals from the mitotic spindle. Active RhoA accumulation, in between the segregating chromosomes, initiates contractile ring formation and is an event crucial for cytokinesis. The formation of a narrow zone of active RhoA at the equator during cytokinesis is a conserved phenomenon and was shown for different organisms. RhoA is locally activated at the equator and transiently anchored to the PM. As a peripheral membrane protein RhoA is able to diffuse within the PM, due to the lipid moiety that is anchored to its C-terminus. Since RhoA molecules are continuously activated at the equator, active RhoA is assumed to diffuse away from the site of activation. However, during cytokinesis a narrow RhoA zone is present at the equator that remains constant over time, indicating that active RhoA does not diffuse away from this local activity zone.

How active RhoA is maintained within a narrow zone remains an open question in the field and was addressed by this thesis using *C. elegans* as model organism.

I addressed this question by testing three main hypotheses.

### **Maintenance of a RhoA activity zone is obtained by:**

#### **(1) The RhoA activation/inactivation cycle driven by GEF and GAP;**

Active RhoA zone formation during cytokinesis is Ect2 dependent and a consequence of signals arising from the mitotic spindle during metaphase to anaphase transition. Restricting active RhoA within a narrow zone at the equator could be achieved by accelerating the low intrinsic hydrolysis rate of RhoA by the GAP. Increased cycles of inactivation and activation of RhoA, incidental with faster RhoA on and off rate to/off the PM, could limit RhoA diffusion within the PM. I addressed this hypothesis by live-cell imaging of one-cell *C. elegans* embryos, expressing a fluorescence-tagged RhoA probe, after knock-down of the GEF and GAP. If increased cycles of the activation and inactivation of RhoA indeed play a role in restricting RhoA into a narrow zone, depletion of the RhoA GAP should widen the RhoA zone.

**(2) Lipid interactions mediated by the two PM-targeting motifs, PBS and CAAX;**

The canonical model predicts that only active RhoA is anchored to the PM. Transient binding of RhoA to the PM is assumed to be driven by the two membrane-targeting motifs at the C-terminus of RhoA. Both motifs together have been shown to be sufficient to localize to the PM in human cells by transient overexpression (Michaelson et al., 2001). Further, the PBS of RhoA in *S. cerevisiae* was shown to be sufficient to target RhoA to the division plane, in the absence of the GEF, due to interactions of the PBS with Phosphatidylinositol-4,5-bisphosphat (PIP<sub>2</sub>) lipids (Yoshida et al., 2009). Enrichment of PIP<sub>2</sub> at the equatorial membrane was proposed also in animal cells (Field et al., 2005b; Emoto et al., 2005). I analyzed whether the interaction with lipids, within the PM, could contribute to narrow RhoA zone formation. To test this, mutations and truncations of the C-terminal membrane-targeting motifs of RhoA were established and analyzed using live-cell imaging.

**(3) Contractile ring components that act as physical barrier;**

The actin network underneath the PM plays a crucial role in cell morphology. The actin cytoskeleton supports the PM in cell shape by generating tension via non-muscle myosin II-mediated contraction. The network of F-actin and actin binding proteins spreads like a web underneath the PM and is anchored to the membrane (Morone et al., 2006). It was proposed in the ‘membrane-skeleton picket fence model’ that the F-actin network could act as a physical barrier for PM-associated proteins (Morone et al., 2006; Sheetz et al., 1980; Sheetz, 1983; Edidin et al., 1991). During cytokinesis RhoA initiates F-actin polymerization via formins, resulting in increased F-actin density at the furrow. In addition, actin cross-linkers, such as anillin and NMY-2, are important key factors for the contractile ring that localize to the equatorial membrane. Increased density of cross-linked F-actin at the equator could limit RhoA diffusion by spatial restriction. I tested this hypothesis by performing FRAP experiments to analyze RhoA turnover at the membrane and compare its mobility in regions of low and high F-actin density. Further, I tested with high-time resolution live-cell imaging how F-actin influences RhoA mobility at the equatorial membrane using particle image velocimetry (PIV) analysis.

## 2 Material and Methods

### 2.1 Material

All material used for this study is listed in the following tables.

**Table 1: Chemicals and Reagents**

<b>Chemicals/Reagents</b>	<b>Supplier</b>
2-Mercaptoethylamine-HCl	Thermo Fisher Scientific
Agar	Carl Roth
Agarose	Carl Roth
Bovine serum albumin	Sigma-Aldrich
Carbenicillin	Applichem
Chloramphenicol	Applichem
CO <sub>2</sub> -independent medium	Thermo Fisher Scientific
dNTPs	Metabion
ECL Prime Western Blotting Detection Reagent	GE Healthcare
Ethanol	Carl Roth
EZ-Vision™ DNA dye (6x loading buffer)	Amresco
FBS	Thermo Fisher Scientific
GelRed® Nucleic Acid Gel Stain	Biotium
Glutathione Sepharose™ 4B protein purification resin	GE Healthcare
Hoechst	BioRad
Isopropanol	Carl Roth
Isopropyl-β-D-thiogalactopyranosid	Sigma-Aldrich
Milk powder	Sigma-Aldrich
Mineral oil	Sigma-Aldrich
Penicillin/Streptomycin	Merck
Phenylmethylsulfonyl fluoride	Sigma-Aldrich
Polybead® microspheres	Polysciences
Poly-L-lysine	Sigma-Aldrich
Quick Start™ Bradford	Bio-Rad
SulfoLink™ Coupling Resin	Thermo Fisher Scientific

Chemicals/Reagents	Supplier
Trichloroacetic acid	Sigma-Aldrich
Triton-X100	Carl Roth
Tween	Carl Roth
X-tremeGENE™ 9	Roche

**Table 2: Solutions and Buffers**

Solution/Buffers	Composition	
10x PBS	Na <sub>2</sub> HPO <sub>4</sub> ·7H <sub>2</sub> O	25.6 g
	NaCl	80 g
	KCl	2 g
	KH <sub>2</sub> PO <sub>4</sub>	2 g
	ddH <sub>2</sub> O	to 1 L
10x Running buffer	Tris	30.3 g
	Glycine	144 g
	ddH <sub>2</sub> O	to 1 L
10x TBS	KCl	2 g
	NaCl	80 g
	Tris	30 g
	pH 7.4 (with HCl)	
	ddH <sub>2</sub> O	to 1 L
1x Running buffer	10x Running buffer	100 ml
	10 % SDS	10 ml
	ddH <sub>2</sub> O	to 1 L
2x Sample buffer (Lämmli)	4x stacking buffer	2 ml
	10 % SDS	4 ml
	Beta-Mercaptoethanol	140 µl
	50 % Glycerol	4 ml
	saturated Bromophenol blue	100 µl
4x Resolving buffer	Tris	18.17 g
	HCl (1 M)	24 ml
	ddH <sub>2</sub> O	to 100 ml
4x Stacking buffer	Tris	6 g
	HCl (1 M)	38.5 ml

<b>Solution/Buffers</b>	<b>Composition</b>	
50 x TAE buffer	SDS	0.4 g
	pH 6.8 (with HCl)	
	ddH <sub>2</sub> O	to 100 ml
50 x TAE buffer	Tris	484 g
	EDTA (0.5 M, pH 8.0)	200 ml
	Glacial Acetic Acid	114.2 ml
	MilliQ H <sub>2</sub> O	to 2L
b-broth	Tryptone	10 g
	NaCl	5 g
	MilliQ H <sub>2</sub> O	1 L
Coomassie destaining solution	100 % Ethanol	250 ml
	Glacial Acetic Acid	50 ml
	ddH <sub>2</sub> O	to 500 ml
Coomassie staining solution	100 % MeOH	100 ml
	Glacial Acetic Acid	50 ml
	Brilliant Blue	0.5 g
	ddH <sub>2</sub> O	to 500 ml
EB buffer	Tris-HCl (10 mM)	
	pH 8.5	
Freezing solution (2x)	NaCl	5.58 g
	KH <sub>2</sub> PO <sub>4</sub>	6.8 g
	Glycerol	300 ml
	NaOH to pH 6.0	0.56 ml
	MilliQ H <sub>2</sub> O	to 1 L
	MgSO <sub>4</sub> (1 M)	60 µL
	(to 200 ml) before use	
LB-agar	Tryptone	10 g
	Yeast extract	5 g
	NaCl	10 g
	MilliQ H <sub>2</sub> O	800 ml
	NaOH (10 M)	460 µl
	Agar	15 g
LB-broth	Tryptone	10 g

<b>Solution/Buffers</b>	<b>Composition</b>	
	Yeast extract	5 g
	NaCl	10 g
	MilliQ H <sub>2</sub> O	800 ml
M9 buffer	Na <sub>2</sub> HPO <sub>4</sub>	5.8 g
	KH <sub>2</sub> PO <sub>4</sub>	3.0 g
	NaCl	0.5 g
	NH <sub>4</sub> Cl	1.0 g
	MilliQ H <sub>2</sub> O	to 1 liter
Mounting medium	4 % n-Propyl-Gallate	
	90 % Glycerol	
	1x PBS	
	store at -20°C	
Nematode Growth Medium (NGM)	NaCl	3 g
	Bacto-Peptone	2.5 g
	Agar	20 g
	ddH <sub>2</sub> O	975 ml
	CaCl <sub>2</sub> (1 M)	1 ml
	MgSO <sub>4</sub> (1 M)	1 ml
	Cholesterol in EtOH (5 mg/ml)	1 ml
	KH <sub>2</sub> PO <sub>4</sub> (1 M, pH 6.0)	25 ml
Transfer buffer	100 % EtOH	200 ml
	Running buffer	100 ml
	ddH <sub>2</sub> O	to 1 L

**Table 3: Enzymes**

<b>Enzyme</b>	<b>Supplier</b>	<b>Catalog number</b>
DpnI	New England Biolabs	R0176
Phusion <sup>®</sup> DNA polymerase + 5x HB buffer	New England Biolabs GmbH	M0530
Proteinase K	AppliChem	A3830
RNase A	New England Biolabs	T3010
RNAseZAP <sup>®</sup>	Thermo Fisher Scientific	AM9780
<i>Taq</i> DNA polymerase + 10 x Standard <i>Taq</i> buffer	New England Biolabs GmbH	M0273

**Table 4: Kits**

<b>Kit</b>	<b>Supplier</b>	<b>Catalog number</b>
Gibson Assembly <sup>®</sup> Cloning Kit	New England Biolabs GmbH	E5510
Invitrogen PureLink <sup>™</sup> HQ Mini Plasmid Purification Kit	Thermo Fisher Scientific	K2100-01
MEGAclear <sup>®</sup> Kit	Ambion	AM1908
MEGAscript <sup>®</sup> T7 Kit	Ambion	AM1334
NucleoSpin <sup>®</sup> Gel and PCR Clean-up	Macherey&Nagel	740609
QiaPrep <sup>®</sup> Spin Miniprep Kit	Qiagen	27104

**Table 5: Antibodies**

<b>Antibody</b>	<b>Host</b>	<b>Supplier</b>	<b>Catalog number</b>
$\alpha$ -Tubulin	mouse	Sigma	T9026
GAM HRP	goat	Bio-Rad	170-6516
GAR HRP	goat	Bio-Rad	170-6515
RHO-1	rabbit	Home-made (#14)	

**Table 6: Equipment**

<b>Equipment</b>	<b>Supplier</b>
-20°C Freezer	Comfort
-80°C Freezer	Thermo Fisher Scientific/ Hera Freeze
Amicon® Ultra Filter	Sigma-Aldrich
Axioscope A1	Zeiss
Cell culture 6 well multi well plate	Greiner Bio One
Centrifuge tubes (0.5 ml, 1.5 ml, 2 ml)	Sarstedt
Centrifuges	Eppendorf
CF Cell Disrupter	Constant Systems Ltd
ChemiDoc® imaging system	Bio-Rad
Coverslips	Carl Roth
Cryo-tubes	Thermo Fisher Scientific
Cuvettes	Sigma-Aldrich
Dialysis tube	Sigma-Aldrich
Falcon tubes (15 ml, 50 ml)	Nerbe plus
Fridge (4°C)	Bosch
Glass pipettes	Brand
Heat block	Labnet
Incubator (37°C)	Heraeus
Incubator shaker	New Brunswick
Laser scanning confocal TCS SP5 microscope	Leica
Metal plate	Home-made
Micro-Injector (Femtojet)	Eppendorf
Microwave	LG
NanoDrop™ 2000	Thermo Fisher Scientific
Nanophotometer device	Implen
Nikon Eclipse Ti	Nikon
Nikon inverted microscope (Eclipse Ti)	Nikon
Parafilm®	Sigma-Aldrich
PCR tubes	Nerbe plus
Petri dishes	Sarstedt
pH strip	Macherey-Nagel



<b>Equipment</b>	<b>Supplier</b>
Pierce™ Disposable Columns (10 ml)	Thermo Fisher Scientific
Pierce™ Protein Concentrator	Thermo Fisher Scientific
Pipette boy	Integra
Pipette tips/Filter tips	Nerbe plus
Pipettes	Gilson
Polyvinylidene difluoride membrane	Carl Roth
Rubber spatula	n.a.
SDS-gel electrophoresis chamber and equipment	Bio-Rad
Slides	Carl Roth
Sonicator water bath	VWR
Sonicator	Fisher Scientific
Stereo microscope	Nikon
Syringe needle	Sarstedt
Thermocycler	Bio-Rad
UltraVIEW VoX spinning disk confocal microscope	Perkin Elmer
Worm incubators (15°C, 20°C, 25°C)	Binder
Worm picker	Home-made
Zeba™ Spin Desalting Column	Thermo Fisher Scientific

**Table 7: Bacterial strains**

<b>Bacterial strain</b>	<b>Source</b>
BL21 (DE3)	Home-made competent cells
DH5α	Home-made competent cells
<i>E. Coli</i> (OP50)	Conradt lab

**Table 8: Softwares**

<b>Software</b>	<b>Supplier</b>
SnapGene®	GSL Biotech LLC
GraphPad Prism	Graphpad Software Inc.
Microsoft Excel	Microsoft Corporation

<b>Software</b>	<b>Supplier</b>
KNIME <sup>®</sup> Analytics Platform	KNIME AG
Fiji (Fiji is just imageJ)	(Schindelin and Arganda, 2012)
Nikon NIS Elements	Nikon
Volocity 6.1.1	Perkin Elmer
Leica Application Suite Software	Leica
R Project for Statistical Computing	The R Foundation

## 2.2 Methods

### 2.2.1 *C. elegans* maintenance

Worm strains were maintained on Nematode Growth Medium (NGM) petri dishes seeded with *E. coli* (OP50) cultured in b-broth following standard protocol (Stiernagle, 2006; Brenner, 1974). Single worms were transferred from one plate to the other using a worm picker. Strains used for this study are listed in Table 9. For maintenance MosSCI strain EG6699 was incubated at 15°C, all other strains were incubated at 20°C.

**Table 9: Worm strains used and generated for this study**

Strain Name	Genotype	Source
N2	Wild-type (ancestral)	(*made by other person)
EG6699	<i>ttTi5605 II; unc-119(ed3) III; oxEx1578</i>	(Frøkjær, 2008)
OD70	<i>ItIs44[<i>pie-1p</i>::mCherry::PH(PLC1delta1)+<i>unc-119(+)</i>]</i>	(Kachur et al., 2008)
BV70	<i>zbls2[<i>pie-1p</i>::LifeAct::RFP + <i>unc-119(+)</i>]</i>	Zhirong Bao
RZB217	<i>plst-1(msn190[<i>plst-1::gfp</i>])IV; zbls2(<i>pie-1p</i>::LifeAct::RFP)</i>	(Ding et al., 2017)
ZAN6	<i>estSi4[pEZ102; <i>prho-1</i>::mCherry::RHO-1RE; <i>cb-unc-119(+)</i>]II; <i>unc-119(ed3) III</i></i>	This study (*Esther Zanin)
ZAN17	<i>estSi9[pEZ107;<i>prho-1</i>::GFP::RHO-1;<i>cb-unc-119(+)</i>]II</i>	This study (*Esther Zanin)
ZAN39	<i>estSi19[pEZ138; <i>prho-1</i>::RHO-1RE; <i>cb-unc-119(+)</i>]II</i>	This study (*Esther Zanin)
ZAN69	<i>estSi37[pEZ98; <i>pani-1</i>::GFP::ANI-1; <i>cb-unc-119(+)</i>]IV</i>	(*Esther Zanin)
ZAN74	<i>estSi39[pEZ153; <i>prho-1</i>::GFP::RHO-1RE6KA; <i>cb-unc-119(+)</i>]II</i>	This study (*Esther Zanin/ Parviz Gomari)
ZAN76	<i>estSi47[pEZ147; <i>prho-1</i>::RHO-1RE6KA; <i>cb-unc-119(+)</i>]II</i>	This study (*Esther Zanin/ Parviz Gomari)
ZAN77	<i>estSi37[pEZ98; <i>pani-1</i>::GFP::ANI-1; <i>cb-unc-</i></i>	This study

<b>Strain Name</b>	<b>Genotype</b>	<b>Source</b> (*made by other person)
	119(+)]IV; si19[pEZ138; prho-1::RHO-1RE; cb-unc-119(+)]II	(*Parviz Gomari)
<b>ZAN122</b>	estSi37[pEZ98; pani-1::GFP::ANI-1; cb-unc-119(+)]IV; Si47[pEZ147; prho-1::RHO-1RE6KA; cb-unc-119(+)]II	This study
<b>ZAN142</b>	estSi79 [pEZ173; prho-1::GFP::RHO-1tail; cb-unc-119(+)]II	This study
<b>ZAN156</b>	estSi102[pEZ175; prho-1::RHO-1ΔCAAX; cb-unc-119(+)]II	This study
<b>ZAN160</b>	estSi106[pEZ176; prho-1::GFP::RHO-1ΔCAAX; cb-unc-119(+)]II	This study
<b>ZAN169</b>	estSi111 [pEZ178; pmex-5::GFP::RHO-16KAtail:tbb-2; cb-unc-119(+)]II	This study
<b>ZAN170</b>	estSi37[pEZ98; pani-1::GFP::ANI-1; cb-unc-119(+)]IV; Si102[pEZ175; prho-1::RHO-1ΔCAAX; cb-unc-119(+)]II	This study
<b>ZAN171</b>	estSi9[pEZ107; <i>prho-1::GFP::RHO-1;cb-unc-119(+)]II</i> ; ItIs44[ <i>pie-lp::mCherry::PH(PLC1delta1)+unc-119(+)]</i>	This study
<b>ZAN196</b>	estSi137[pEZ177; <i>pmex-5::GFP::PBS-CAAX::tbb-2;cb-unc-119(+)]II</i>	This study
<b>ZAN253</b>	estSi169[pEZ221; prho-1::RHO-16KAΔCAAX; cb-unc-119(+)]II	This study
<b>ZAN262</b>	estSi37[pEZ98; pani-1::GFP::ANI-1; cb-unc-119(+)]IV; Si169[pEZ221; prho-1::RHO-16KAΔCAAX; cb-unc-119(+)]II	This study
<b>ZAN307</b>	ani-1(mon7[mNeonGreen <sup>3</sup> xFlag::ani-1]) III; ItIs44[ <i>pie-lp::mCherry::PH(PLC1delta1)+unc-119(+)]V</i>	This study (*Esther Zanin)
<b>ZAN329</b>	estSi9[pEZ107; prho-1::GFP::RHO-1RE; cb-unc-119(+)]II; zbls[ <i>pie-1::lifeact-RFP + unc-119(+)]</i>	This study (*Isabel Schulz-Pernice)

### 2.2.2 Worm freezing

For worm freezing three medium-size NGM plates (60 mm diameter) seeded with *E. coli* OP50 were set up with four L4 hermaphrodites each and were incubated at 20°C. When no bacteria lawn was left on the plates and a lot of freshly starved L1/L2-stage larvae were present, worms were washed off with 3.5 ml M9 buffer and were transferred and collected in a 15 ml falcon tube. Freezing solution (2x) was added in a 1:2 ratio. Worms were suspended and distributed into five cryo-tubes. Finally, worms were frozen at -80°C.

### 2.2.3 Worm lysis and genotyping

For genotyping worms were lysed prior to polymerase chain reaction (PCR) amplification. Single worms were lysed in 4.25 µl H<sub>2</sub>O, 0.5 µl Standard *Taq* Buffer and 0.25 µl Proteinase K. Lysates were incubated at 65°C for 1 h and 95°C for 15 min in a thermocycler. Worm lysates were subsequently used as template for PCR.

### 2.2.4 Worm crosses

Worm crosses were set up on small-size NGM plates (35 mm diameter). To provide worms with only little amount of *E. coli* OP50 as food source, two scoops of a seeded bacteria lawn was transferred to a small NGM plate using the worm picker. Wild-type population contain only 0.2 % male (XO; only one X-chromosome) because they have their origin in X-chromosome loss of hermaphrodite self-progeny during gametogenesis, which is a rare event (Hodgkin and Doniach, 1997). To achieve higher number of males of a desired strain, worms were injected with *him-8* dsRNA (high incidence of males). Knock-down of HIM-8 results in increased male frequency (up to 30 %) as a result of increased X-chromosome nondisjunction (Hodgkin et al., 1979).

Nine males of strain A were transferred to the NGM plate together with three L4 hermaphrodites of strain B and were incubated at 20°C. After 24 h the three hermaphrodites were singled on small NGM plates, seeded with *E. coli* OP50, and were incubated at 20°C. F1 progeny of the singled worms was observed for the frequency of males. If mating was successful approx. 50 % of the F1 progeny should be male in contrast to a low frequency of 0.2 % in wild-type population (Fay, 2006). If all alleles of interest carried a fluorescent marker, mating could be verified in addition by fluorescence microscopy. A positive mating plate was chosen and 10 L4 hermaphrodites (F1) were

singled to small seeded NGM plates. Once F2 progeny was observed on the plates (young larvae stage), F1 mother worms were tested for the presence of all alleles of interest either by fluorescence microscopy (if all had a fluorescent marker present) or by PCR. A positive plate was used to further continue by singling out an appropriate number of F2 progeny (L4 larvae) on small seeded NGM plates. The number of worms to be singled out was dependent on the number (and position) of the alleles to be crossed following Mendel's law of segregation (Mendel). When F3 progeny was hatched, F2 mother worms were tested for the presence of the alleles of interest: (1) by fluorescence-microscopy (if fluorescent markers were crossed) using an Axioscope A1 (Zeiss) and (2) by PCR. F3 progeny of positive mother worms was further tested for homozygosity (fluorescence-microscopy and PCR). If 10/10 tested F3 progeny worms were positive for the alleles of interest the strain was processed as homozygous.

### 2.2.5 Plasmid generation

Plasmids used for this study are shown in Table 10. For fluorescently-tagged transgenes GFP, mCherry and mKate2 were used.

For all *rho-1* transgenes pCFJ350 was used as targeting vector. The transgenes were regulated by endogenous promoter (1991 bp) and 3'UTR (1308 bp), which was cloned into the vector together with *rho-1* sequence and an N-terminal GFP-tag with a short GS-linker (ggaggtggaggatcc). The promoter, 3'UTR and *rho-1* sequence were amplified from genomic DNA. Exon three was re-encoded (326 bp) to achieve RNAi-resistance. The plasmid carrying *gfp::rho-1* (pEZ107) was used as template to clone all other plasmids coding for *rho-1* transgenes. Site-directed mutagenesis was performed to introduce mutations for *rho-1*<sup>6KA</sup> (pEZ147), where all six lysine were mutated to alanine. Gibson Assembly<sup>®</sup> cloning was used to delete the last four AAs to generate *rho-1*<sup>ΔCAAX</sup> and *rho-1*<sup>6KAΔCAAX</sup> (using pEZ138 as template). In order to generate the same RHO-1 plasmids without fluorescence-tag, the sequence for the fluorophore was removed by Gibson Assembly<sup>®</sup> cloning. GFP::PBS-CAAX expression was too weak when controlled by endogenous regulatory regions (pEZ173). Therefore, the construct was controlled by *mex-5* promoter (488 bp) and *tbb-2* 3'UTR (330 bp; (Zeiser and Frøkjær, 2011)). The promoter, 3'UTR, GFP and the last exon of *rho-1* were cloned into pCFJ350 by Gibson Assembly<sup>®</sup> cloning (pEZ177).

**Table 10: Plasmids used and generated in this study**

Plasmid	Description	Source
		(*made by other person)
<b>pCFJ350</b>	<i>C. elegans</i> targeting vector for MosSCI method	(Frøkjær, 2012)
<b>pGEX-4T-1</b>	Bacterial vector for expressing fusion proteins	Stephane Rolland
<b>pET-19b</b>	Bacterial vector for expressing fusion proteins	Conradt lab
<b>pcDNA5</b>	Mammalian expression vector	Invitrogen
<b>pBC1454</b>	<i>C. elegans</i> expression vector providing <i>mai-2</i> promoter and 3'UTR	Conradt lab
<b>pRF4</b>	<i>C. elegans</i> extrachromosomal marker <i>rol-6(su1006)</i>	Nadin Memar; (Mello et al., 1991)
<b>pEZ102</b>	<i>prho-1::mCherry::RHO-1<sup>RE</sup></i>	Esther Zanin
<b>pEZ107</b>	<i>prho-1::GFP::RHO-1<sup>RE</sup></i>	Esther Zanin
<b>pEZ138</b>	<i>prho-1::RHO-1<sup>RE</sup></i>	Esther Zanin
<b>pEZ147</b>	<i>prho-1::RHO-1<sup>RE6KA</sup></i>	This study (*Cornelia Sigl)
<b>pEZ153</b>	<i>prho-1::GFP::RHO-1<sup>RE6KA</sup></i>	This study (*Parviz Gomari)
<b>pEZ162</b>	RHO-1 <sup>ΔCAAX</sup> cDNA in pGEX-4T	This study
<b>pEZ173</b>	<i>prho-1::GFP::RHO-1<sup>tail</sup></i> (last Exon of RHO-1; PBS::CAAX)	This study
<b>pEZ175</b>	<i>prho-1::RHO-1<sup>ΔCAAX</sup></i>	This study
<b>pEZ177</b>	<i>pmex-5::GFP::RHO-1<sup>tail</sup>::tbb-2</i> (last Exon of RHO-1; PBS::CAAX)	This study
<b>pEZ212</b>	RHO-1 <sup>Q63LΔCAAX</sup> Nanobody domain in pGEX-4T	This study
<b>pEZ217</b>	RHO-1 <sup>Q63LΔCAAX</sup> -dimer cDNA in pET19-b (Nanobody domain for immunization)	This study
<b>pEZ221</b>	<i>prho-1::RHO-1<sup>6KAΔCAAX</sup></i>	This study
<b>pEZ222</b>	RHO-1 <sup>Q63LΔCAAX</sup> cDNA in pET19-b (selection Nanobody; GTP loaded probe)	This study
<b>pEZ235</b>	RHO-1 <sup>ΔCAAX</sup> cDNA in pET19-b (selection Nanobody; GDP loaded probe)	This study
<b>pEZ267</b>	VHH0166-GFP in pcDNA5	This study

Plasmid	Description	Source (*made by other person)
pEZ269	VHH0169-GFP in pcDNA5	This study
pEZ270	VHH0172-GFP in pcDNA5	This study
pEZ271	VHH0175-GFP in pcDNA5	This study
pEZ272	VHH0176-GFP in pcDNA5	This study
pEZ273	VHH0168-GFP in pcDNA5	This study
pEZ274	VHH0171-GFP in pcDNA5	This study
pEZ275	VHH0174-GFP in pcDNA5	This study
pEZ276	VHH0178-GFP in pcDNA5	This study
pEZ281	VHH0167-GFP in pcDNA5	This study
pEZ282	VHH0173-GFP in pcDNA5	This study
pEZ286	VHH0175-GFP in pBC1454	This study
pEZ287	VHH0178-GFP in pBC1454	This study
pEZ288	VHH0171-GFP in pBC1454	This study

### 2.2.5.1 PCR amplification

PCR was performed using *Taq* DNA- (New England Biolabs GmbH; M0273) or Phusion<sup>®</sup> DNA polymerase (New England Biolabs GmbH; M0530), depending on the application and fragment size to be amplified. In general PCR amplification to generate dsRNA was performed using *Taq* DNA polymerase and fragments for Gibson Assembly<sup>®</sup> cloning were amplified using Phusion<sup>®</sup> DNA polymerase. Template and polymerase used are indicated in the respective sections. Elongation time ( $t_{\text{elong}}$ ) was calculated in respect to the fragment size amplified and the polymerase used (*Taq* DNA: 1 min/bp and Phusion<sup>®</sup> DNA: 0.5 min/bp). Oligonucleotides were designed and annealing temperature ( $T_m$ ) of the primers was determined in SnapGene software (<https://www.snapgene.com>). The length of the oligonucleotide was set to a minimum of 19 bp with a GC content of 40-60 %. The general setup for a standard reaction and thermocycler conditions for *Taq* DNA polymerase and Phusion<sup>®</sup> DNA polymerase are shown in the following tables (Table 11-Table 14). Reactions were set up on ice. PCR products were tested for correct size using agarose-gel electrophoresis with a 0.8 % agarose gel in 1x TAE buffer. A ChemiDoc<sup>®</sup> imaging system from Bio-Rad was used to analyze the gel.



**Table 11: PCR setup for standard reaction using *Taq*-DNA polymerase**

Component	Concentration	Volume for 25 $\mu$ l reaction
10X Standard <i>Taq</i> Reaction Buffer	1X	2.5 $\mu$ l
10 mM dNTPs	200 $\mu$ M	0.5 $\mu$ l
10 $\mu$ M Forward Primer	0.2 $\mu$ M (0.05–1 $\mu$ M)	0.25 $\mu$ l
10 $\mu$ M Reverse Primer	0.2 $\mu$ M (0.05–1 $\mu$ M)	0.25 $\mu$ l
Template DNA	<1,000 ng	*variable
<i>Taq</i> DNA Polymerase	1.25 units/ 50 $\mu$ l PCR	0.125 $\mu$ l
H <sub>2</sub> O		to 25 $\mu$ l

\*Template DNA: genomic DNA (1 ng - 1  $\mu$ g); plasmid DNA (1 pg - 1 ng)

**Table 12: Thermocycler conditions for *Taq*-DNA polymerase**

Step	Temp	Duration
Initial Denaturation	95°C	30 s
Denaturation	95°C	10 s
Primer Annealing	T <sub>m</sub>	30 s
Elongation	68°C	t <sub>elong</sub> (1 min/kb)
Final Extension	68°C	5 min
Hold	12°C	5 min

} 35

**Table 13: PCR setup for standard reaction using Phusion® DNA polymerase**

Component	Concentration	Volume for 50 $\mu$ l reaction
5X Phusion HF or GC Buffer	1X	10 $\mu$ l
10 mM dNTPs	200 $\mu$ M	1 $\mu$ l
10 $\mu$ M Forward Primer	0.5 $\mu$ M	2.5 $\mu$ l
10 $\mu$ M Reverse Primer	0.5 $\mu$ M	2.5 $\mu$ l
Template DNA	< 250 ng	*variable

Component	Concentration	Volume for 50 $\mu$ l reaction
Phusion DNA Polymerase	1.0 unit/ 50 $\mu$ l PCR	0.5 $\mu$ l
H <sub>2</sub> O	-	to 50 $\mu$ l

\*Template DNA: genomic DNA (50 ng - 250 ng); plasmid DNA (1 pg - 10 ng)

**Table 14: Thermocycler conditions for Phusion<sup>®</sup> DNA polymerase**

Step	Temp	Duration
Initial Denaturation	98°C	30 s
Denaturation	98°C	10 s
Primer Annealing	T <sub>m</sub>	30 s
Elongation	72°C	t <sub>elong</sub> (0.5 min/kb)
Final Extension	72°C	5-10 min
Hold	12°C	5 min

### 2.2.5.2 Gibson Assembly<sup>®</sup> cloning

Cloning was performed by Gibson Assembly<sup>®</sup> (Gibson et al., 2009) (New England Biolabs GmbH; E5510) using standard protocol. First PCR fragments were amplified using Phusion<sup>®</sup> DNA polymerase. Primers were designed for all PCR fragments using SnapGene software (<https://www.snapgene.com>). As template either genomic DNA or plasmids from the lab were used (information is provided in 2.2.5). PCR fragments were tested for correct size on a 0.8 % agarose gel. If fragments were amplified from plasmids, PCR products were treated with 1  $\mu$ l DpnI/50  $\mu$ l reaction for 1 h at 37°C. Next all fragments were purified following the protocol of the DNA purification kit (NucleoSpin<sup>®</sup> Gel and PCR Clean-up, Macherey&Nagel; 740609). If several bands were visible on the agarose gel, the band with the correct size was cut out and purification was performed using the same PCR clean-up kit, following instructions for gel-extraction. Concentration of the purified DNA fragments was determined using a Nanophotometer device (Implen). Gibson Assembly<sup>®</sup> was performed following the Gibson Assembly<sup>®</sup> protocol provided from New England Biolabs GmbH. The amount of pmols of each fragment was calculated using Formula 1. Inserts were used in a 2-fold molar excess in respect to the vector.

**Formula 1: Calculation for total amount of fragments to be used for Gibson Assembly.**

$$\text{pmols} = (\text{weight in ng}) \times 1000 / (\text{bp} \times 650 \text{ Daltons})$$

Total reaction volume was reduced to 15  $\mu\text{l}$  by using only 7.5  $\mu\text{l}$  Gibson Assembly Master Mix (2x) and 7.5  $\mu\text{l}$  of PCR product (+ deionized  $\text{H}_2\text{O}$ ) accordingly. The reaction was incubated at 50°C for 15 min in a thermocycler and subsequently 10  $\mu\text{l}$  of the reaction was transformed in 100  $\mu\text{l}$  *E. coli* (DH5 $\alpha$ ) home-made competent cells.

**Table 15: Gibson Assembly Protocol**

Reaction Mix	Volume [ $\mu\text{l}$ ]
Total Amount of Fragments (0.02-0.5 pmols)	X
Gibson Assembly Master Mix (2x)	7.5
Deionized $\text{H}_2\text{O}$	7.5-X
Total Volume	15

**2.2.5.3 Transformation**

For transformation a vial with 100  $\mu\text{l}$  *E. coli* (DH5 $\alpha$ ; home-made competent cells) was thawed on ice for 10 min. 10  $\mu\text{l}$  of the Gibson reaction mix (Table 15) was added to the competent cells, followed by 20 min incubation on ice and a subsequent heat-shock at 42°C for 45 s. The tube was incubated on ice for 2 min and 1 ml LB-broth was added. Cells were incubated at 37°C for 45 min and were centrifuged at 400 g for 5 min. Supernatant was removed and cells were resuspended in approx. 100  $\mu\text{l}$  supernatant left in the tube. Cells were spread on LB-Carb (carbenicillin; 0.1 mg/ $\mu\text{l}$ ) plates and were incubated at 37°C for 16-18 h.

**2.2.5.4 Colony-PCR, plasmid purification and sequencing**

Colonies were first tested by colony-PCR, if positive cloning was detected by differences in fragment size. If not, colonies were directly tested by purifying plasmids followed by sequencing. For colony-PCR, primers were chosen to amplify DNA at the transition between two fragments that were assembled by Gibson Assembly<sup>®</sup> cloning. DNA amplification was performed using *Taq* DNA Polymerase following standard protocol (2.2.5.1). For plasmid purification, colonies were inoculated in 5 ml LB-broth containing

0.1 mg/ml Carb and were incubated at 37°C for 16-18 h (overnight) at 180 rpm. Two 2 ml centrifuge tubes were filled with the culture and were centrifuges at maximum speed for 10 min. The supernatant was discarded and one pellet was frozen at -20°C. The other pellet was used for plasmid purification. Plasmids were purified using QiaPrep Spin miniprep kit (Qiagen; 27104) and DNA was sent for in-house sequencing, offered by the Ludwig-Maximilians-University Munich (<http://www.gi.bio.lmu.de/sequencing>). For sequencing the method Cycle, Clean and Run, BigDye v.3.1 was used. The amount of DNA was chosen according to the protocol provided on the website (plasmids 150-300 ng). The sequencing primer was added with a concentration of 5 pmol/μl and the total volume was brought to 7 μl with EB buffer. For MosSCI integration, plasmids from the second frozen pellet of the overnight culture were purified using Invitrogen PureLink™ HQ Mini Plasmid Purification kit (Thermo Fisher Scientific; K2100-01), which provides higher purity. Plasmids were eluted in sterile double-distilled water (ddH<sub>2</sub>O).

### 2.2.6 Mos1-mediated single-copy insertion (MosSCI)

To insert transgenes as single-copy into *C. elegans* genome universal MosSCI technique was used. Universal MosSCI provides worm strains that inherit an insertion cassette for each chromosome of the *C. elegans* genome. Insertion sites were engineered into the genome, which provide well defined landing sites. MosSCI strains contain an *unc-119* mutation as selection marker; therefore worms show an uncoordinated phenotype. The insertion cassette consists of a left and right recombination site, separated by the Mos1 transposon. Targeting vectors provide homology to the recombination sites, *unc-119(+)* and a transgene of interest can be cloned in between the homology regions. By co-injection of the targeting vector, together with a plasmid coding for the transposase (Table 16; pCFJ601), the transposon will be excised and a repair process inserts the transgene and *unc-119(+)* from the targeting vector into the insertion cassette. Therefore, worms loose the uncoordinated phenotype when an extrachromosomal array or an insertion into the genome is present (Frøkjær, 2008).

MosSCI integration was performed by microinjections of an injection mix containing the plasmids listed in Table 16. All *rho-1* transgenes were integrated on chromosome II. The universal MosSCI strain EG6699 was injected. The injection mix was first centrifuged at room temperature (RT) for 10 min at maximum speed and 0.5 μl was loaded into a needle that was mounted in a Micro-Injector (Femtojet Eppendorf) attached to a microscope

(Nikon Eclipse Ti). Young hermaphrodites were immobilized on 0.2 % agar-pads, covered with mineral oil to prevent worms from drying. Injections were performed into the gonad of young hermaphrodites, which subsequently were rescued from the agar-pad onto a seeded medium NGM plate (3 worms/plate). Injected worms were incubated at 25°C for 7-10 days until worms were starved. Rescue worms were identified as wild-type movers, indicating either expression from an extrachromosomal array or as integration into the genome. To identify the latter, three more plasmids were included in the injection mix (pGH8, pCFJ90 and pCFJ104) and were co-injected providing mCherry-reporters that are only visible if expressed as extrachromosomal array. Therefore, wild-type movers negative for mCherry-markers represented worms with a stable integration of the transgene into the genome. Homozygous integration is a rare event, therefore mCherry-negative wild-type movers were singled on small plates and incubated at 20°C and later generations were tested for homozygosity. The F1 generation of two of the singled worms was further singled out (16 worms each) and was incubated at 20°C. Following Mendel's law of segregation 25 % of the progeny should be homozygous for the integration. In the presence of a fluorescent marker this could already be tested by fluorescence-microscopy (Axioscope A1; Zeiss) and was further verified by PCR (Phusion<sup>®</sup> DNA polymerase) after worm lysis (2.2.3).

**Table 16: Composition of MosSCI injection mix**

Plasmid	Description	Final Concentration [ng/μl]
pCFJ601	<i>Peft-3::transposase</i>	50
pEZXX	Transgene of interest in targeting vector	50
pMA122	<i>Phsp::peel-1</i>	10
pGH8	<i>Prab-3::mCherry</i> (Pan-neuronal)	10
pCFJ90	<i>Pmyo-2::mCherry</i> (pharynx muscle)	2.5
pCFJ104	<i>Pmyo-3::mCherry</i> (body muscle)	5

### 2.2.7 Generation of dsRNA

For RNAi experiments the respective targeting sequence was amplified by PCR using *Taq* DNA polymerase (2.2.5.1). As template either cDNA (complementary DNA) or genomic DNA was used as indicated in Table 17. Primers were designed for the specific regions, containing a T7 overhang for both the forward and the reverse primer. PCR products were tested on a 0.8 % agarose gel and were purified using a DNA purification kit

(NucleoSpin<sup>®</sup> Gel and PCR Clean-up, Macherey&Nagel; 740609). Purified PCR products were used as template for *in vitro* transcription using MEGAscript<sup>®</sup> T7 kit (Ambion; AM1334). Before setting up the *in vitro* transcription reaction all surfaces and pipettes were cleaned with RNaseZAP<sup>®</sup> (ThermoFisher; AM9780) and filter tips were used. A minimum of 1 µg PCR product was used for *in vitro* transcription and the reaction was set up with double amounts (total of 40 µl reaction; Table 17). The reaction was assembled at RT and was incubated at 37°C for six hours. To remove template DNA, 1 µl Turbo DNase was added and incubated for 15 min at 37°C. RNA was purified using MEGAclean<sup>®</sup> kit (Ambion; AM1908). Concentration of purified dsRNA was measured using a Nanophotometer device (Implen) and correct size was verified by agarose gel electrophoresis.

**Table 17: Composition of *in vitro* transcription reaction**

Component	Amount
Nuclease-free Water	to 40 µl
ATP solution	4 µl
CTP solution	4 µl
GTP solution	4 µl
UTP solution	4 µl
10x Reaction Buffer	4 µl
Template DNA	>1 µg
Enzyme Mix	4 µl

### 2.2.8 Microinjection of dsRNA

RNAi experiments were performed by microinjections. The concentration of *rho-1* dsRNA was consistent for all experiments with a concentration of 0.42 µg/µl. For double RNAi experiments dsRNAs were mixed with final concentrations shown in Table 18. If three RNAs were co-injected *rho-1* dsRNA was used with a concentration of 0.42 µg/µl and the two remaining dsRNAs were mixed 1:1 resulting in half of the indicated concentrations in Table 18. The dsRNA (dsRNA mix) was centrifuged at 4°C for 10 min at full speed and 0.5 µl was loaded into an injection needle, which was mounted in a Micro-Injector (Femtojet Eppendorf) attached to a microscope (Nikon Eclipse Ti). Young hermaphrodites were mounted on a 0.2 % agar-pad covered with mineral oil. The needle was placed either

between the pharynx and the gonad or in the tail region and dsRNA was injected into the body cavity. The worms were rescued from the agar pad by pipetting 10  $\mu$ l M9 buffer onto the worm and 10  $\mu$ l M9 buffer on a seeded NGM plate. The worms were transferred with a worm picker from the agar pad into the drop of M9 buffer on the fresh plate. Injected worms were collected on a medium plate. For live-cell imaging worms were incubated at 20°C for the time indicated in Table 18.

**Table 18: RNAi experiments**

Gene	PCR template	Oligonucleotides <i>*T7 sequence is underlined</i>	Final conc. [ $\mu$ g/ $\mu$ l]	Incubation at 20°C [h]
<i>rho-1</i>	genomic DNA	1. <u>TAATACGACTCACTATAGG</u> GTCGAACTTGCTCTATGGGAT 2. <u>TAATACGACTCACTATAGG</u> GCAGAGCACTCCAAATATGC	0.42	27-31
<i>ect-2</i>	cDNA	1. <u>TAATACGACTCACTATAGG</u> AACTCCCCGCACCCGTGTAAC 2. <u>TAATACGACTCACTATAGG</u> AAGTAGGGTGTAATTTCAATTTGAAC	0.4	18-22
<i>rga-3/4</i>	genomic DNA	1. <u>TAATACGACTCACTATAGG</u> GCAACGCGTCGAAACATCG 2. <u>TAATACGACTCACTATAGG</u> GTTGGAGTGGCAGTTGGA	2.3	23-27
<i>cyk-1</i>	cDNA	1. <u>TAATACGACTCACTATAGG</u> TTGGAGTTCGATGCAGAAGA 2. <u>TAATACGACTCACTATAGG</u> TTGCCTTGTCAGGAACTGAA	0.45	27-31
<i>arx-2</i>	cDNA	1. <u>TAATACGACTCACTATAGG</u> CAGCTTCGTCAAATGCTTG 2. <u>TAATACGACTCACTATAGG</u> TATTTCCATGCAATACGCG	0.12	21-25
<i>nmy-2</i>	cDNA	1. <u>TAATACGACTCACTATAGG</u> AATTGAATCTCGGTTGAAGGAA 2. <u>TAATACGACTCACTATAGG</u> ACTGCATTTACGCATCTTATG	0.29	20-24
<i>ani-1</i>	genomic DNA	1. <u>TAATACGACTCACTATAGG</u> AGCCGGAGTTGGAAAGCTG 2. <u>TAATACGACTCACTATAGG</u> CCTATTCTTTTCCAAACGTTGC	0.56	27-31; 18-22 (part. depletion)

Gene	PCR template	Oligonucleotides <i>*T7 sequence is underlined</i>	Final conc. [µg/µl]	Incubation at 20°C [h]
<i>him-8</i>	cDNA	1. <u>TAATACGACTCACTATAGG</u> GATGCCACTTCTCTTGGACTTTG 2. <u>TAATACGACTCACTATAGG</u> AGACGGTGTAGACAACGATGG	0.59	

### 2.2.9 Embryonic lethality assay

Injected and non-injected (control) young adult hermaphrodites were incubated at 20°C for 24 h. Worms were singled to small seeded NGM plates and were grown for another 24 h at 20°C. Mother worms were removed from the plate and the progeny was counted 24 h later. Larvae and embryos were counted on each plate. The total number represented the brood size and embryonic lethality was calculated by dividing the number of embryos by the brood size. Results are pooled from at least three individual experiments.

### 2.2.10 Antibody generation against RHO-1

To generate a polyclonal antibody against RHO-1 the entire sequence was used for antigen preparation, except the last four AAs (CAAX-motif) that are responsible for PM-targeting and binding. Gibson Assembly<sup>®</sup> cloning primers were designed to amplify *rho-1*<sup>ΔCAAX</sup> sequence from cDNA and to amplify the backbone from pGEX-4T-1 plasmid. An N-terminal glutathione-S-transferase (GST)-tag was provided by the pGEX-4T-1 vector. The fragments were amplified by PCR using Phusion<sup>®</sup> DNA polymerase (New England Biolabs GmbH; M0530) and were purified following the protocol of the DNA purification kit (NucleoSpin<sup>®</sup> Gel and PCR Clean-up, Macherey&Nagel; 740609). Gibson Assembly<sup>®</sup>, transformation, colony-PCR, plasmid purification and sequencing were performed as described in section 2.2.5.

#### 2.2.10.1 Antigen expression and purification

Overexpression was performed in *E. coli* BL21 (DE3; home-made competent cells). Cells were transformed with the plasmid pEZ162 (GST::RHO-1<sup>ΔCAAX</sup>) or pGEX-4T-1 (GST) as described in 2.2.5.3. Next day, 20 ml LB-Carb (0.1 mg/µl) was inoculated with a single colony and was incubated for 16-18 h at 37°C. The main culture of 2 L LB-Carb was



inoculated with 2 ml of the pre-culture and was incubated at 37°C and 180 rpm until (optical density)  $OD_{600} = 0.6-0.8$  was reached. 1 ml sample was taken as reference before isopropyl- $\beta$ -D-thiogalactopyranosid (IPTG) addition. The sample was centrifuged at 4000 g, 4°C for 15 min. The supernatant was discarded and the pellet was frozen at -20°C. Then, 0.1 mM IPTG were added to the flask and the culture was incubated at 25°C, 180 rpm for 18 h. Again 1 ml sample ('after IPTG') was centrifuged at 4000 g, 4°C for 15 min. The rest of the culture was centrifuged in 500 ml centrifuge buckets at 4000 g for 15 min at 4°C. The pellet was transferred into 50 ml falcon tubes and was flash frozen in liquid nitrogen. The two samples, before and after IPTG, were tested for protein expression and solubility. The frozen pellets were thawed and 500  $\mu$ l extraction buffer (Table 19) was added to the tube. Cells were sonicated with 50 % amplitude by performing six cycles with 10 s/30 s on/off rate. Then, samples were centrifuged at 4°C, full speed for 15 min. The supernatant was separated and samples of the supernatant as well as the pellet were run on a SDS-gel and subsequently analyzed by coomassie staining and destaining to test for solubility.

Subsequently, frozen pellets of the main culture were thawed and sonicated in 10 ml extraction buffer on ice. The proteins were purified using Glutathione Sepharose<sup>TM</sup> 4B protein purification resin (GE Healthcare; 17075601). A column (Pierce<sup>TM</sup> Disposable Columns, 10 ml; Thermo Fisher Scientific; 29924) was prepared following the protocol provided by the supplier using 2 ml of Glutathione Sepharose<sup>TM</sup> 4B resin. The following steps were performed at 4°C. The resin was equilibrated by washing the column three times with 10 ml extraction buffer. The supernatant of the sonicated and centrifuged sample was added to the column, which was sealed with parafilm and subsequently was incubated for 30 min on a rotating wheel. The column was replaced on a stand. The following washing steps were performed once the beads were settled: (1) three times extraction buffer (Table 19) , (2) three times extraction buffer + 200 mM NaCl and (3) three times wash buffer (50 mM Tris-HCl, pH8). All washing steps were performed by adding 10 ml of the buffer to the column and the liquid was passed through by gravity flow. The antigen was eluted into five fractions; 2 ml elution buffer (Table 19) was added to the column per fraction and was incubated for 10 min before collected in a 2 ml centrifuge tube. All fractions were tested on a coomassie gel and protein concentration was determined by Bradford assay (2.2.10.2). The purified GST::RHO-1 antigen (21 mg in total) was sent to Davids Biotechnology GmbH where two rabbits were immunized.

**Table 19: Buffers used for Affinity Chromatography**

<b>Extraction buffer</b>	<b>Elution buffer</b>
50 mM Tris-HCl, pH8	50 mM Tris-HCl, pH8
100 mM NaCl	100 mM NaCl
10 % NP-40	10 % NP-40
Complete <sup>TM</sup> Protease Inhibitor (EDTA-free) (Roche; 04693132001)	10 mM Gluthathione

### 2.2.10.2 Bradford assay

Protein concentration was determined by Bradford assay. First, a standard curve of five different concentrations of 100  $\mu$ l bovine serum albumin (BSA) in H<sub>2</sub>O was prepared in a cuvette as listed in Table 20. Next, 1 ml of Quick Start<sup>TM</sup> Bradford 1x reagent (Bio-Rad; 5000205) was added to each sample and was incubated for 5 min at RT in the dark. Subsequently, OD<sub>595</sub> was measured using a Nanophotometer device (Implen). Using the measured standard curve, protein concentration of the purified antigen was determined. The sample was diluted in H<sub>2</sub>O in ratios of 1:5, 1:10 and 1:20 (100  $\mu$ l total) in a cuvette and 1 ml Quick Start<sup>TM</sup> Bradford 1x reagent was added to each dilution. Concentration was measured using the Nanophotometer device calibrated with the standard curve.

**Table 20: Standard curve Bradford Assay**

<b>Standard #</b>	<b>Concentration BSA [<math>\mu</math>g/ml]</b>
1	0
2	5
3	10
4	20
5	40

### 2.2.10.3 RHO-1 antibody purification

After successful immunization, the received sera of the two rabbits were purified. Purification was performed in two-step affinity purification using SulfoLink<sup>TM</sup> Coupling Resin (Thermo Scientific; 20401). When preparing the antigen, the GST-tag was not

removed from RHO-1. Therefore, GST antibodies first needed to be removed from the received sera, to only purify RHO-1 antibody. To achieve this goal, two columns were prepared: (1) GST and (2) GST::RHO-1 coupled to the resin.

First, disulfide bonds were reduced using 2-mercaptoethylamine-HCl (2-MEA). For this, 8.5 mg of GST::RHO-1 and 16 mg GST antigen were reduced to a volume of 1 ml in (0.1 M sodium phosphate buffer + 5 mM EDTA-Na; pH6) using a Pierce<sup>TM</sup> Protein Concentrator (Thermo Fisher Scientific; 88536). The protein solutions were added to 50 mM 2-MEA and were incubated at 37°C for 1.5 h. A Zeba<sup>TM</sup> Spin Desalting Column (Thermo Fisher Scientific; 89893) was used to remove 2-MEA, to exchange to coupling buffer and to reduce the volume to 2 ml. For affinity chromatography 4 ml of SulfoLink<sup>TM</sup> Coupling Resin was transferred into 10 ml Pierce<sup>TM</sup> Disposable Columns (Thermo Fisher Scientific; 29924) to obtain 2 ml resin. The column was equilibrated with 10 ml coupling buffer (Table 21). The protein solution (in 2 ml coupling buffer) was added to the resin and was mixed by end-over-end mixing for 15 min at RT. The column was placed in an upright position, in order for the resin to settle down, for 30 min at RT. Subsequently, the flow-through was collected in a fresh tube. The column was washed with 10 ml coupling buffer and 2 ml quenching reagent (Table 21) was added, followed by 15 min mixing at RT and 30 min incubation without mixing. After removing the solution by gravity flow, the column was washed with: (1) 15 ml wash buffer (Table 21) and (2) 10 ml storage buffer (Table 21) and was stored at 4°C.

**Table 21: Buffers used for cross linking of proteins to SulfoLink<sup>TM</sup> Coupling Resin**

Coupling buffer	Quenching reagent	Wash buffer	Storage buffer
50 mM Tris, pH 8.5	50 mM L-Cystein- HCl	1 M NaCl	1x PBS
5 mM EDTA-Na	In coupling buffer		0.05 % sodium azide (NaN <sub>3</sub> )

The prepared columns were equilibrated to RT and the storage buffer was removed by gravity flow. The resin was washed with 6 ml binding buffer. Next, 5 ml serum was mixed with 500 µl 10x PBS, which was added to the GST-column and was incubated by end-over-end mixing at 4°C for 16 h (overnight). The next morning the beads were settled for 1 h at 4°C. The flow through was collected in a 15 ml falcon tube (ΔGST serum) and the column was washed: (1) in 30 ml binding buffer (Table 22) and (2) 30 ml 1x PBS. For

elution, nine 2 ml centrifuge tubes were prepared with 200  $\mu$ l 1M Tris-HCl, pH8.5. Subsequently, 8 ml 0.2 M Glycine, pH2.5 was added to the column and 1 ml fractions were collected in the prepared 2 ml tubes with an incubation time of 1 min between each elution. The tubes were inverted to mix and neutralize the solution and were kept on ice. The pH was tested with a pH strip (the acidic elutions were neutralized by 1 M Tris-HCl, pH8.5). When all fractions were collected the column was washed with 20 ml 10 mM Tris pH8.0 and the pH was tested to be 7 or more. Afterwards the column was washed with 20 ml 1x PBS and 10 ml storage buffer. The column was stored at 4°C and was used for further rounds of purification. The same procedure was performed using the flow through ( $\Delta$ GST serum) of the serum that was first applied to the GST-column. The flow through contained the RHO-1 antibody that was further purified using the GST::RHO-1 coupled column as described for GST antibody purification.

**Table 22: Binding buffer used for GST and RHO-1 antibody purification**

Binding buffer
1x PBS
500 mM NaCl
0.1% Triton X-100

### 2.2.11 Nanobody generation against active, GTP loaded RHO-1

The antigen for the RHO-1 nanobody was designed as dimer that was specific for active GTP loaded RHO-1. Site-directed mutagenesis was performed to generate constitutively active RHO-1 by exchanging glutamine at position 63 to leucine. The plasmid generated to express GST-RHO-1 for antibody generation was used as template (pEZ162), providing *rho-1* sequence with a deletion of the CAAX-motif. The Q63L mutation was introduced by Gibson Assembly<sup>®</sup> cloning where the oligonucleotide was designed carrying the mutation. PCR, Gibson Assembly<sup>®</sup>, transformation, plasmid purification and sequencing were performed as described in 2.2.5. The purified plasmid was used as further template to amplify the mutated *rho-1* sequence, which was assembled as dimer with a short GS-linker into pET19-b backbone that provided a 10x His-tag. Gibson assembly oligonucleotides were designed to introduce the linker between the two *rho-1* sequences. Fragments were amplified by PCR (Phusion<sup>®</sup> DNA polymerase), cloning was performed by Gibson Assembly<sup>®</sup> and transformation, plasmid purification and sequencing was

performed as described in 2.2.5. In addition, two more recombinant proteins were expressed and purified: (1) RHO-1<sup>Q63L</sup> monomer and (2) RHO-1 wildtype. Both were used for subsequent biopanning and selection.

### **2.2.11.1 Antigen expression and purification for immunization and biopanning**

The following describes protein expression and purification for all three recombinant proteins. Overexpression of His-tagged RHO-1<sup>Q63L</sup> dimer (for immunization), RHO-1<sup>Q63L</sup> monomer and RHO-1 wildtype (for biopanning) was performed in the presence of chaperones to increase solubility in *E. coli* BL21 (DE3) after IPTG induction. Each plasmid was co-transformed with the plasmid expressing the bacterial chaperones GroEL/ES (Hsp60/Hsp10 in eukaryotes; plasmid #277; provided by Prof. Dr. Itzen). Transformation was performed as described in section 2.2.5.3, 1 µl of each plasmid was pipetted into 50 µl BL21 (DE3) competent cells. The plasmids coding for RHO-1 proteins was Carb resistant and the plasmid #277 had a Chloramphenicol resistance. A single colony was used to inoculate the pre-culture containing LB-Carb/Chloramphenicol (0.1 mg/ml and 34 µg/ml, respectively). The culture was incubated at 37°C, 180 rpm for 16-18 h. The main culture was inoculated with the pre-culture in a ratio of 1:100 (6.5 L for RHO-1<sup>Q63L</sup> dimer and 3 L each for RHO-1<sup>Q63L</sup> and RHO-1 wildtype) and was incubated at 37°C, 180 rpm until OD<sub>600</sub> = 0.6-0.8 was reached. Subsequently, 0.5 mM IPTG was added and the culture was incubated at 20°C or 25°C for 16-18 h for RHO-1<sup>Q63L</sup> dimer or RHO-1<sup>Q63L</sup> monomer and RHO-1 wildtype, respectively. Cells were harvested by centrifugation at 4000 rpm at 4°C for 15 min and were collected in 50 ml falcon tubes. The supernatant was discarded and the pellets were flash frozen in liquid nitrogen and stored at -80°C. The overexpression of His::RHO-1<sup>Q63L</sup> was repeated one more time to collect pellets of a total of 13 L culture.

The following steps I performed in the lab of Prof. Dr. Aymelt Itzen with the help of Dr. Sophie Vieweg at the Technical University Munich. Bacterial pellets were thawed, 10 ml extraction buffer (buffer A; Table 23) + 1 mM phenylmethylsulfonyl fluoride (PMSF) was added per pellet and all suspensions were pooled. Extraction was performed by French Press (CF Cell Disrupter; Constant Systems Ltd), followed by centrifugation of the lysates (40 min, 4000 rpm, 4°C). The protein was purified via the His-tag using an Äkta<sup>TM</sup> chromatography system (GE Healthcare) equipped with a nickel-column. First the

column was equilibrated with buffer A and buffer B (Table 23). Next, the supernatant was applied to the column. The column was subsequently washed with buffer A and finally the protein was eluted in several fractions in buffer B. After purification the fractions were tested on a coomassie gel and all positive fractions were further purified by size-exclusion (Äkta™ chromatography system) to eliminate RHO-1 monomer and/or chaperones. The pooled positive fractions were first dialyzed using dialysis buffer containing 100 µM ATP to release chaperone-RHO-1 binding, which would subsequently be eliminated by size-exclusion. Dialysis was performed overnight in a dialysis tube at 4°C. The sample was concentrated to 2 ml using Amicon concentrators (30.000 MW cutoff). Size-exclusion chromatography was performed using an Äkta™ size-exclusion column. Elutions were tested by coomassie gel and the concentration was measured by NanoDrop™ 2000 (Thermo Fisher Scientific; ND-2000). Positive elutions were pooled and concentrated.

The purified proteins were tested for GDP and GTP loading using high performance liquid chromatography (HPLC) (Thermo Fisher Scientific). A standard Gmix was used as reference containing GMP, GDP and GTP. The purified antigen was prepared as 50 µM in 50 µl GF buffer (Table 25) and was incubated for 5 min at 90°C. Subsequently, the probe was centrifuged at maximum speed for 10 min. The supernatant was transferred into a new tube and 30 µl were used for HPLC analysis. By comparing the retention time of RHO-1<sup>Q63L</sup> dimer, RHO-1<sup>Q63L</sup> monomer and RHO-1 wildtype with the Gmix, GDP or GTP was verified.

**Table 23: Buffers used for affinity purification**

<b>Component</b>	<b>Buffer A</b>	<b>Buffer B</b>
Tris-HCL	20 mM	20 mM
NaCl	100 mM	100 mM
Imidazole	10 mM	500 mM
GDP/GTP*	10 µM	10 µM
b-mercapto	2 mM	2 mM
MgCl <sub>2</sub>	1 mM	1 mM

pH7.8

**Table 24: Dialysis Buffer**

Component	Dialysis Buffer
Hepes	20 mM
NaCl	100 mM
MgCl <sub>2</sub>	1 mM
DTT	1 mM
GDP/GTP*	10 μM
ATP	100 μM

pH7.5

**Table 25: Buffer for size-exclusion**

Component	GF Buffer
di-Natriumhydrogenphosphat	20 mM
Sodium dihydrogenphosphat	20 mM
NaCl	50 mM
MgCl <sub>2</sub>	1 mM
GDP/GTP*	10 μM
DTT	1 mM

pH7.5

\*For all buffers: GDP was added for RHO-1 wildtype and GTP was added for RHO-1<sup>Q63L</sup> dimer and monomer to stabilize the proteins in the respective state.

### 2.2.11.2 Cloning of V<sub>H</sub>H sequences

Sequences received from ChromoTek were cloned with a C-terminal GFP-tag: (1) into the expression vector pcDNA5 for transient transfection in HeLa cells and (2) into the expression vector pBC1454 with the regulatory regions *mai-2* promoter and 3'UTR to test expression and localization in *C. elegans* by microinjections. The GFP-tag was separated by a (GGGGS)<sub>4</sub> linker for both strategies. Cloning (Gibson Assembly<sup>®</sup>), transformation and plasmid purification were performed as described in sections 2.2.5.2-2.2.5.4.

### **2.2.11.2.1 Transient transfection of HeLa cells to test V<sub>H</sub>H sequences *in vivo***

HeLa cells were grown in high glucose Dulbecco's modified Eagle's medium (DMEM) containing 10 % superior fetal bovine serum (FBS) and 1 % Penicillin/Streptomycin at 37°C with 5 % CO<sub>2</sub>. The day before transfection, a 6-well plate was prepared with glass coverslips and a total number of 70.000 cells/well were plated. Cells were incubated at 37°C with 5 % CO<sub>2</sub> overnight. X-tremeGENE™ 9 transfection reagent (3 µl) was diluted with serum-free medium (100 µl) in a 3:1 ratio and 1 µg DNA was added. The transfection reagent DNA complex was incubated for 15 min at RT and was then added to the cells in a dropwise manner. Protein expression was tested 24 h later by confocal spinning disc microscopy (UltraVIEW VoX spinning disk confocal microscope; PerkinElmer) with a 488-laser line and 100 % laser power.

### **2.2.11.2.2 Microinjections to test V<sub>H</sub>H sequences in *C. elegans***

DNA transformation in *C. elegans* was performed by microinjections. The plasmid carrying the GFP-tagged V<sub>H</sub>H sequence was injected with the transformation marker *rol-6(su1006)* (pRF4). The injection mix was prepared containing 100 ng/µl pRF4 and 3 ng/µl of the plasmid carrying the V<sub>H</sub>H sequence to be tested (Table 10; last three rows). The DNA mix was centrifuged at maximum speed for 10 min at RT and 0.5 µl was loaded in an injection needle. Microinjections of N2 worms were performed as described in 2.2.6. After injections worms were incubated at 25°C and F1 progeny rollers were imaged using confocal spinning disk microscopy (UltraVIEW VoX spinning disk confocal microscope; PerkinElmer) with a 488-laser line and 100 % laser power.

## **2.2.12 Western Blot analysis**

Worms were picked in 500 µl M9 buffer in a 1.5 ml centrifuge tube on ice. The worms were washed by removing and replacing 450 µl M9 buffer. This step was performed three times. Finally, the volume of M9 buffer was reduced to 25 µl and 25 µl 2x sample buffer (Lämmli buffer) was added to reach a concentration of approximately 1 worm/µl. After 5 min incubation at 95°C, worms were sonicated in a water bath at 60°C for 20 min, followed by another incubation step at 95°C for 5 min in a heat block. Subsequently, the sample was centrifuged at 200 g for 3 min and 20 µl was loaded per lane of a 10 % Acrylamide SDS-gel (Table 26). The gel was set up in an electrophoresis chamber (Bio-Rad) containing 1x running buffer and was run for 45 min at 120 V. Subsequently, a



polyvinylidene difluoride (PVDF) membrane was activated with 100 % EtOH and was used to blot the proteins from the SDS-gel onto the membrane. Blotting was performed in transfer buffer for 1.5 h at 4°C with 200 mA/membrane. The membrane was blocked in 5 % milk/TBS-T (1x TBS + 0.1 % Tween) and was incubated with rabbit anti-RHO-1 (Home-made #14; 1:2000) and mouse anti  $\alpha$ -tubulin (Sigma; T9026; 1:10000). Incubation of the primary antibody was performed at 4°C for 16-18 h (overnight). Three washes in TBS-T were performed at RT for 5 min each. As secondary antibody HRP-conjugated rabbit (Bio-Rad; 170-6515; 1:15.000) and HRP-conjugated mouse (Bio-Rad; 170-6516; 1:7500) were used and the membrane was incubated at RT for 45 min. After three more washes in TBS-T (5 min at RT each), proteins were detected on the membrane using ECL Prime Western Blotting Detection Reagent (GE Healthcare; RPN2232). Detection was performed using ChemiDoc<sup>®</sup> imaging system (Bio-Rad).

**Table 26: Composition of SDS-gel for SDS-gel electrophoresis**

Component	Resolving Gel (10 %)	Stacking Gel
Acrylamide 40 %	1 ml	0.18 ml
Resolving buffer	1 ml	-
Stacking buffer	-	0.5 ml
Water	2 ml	1.32 ml
APS 10 %	30 $\mu$ l	15 $\mu$ l
TEMED	4 $\mu$ l	3.75 $\mu$ l

### 2.2.13 Live-cell imaging using spinning disk confocal microscopy

Live-cell imaging was performed using a Nikon inverted microscope (Eclipse Ti), equipped with a confocal spinning disk unit and NIS Elements software. Images were acquired using a 100x 1.45-NA Plan-Apochromat oil immersion objective and an Andor DU-888 X-11056 camera. A 488 nm and 561 nm laser were used to image GFP- and red-fluorescent probes (mCherry (mCh), RFP, mKate2). Image acquisition was performed with an exposure time of 200 ms and a quad filter was used for both channels. For some images differential interference contrast (DIC) or transmission images were acquired for the central plane as indicated in the individual sections.

Imaging of HeLa cells and *C. elegans* embryos expressing GFP-tagged V<sub>H</sub>H sequences was performed using an UltraVIEW VoX spinning disk confocal microscope

(PerkinElmer), attached to an Axio Observer D1 (Zeiss). The microscope was equipped with a 63x 1.4-NA Plan-Apochromat oil immersion objective (Zeiss), an EMCCD C9100-50 camera (Hamamatsu) and a 488 nm laser. The software Volocity 6.1.1 (PerkinElmer) was used. Single snapshots of HeLa cells in anaphase and *C. elegans* embryos in different developmental stages were acquired for GFP-channel.

For sample preparation an agar pad was prepared on a 76 mm x 26 mm slide by pipetting 90  $\mu$ l of 2 % agar on the slide and the drop was covered with a second slide and left for cooling. In the meanwhile, gravid hermaphrodites were transferred into 4  $\mu$ l M9 buffer on an 18 mm x 18 mm coverslip and were dissected using a syringe needle and a stereo microscope. The coverslip was inverted onto the agar pad and the edges were sealed with Vaseline to prevent evaporation. The sample was mounted on the microscope with the coverslip towards the objective. Early embryos were first detected using a 10x objective, the position was saved in the software and the objective was changed to 100x for imaging.

### **2.2.13.1 Central- and cortical plane imaging**

Two positions were set using transmission light: (1) a single central plane and (2) three cortical z-planes (with 0.75  $\mu$ m distance). The focus for the central plane was set where the nuclei and the outline of the embryo were sharply visible. For the cortical plane the objective was lowered to focus on the cortex that was closer to the coverslip. The cortical plane was in focus when the granules within the embryo were just about to lose focus and became blurry. From the focus set for the cortex, two planes  $\pm$  0.75  $\mu$ m were acquired in addition. The central plane was imaged in DIC and fluorescent channels according to the fluorophores expressed. Cortical images were acquired for fluorescent channels only. For dual color imaging the channels alternated before the z-plane was changed. Imaging was started when the two nuclei met in the center of the embryo prior to nuclear envelope breakdown (NEBD) and was continued for a duration of 15 min with a frame rate of 16 s.

### **2.2.13.2 High-time resolution imaging (cortical plane only)**

High-time resolution imaging was performed only at the cortex. The focus was set as described in 2.2.13.1 (cortex) except that only one z-plane was imaged. Prior to imaging embryos were followed in transmitted light and acquisition was started approx. 80 s-90 s after NEBD. Images were acquired in dual color (GFP and red-fluorescent channel) every 2.75 s for a duration of 5 min.

## **2.2.14 Image analysis**

All image analysis was performed in Fiji (Schindelin and Arganda, 2012), Microsoft Excel, KNIME<sup>®</sup> Analytics Platform and GraphPad Prism. For visualization and analysis of the cortical plane, only a single z-plane was used. Dual color images were treated separately and channels were merged at the end.

### **2.2.14.1 Image representation**

For image representation of all central plane images, the background signal outside the embryo was measured and the mean intensity was subtracted. For all cortical images, each channel was edited by using a semi-automated macro (Appendix 1 and Appendix 2), which is described in the following: The user draws a box in the anterior of the embryo to measure mean intensity. For the GFP (488 nm laser line) and the red (561 nm laser line) channel 80 % and 90 % of the mean intensity was subtracted from the overall signal, respectively. Subsequently, a ‘Gaussian Blur’ filter was applied with a sigma of 1 followed by an ‘Unsharp Mask’ filter with a radius of 2 pixels and a Mask Weight of 0.6. Central- and cortical plane images were rotated with bicubic interpolation to orient the anterior to the left and the posterior to the right (Figure 10). Figures were assembled using Affinity Designer software.

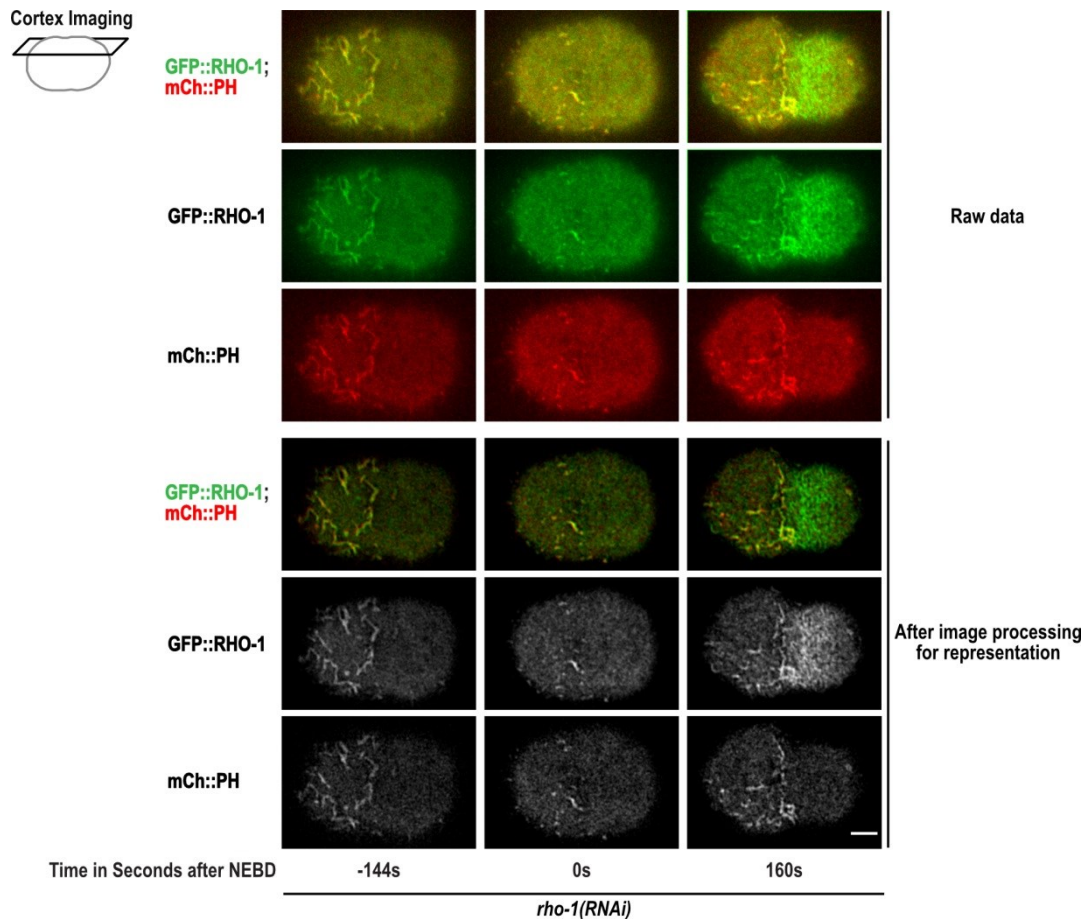


**Figure 10: Image processing for representation of the cortical plane.** Example of a cortical live-cell spinning disk microscopy image showing a one-cell embryo (shown in Figure 20) as raw data and after image processing. Image processing was applied for all cortical images for representation purposes that are shown in the figures throughout this work.

### 2.2.14.2 Cytokinesis timing analysis

Cytokinesis timing was assayed on central plane images. The timing from NEBD to back-to-back membrane formation as well as the timing from back-to-back to full ring ingression was measured. NEBD was determined in DIC channel, as the time point where the border of the nucleus was no longer visible. Back-to-back membrane formation was determined in the GFP-channel as the time point of first slight ingression where the membrane started to form a double membrane. Full ring ingression was determined in GFP-channel and represented the time point where ring ingression was completed.

### 2.2.14.3 Line-scan and zone width analysis

Line-scan and zone width analysis were performed on single cortical plane images. A line with a line width of 40 pixel was drawn from the anterior to the posterior. The intensity

along that line was plotted (cortical intensity) and the data was saved in an Excel file. Further, background intensity was measured outside the embryo and the cytoplasmic signal on central plane images (mean intensity cytoplasm center) was measured in a box at the anterior for the same time point. Values were determined for all embryos and time points of interest and were saved in Excel files. Further analysis was performed in KNIME<sup>®</sup> workflows.

*Line-scan analysis:* The cortical intensities were normalized to the cytoplasmic signal measured at the central plane (cortical intensity/mean intensity cytoplasm center). For each embryo and for each time point the length of the embryo was normalized to 0 % anterior and 100 % posterior. Further, embryonic length was divided into intervals where the mean normalized intensity was calculated for 0-10 %, 10-20 % ..., 90-100 % embryonic length. Mean normalized intensities of all embryos were plotted against embryonic length intervals (5 % [0-10 %] - 95 % [90-100 %]) for individual time points using GraphPad Prism.

*Zone width analysis:* Background intensity was subtracted from cortical intensities (Intensity-BG). Embryonic length was normalized to 0 % anterior and 100 % posterior and the mean of the first 30 % was calculated. Moving Average was applied on Intensity-BG values using 'center simple' method with a 'Window Length' of 15 (MA-Intensity). Subsequently, the mean of the first 30 % was subtracted from the MA-Intensity to shift the baseline and to eliminate anterior signal that could arise from anterior GFP::RHO-1 PH-positive foci (MA-Intensity – 30 %). The maximum intensity was determined for the MA-Intensity – 30 % values representing the GFP::RHO-1 peak and all values were normalized to the maximum (maximum=1). Values below 0.5 were eliminated and zone width was calculated as the difference between the remaining values of maximum and minimum embryonic length. Individual zone width data was plotted for all embryos analyzed for defined time points in GraphPad Prism.

#### **2.2.14.4 Co-localization analysis of equatorial foci**

Co-localization was determined between equatorial structures of GFP::RHO-1 or PLST-1::GFP and LifeAct::RFP on single cortical images 160 s after NEBD. Equatorial structures were first segmented by using the same macros used for image representation purposes (2.2.14.1). However, for both the GFP and the RFP channel 90 % of the mean intensity measured in a box at the anterior was subtracted for identical treatment of the two

channels. Next the ‘Gaussian Blur’ filter (sigma=1) and the ‘Unsharp Mask’ filter (radius=2; mask=0.6) were applied. Images were rotated (bicubic interpolation) to orient the anterior to the left and the posterior to the right. The equatorial region was analyzed for co-localization with a box size of 4.5  $\mu\text{m}$  x 13  $\mu\text{m}$ . The plugin ‘Coloc2’ in Fiji was used for analysis with the following settings: ‘Threshold regression’=Costes; ‘PSF’=3.0; ‘Costes randomizations’=50. A second analysis was performed to test for true co-localization where the RFP-channel was rotated 180° (randomized) and co-localization was analyzed again using same settings in ‘Coloc2’.

### **2.2.14.5 Structure analysis of equatorial foci**

Structure analysis was performed for equatorial GFP::*RHO-1* foci, that did not co-localize with the membrane marker (mCh::*PH*), for defined time points indicated in the Figures. For analysis, single cortical images were used. A semi-automated macro was used to first segment GFP::*RHO-1* and mCh::*PH* foci, then PH-positive GFP::*RHO-1* foci were eliminated and subsequently further segmentation was used to identify single particles at the equator that were analyzed for several characteristics described below.

The following describes the operations performed by the macro. First the user duplicates the image by choosing the time point of interest and z-plane to analyze for GFP and mCherry channel. The substack is saved. Channels are split and saved separately. The user draws a box in the anterior of the embryo for both channels and the mean intensity is subtracted from the images. Subsequently, a ‘Gaussian Blur’ filter (sigma=1) and ‘Unsharp Mask’ filter (radius=2; mask=0.6) were applied as described in section 2.2.14.1. The overall intensity of both channels is measured by a box drawn by the user. Since mCherry intensities are weaker compared to GFP intensities, the red channel is multiplied by the ratio of GFP/mCherry intensities. Subsequently, the red channel is subtracted from the green channel leaving only PH-negative GFP::*RHO-1* foci behind. Next an ‘Auto Threshold’ with the method ‘Moments’ is applied (white objects on black background) to identify GFP::*RHO-1* particles. To separate individual foci ‘Watershed Irregular Features’ provided from the BioVoxxel Toolbox is used with following settings: ‘Erosion cycle number’=1; ‘Convexity threshold’=0; ‘Separator size’=4-infinity. Small foci in between particles are eliminated by ‘Remove Outliers’ with a radius of 1.5 pixel and a threshold of 50 for bright outliers. A binary image is generated and particles are analyzed (‘Particle Analyzer’) with following settings: ‘Size’=0-Infinity; ‘Circularity’=0-1. Particles identified are saved as regions of interest (ROIs) in the ROI manager and can be applied to the

original image of the GFP::RHO-1 channel (Figure 31 B). Using the saved ROIs the mean intensity, area, perimeter and circularity were measured for each particle and were saved in Excel files. All particles with an area  $< 0.1 \mu\text{m}^2$  were eliminated in a KNIME® workflow. Finally, all foci were plotted together in one graph for the number of embryos analyzed using GraphPad Prism. The perimeter represents the length of the outside boundary of the selection and the circularity is calculated by Formula 2.

**Formula 2: Calculation of circularity in Fiji**

$$\text{Circularity} = 4\pi * \frac{\text{Area}}{\text{Perimeter}^2}$$

### 2.2.14.6 PIV analysis

To assay GFP::RHO-1 and LifeAct::RFP dynamics, high-time resolution images were analyzed using the PIV plugin in Fiji (Tseng and Duchemin, 2012). Cortical images were first segmented as described in 2.2.14.4 separately for GFP and RFP channels. In brief 90 % of mean signal was subtracted; ‘Gaussian Blur’ and ‘Unsharp Mask’ filters were applied. Images were rotated (bicubic interpolation) with the anterior to the left and the posterior to the right and were cropped to a size of 288 pixel x 192 pixel. Analysis was performed for 15 consecutive time points ( $t_1 = 146 \text{ s}$  to  $t_{15} = 185 \text{ s}$  after NEBD) using a macro script, provided from the PIV-ImageJ plugin website for batch mode and batch plotting of PIV results (<https://sites.google.com/site/qingzongtseng/piv>). ‘Iterative PIV (Advanced)’ was applied with the following settings: ‘PIV1 interrogation window size’=32 (SW1, VS1=32); ‘PIV2 interrogation window size’=16 (SW2, VS2=16); ‘PIV3’=0; ‘Correlation threshold’=0.6. Results are given for the first (PIV1) and second pass (PIV2). For analysis only the second pass results (PIV2) were used, which were saved as separate text files for each correlated image pair ( $t_{x+1} - t_x$ ). The text file provided the following information (first five columns) that are important to generate the vector fields: (1) the position in x/y (2) the displacement of the vector given by the x and y component  $ux1$  and  $uy1$  and (3) the magnitude of the vector ( $mag1$ ). Single text files for all time points were loaded and merged in a KNIME® workflow for both channels GFP::RHO-1 and LifeAct::RFP and were the basis for the following analysis.

An equatorial and anterior region was defined by a box, spanning six vectors each, to compare the dynamics within and outside the RHO-1 zone. All images were cropped to the

same size, therefore the region for anterior and equator were integrated into the KNIME® workflows by x/y coordinates. For *nmy-2(RNAi)* and *cyk-1(RNAi)* embryos, GFP::RHO-1 zone was slightly shifted towards the anterior compared to control (*rho-1(RNAi)*), therefore the equatorial region was defined one vector row closer to the anterior.

#### 2.2.14.6.1 Velocity distribution assay

The magnitude of the vector describes the distance in pixel of the displacement from one time frame to the next. Velocity is distance over time. Therefore, the magnitude was converted into velocity in  $\mu\text{m}/\text{min}$  for anterior and equator using Formula 3. Velocities were calculated for the six vectors within the anterior and equatorial region for all 15 time points. Therefore, a total of 90 vectors were analyzed per embryo. For both regions velocities were classified into intervals of  $10 \mu\text{m}/\text{min}$  ( $0-10 \mu\text{m}/\text{min}$ ;  $10-20 \mu\text{m}/\text{min}$ ...,  $50-60 \mu\text{m}/\text{min}$ ) and the amount of vectors within each interval was determined to generate a velocity distribution plot. The mean amount of vectors for all embryos analyzed was plotted against the velocity intervals using GraphPad Prism for anterior and equator.

#### Formula 3: Conversion of magnitude into velocity

$$\text{Velocity } [\mu\text{m}/\text{min}] = ((\text{mag1}[\text{pixel}] / 7.6243 [\text{pixel}/\mu\text{m}]) * 60 [\text{s}/\text{min}]) / 2.75 [\text{s}]$$

with: mag1 [pixel] = length in pixel measured by PIV analyzer in Fiji  
 7.6243 pixel/ $\mu\text{m}$  = image scale  
 2.75 s = imaging time interval

#### 2.2.14.6.2 Velocity correlation assay

The correlation between the velocities of GFP::RHO-1 and LifeAct::RFP was determined for each vector within the anterior and equatorial region and each time point. Mean correlation was represented by the Pearson's Correlation Coefficient  $\rho$  generated in KNIME. Individual correlation was plotted in a dot plot using GraphPad Prism.

#### 2.2.14.6.3 Orientation correlation assay

Correlation between the orientation of GFP::RHO-1 and LifeAct::RFP vectors (angle between two vectors) at the same position was determined in a KNIME® workflow. The correlation was represented by the angle between the two vectors for each position within the anterior and equatorial region for all time points. A small angle ( $0^\circ$ ) represented high correlation and therefore similar direction of displacement, whereas angles closer to  $180^\circ$  represented opposite orientation. The angle between the two vectors was calculated using



Formula 4. Angles were categorized within intervals of 30° (0°- 30°, 30°- 60°..., 150°- 180°) and the amount of vectors within each interval was plotted in percentage as mean for all embryos analyzed.

**Formula 4: Calculation of the angle between two vectors**

$$\cos\varphi = \frac{\vec{u} \cdot \vec{v}}{|\vec{u}| \cdot |\vec{v}|} \quad \rightarrow \quad \varphi = \cos^{-1} \left( \frac{\vec{u} \cdot \vec{v}}{|\vec{u}| \cdot |\vec{v}|} \right)$$

with:  $\vec{u}$  = vector  $\begin{pmatrix} u_x \\ u_y \end{pmatrix}$  GFP::RHO-1  
 $\vec{v}$  = vector  $\begin{pmatrix} v_x \\ v_y \end{pmatrix}$  LifeAct::RFP  
 $|\vec{u}|$  = mag1 (length) vector GFP::RHO-1  
 $|\vec{v}|$  = mag1 (length) vector LifeAct::RFP

### 2.2.14.7 Alignment assay

Alignment of GFP::RHO-1 and LifeAct::RFP equatorial structures were assayed using high-time resolution images. Cortical images were processed as described in 2.2.14.4. In brief 90 % of mean signal was subtracted; ‘Gaussian Blur’ and ‘Unsharp Mask’ filters were applied and images were rotated (‘bicubic interpolation’) to orient anterior left and posterior right. Structure alignment was measured for four time points (97 s, 119 s, 146 s and 160 s after NEBD) in an equatorial region of 4.5 μm x 13 μm using the Fiji algorithm ‘Directionality’. The method ‘local gradient orientation’ was used with 90 bins between -90° and 90°. The result was saved in an Excel file. Alignment along the anterior-posterior axes represented 0° whereas 90° and -90° showed perpendicular alignment representing orientation along the equator. For each positive and the corresponding negative value the sum was calculated. Therefore, the number of bins was reduced to 45 (0°- 90°). For all embryos analyzed the mean frequency of orientation within the 45 bins was plotted as percentage in a polar plot generated in R (<http://www.r-project.org>; the R script was provided by Nikhil Mishra). Random orientation was represented by equal distribution of frequencies for the different bins with a mean frequency of 2.2 %. The polar plot was generated for GFP::RHO-1 and LifeAct::RFP for all four time points. To determine the timing of alignment the mean percentage within the bins between 70°- 90° was calculated. An increase in the frequency represents alignment along the equator. Mean percentage of 70°-90° directionality was plotted for the four time points in GraphPad Prism.

### 2.2.14.8 FRAP experiments

FRAP experiments were performed using a Nikon inverted microscope (Eclipse Ti) equipped with a FRAP unit and NIS Elements software. Images were acquired using a 100x 1.45-NA Plan-Apochromat oil immersion objective and an Andor DU-888 X-11056 camera. Imaging was performed using a 488-laser line with 200 ms exposure time. The readout mode was set to EM Gain 20 MHz at 16-bit with an EM Gain Multiplier of 140 and Conversion Gain set to 'Gain2'. For photobleaching 100 % laser power was used. Samples for FRAP imaging were prepared using Polybead<sup>®</sup> microspheres (Polysciences; 18329-5) for mounting. A 1:10 dilution in M9 buffer was prepared and 4  $\mu$ l of the beads/M9 buffer dilution was pipetted onto an 18 mm x 18 mm coverslip. Gravid hermaphrodites were directly dissected in the drop of beads/M9 buffer dilution using a syringe needle. Embryos were isolated from remaining worm body parts and the coverslip was inverted onto a slide with the size of 76 mm x 26 mm. The slide was mounted on the microscope and early embryos were identified with a 10x objective. The position was saved in the software and the objective was changed to 100x. The bleaching region was set to 5.07  $\mu$ m x 5.07  $\mu$ m for all experiments. Imaging was performed for a single cortical z-plane as described in 2.2.13.1 and 2.2.13.2. Three images were acquired pre-bleaching and then the ROI was bleached for the minimum time duration possible (524 ms). Subsequently, 200 loops were acquired with no delay intervals (0.22 s).

*Photobleaching of an anterior region right after NEBD:* These experiments were performed in the presence of endogenous RHO-1 (without *rho-1(RNAi)*) for embryos expressing GFP::RHO-1 and GFP::PBS-CAAX. The bleaching area of 5.07  $\mu$ m x 5.07  $\mu$ m was set at the anterior of the embryo at a time point right after NEBD. First NEBD was determined in transmitted light and then imaging was started (pre-bleach imaging, bleaching, post-bleach imaging) using GFP-channel only.

*Photobleaching of an anterior (low F-actin density) and an equatorial (high F-actin density) region:* Photobleaching experiments at the anterior were performed right after NEBD and 160 s after NEBD at the equator, for embryos expressing GFP::RHO-1 after RHO-1 depletion by RNAi injections. The bleaching area of 5.07  $\mu$ m x 5.07  $\mu$ m was used for both the anterior and equatorial region. Each embryo was only bleached once. NEBD was determined in transmitted light as a reference for bleaching experiments.

### 2.2.14.8.1 FRAP analysis

The analysis of FRAP experiments was performed in Fiji and Microsoft Excel. The fluorescence recovery (FR) was measured by drawing a box along the bleaching area ( $FR_{ROI}$ ;  $ROI_{bleach}=5.07 \mu\text{m} \times 5.07 \mu\text{m}$ ). The intensity profile within the box was plotted over time using the Fiji algorithm ‘Plot Z-axis Profile’ and data was saved in Excel. Fluorescence recovery was further measured at two more positions using the same sized box ( $ROI_{bleach}$ ): (1) within the embryo outside the ROI (acquisition bleach;  $FR_{cortex}$ ) and (2) the background outside the embryo ( $FR_{BG}$ ) (Figure 11). For both areas the Z-axis profile was plotted and all data were saved in the same Excel file ( $FR_{ROI}$ ,  $FR_{cortex}$ ,  $FR_{BG}$ ). First,  $FR_{BG}$  was subtracted from  $FR_{ROI}$  and  $FR_{cortex}$  for all individual time points. Next, mean of the first three values (pre-bleach imaging) was calculated for both  $FR_{ROI}$  and  $FR_{cortex}$  and all remaining values were normalized to the mean accordingly. Subsequently, normalized  $FR_{ROI}$  values were divided by normalized  $FR_{cortex}$  values, to consider acquisition bleaching. Calculations are summarized in Formula 5. Normalized values were plotted against time.

Half time of recovery ( $t_{1/2}$ ) represents the time where half intensity of the plateau value is reached, which was determined by using a Jython script provided by ImageJ to analyze FRAP movies ([https://imagej.net/Analyze\\_FRAP\\_movies\\_with\\_a\\_Jython\\_script](https://imagej.net/Analyze_FRAP_movies_with_a_Jython_script)). For Figure 28 C (GFP::RHO-1) and Figure 35 D, E (low F-actin) the datasets were pooled from individual experiments and plotted together for both figures. Of note, the dataset includes embryos that were *rho-1(RNAi)* injected and non-injected. Since the anterior GFP::RHO-1 patches were shown to be independent of endogenous RHO-1 and the mean of the two individual datasets were comparable ( $2.02 \pm 0.2 \text{ s}$  ( $n=7$ ) and  $2.1 \pm 0.36 \text{ s}$  ( $n=4$ )), the datasets were pooled and used for both figures (Figure 28 C, Figure 35 D, E).

#### Formula 5: Normalization of recovery curves

$$FR_{ROI\_norm} = \frac{\overline{FR_{cortex \text{ pre-bleach}}}}{\overline{FR_{cortex}(t) - FR_{BG}(t)}} * \frac{FR_{ROI}(t) - FR_{BG}(t)}{\overline{FR_{ROI \text{ pre-bleach}}}}$$

$$\text{with: } \overline{FR_{cortex \text{ pre-bleach}}}, \overline{FR_{ROI \text{ pre-bleach}}} = \frac{1}{3} \sum_{t=1}^{t=3} FR_X(t) - FR_{BG}(t);$$

$t_1$ - $t_3$ : first three images acquired pre-bleaching

### 2.2.14.8.1.1 Lateral Diffusion analysis

To test for lateral diffusion of GFP::*RHO-1* within the PM, the bleaching ROI was divided into two areas, an outside ROI ( $FR_{ROI\_Outside}$ ) and an inside ROI ( $FR_{ROI\_Inside}$ ) (Figure 11). The outside ROI covered the area between  $ROI_{bleach}$  and a box of the size of  $4.07 \mu\text{m} \times 4.07 \mu\text{m}$  (area of  $9.14 \mu\text{m}^2$ ). The inside ROI was set to  $1.97 \mu\text{m} \times 1.97 \mu\text{m}$  (area of  $3.88 \mu\text{m}^2$ ). Recovery curves were normalized to the background and acquisition bleach as described for FRAP analysis (2.2.14.8.1). Both normalized recovery curves were plotted against time.

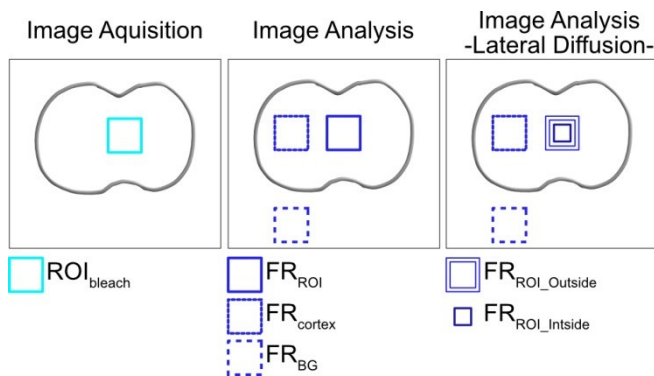


**Figure 11: FRAP image acquisition and analysis.** Schematic showing the  $ROI_{bleach}$  (light blue; left) for photobleaching during image acquisition and ROIs used for image analysis (dark blue; two panels on the right). Acquisition bleaching was measured in a box outside the bleaching area ( $FR_{cortex}$ ; dashed dark blue box inside embryo) and background signal was measured outside the embryo ( $FR_{BG}$ ; dashed dark blue box outside embryo) for normalization of recovery curves. For lateral diffusion analysis the  $ROI_{bleach}$  was divided into an outside ( $FR_{ROI\_Outside}$ ) and inside ( $FR_{ROI\_Inside}$ ) area where recovery was determined individually.

### 2.2.14.9 Statistical analysis

Statistical analysis was performed in GraphPad Prism. First the data sets were tested for normal distribution. If the data were normally distributed, a parametric test (Student's *t* test) was performed otherwise a non-parametric test was used. As non-parametric test either Wilcoxon or Mann-Whitney-U tests were performed. The individual test used is mentioned in the figure legend accordingly. Graphs showing mean values are presented with error bars that represent either standard deviation (SD) or standard error of the mean (SEM) indicated in the individual sections (figure legend).

### 3 Results

The small GTPase RhoA is the key initiator for contractile ring assembly (Jantsch, 2000; Kishi et al., 1993; Drechsel et al., 1997) and is known to form a narrow zone of active RhoA at the equatorial membrane during cytokinesis (Yonemura and Hirao, 2004; Bement and Benink, 2005; Takaishi et al., 1995; Nishimura and Yonemura, 2006; Kamijo et al., 2006; Yüce et al., 2005). However, how this narrow zone of active RhoA is maintained at the equator is still an open question in the field. To study RhoA dynamics and to elucidate its temporal and spatial regulation during cytokinesis, I first established a RhoA (hereafter referred to as the *C. elegans* homologue RHO-1) probe that was used for *in vivo* studies in the *C. elegans* one-cell embryo. Three different approaches were used: (1) integration of a single-copy GFP-tagged RNAi-resistant *rho-1* transgene into *C. elegans* genome (2) CRISPR/Cas9 to tag endogenous *rho-1* with a fluorophore and (3) generation of a nanobody to specifically visualize active RHO-1 *in vivo*.

A genetic replacement system was established, where GFP-tagged and non-tagged RNAi-resistant *rho-1* transgenes were integrated into *C. elegans* genome and endogenous RHO-1 was depleted by RNAi. Using this tool, I elucidated mechanisms that control narrow RHO-1 zone formation and maintenance during cytokinesis. I performed localization studies of GFP::RHO-1 during cytokinesis using live-cell confocal spinning disk microscopy and tested the contribution of: (1) the RHO-1 activation/inactivation cycle driven by GEF and GAP, (2) lipid interactions mediated by the two PM-targeting motifs, PBS and CAAX and (3) the actin cytoskeleton.

#### **3.1 Generation of fluorescently-labeled RHO-1 to study its localization and dynamics in *C. elegans* one-cell embryos**

To elucidate mechanisms that regulate the maintenance of a narrow RHO-1 zone at the equator, my first goal was to establish a functional probe to visualize RHO-1 in the *C. elegans* one-cell embryo. The aim was to generate a tool that allows following RHO-1 localization and dynamics during live-cell imaging in the absence of endogenous RHO-1. However, tagging RhoA with a fluorophore and remaining its function is not trivial (Yonemura and Hirao, 2004). The attempt to tag small GTPases with a fluorophore were performed back in 2001 and showed a uniform and mainly cytosolic localization of RhoA. In contrast, Rac1 and Cdc42 localized in a more specific and non-uniform pattern

(Michaelson et al., 2001). To my knowledge, previous RhoA localization studies were performed either in fixed samples or *in vivo* in the presence of endogenous RhoA (Budnar et al., 2019; Michaelson et al., 2001; Abreu, 2014; Motegi and Sugimoto, 2006; Nakayama et al., 2009; Yonemura and Hirao, 2004; Schonegg and Constantinescu, 2007; Yoshida et al., 2009).

An alternative approach in the field is to use an active RhoA binding protein, such as rhotekin (Bement and Benink, 2005) or anillin (Piekny and Glotzer, 2008), as biosensors to detect active RhoA. The domains are tagged with a fluorophore and can be used for live-cell imaging. These approaches were favored to overcome the limitations of tagging RhoA with a fluorophore (Michaelson et al., 2001). However, using a downstream effector only allows detection of the active state of the protein and is therefore less favorable for studying RhoA dynamics in general. Therefore, I was aiming for a tool, where RHO-1 is labeled with a fluorophore to generate a direct system that allows following RHO-1 in a most physiological manner. To achieve this goal, one possibility is to introduce a transgene into the genome as single-copy integration. Endogenous RHO-1 needs to be knocked down by RNAi. A second strategy is to directly introduce a fluorophore into the endogenous locus using CRISPR/Cas9 (Dickinson and Goldstein, 2016). I pursued both strategies in the following.

### **3.1.1 Generation of a genetic replacement system to monitor GFP::*RHO-1* in early *C. elegans* embryos by live-cell imaging**

My supervisor Dr. Esther Zanin established a genetic replacement system for RHO-1 in *C. elegans*. For this system, a *rho-1* transgene was generated that was RNAi-resistant and GFP-tagged. RNAi-resistance was achieved by codon-swapping within a region of 326 nucleotides of exon 3 (Figure 12). The GFP-tag was fused to the amino-terminus (N-terminus) separated by a short GS-linker (glycine and serine). The transgene was regulated by *rho-1* endogenous regulatory regions (1991 bp *rho-1* promoter, 1308 bp 3'UTR) and was introduced into *C. elegans* genome on chromosome II using MosSCI method (Frøkjær, 2008). For endogenous RHO-1 depletion, dsRNA was generated targeting the original nucleotide sequence of the re-encoded region as indicated in Figure 12 B.

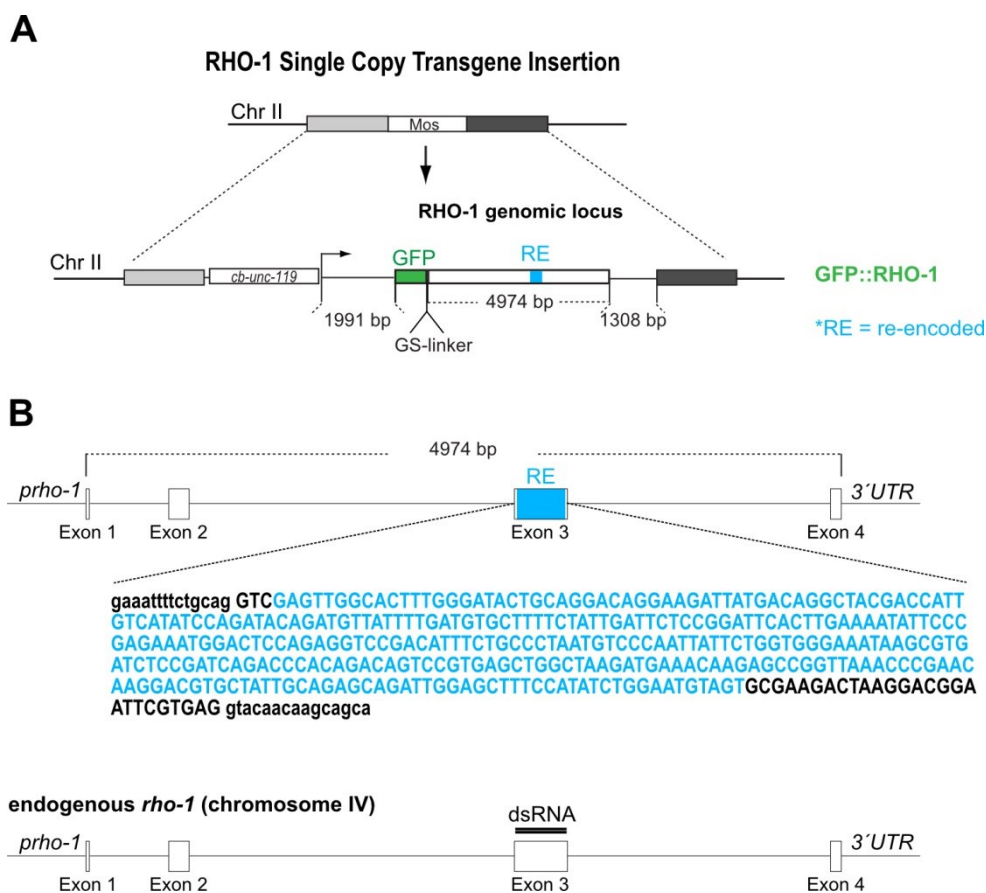


**Figure 12: Generation of a genetic replacement system, where a GFP-tagged *rho-1* transgene is integrated into *C. elegans* genome and endogenous RHO-1 can be depleted by dsRNA injection. (A) Schematic showing the principle of the genetic replacement system. Single-copy integration of GFP-tagged *rho-1* transgene with endogenous regulatory regions was achieved by MosSCI technique. (B) Exon 3 was re-encoded to render the transgene RNAi-resistant (blue nucleotide sequence flanked by black endogenous regions). Knock-down of endogenous RHO-1 was performed by injecting dsRNA, targeting the endogenous sequence of exon 3.**

RHO-1 is essential for cytokinesis and the regulation of the cytoskeleton and is therefore indispensable for embryonic development (Motegi and Sugimoto, 2006; Sönnichsen et al., 2005). The strain expressing GFP::RHO-1 was used to test, whether first division failure and embryonic lethality could be rescued in the absence of endogenous RHO-1. Experiments were performed by live-cell imaging of the zygote using confocal spinning disk microscopy after *rho-1* dsRNA injection. Knock-down of endogenous RHO-1 in control worms (only endogenous *rho-1* loci) resulted in 84.6 % cytokinesis failure. This was rescued by GFP::RHO-1 (7 % cytokinesis failure), indicating that GFP-tagged RHO-1 replaces endogenous RHO-1 during first cell division of the *C. elegans* one-cell embryo (Figure 13 A, B). Next, I tested whether endogenous RHO-1 could also be replaced by GFP::RHO-1 during embryonic development by performing lethality tests. The progeny of

worms injected with *rho-1* dsRNA was counted and the number of lethal worms was determined. GFP::RHO-1 expressing worms showed 97 % embryonic lethality comparable to control (100 % lethality) indicating that GFP::RHO-1 cannot replace endogenous RHO-1 during embryonic development (Figure 13 C). Expression and localization of GFP::RHO-1, in *rho-1(RNAi)* embryos, was analyzed by live-cell imaging. The GFP::RHO-1 signal was observed as expected at the plasma membrane during ring ingression and at cell-cell contacts in *C. elegans* embryos (Yonemura and Hirao, 2004; Bement and Benink, 2005; Takaishi et al., 1995; Nishimura and Yonemura, 2006; Kamijo et al., 2006; Yüce et al., 2005) (Figure 13 A).

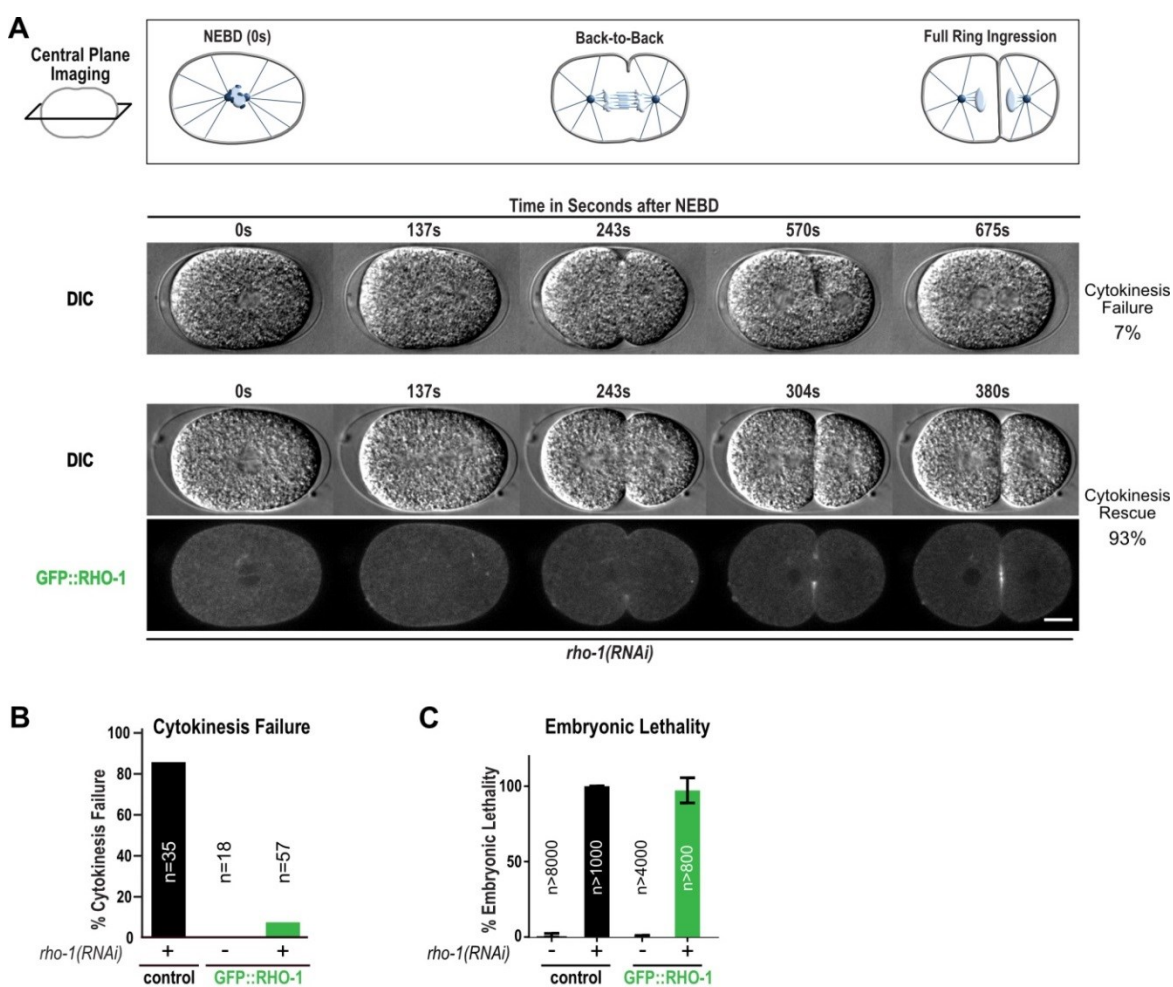


**Figure 13: GFP::RHO-1 can replace endogenous RHO-1 during first cell division of the one-cell *C. elegans* embryo.** (A) Schematic showing time points of NEBD, back-to-back membrane formation and full ring ingression. Time-lapse images of the first division of a one-cell embryo expressing GFP::RHO-1 after *rho-1(RNAi)*. Central plane images are shown for DIC (top; cytokinesis failure and cytokinesis rescue) and GFP (488-laser line; bottom) channel. Time represents seconds after NEBD. Scale bar=10  $\mu$ m. (B) Cytokinesis failure assay of first cell division for control (black) and GFP::RHO-1 (green) expressing embryos in the absence and presence of endogenous RHO-1 as indicated; n=number of embryos. (C) Embryonic lethality assay for control (black) and GFP::RHO-1 (green) expressing embryos in the presence and absence of endogenous RHO-1. Error bars are SD; n=number of embryos and larvae counted.



### 3.1.1.1 N-terminal tagging of RHO-1 impairs RHO-1 function during embryonic development but not during first cell division

I showed that GFP::RHO-1 was functional during first cell division, however it impaired embryonic viability during further development. RHO-1 is a small protein of 192 AAs. Adding the GFP-tag with 238 AAs could compromise its functionality. Alternatively the endogenous regulatory *rho-1* sequence, used in the MosSCI system, could be not sufficient to express GFP::RHO-1 in all cells needed for the developing embryo. To distinguish between those two possibilities, a MosSCI line expressing RNAi-resistant RHO-1 without GFP-tag but with the same regulatory regions was tested (Figure 14 A; RHO-1; generated by Esther Zanin). The transgene was characterized using cytokinesis failure and embryonic lethality assays as performed for GFP::RHO-1 expressing worms (experiments were performed with the help of Parviz Gomari). In the absence of endogenous RHO-1, RNAi-resistant RHO-1 rescued cytokinesis failure of the first cell division (Figure 14 B). Interestingly, untagged RHO-1 also rescued embryonic lethality (Figure 14 C), suggesting that the GFP-tag induced embryonic lethality. To test whether N-terminal tagging of RHO-1 impairs its function during development *per se* or whether this is specific to the GFP-tag, the fluorophore was exchanged to mCherry and the transgene was integrated on chromosome II using MosSCI method (Figure 14 A; mCh::RHO-1). Live-cell imaging showed that mCh::RHO-1 localized to the PM (Figure 14 D) in the same way as GFP::RHO-1 (Figure 13 A). Next, embryonic lethality tests were performed (with the help of Zerina Kurtovic), which showed that in the absence of endogenous RHO-1, mCh::RHO-1 could not rescue embryonic lethality (Figure 14 C). However, first division failure was rescued in 91 % of embryos imaged (Figure 14 B), indicating that tagging RHO-1 at its N-terminus *per se* impairs embryonic viability.

In summary, we established a genetic replacement system for RHO-1 in *C. elegans* that can be used to study RHO-1 localization, dynamics and function *in vivo*. We generated three different *rho-1* transgenes that were functional during first cell division of the one-cell *C. elegans* embryo after knock-down of endogenous RHO-1 by RNAi. All transgenes were integrated as single-copy insertion, at the same position on chromosome II, and were regulated by endogenous regulatory regions. Two transgenes were tagged with a fluorophore (GFP or mCherry) at the N-terminus. Both fluorescently-tagged RHO-1 localized to the PM and can be used to visualize RHO-1

*in vivo*. For functionality studies a non-tagged *rho-1* transgene was generated, which was fully functional also during embryonic development and rescued embryonic lethality.

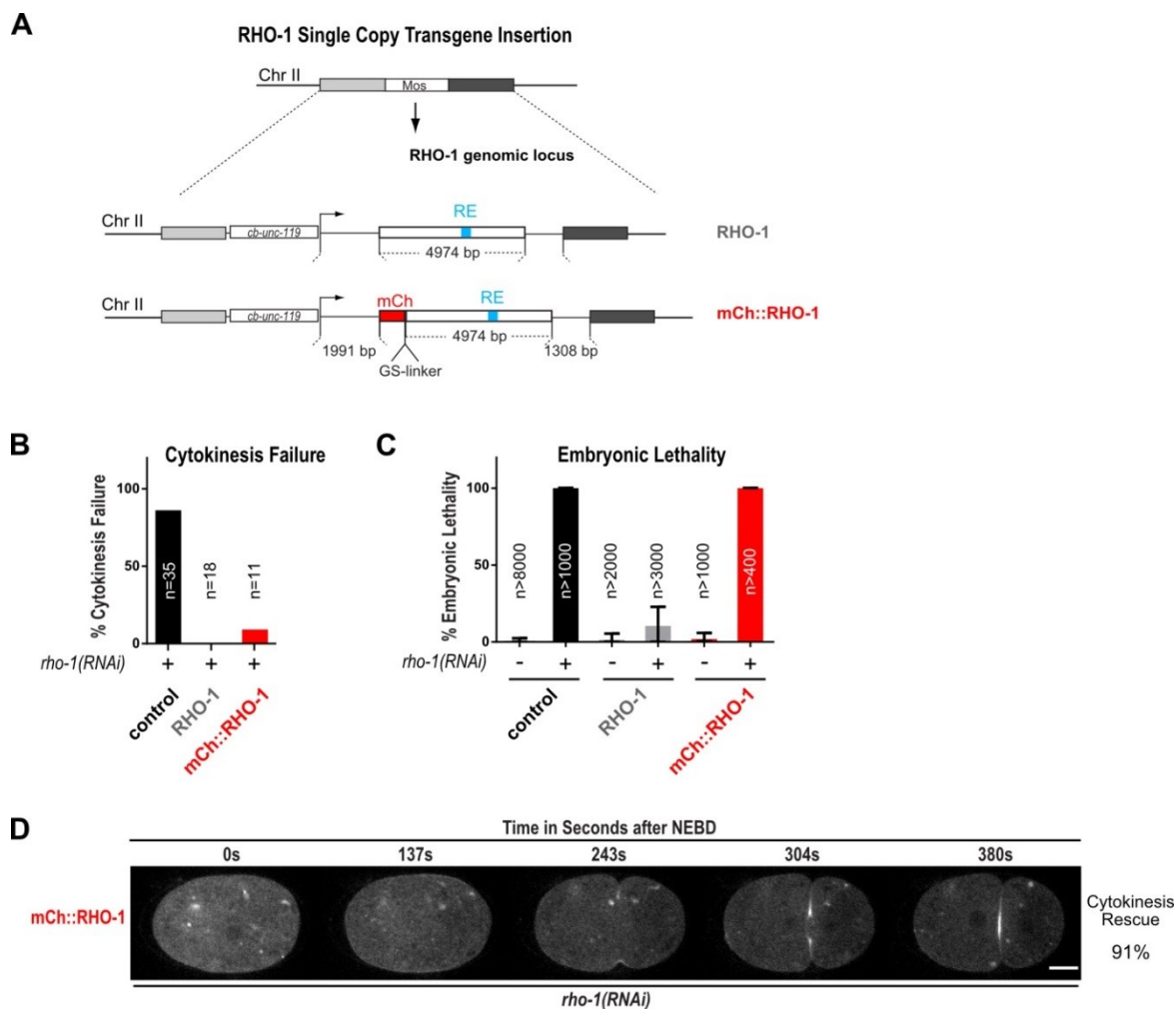


**Figure 14: N-terminal tagging of RHO-1 impairs its function during embryonic development but not during first cell division.** (A) Schematic showing single-copy insertions to generate RNAi-resistant non-tagged and mCherry-tagged *rho-1* transgenes using MosSCI method (generated by Esther Zanin). The transgenes were expressed using endogenous regulatory regions and were re-encoded to achieve RNAi-resistance (blue region) analog to GFP::RHO-1 transgene (Figure 12 A). (B) Cytokinesis failure assay for control (black), RHO-1 (gray) and mCh::RHO-1 (red) expressing embryos in the absence of endogenous RHO-1. Control is reproduced from Figure 12 B. (C) Embryonic lethality tests for control (black), RHO-1 (gray) and mCh::RHO-1 (red) expressing embryos with and without *rho-1(RNAi)*. Control is reproduced from Figure 12 C. Error bars are SD. (D) Representative central plane confocal time-lapse images of a one-cell embryo expressing mCh::RHO-1 in the absence of endogenous RHO-1. Time is seconds after NEBD. Scale bar=10  $\mu$ m. n=number of embryos analyzed.

### **3.1.2 CRISPR/Cas9 as an approach to tag *rho-1* at the endogenous locus**

The described genetic replacement system can be used to study RHO-1 localization and function in the early *C. elegans* one-cell embryo. The system is based on the introduction of a transgene in addition to the endogenous locus of the gene of interest; therefore depletion of the endogenous protein is required. Lethality tests revealed that, in the absence of endogenous RHO-1, worms expressing RHO-1 with an N-terminal fluorescent tag were not viable. Therefore, crossing the strain into a null mutant *rho-1* background was not an option. Next, I tested whether directly tagging endogenous RHO-1 with a fluorophore by CRISPR/Cas9 could be used to generate a functional RHO-1 probe (Dickinson and Goldstein, 2016).

#### **3.1.2.1 Three different approaches of endogenous *rho-1* tagging with a fluorophore using CRISPR/Cas9 resulted in homozygous sterile animals**

First, the knock-in of the fluorophore mKate2 (Turek et al., 2013) was designed at the N-terminus of endogenous RHO-1 (Figure 15 B; I). The fluorophore mKate2 was used to generate a strain expressing a red fluorescent marker for RHO-1. It is a bright fluorescence probe with high photostability and low cytotoxicity, therefore well suited for live-cell imaging and favored over mCherry. The fluorophore was separated by the same GS-linker used for the transgenes generated for the genetic replacement system (GFP::*RHO-1* and mCh::*RHO-1*). CRISPR/Cas9 gene modification was performed by the company SunyBiotech (<https://www.sunybiotech.com>). Insertion of mKate2 into the genome resulted in homozygous sterile progeny. Therefore, the strain was balanced by the company using the balancer *nT1(IV;V)* provided with a GFP-reporter. This result strengthened the finding that tagging RHO-1 with a fluorophore at the N-terminus impairs RHO-1 function.

Next, a knock-in of mKate2 was designed at the C-terminus of RHO-1, to test whether C-terminal tagging of RHO-1 rescues embryonic lethality. RHO-1 is post translationally modified at the C-terminus at the CAAX-motif (Figure 2 B and Figure 15 A). A lipid moiety is anchored to the cystein of the CAAX-motif and the last three AAs are cleaved off (Clarke, 1992). Therefore, tagging RHO-1 directly at the C-terminus is not possible, because the tag would be cleaved off. Additionally, to the CAAX-motif, RHO-1 is

provided by a second PM-targeting motif; a PBS which is located upstream of the CAAX-motif (Michaelson et al., 2001) (Figure 15 A). To ensure that PM localization of RHO-1 is not impaired by tagging the protein with a fluorophore at the C-terminus, mKate2 was introduced upstream of both PM-targeting motifs (the PBS and the CAAX) at K182 (Figure 15 B; II). K182 represents the first out of six lysines of the PBS. To provide a full stretch of six lysines, an additional lysine (AAG) was added to the sequence (Figure 15 B, II). The fluorophore mKate2 was flanked by a GS-linker on each site (Figure 15 B; II). CRISPR/Cas9 genome editing was performed by SunyBiotech. Tagging endogenous RHO-1 at its C-terminus, upstream of the PM-targeting motifs, again resulted in homozygous sterile progeny, suggesting that changing the location of the fluorophore does not rescue embryonic lethality. The C-terminally-tagged RHO-1 CRISPR/Cas9 strain was balanced by *nT1(IV;V)* balancer (SunyBiotech).

The third approach was adopted from a publication, where the authors successfully introduced a super folder GFP-tag (sfGFP) within the coding sequence of the small GTPase CDC42 in fission yeast (Bendezú et al., 2015). My supervisor Esther Zanin designed the insertion of sfGFP into the *rho-1* sequence, based on the construct built in Bendezú *et al.* (Figure 15 B; III). The gene knock-in was performed by SunyBiotech. Internal-tagging (IT) of RHO-1 with sfGFP at Q136 (sfGFP::RHO-1<sup>IT</sup>) resulted in homozygous sterile progeny. Therefore the strain was balanced using the balancer *nT1(IV;V)* provided with a GFP-reporter (performed by Suraj Shaji).

For all strains received from SunyBiotech correct gene modification was verified by sequencing. Further it was tested whether mKate2::RHO-1, RHO-1::mKate2 and sfGFP::RHO-1<sup>IT</sup> localized to the PM in heterozygous animals. Indeed, all three CRISPR RHO-1 modifications localized to the PM comparable to GFP- and mCh-tagged RHO-1 (MosSCI lines) (Figure 22). However, the CRISPR/Cas9 strains are not viable as homozygotes and could therefore not be used to study RHO-1 dynamics without endogenous RHO-1 in the background. In summary, three different heterozygous CRISPR/Cas9 knock-in strains were generated, where RHO-1 was tagged with a fluorophore: (1) at the N-terminus, (2) at the C-terminus (upstream the PM-targeting motifs) and (3) internally. All three strains were homozygous lethal, suggesting that tagging RHO-1 *per se* impairs its function, highlighting the difficulty of generating a functional RHO-1 probe. This result further strengthens the advantage of the genetic replacement system. There, worms can be grown in the background of endogenous

RHO-1, which then can be selectively depleted by RNAi for an experiment. This way functional fluorescently-tagged RHO-1 can be followed during cytokinesis in the one-cell embryo.

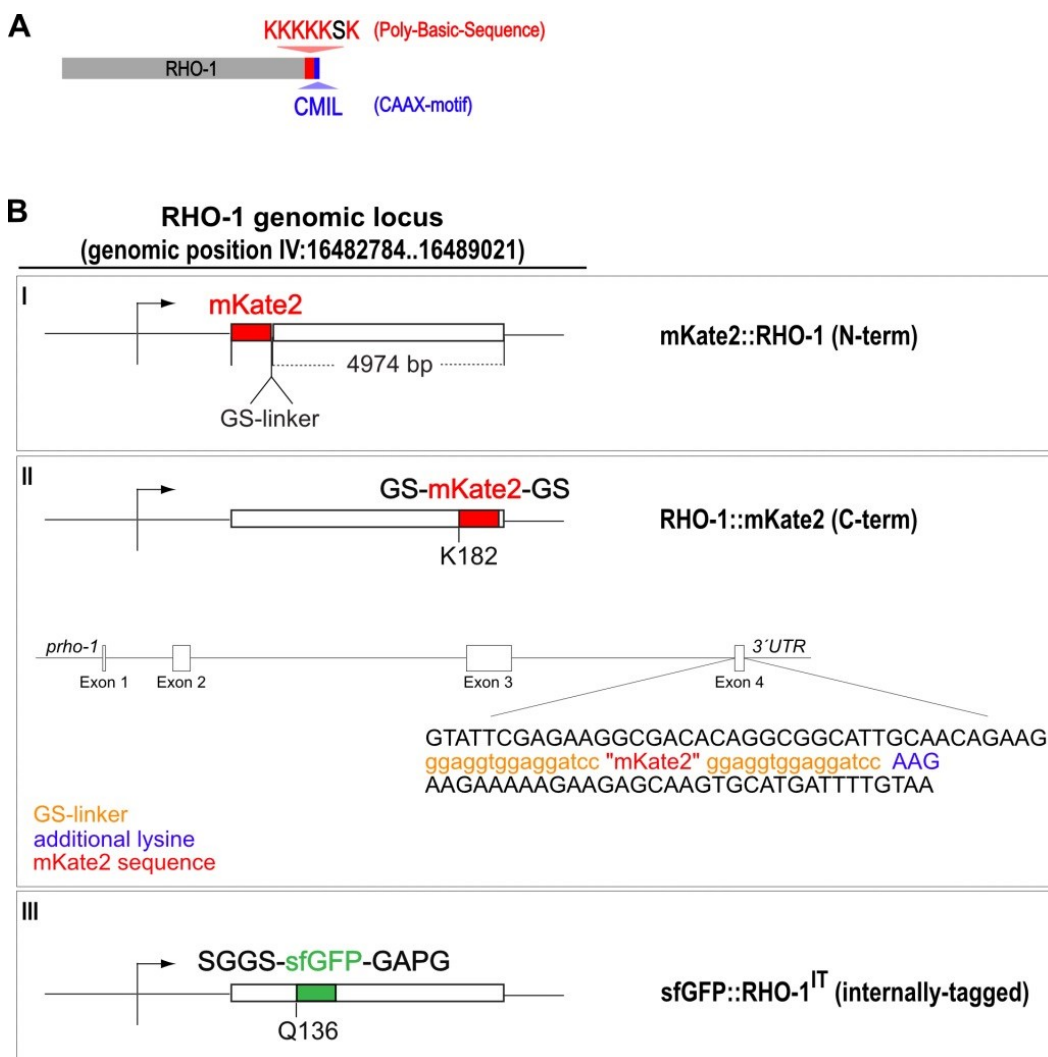


**Figure 15: Approaches to tag endogenous RHO-1 using CRISPR/Cas9.** (A) Schematic of RHO-1 showing the two PM-targeting motifs at its C-terminus: the poly-basic-sequence (PBS) and the CAAX-motif. (B) Schematic of RHO-1 genomic locus on chromosome IV. Three different approaches of endogenous *rho-1*-tagging (I-III) are shown. **I** The fluorophore mKate2 was introduced at the N-terminus, separated by a GS-linker (orange sequence shown in (II)). **II** Schematic representing C-terminal RHO-1-tagging. The fluorophore mKate2 was introduced at exon 4 flanked by two GS-linker (orange). GS-mKate2-GS was inserted after the codon of the first lysine within the PBS. An additional lysine was introduced (AAG; blue) to ensure a stretch of six lysines for the PBS. **III** Internally-tagged RHO-1 based on sequence homology in (Bendezú et al., 2015).

### 3.1.3 Generation of a RHO-1 nanobody to specifically monitor active RHO-1 *in vivo*

I showed that our tool can be used to follow RHO-1 dynamics during cytokinesis in the one-cell embryo. However, those systems are limited to detect RHO-1 *per se*, without distinguishing between the active and inactive form. RHO-1 is a small GTPase and its regulation is well characterized (Bishop and Hall, 2000). In *C. elegans* RHO-1 activation is driven by the GEF ECT-2, where GDP is exchanged for GTP. The low intrinsic GTP hydrolysis of RHO-1 is accelerated by the GAPs RGA-3 and RGA-4 (Schmutz et al., 2007; Schonegg and Constantinescu, 2007; Zanin et al., 2013), which as a consequence results in inactive RHO-1 (Bos et al., 2007; Bourne et al., 1990) (Figure 2 A). Thus, I wanted to establish a system to specifically detect active GTP-bound RHO-1 *in vivo*. It was discovered in 1993 that camelids produce antibodies that do not contain light chains (Hamers, 1993). The single antigen specific N-terminal domain ( $V_{\text{H}}\text{H}$ ) of these antibodies is only 1/10<sup>th</sup> of the size of conventional antibodies but with similar selectivity. Therefore, these  $V_{\text{H}}\text{H}$  sequences can be used as nanobodies for *in vivo* studies, where they can be expressed via expression vectors. The sequences can be tagged with a fluorophore to create a Chromobody (Figure 16 A), which can be used to visualize proteins *in vivo* (Schmidthals et al., 2010; Rothbauer et al., 2006). My aim was to create a Chromobody specific for active GTP-bound RHO-1. To reach that goal, I designed a constitutively active RHO-1 antigen, which was then used to immunize alpacas by the company ChromoTek (<https://www.chromotek.com>). ChromoTek further performed biopanning to select for specificity of different  $V_{\text{H}}\text{H}$  sequences that were isolated from blood of the immunized animals. At the end, I received several  $V_{\text{H}}\text{H}$  sequences that showed specificity for active RHO-1 *in vitro* (ELISA performed by ChromoTek). I cloned these sequences into expression vectors, tagged with GFP, to test its specificity *in vivo*: (1) in HeLa cells and (2) in *C. elegans* (Figure 16 A).

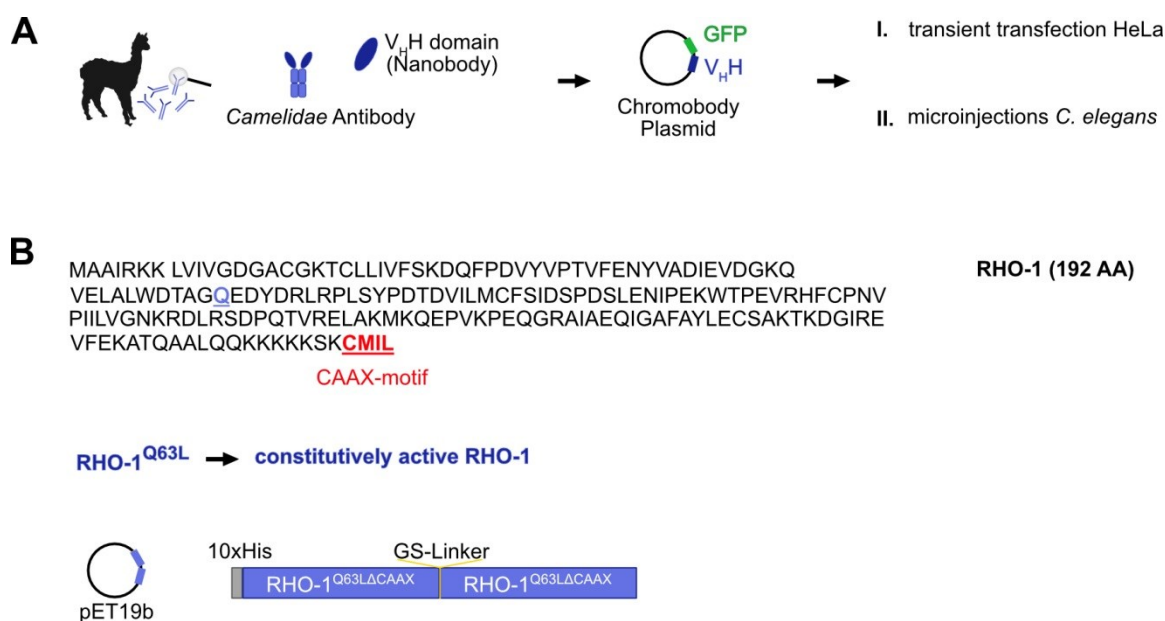


**Figure 16: Generation of a RHO-1 Nanobody to specifically monitor active RHO-1 *in vivo*.** (A) *Camelidae* produce heavy-chain antibodies, which bind antigens with the single variable domain V<sub>H</sub>H. Identified V<sub>H</sub>H sequences can be tagged with a fluorophore to generate a Chromobody, which subsequently can be expressed in cells. (B) RHO-1 protein (AA) sequence used for immunization; the CAAX-motif at the C-terminus is highlighted in red, which was removed for protein purification. glutamine (Q)63 is highlighted in blue and represents the AA that was changed to leucine, in order to achieve constitutively active RHO-1. RHO-1<sup>Q63L</sup> was designed as dimer to increase protein size and immunogenicity. The sequence of the dimer was cloned into pET19-b vector providing an N-terminal 10x His-tag for protein overexpression and purification.

### 3.1.3.1 Antigen preparation and verification of GDP and GTP loaded state.

To obtain constitutively active RhoA, glutamine at residue 63 was exchanged to leucine (Figure 16 B), which destroys GTPase activity of RhoA and therefore keeps RhoA in its active GTP loaded state (Longenecker et al., 2003; Subauste et al., 2000). Q63 is conserved in *C. elegans* and therefore this point mutation was introduced to generate constitutively active RHO-1<sup>Q63L</sup>. The CAAX-motif was deleted from the C-terminus, to prevent PM binding and to increase protein solubility. RHO-1 is a small protein with the size of 21.5 kDa. To increase immunogenicity and epitope density, the antigen was designed as a dimer. The two RHO-1<sup>Q63L</sup>CAAX sequences were separated by a short GS-linker. The dimer sequence was cloned into pET19-b expression vector downstream of the provided 10x His-tag (Figure 16 B). Protein expression was performed in *E. coli* BL21 (DE3).

The following steps I performed in the lab of Prof. Dr. Itzen at the TU Munich with the help of Dr. Sophie Vieweg. The protein was extracted by french press and was purified using an Äkta™ chromatography system, equipped with a nickel column. The purified protein was tested by SDS-gel electrophoresis and was further purified using size exclusion chromatography. Finally, the RHO-1<sup>Q63L</sup> dimer was detected by immunoblot using home-made  $\alpha$ -RHO-1 antibody (see section 3.2) (Figure 17 A). The dimer was tested for GTP loading using HPLC. As a reference a Gmix standard was used containing GMP, GDP and GTP. HPLC analysis revealed that RHO-1<sup>Q63L</sup> dimer was GTP loaded (Figure 17 B), indicating that the antigen indeed represented the active form of RHO-1. Finally, the purified and verified active RHO-1<sup>Q63L</sup> dimer was used for immunization of alpacas by the company ChromoTek.

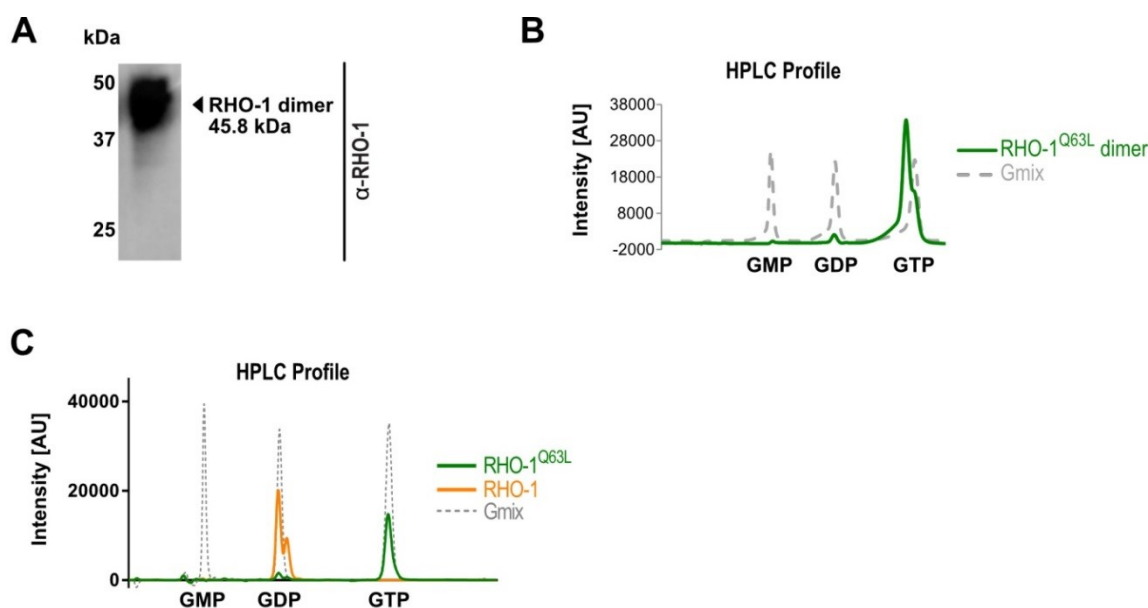


**Figure 17: Antigen preparation and verification of GDP and GTP loaded state.** (A) Immunoblot verifying purified RHO-1 dimer probed with  $\alpha$ -RHO-1 antibody. (B, C) HPLC profiles of purified RHO-1 antigens compared to a Gmix (gray) including GMP, GDP and GTP. (B) RHO-1<sup>Q63L</sup> dimer (green) was mainly GTP loaded. (C) RHO-1<sup>Q63L</sup> monomer (green) was GTP loaded whereas RHO-1 (orange) was GDP loaded.

Following successful immunization, the company performed biopanning to test several sequences for specificity. The blood of immunized animals was collected, lymphocytes were isolated and mRNA was extracted. Using RT-PCR the sequences were transcribed into cDNA and inserted into a vector. This way, a semisynthetic library was generated,



which was further selected for antigen specificity using phage display. For selection, I provided two more antigens: (1) RHO-1<sup>Q63L</sup> monomer and (2) RHO-1 wildtype monomer. After purification both monomers were tested for GTP or GDP loading using HPLC. I verified that RHO-1<sup>Q63L</sup> was mainly GTP-bound and RHO-1 occurred mainly in the GDP-bound state (Figure 17 C). The wildtype monomer was used to test for RHO-1 specificity *per se* and the GTP loaded RHO-1<sup>Q63L</sup> monomer for active RHO-1. I received 12 candidates from the company, of which eight sequences were specific for active RHO-1 and the remaining four sequences showed cross reactivity for active and inactive RHO-1 (Table 27).

**Table 27: V<sub>H</sub>H sequences received from ChromoTek**

Candidate	Specificity tested by ELISA (CromoTek)	Specificity tested in HeLa cells		Specificity tested in <i>C. elegans</i>	
		Expression vector tested	Specific PM localization	Expression vector tested	Specific PM localization
V <sub>H</sub> H0166	RHO-1 GTP	*(pEZ267)	no		
V <sub>H</sub> H0167	Low cross reactivity	*(pEZ281)	no		
V <sub>H</sub> H0168	RHO-1 GTP	*(pEZ273)	no		
V <sub>H</sub> H0169	RHO-1 GTP	*(pEZ269)	no		
V <sub>H</sub> H0171	RHO-1 GTP	*(pEZ274)	no	** (pEZ288)	no
V <sub>H</sub> H0172	Low cross reactivity	*(pEZ270)	no		
V <sub>H</sub> H0173	Cross reactivity	*(pEZ282)	no		
V <sub>H</sub> H0174	Cross reactivity	*(pEZ275)	no		
V <sub>H</sub> H0175	RHO-1 GTP	*(pEZ271)	no	** (pEZ286)	no
V <sub>H</sub> H0176	RHO-1 GTP	*(pEZ272)	no		
V <sub>H</sub> H0177	RHO-1 GTP				
V <sub>H</sub> H0178	RHO-1 GTP	*(pEZ276)	no	** (pEZ287)	no

\* Plasmids generated with pcDNA5 vector;

\*\* Plasmids generated with pBC1454 vector

### 3.1.3.2 *In vivo* tests of GFP-tagged nanobody sequences showed no specificity for RhoA in HeLa cells and RHO-1 in *C. elegans*

The final 12 RHO-1 specific candidates were received as plasmids. Next the V<sub>H</sub>H sequences (Table 27) were tested to detect endogenous active RHO-1 *in vivo*. *C. elegans* RHO-1 and human RhoA are 96 % similar. Since transient expression of transgenes is much faster in HeLa cells than in *C. elegans*, nanobodies were first tested in HeLa cells. The sequences listed in Table 27 were cloned into pcDNA5 vector with a C-terminal GFP-tag separated by a (GGGGS)<sub>4</sub>-linker. The plasmids were transiently transfected and expression was verified by GFP signal. All tested transgenes showed GFP expression in the cytoplasm, however none of them showed enrichment at the PM during anaphase (Figure 18 A; Table 27). Since in HeLa cells the nanobodies tested showed no specific RhoA signal, they were tested in *C. elegans*. Three of the candidates were tested (Table 27). The sequences were cloned into pBC1454 with *mai-2* promoter and 3'UTR in addition to a C-terminal GFP-tag, separated by a (GGGGS)<sub>4</sub>-linker. Using microinjections, the vector carrying the construct was injected with the co-injection marker *rol-6(su-1006)* (pRF4). Roller worms were screened for GFP expression. The three sequences tested (VHH0171, VHH0175 and VHH0178) showed GFP expression in adult worms. However, there was no specific plasma membrane localization detectable in early *C. elegans* embryos (Figure 18 B; Table 27). The overall GFP-signal in early embryos was very low. Therefore, for future experiments positive and negative controls are required to verify expression of V<sub>H</sub>H::GFP transgenes.

In summary, a GTP-bound RHO-1 dimer was purified, which was used for immunization of alpacas to generate a nanobody against active RHO-1. Received were 12 different sequences shown to be specific in recognizing RHO-1 using ELISA (performed by ChromoTek; Table 27). Testing of 11 sequences in HeLa cells, by transient transfection and live-cell imaging, showed cytosolic GFP expression, however no enrichment at the PM. First tests were performed also in *C. elegans* by microinjections of GFP-tagged V<sub>H</sub>H sequences followed by live-cell imaging. Unfortunately, none of these three V<sub>H</sub>H sequences were positive in recognizing RHO-1 *in vivo*, although additional tests are required.

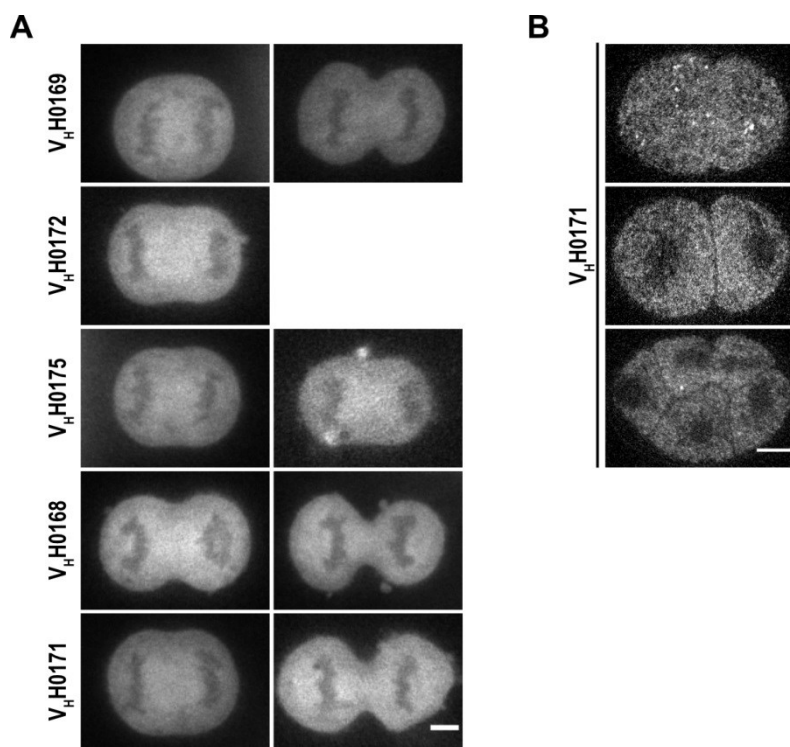


**Figure 18:** *In vivo* tests of GFP-tagged nanobodies showed no specific plasma membrane enrichment. (A) Anaphase HeLa cells; scale bar=5  $\mu\text{m}$ ,  $n>10$ . (B) One-, two- and four-cell *C. elegans* embryos; scale bar=10  $\mu\text{m}$ ,  $n>10$ .

### 3.2 Generation of a RHO-1 antibody to test endogenous- and transgenic RHO-1 expression levels

Our genetic replacement system requires the depletion of endogenous RHO-1. To assay the overall protein level in control and GFP::RHO-1 expressing worms, and to test the *rho-1(RNAi)* knock-down efficiency, an antibody against RHO-1 was generated. For antibody generation, first a RHO-1 antigen was overexpressed and purified. The RHO-1 sequence was used without the last four amino acids to eliminate the CAAX-motif (Figure 19 A) as described in section 3.1.3.1. Protein expression was performed in *E. coli* BL21 (DE3) and protein purification was achieved by affinity purification via GST-tag (Figure 19 A). Purified RHO-1 was sent for immunization of two rabbits to the company Davids Biotechnology GmbH (<https://www.davids-bio.de>). The antibody from the received sera of the rabbits was purified and subsequently tested by immunoblot. The purified antibody for RHO-1 detected the antigen in western blot analysis at the correct size of 21.5 kD and also detected RHO-1 from worm lysates (Figure 19 B).

Subsequently, the RHO-1 antibody was used to test for expression levels in our genetic replacement system compared to endogenous RHO-1 levels. Control (N2), RHO-1 and GFP::RHO-1 expressing worms, with and without *rho-1(RNAi)*, were lysed and worm lysates were used for immunoblotting. The blot was probed with  $\alpha$ -RHO-1 and  $\alpha$ -tubulin as loading control. Endogenous RHO-1 (+ transgenic RHO-1) and GFP::RHO-1 were detected at correct sizes by the antibody (Figure 19 B; 21.5k Da and 48.5 kDa, respectively). Expression levels of endogenous RHO-1 were strongly reduced after *rho-1(RNAi)* whereas untagged RHO-1 was expressed at similar levels as endogenous RHO-1. GFP-tagged RHO-1 expression was higher than endogenous RHO-1 levels (Figure 19 B).

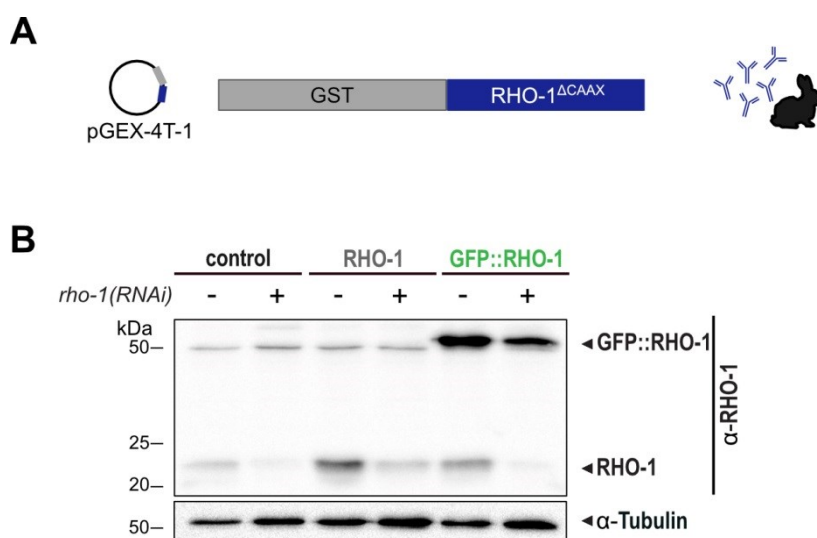


**Figure 19: Generation and validation of a RHO-1 antibody.** (A) For antigen preparation RHO-1 sequence without the CAAX-motif was cloned into pGEX-4T-1 vector in addition to a GST-tag for overexpression and purification. Purified antigen was used for immunization of two rabbits by the company Davids Biotechnology GmbH. (B) Immunoblot for control (N2), RHO-1 and GFP::RHO-1 expressing worms in the presence and absence of endogenous RHO-1 as indicated. Blots were probed with  $\alpha$ -RHO-1 and  $\alpha$ -tubulin as loading control.

### 3.3 How is active RHO-1 maintained in a narrow zone at the equatorial membrane during cytokinesis?

With our established tool I addressed the aims of this thesis introduced in section 1.6. In brief, RHO-1 is required for cytokinesis and initiates the formation of the contractile ring, which is indispensable for cell division (Jantsch, 2000; Kishi et al., 1993; Drechsel et al., 1997). Local activation of RHO-1 at the equatorial membrane, in between the segregating chromosomes, needs tight spatial and temporal regulation (Mishima, 2016; D'Avino et al., 2005). The activation of RHO-1 is mediated by the GEF ECT-2 at the PM (Yüce et al., 2005; Somers and Saint, 2003). As a peripheral membrane protein RHO-1 is thought to be able to diffuse within the PM. Considering the ability of free diffusion and the low intrinsic hydrolysis rate of RHO-1, the question arises how RHO-1 is restricted within a narrow zone at the equator (Bement et al., 2006). I tested three main hypotheses; Maintenance of a RHO-1 activity zone is obtained by:

- (1) the RHO-1 activation/inactivation cycle driven by GEF and GAP,
- (2) lipid interactions mediated by the two PM-targeting motifs, PBS and CAAX and
- (3) contractile ring components that act as physical barrier.

#### 3.3.1 GFP::RHO-1 is present in two distinct pools at the plasma membrane during cell division of the one-cell *C. elegans* embryo

I started by investigating RHO-1 localization during cytokinesis. The canonical model predicts that RHO-1 activation occurs in its PM-associated state (Michaelson et al., 2001; Van Unen et al., 2015). Therefore, a membrane marker was crossed into the strain expressing GFP::RHO-1 to identify PM-localized RHO-1. The membrane marker consists of the mammalian PLC181 PH domain fused to mCherry (mCh::PH). The PH domain binds to phospholipids (preferentially PIP<sub>2</sub>) of the PM (Audhya et al., 2005; Hurley and Meyer, 2001). Subsequently, the strain co-expressing GFP::RHO-1 and mCh::PH was used to perform live-cell imaging of one-cell embryos. Imaging was performed using confocal spinning disk microscopy. Localization was followed in the presence and absence of endogenous RHO-1, which was depleted by *rho-1(RNAi)*. Early embryos were imaged starting prior to NEBD. Image acquisition was performed every 16 s for a duration of 15 min. Images were acquired at the central- and the cortical plane (2.2.13.1).

Cortical imaging revealed that, in the presence and absence of endogenous RHO-1, GFP::RHO-1 localized into anterior patches that were most dominant prior to NEBD (Figure 20; -144 s). These patches co-localized with the membrane marker. At the central plane GFP::RHO-1 localized to the PM, best visible at cell-cell contacts after first cell division (Figure 20; 610 s). Surprisingly, only in the absence of endogenous RHO-1 a narrow GFP::RHO-1 zone was visible at the equatorial cortex (Figure 20; 160 s), suggesting that endogenous RHO-1 is favored when both the endogenous and transgenic GFP::RHO-1 are present. Interestingly, in the absence of endogenous RHO-1, GFP::RHO-1 forms a dense meshwork of filamentous-like structures at the equatorial cortex during cytokinesis. In contrast to the anterior patches, where GFP::RHO-1 and mCh::PH co-localized at the equator, only GFP::RHO-1 was enriched (Figure 20; insets 160 s). Similar anterior structures were described during polarization of the *C. elegans* one-cell embryo for RHO-1, CDC-42 and the PM, by using the same PH membrane marker however in the presence of endogenous protein (Motegi and Sugimoto, 2006; Nakayama et al., 2009). In a recent publication the authors focused on these dynamic cortical PIP<sub>2</sub> structures labeled by the PH marker. By elucidating the origin of these foci, they found that the PH marker co-localized with ECT-2, RHO-1 and CDC-42 as well as partially with F-actin (Scholze et al., 2018). The authors concluded interdependency between F-actin and PIP<sub>2</sub> structures. Another study showed that these anterior foci are filopodia-like structures that appear as local enrichment due to membrane protrusions (Hirani et al., 2019). Therefore, these anterior structures are rather caused by changes in membrane topology than by real accumulation of RHO-1. Taking these information into account, I am hypothesizing that anterior GFP::RHO-1 represents PM-associated RHO-1 that, due to membrane protrusions and/or ruffles, occurs as enriched foci. In contrast, GFP::RHO-1 at the equator is a direct enrichment of RHO-1, since the mCh::PH signal is not concentrated in the same manner at this location (Figure 20).

I showed that during cell division GFP::RHO-1 is present in two distinct pools: (1) anterior GFP::RHO-1 foci co-localizing with PH-positive patches and (2) an equatorial narrow and dense meshwork of GFP::RHO-1 filamentous-like structures that do not co-localize with the PH marker. While the anterior pool formed in the presence of endogenous RHO-1, the equatorial meshwork only formed in the absence of endogenous RHO-1. These results show the importance of depleting endogenous RHO-1 to study the equatorial pool. Therefore, throughout my work presented here, all experiments were performed in the absence of endogenous RHO-1 if not stated otherwise. In contrast to anterior patches,

equatorial GFP::RHO-1 did not localize together with PH structures, indicating that the RHO-1 meshwork represents an accumulation of the protein, rather than an increased signal due to membrane folds.

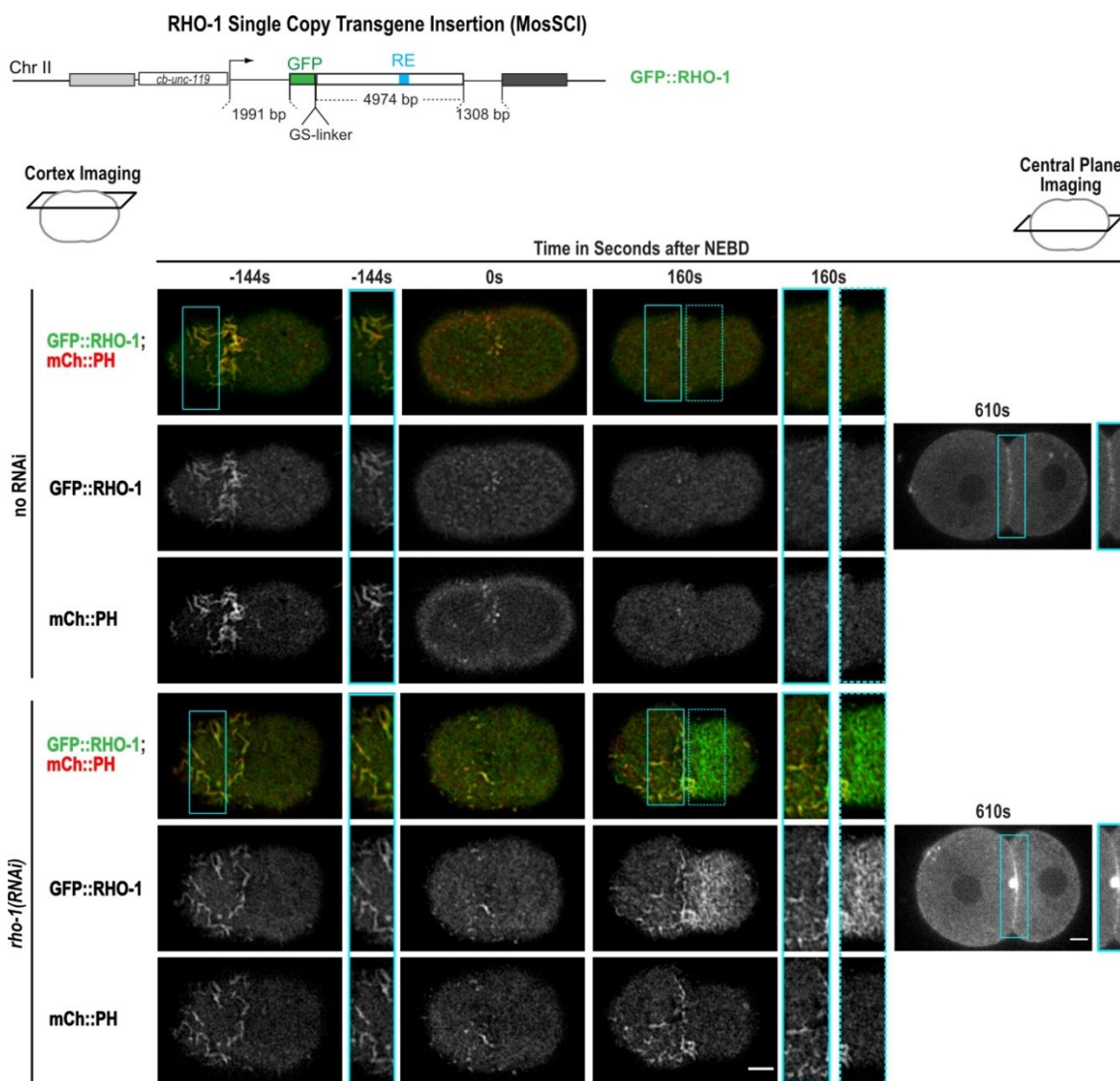


**Figure 20: GFP::RHO-1 localizes into two distinct pools during cytokinesis.** Localization study of GFP::RHO-1 during first cell division of one-cell embryos using the established genetic replacement system. Representative confocal time-lapse images of one-cell embryos expressing GFP::RHO-1 (green) and mCh::PH (red) in the presence (top three rows; n=7) and absence (bottom three rows; n=9) of endogenous RHO-1. Cortical single z-plane images (left) and central plane images (right) from the same embryo are shown for the indicated time points. Time in seconds after NEBD. Insets highlight the anterior and equatorial pool of GFP::RHO-1 for cortical images. Insets at the central plane highlight PM-localized GFP::RHO-1 at cell-cell contacts in two-cell embryos. Scale bars=5  $\mu$ m.

### 3.3.1.1 The dense RHO-1 meshwork at the equatorial membrane is not an artifact of the GFP-tag

GFP::RHO-1 localized to the PM in early *C. elegans* embryos and a narrow GFP::RHO-1 zone was only visible in the absence of endogenous RHO-1 (Figure 20). Interestingly, GFP::RHO-1 formed a dense RHO-1 meshwork at the equatorial membrane during cytokinesis. To verify that filamentous-like structures of GFP::RHO-1 at the equator are not an artifact of the GFP-tag, the same experiments were performed using the strain expressing RNAi-resistant mCh::RHO-1 that was characterized in 3.1.1.1 (Figure 14). Endogenous RHO-1 was depleted by RNAi and first cell division was followed by confocal spinning disk live-cell imaging. I found that the dense meshwork of RHO-1 at the equator was also formed when the protein was tagged with mCherry (Figure 21) instead of GFP. This strengthens the finding of a dense meshwork of RHO-1 filamentous-like structures at the equatorial cortex.

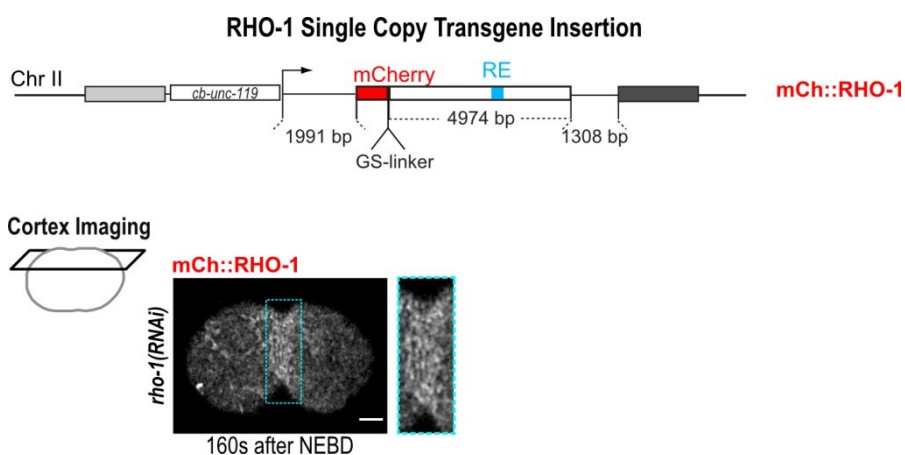


**Figure 21: RHO-1 tagged with mCherry also forms a dense meshwork at the equatorial membrane.** Representative cortical confocal time-lapse image of a one-cell *C. elegans* embryo expressing mCh::RHO-1 in the absence of endogenous RHO-1 160 s after NEBD (n=6). Inset highlights equatorial mCh::RHO-1 in a dense meshwork of filamentous-like structures. Scale bar=5  $\mu$ m.

The three generated heterozygous CRISPR/Cas9 lines (section 3.1.2.1) also showed expression and localization of endogenously tagged RHO-1 to the PM. I tested whether endogenously tagged RHO-1 in the presence of a wild-type RHO-1 allele also forms a dense meshwork of RHO-1 at the equator. The heterozygous balanced strains expressing mKate2::RHO-1, RHO-1::mKate2 and sfGFP::RHO-1<sup>IT</sup> (Figure 15) were imaged using spinning disk confocal microscopy. All three CRISPR/Cas9-tagged Rho-1 variants



localized to the PM in central plane images. Interestingly, and in contrast to the N- and C-terminally-tagged RHO-1 CRISPR/Cas9 lines, only internally-tagged sfGFP::RHO-1<sup>IT</sup> was enriched at the equatorial membrane in cortical imaging (Figure 22). The localization pattern was similar to the one observed for GFP::RHO-1 in the MosSCI-generated strain. The main difference between the two strains is that GFP::RHO-1 becomes only visible at the equator in the absence of endogenous RHO-1, however sfGFP::RHO-1<sup>IT</sup> is also visible at the equator in the presence of endogenous RHO-1. Of note, the two strains are of different nature: (1) GFP::RHO-1 is introduced in addition to the endogenous *rho-1* locus and (2) sfGFP::RHO-1<sup>IT</sup> is a gene modification of the endogenous locus itself. Therefore, by depleting endogenous RHO-1 in the GFP::RHO-1 expressing strain, the total RHO-1 level should theoretically be reduced to the levels of the heterozygous CRISPR/Cas9 strain where one allele is modified and the other one codes for endogenous RHO-1. The N- and C-terminally-tagged RHO-1 CRISPR/Cas9 strains did not show any enrichment at the equator, indicating that either internal-tagging of RHO-1 or the fluorophore used (sfGFP) partially maintains functionality of RHO-1, yet is not sufficient for embryo production without wildtype RHO-1 in the background. In summary, the sfGFP::RHO-1<sup>IT</sup> is a third independent strain that shows similar filamentous-like structures at the equator for RHO-1. I showed with three different strains, expressing three different fluorescent markers, and using two individual methods for protein-tagging that RHO-1 forms a dense meshwork of filamentous-like structures at the equatorial membrane.

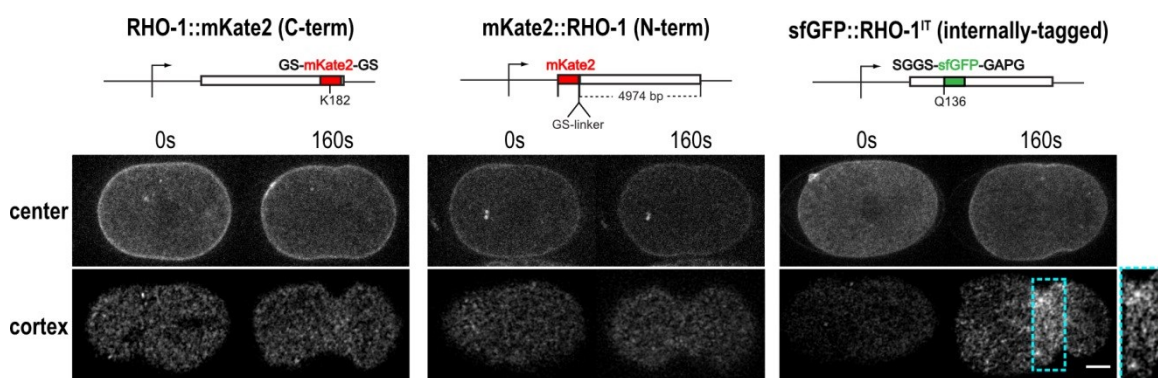


**Figure 22: Internally-tagged RHO-1 localizes into a narrow RHO-1 zone at the equatorial membrane.** Representative central- and cortical plane confocal time-lapse images of CRISPR/Cas9-tagged one-cell embryos, expressing heterozygous RHO-1::mKate2 (left; n=2), mKate2::RHO-1 (middle; n=5) and sfGFP::RHO-1<sup>IT</sup> (right; n=4) 0 s and 160 s after NEBD. Inset highlights equatorial sfGFP::RHO 1<sup>IT</sup> in a dense meshwork. Scale bar=5 μm.

### **3.3.2 How does RHO-1 regulation by GAPs and GEF contribute to the localization of RHO-1 in the two observed membrane pools?**

The GFP::*RHO-1* reporter showed two pools of PM-localized *RHO-1*. While the equatorial pool was expected to be locally activated by *ECT-2* (Yüce et al., 2005; Somers and Saint, 2003), the dependency on *ECT-2* for anterior patches remained elusive. Therefore, the contribution of *ECT-2* on *RHO-1* PM localization in both pools was tested.

One possibility of narrow RhoA zone restriction is the proposed ‘RhoA flux model’ (Bement et al., 2006; Miller and Bement, 2009). An accelerated cycle of activation and inactivation of RhoA, driven by the GEF and GAP, was proposed to contribute to the maintenance of a narrow RhoA zone. I tested whether the inactivation of *RHO-1* by the GAPs *RGA-3* and *RGA-4* contribute to narrow *RHO-1* zone restriction.

#### **3.3.2.1 The equatorial RHO-1 zone but not anterior foci are ECT-2 dependent**

The canonical model predicts that *RHO-1* is locally activated at the equatorial membrane by active *ECT-2* (Yüce et al., 2005; Somers and Saint, 2003). Therefore, in the absence of *ECT-2* no accumulation of *RHO-1* at the equator is expected. However, whether *RHO-1* can localize into anterior PH-positive foci remained unknown. I tested whether depletion of *ECT-2* by RNAi impaired the localization of *RHO-1* into any of the two pools. Endogenous *RHO-1* and *ECT-2* were co-depleted by RNAi. GFP::*RHO-1* and mCh::*PH* localization was followed during first cell division using confocal spinning disk microscopy.

As expected, early embryos failed cytokinesis in the absence of *ECT-2* (Nishimura and Yonemura, 2006; Kamijo et al., 2006; Yüce et al., 2005). In line with cytokinesis failure, no GFP::*RHO-1* accumulated at the equatorial cortex (Figure 23 A). Line-scan analysis was performed to quantitatively analyze *RHO-1* zone formation on single cortical z-planes. The intensity profile was plotted from the anterior (0 %) to the posterior (100 %) at NEBD and 160 s after NEBD. Cytoplasmic signal was measured at the anterior on central plane images, which was used to normalize cortical intensities. While in control embryos GFP::*RHO-1* accumulated into a *RHO-1* zone 160 s after NEBD, in the absence of *ECT-2*, GFP::*RHO-1* no longer formed an equatorial zone (Figure 23 B). Interestingly, GFP::*RHO-1* was still able to localize into PH-positive foci in the absence of *ECT-2*,

similar to the anterior pool of control embryos (Figure 23 A). This result suggested that the two pools of RHO-1 are differently regulated. Anterior PH-positive RHO-1 foci are ECT-2 independent, however the equatorial RHO-1 meshwork only forms in the presence of ECT-2 and thus depends on RHO-1 activation by the GEF ECT-2.

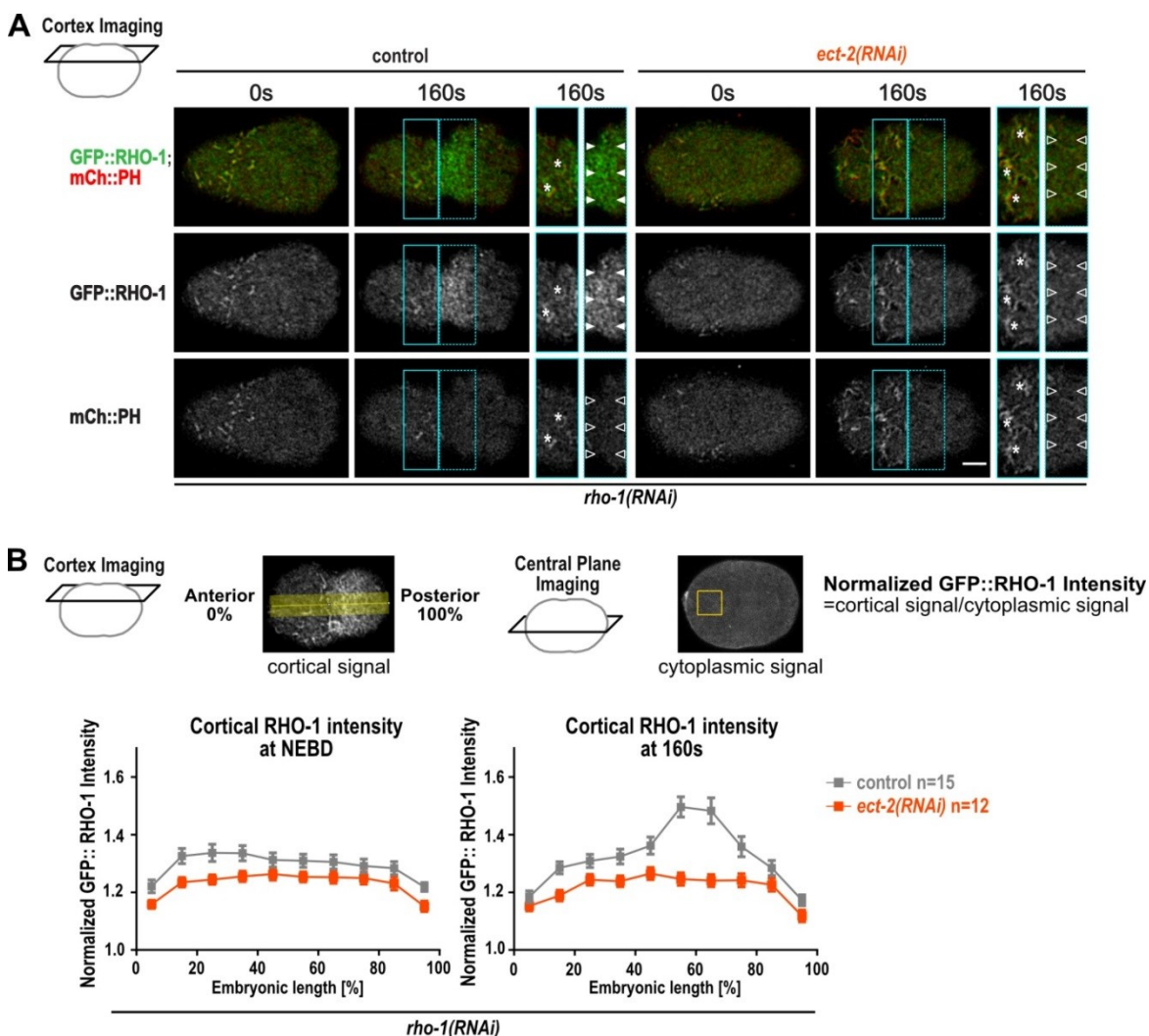


**Figure 23: The equatorial GFP::RHO-1 zone but not anterior foci are ECT-2 dependent.** (A) Representative cortical confocal time-lapse images of a control (left) and an *ect-2(RNAi)* embryo (right) expressing GFP::RHO-1 (green) and mCh::PH (red) for two indicated time points. Time represents seconds after NEBD. Scale bar=5  $\mu$ m. Insets for 160 s highlight the presence (solid arrowheads) and absence (blank arrowheads) of the RHO-1 zone/PH signal at the equator. Asterisks show the presence of anterior patches of GFP::RHO-1 and mCh::PH. (B) Schematic showing line-scan analysis. Cortical intensity profile was measured from the anterior (0 %) to the posterior (100 %). Cytoplasmic signal was measured in an anterior region at the central plane as illustrated. Cortical signal was normalized by dividing the cytoplasmic signal from each value along the anterior posterior line. Mean normalized cortical GFP::RHO-1 intensity is plotted along embryonic length for two indicated time points. Error bars are SEM; n=number of embryos analyzed.

### 3.3.2.2 GFP::**RHO-1** localization into PH-positive anterior foci and into the equatorial RHO-1 zone is independent of RGA-3/4

I showed that the equatorial dense GFP::**RHO-1** meshwork is dependent on ECT-2 and therefore depends on the activation of RHO-1. Fast RHO-1 cycling between the active and inactive form is termed ‘RhoA flux’ and it was proposed that rapid flux might contribute to narrow RhoA zone formation (Bement et al., 2006; Miller and Bement, 2009). Following this hypothesis, depletion of the GAPs RGA-3/4 is expected to result in a broadening of the RHO-1 zone. To test this prediction, RGA-3/4 double RNAi was performed. Depletion of both GAPs was shown to induce premature RHO-1 activation causing cortical anillin accumulation in metaphase (Zanin et al., 2013). Therefore, only mild RGA-3/4 knock-down was performed, to prevent premature RHO-1 activation and to study the effect of RGA-3/4 during anaphase. I designed dsRNA that targeted both RGA-3 and RGA-4. Live-cell imaging revealed that GFP::**RHO-1** still localized into both pools after mild RGA-3/4 depletion (Figure 24 A), suggesting that inactivation of RHO-1 by the two GAPs plays a minor role in RHO-1 localization *per se*. Line-scan analysis showed that GFP::**RHO-1** was distributed along the cortex during NEBD and formed a RHO-1 zone 160 s after NEBD comparable to control (Figure 24 B). This result indicated that mild RGA-3/4 depletion does not inhibit the formation of a RHO-1 zone.

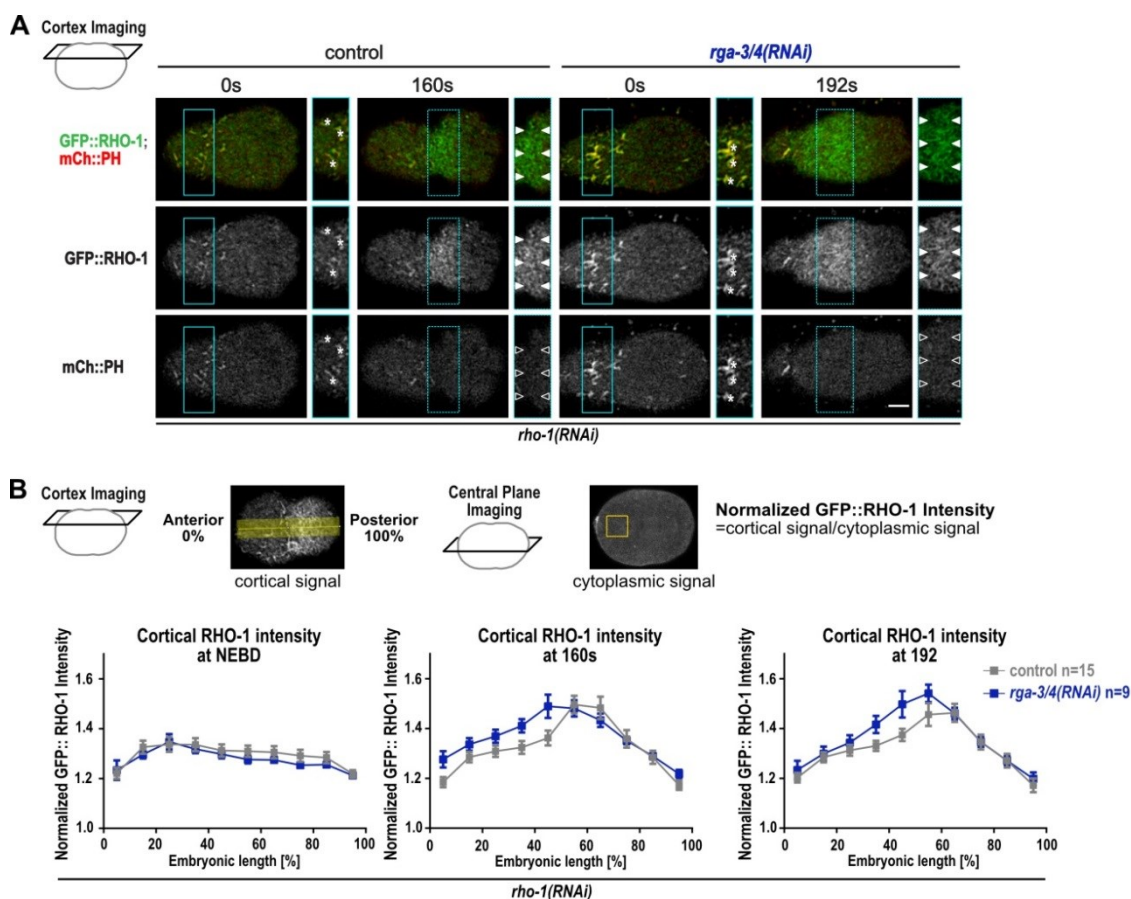


**Figure 24: GFP::RHO-1 localization into PH-positive anterior foci and into the equatorial RHO-1 zone is independent of RGA-3/4.** (A) Representative cortical confocal time-lapse images of a control (left) and an *rga-3/4(RNAi)* embryo (right) expressing GFP::RHO-1 (green) and mCh::PH (red) for two indicated time points. Time represents seconds after NEBD. Control is reproduced from Figure 23 A. Scale bar=5  $\mu$ m. Insets for 0 s highlights GFP::RHO-1 and mCh::PH patches (white asterisks) at the anterior of the cell. Insets for 160 s highlight the presence (solid arrowheads) of the RHO-1 zone and the absence (blank arrowheads) of PH signal at the equator. (B) Schematic showing line-scan analysis. Cortical intensity profile was measured from the anterior (0 %) to the posterior (100 %). Cytoplasmic signal was measured in an anterior region at the central plane as illustrated. Cortical signal was normalized by dividing the cytoplasmic signal from each value along the anterior posterior line. Mean normalized cortical GFP::RHO-1 intensity is plotted along embryonic length. Control graph and images are reproduced from Figure 23 B. Error bars are SEM; n=number of embryos analyzed.

### 3.3.2.3 ‘RhoA flux’ mediated by RGA-3/4 regulates cytokinesis timing

I found that GFP::RHO-1 still localized into anterior PH-positive patches and into a RHO-1 zone at the equatorial membrane in *rga-3/4(RNAi)* embryos. However, mild depletion of RGA-3/4 in the one-cell embryo led to stronger membrane ruffling and morphological changes (Figure 24 A). Timing of cytokinesis was quantified using central plane images as illustrated in Figure 25 A. Interestingly, cytokinesis timing analysis revealed that mild depletion of RGA-3/4 impaired ring assembly represented by the timing

of NEBD to back-to-back membrane formation ( $233 \pm 22$  s in control and  $264 \pm 36$  s in *rga-3/4(RNAi)* embryos). The timing from back-to-back membrane formation to full ingressión was faster in *rga-3/4(RNAi)* compared to control ( $101 \pm 42$  s and  $151 \pm 27$  s, respectively), which at the end resulted in similar timing from NEBD to full ring ingressión (Figure 25 A, B). This suggested that ‘RhoA flux’, mediated by GAP activity, influences cytokinesis timing. In particular, GAP activity plays a role in fast ring assembly and in slowing down ring ingressión.

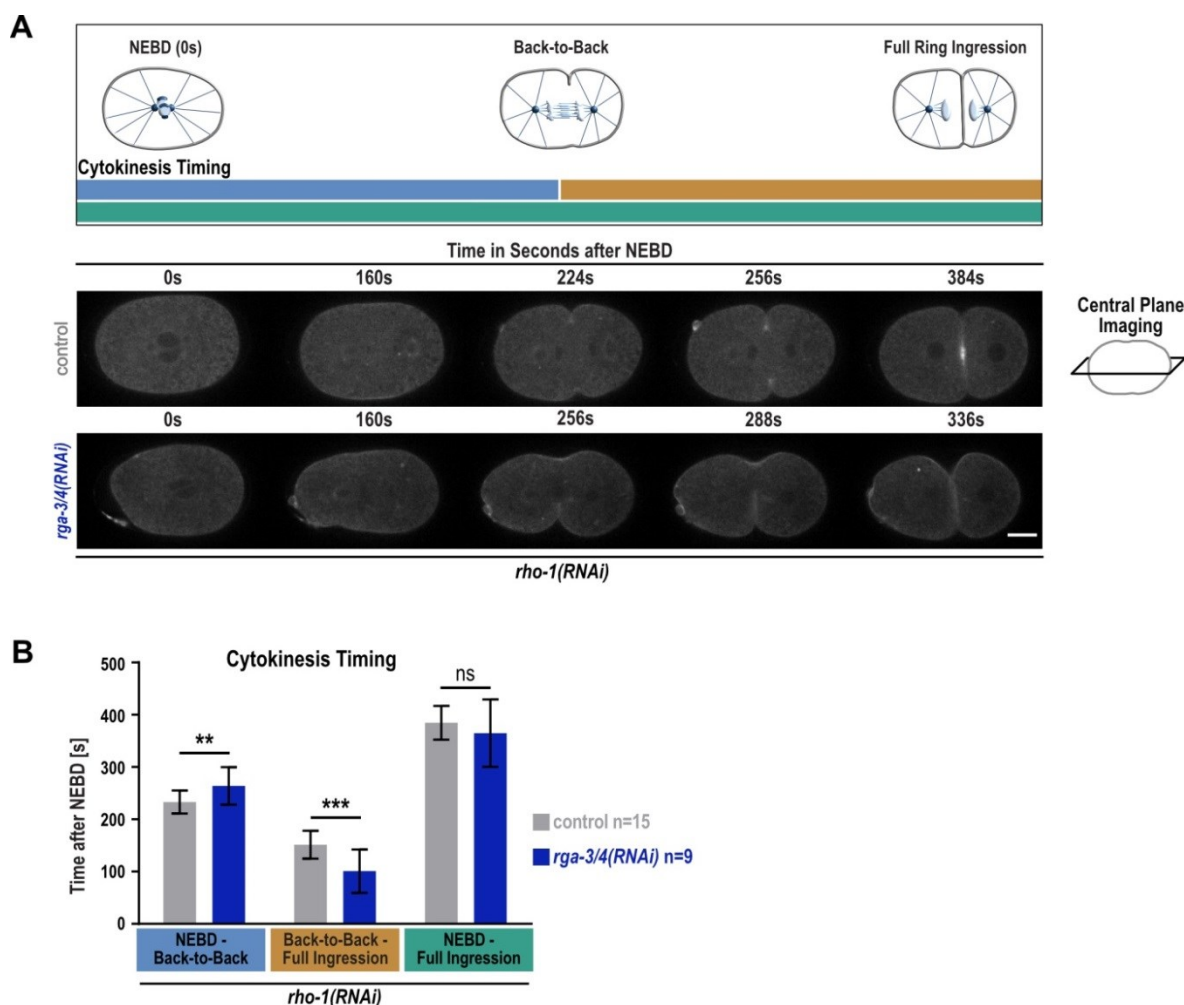


**Figure 25: ‘RhoA flux’ mediated by RGA-3/4 regulates cytokinesis timing. (A)** Representative central plane confocal time-lapse images of a control (top row;  $n=15$ ) and an *rga-3/4(RNAi)* embryo (bottom row;  $n=9$ ) expressing GFP::RHO-1 at indicated time points. Schematic represents time points of NEBD (0 s), back-to-back membrane formation and full ring ingressión. Time is shown in seconds after NEBD. Scale bar=10  $\mu$ m. **(B)** Cytokinesis timing analysis based on the schematic in (A) for control (grey) and *rga-3/4(RNAi)* (blue) embryos. Timing was determined on central plane time-lapse images. Error bars are SD;  $n$ =number of embryos analyzed. P-values were determined by Student’s *t* test (NEBD-back-to-back) or Mann-Whitney-U test (NEBD- and back-to-back to full ingressión) (ns=not significant; \*\* $P<0.01$ ; \*\*\* $P<0.001$ ).

### 3.3.2.4 Restricting RHO-1 into a narrow zone depends on RGA-3/4

Line-scan analysis revealed that embryos with a mild depletion of RGA-3 and RGA-4 still formed a RHO-1 zone, with comparable intensities to control, 160 s after NEBD (Figure 24 B). Cytokinesis timing in *rga-3/4(RNAi)* embryos was delayed in terms of NEBD to back-to-back membrane formation and consequently showed a delay in ring assembly (Figure 25 B). Therefore, line-scan analysis was also performed for the time point 192 s after NEBD, representing the time point where 6/9 embryos analyzed showed a delayed assembled RHO-1 zone. For control embryos GFP::RHO-1 intensity slightly decreased from 160 s to 192 s, whereas the intensity of GFP::RHO-1 in *rga-3/4(RNAi)* embryos slightly increased and showed a higher intensity level compared to control 192 s after NEBD (Figure 24 B). This confirmed the delay in ring assembly determined by cytokinesis timing analysis on central plane images.

Finally, the hypothesis was tested that a fast ‘RhoA flux’, which is mediated by the GEF and GAPs, controls narrow RHO-1 zone formation. For the line-scan analysis, mean intensity of control (n=15) and *rga-3/4(RNAi)* embryos (n=9) was plotted along embryonic length from the anterior to the posterior. To measure RHO-1 zone width, single line-scans of individual embryos were used as shown in Figure 24 B. Zone width was determined at the time point where the ring was assembled (RHO-1 zone was formed). For control this time point was reached 160 s after NEBD. Due to the delay in ring assembly (Figure 25 B), zone width in *rga-3/4(RNAi)* embryos was analyzed 192 s after NEBD for 6/9 embryos. The remaining three embryos showed a weaker phenotype and ring assembly occurred already 160 s after NEBD comparable to control. Therefore, 3/9 *rga-3/4(RNAi)* embryos were analyzed 160 s after NEBD. Individual line-scans were normalized to the mean intensity of the first 30 % as illustrated in Figure 26 A. Zone width was determined at half maximum of the intensity peak, representing the RHO-1 zone (Figure 26 A). Interestingly, zone width analysis showed a broader RHO-1 zone in *rga-3/4(RNAi)* embryos compared to control ( $27 \pm 5$  % and  $19 \pm 3$  % embryonic length, respectively). This result indicated that RGA-3/4 plays a minor role in RHO-1 localization to the equatorial region, however an increase of GAP activity of RHO-1 by RGA-3/4 is indeed required to restrict RHO-1 zone width. Next, it was tested whether an increase in RHO-1 zone width correlates with altered GFP::RHO-1 structures at the equatorial cortex. Analysis was performed using the same cortical time-lapse images and time points that were used for zone width analysis. Only PH-negative, active GFP::RHO-1 foci were considered for structure analysis, which was

performed in Fiji (Figure 26 B). GFP::RHO-1 foci were segmented and particles were analyzed for circularity and perimeter using ‘Analyze Particles’ in Fiji. For both characteristics there was no difference between *rga-3/4(RNAi)* and control embryos (Figure 26 B), indicating that mild depletion of RGA-3/4 broadens RHO-1 zone width without changing GFP::RHO-1 structures at the equatorial membrane.

In summary, I showed that GFP::RHO-1 is able to localize to the PM in an ECT-2 independent manner, co-localizing with PH-positive foci. ECT-2 dependent, active GFP::RHO-1 localized to the equatorial membrane forming a dense meshwork of filamentous-like structures. Mild depletion of RGA-3/4 did not alter GFP::RHO-1 localization in any of the two pools that were observed for control embryos, neither was structure formation at the equator affected. However, cytokinesis timing and RHO-1 zone width are dependent on GTP hydrolysis rates, mediated by the two GAPs RGA-3 and RGA-4, suggesting that a rapid ‘RhoA flux’ indeed restricts narrow RHO-1 zone formation, as previously described by the ‘RhoA flux model’.

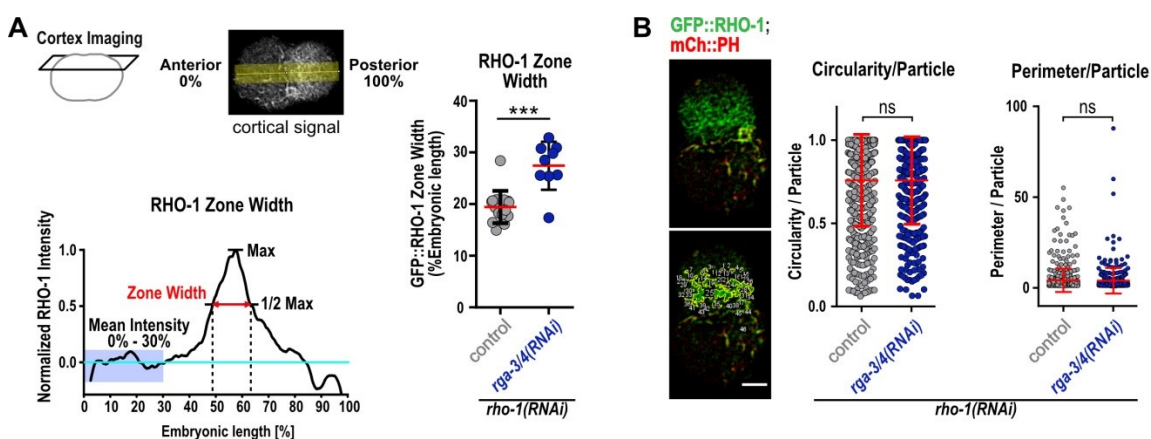


**Figure 26: Narrow GFP::RHO-1 zone width is restricted by RGA-3/4.** (A) GFP::RHO-1 zone width analysis for individual embryos was performed using cortical line-scans. The baseline was shifted by dividing all values by the mean of the first 30 %. The width at half maximum was determined and represents the zone width of the equatorial RHO-1 zone as illustrated. GFP::RHO-1 zone width was determined for control (gray; n=15) and *rga-3/4(RNAi)* embryos (blue; n=9). Control and 3/9 *rga-3/4(RNAi)* embryos were measured 160 s after NEBD. Zone width in 6/9 *rga-3/4(RNAi)* embryos was measured 192 s after NEBD due to a delay in RHO-1 zone formation. Each dot represents the zone width of an individual embryo. P-values were determined by Mann-Whitney-U test (\*\*\*P<0.001). Error bars are SD. (B) Structure analysis for control (gray; n=15) and *rga-3/4(RNAi)* embryos (blue; n=19) using the same time-lapse images and time points used for zone width analysis in (A). Only PH-negative, active GFP::RHO-1 foci were analyzed. Therefore the mCh::PH signal was subtracted from GFP::RHO-1. Individual structures were segmented and analyzed using the plugin ‘Particle Analyzer’ in Fiji. Each dot represents a single GFP::RHO-1 foci. Individual foci were tested for circularity and perimeter. P-values were determined by Mann-Whitney-U test (ns=not significant). Error bars are SD. Scale bar=5  $\mu$ m.



### 3.3.3 How do the two PM-targeting motifs of RHO-1 contribute to its localization in the two observed membrane pools?

RHO-1 forms a narrow zone at the equatorial membrane (Bement and Benink, 2005; Takaishi et al., 1995; Nishimura and Yonemura, 2006; Kamijo et al., 2006; Yüce et al., 2005; Yonemura and Hirao, 2004). I confirmed the presence of a narrow RHO-1 zone in the *C. elegans* zygote, by using our genetic replacement system. I further showed that a rapid ‘RhoA flux’, through the GDP/GTP cycle, is required to restrict narrow RHO-1 zone. To elucidate further mechanisms that maintain RHO-1 at the equatorial membrane, I subsequently tested how the two PM-targeting motifs, the PBS and the CAAX-motif, contribute to RHO-1 zone formation and maintenance. Previous experiments in *S. cerevisiae* showed that the PBS targets Rho1 to the division site (Yoshida et al., 2009). The PBS and the CAAX-motif are conserved in different organisms (Figure 27 A). Therefore, I tested whether the PBS and/or the CAAX-motif also drive equatorial membrane localization in *C. elegans* and whether the interaction of these motifs with lipids contributes to the restriction of a narrow RHO-1 zone.

#### 3.3.3.1 The PBS and CAAX-motif localize RHO-1 to the PM representing a prerequisite for cytokinesis

To test the contribution of the two PM-targeting motifs to RHO-1 localization, the PBS was mutated (RHO-1<sup>6KA</sup>) and the CAAX-motif was deleted (RHO-1<sup>ΔCAAX</sup>) (Figure 27 A, B). The PBS was mutated by exchanging six lysines to alanines, in order to remove positive net charges and to avoid interaction with the negatively charged lipids of the PM. The CAAX-motif was deleted to prevent prenylation. Both transgenes were integrated by MosSCI method and were RNAi-resistant as well as GFP-tagged in the same way as control (GFP::RHO-1) (Figure 12). Live-cell imaging was performed using confocal spinning disk microscopy. I found that RHO-1 lacking either of the two PM-targeting motifs no longer localized to the PM (Figure 27 C). While GFP::RHO-1 expressing embryos rescued cytokinesis failure in 93 %, GFP::RHO-1<sup>6KA</sup> and GFP::RHO-1<sup>ΔCAAX</sup> only rescued cytokinesis in 47 % and 25 %, respectively.

I previously showed that the GFP-tag impairs RHO-1 function in later development resulting in embryonic lethality (Figure 13 C). However, RHO-1 without GFP-tag rescued embryonic lethality (Figure 14 C). Therefore, the functionality of the two RHO-1 mutants lacking either of the PM-targeting motifs without GFP-tag was tested by embryonic

lethality test. The mutant transgenes were RNAi-resistant and worms were injected with *rho-1* dsRNA. The progeny (larvae and dead embryos) of injected young hermaphrodites was counted 48 h later. Wild-type RHO-1 expressing worms rescued embryonic lethality, whereas RHO-1<sup>6KA</sup> and RHO-1<sup>ΔCAAX</sup> did not (Figure 27 D), indicating that both motifs are required for embryonic viability and therefore for RHO-1 function.

Whether RHO-1 function was impaired during first cell division was tested by performing live-cell imaging of one-cell embryos expressing RHO-1<sup>6KA</sup> or RHO-1<sup>ΔCAAX</sup> in comparison to embryos expressing RHO-1 in the absence of endogenous RHO-1. To follow ring assembly and ingression, GFP-tagged Anillin (ANI-1) was used as readout. ANI-1 is a downstream effector of RHO-1 and a scaffold protein that cross-links several contractile ring components (Field and Alberts, 1995; Piekny and Glotzer, 2008; Straight et al., 2005). For functionality studies RNAi-resistant wild-type RHO-1 and mutants (RHO-1<sup>6KA</sup> and RHO-1<sup>ΔCAAX</sup>) were crossed into a GFP::ANI-1 expressing strain. After *rho-1* dsRNA injections, one-cell embryos were imaged and analyzed for ring ingression. Central plane live-cell images were scored for “full ring ingression”, “ingression-regression” and “no furrow formation” as represented in Figure 27 E. While RHO-1 expressing embryos showed 100 % full ring ingression, RHO-1<sup>6KA</sup> and RHO-1<sup>ΔCAAX</sup> only showed 73 % and 47 % partial functionality, respectively (Figure 27 E). Partial functionality included embryos showing “full ring ingression” and “ingression-regression” phenotype. Deletion of the CAAX-motif showed a stronger phenotype than mutating the PBS, suggesting that the contribution of the PBS rather supports the main PM anchoring function of the lipid moiety. Functionality studies of the two mutants (RHO-1<sup>6KA</sup> and RHO-1<sup>ΔCAAX</sup>) revealed only a partial cytokinesis defect, although both GFP-tagged mutants were not detected on the PM. This can be explained in two ways: (1) each of the two motifs act as an individual PM anchor, which together fulfill stable localization or (2) RHO-1 stabilization at the equatorial membrane, in addition, is driven by protein-protein interaction. To distinguish between those two possibilities, I generated a mutant in which the 6KA mutation was combined with the CAAX-deletion and performed the same functionality studies (RNAi-resistant RHO-1<sup>6KAΔCAAX</sup> without GFP-tag). Without the two PM-targeting motifs, RHO-1<sup>6KAΔCAAX</sup> was no longer functional in the absence of endogenous RHO-1 (Figure 27 E), indicating that PM-targeting, driven by the two motifs, is a prerequisite for RHO-1 function during cytokinesis. This further suggests that RHO-1 stabilization at the PM cannot be substituted by protein-protein interaction. In summary, I showed that both

C-terminal motifs of RHO-1, the PBS and the CAAX-motif, are required for RHO-1 localization to the PM representing a prerequisite for RHO-1 function and cytokinesis.

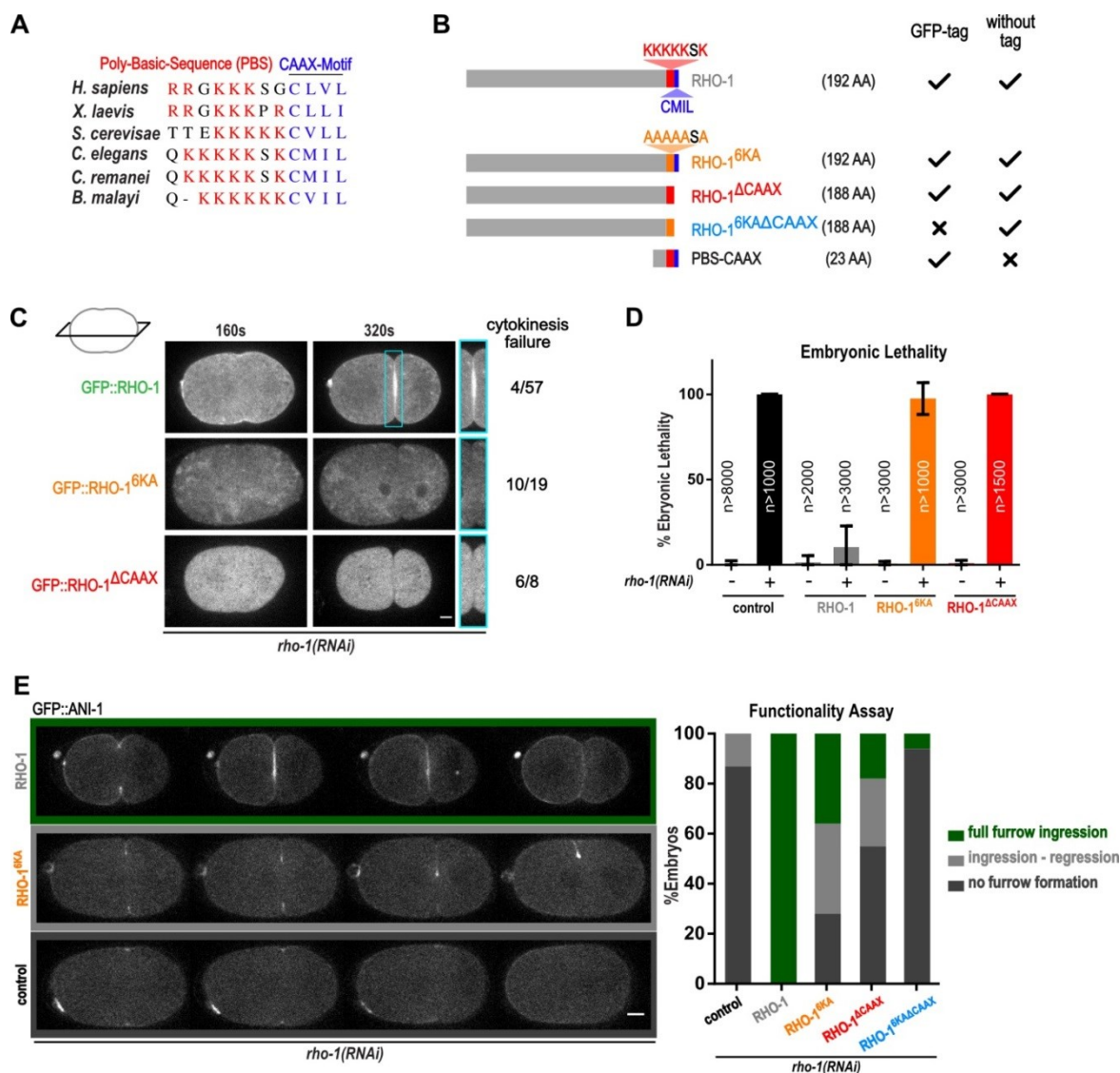


**Figure 27: The PBS and CAAX-motif mediate RHO-1 PM binding, which represents a prerequisite for cytokinesis. (A)** Sequence alignment showing that the PBS and the CAAX-motif are highly conserved in different organisms. **(B)** Schematic representation of RHO-1 proteins used to study the contribution of the PBS and CAAX-motif in PM-targeting and RHO-1 function. All mutants were RNAi-resistant. The PBS was mutated by exchanging six lysines for alanines (RHO-1<sup>6KA</sup>) and the CAAX-motif was deleted from the coding sequence (RHO-1<sup>ΔCAAX</sup>). In addition, a double mutant was generated (RHO-1<sup>6KAΔCAAX</sup>) and a construct only expressing the last 23 AAs (last exon) of RHO-1 including the PBS and CAAX-motif (PBS-CAAX). Transgenes were integrated into *C. elegans* genome, with and without GFP-tag as indicated, using MosSCI method analog to GFP::RHO-1 and RHO-1 as described in Figure 12 A and Figure 14 A. **(C)** Representative central plane confocal time-lapse images of worms expressing GFP::RHO-1 (green), GFP::RHO-1<sup>6KA</sup> (orange) and GFP::RHO-1<sup>ΔCAAX</sup> (red) at the indicated time points. Insets highlight cell-cell contacts of two-cell embryos showing the presence and absence of GFP::RHO-1. Scale bar=5 μm. Cytokinesis failure shows number of embryos failing cytokinesis in respect to total number of embryos imaged. **(D)** Embryonic lethality assay was performed in the presence and absence of endogenous RHO-1 for control (black), RHO-1 (gray), RHO-1<sup>6KA</sup> (orange) and RHO-1<sup>ΔCAAX</sup> (red) expressing worms. Error bars are SD; n=number of progeny counted.

**(E)** Functionality of the different transgenes was tested by depleting endogenous RHO-1 by RNAi and ring ingression was analyzed by GFP::ANI-1, performing confocal time-lapse imaging. Functionality was scored into three categories: full furrow ingression (green), ingression-regression (light gray) and no furrow formation (dark gray). For each category one example embryo is shown on the left, expressing GFP::ANI-1 and the transgene indicated (central plane confocal time-lapse images; Scale bar=10  $\mu$ m.). Control refers to only endogenous RHO-1 present. Functionality assay was performed for control (n=22), RHO-1 (gray; n=12), RHO-1<sup>6KA</sup> (orange; n=11), RHO-1<sup>ACAAAX</sup> (red; n=12) and RHO-1<sup>6KAACAAAX</sup> (blue; n=15) expressing embryos in the background of GFP::ANI-1 and in the absence of endogenous RHO-1 (graph on the right).

### 3.3.3.2 The PBS and CAAX-motif together are sufficient to localize RHO-1 to the PM

I showed that the two PM-targeting motifs are required for RHO-1 localization to the PM. Functionality studies revealed that RHO-1, lacking either of the two PM-targeting motifs, is not functional. Therefore, the GFP-tagged RHO-1 PM-targeting mutants could not be used to study their role in active RHO-1 zone formation and maintenance. To test whether the PM-targeting motifs are sufficient for equatorial enrichment during anaphase, experiments were performed only using the PBS and CAAX-motif without the RHO-1 GTPase domain.

For this, a MosSCI strain expressing a transgene coding for the last 23AAs (last exon) of RHO-1, including the PBS and the CAAX-motif, tagged with GFP was generated (Figure 27 B). The transgene was regulated by *mex-5* promoter (488 bp) and *tbb-2* 3'UTR (330 bp) regulatory regions (Zeiser and Frøkjær, 2011), since expression by the endogenous regulatory sequences was very low. Localization studies were performed by live-cell imaging. In the presence of endogenous RHO-1 GFP::PBS::CAAX localized to the PM in central plane images, showing a uniform appearance around the cell periphery (Figure 28 A). *In vitro* studies from 1998 and 2001 showed that RhoA can form dimers, in its GDP- and GTP loaded state, driven by the C-terminal PBS (Zhang et al., 2001; Zhang and Zheng, 1998b). If the PBS is also sufficient for dimerization *in vivo*, PM localization of GFP::PBS::CAAX could also be mediated by dimer formation of GFP::PBS::CAAX with endogenous RHO-1. To exclude this possibility, endogenous RHO-1 was depleted by RNAi and GFP::PBS::CAAX localization was analyzed in the one-cell embryo using live-cell microscopy. Interestingly, GFP::PBS::CAAX localized to the PM, even in the absence of endogenous RHO-1 (Figure 28 A), indicating that the two motifs together are sufficient for PM-targeting and localization.

I showed that the PBS and CAAX-motif are sufficient to localize RHO-1 to the PM in the presence and absence of endogenous RHO-1, indicating that this localization is independent of the GTPase domain. Together with the finding that GFP::RHO-1 localized to the PM in the absence of ECT-2, this suggests that there is a pool of RHO-1 that is targeted to the PM only driven by the two PM-targeting motifs. To further test this hypothesis, FRAP experiments were performed right after NEBD, where membrane-targeting of RHO-1 was ECT-2 independent. If the PBS and CAAX-motif are sufficient for PM localization, similar recovery rates were expected after photobleaching for GFP::PBS-CAAX compared to GFP::RHO-1. Otherwise a slower recovery for GFP::PBS-CAAX would be expected, if RHO-1 regulation by effectors plays an additional role. A region (5.07  $\mu\text{m}$  x 5.07  $\mu\text{m}$ ) was bleached at the anterior of the zygote right after NEBD. Fluorescence recovery was followed by live-cell imaging for GFP::RHO-1 and GFP::PBS::CAAX in the presence of endogenous RHO-1. FRAP recovery curves of GFP::RHO-1 and GFP::PBS-CAAX showed similar recovery and halftime of recovery (Figure 28 B, C), suggesting that indeed the two motifs, independent of the RHO-1 GTPase domain, are the driving motifs for PM localization. In summary, I showed with live-cell imaging that the two PM-targeting motifs of RHO-1, the PBS and the CAAX-motif together, are sufficient for PM localization. I further confirmed that finding by FRAP experiments, indicating that indeed ECT-2 independent PM localization is forced by the PBS and the CAAX-motif.

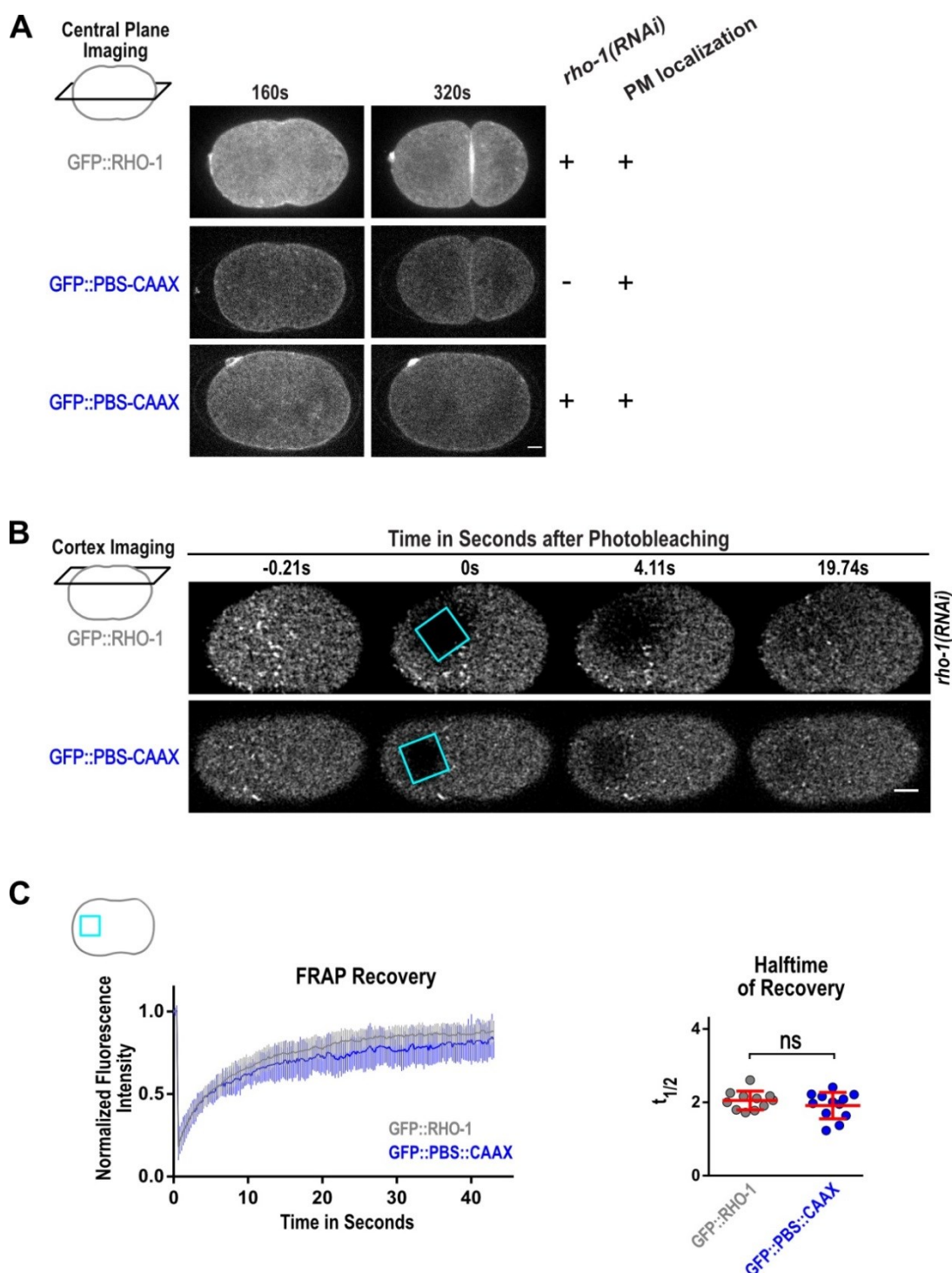


**Figure 28: The PBS and CAAX-motif together are sufficient to localize RHO-1 to the PM.** (A) Central plane confocal time-lapse images of embryos expressing GFP::RHO-1 (top row) or GFP::PBS-CAAX (two bottom rows) in the presence and absence of endogenous RHO-1 as indicated showing PM localization. Time represents seconds after NEBD. (B) Representative cortical plane FRAP time-lapse images of a one-cell embryo expressing GFP::RHO-1 in the absence of endogenous RHO-1 (top row) and a one-cell embryo expressing GFP::PBS-CAAX (bottom row). Time represents seconds relative to photobleaching, which was performed right after NEBD. Light blue box simulates bleached region. Scale bar=5  $\mu$ m. (C) FRAP recovery curves and halftime of recovery ( $t_{1/2}$ ) is shown for individual embryos expressing GFP::RHO-1 (gray; pooled experiments from *rho-1(RNAi)* injected and non-injected embryos as described in 2.2.14.8.1) and GFP::PBS-CAAX (blue). Error bars are SD. P-values were determined by Student's t test (ns=not significant).

### 3.3.3.3 The PBS and CAAX-motif are not sufficient to specifically accumulate RHO-1 at the equator

Central plane imaging revealed that the PBS and CAAX-motif together are sufficient to localize RHO-1 to the PM *per se*. However, whether one or both of the motifs contribute to a specific accumulation of RHO-1 to the equatorial cortex remained elusive. I tested this by performing live-cell imaging of embryos expressing GFP::PBS-CAAX at the cortical plane in the absence of endogenous RHO-1. GFP::PBS-CAAX localized into anterior PH-positive patches, however GFP::PBS-CAAX was not enriched in an equatorial zone 160 s after NEBD, where a GFP::RHO-1 zone was formed in control embryos (Figure 29 A). This observation was quantified by line-scan analysis (Figure 29 B) as described in 3.3.2.1. Interestingly, GFP::PBS-CAAX showed a similar localization as GFP::RHO-1 in the absence of ECT-2 (Figure 23 A), strengthening the hypothesis that RHO-1 independently of its activator ECT-2 localizes to the PM, driven by the PBS and CAAX-motif only.

In summary, I showed that the PBS and CAAX-motif are required and sufficient to localize RHO-1 to the PM, where it localizes into PH-positive foci. This localization is independent of the GTPase domain of RHO-1. Accumulation of RHO-1 into a narrow zone at the equator is dependent on ECT-2 function and cannot be forced by the PBS and CAAX-motif alone. Therefore, these findings indicate that PM localization driven by the PBS and CAAX is required for cytokinesis, however whether the interaction of the two PM-targeting motifs with lipids contributes to the restriction of the narrow RHO-1 zone remains to be tested in the future.

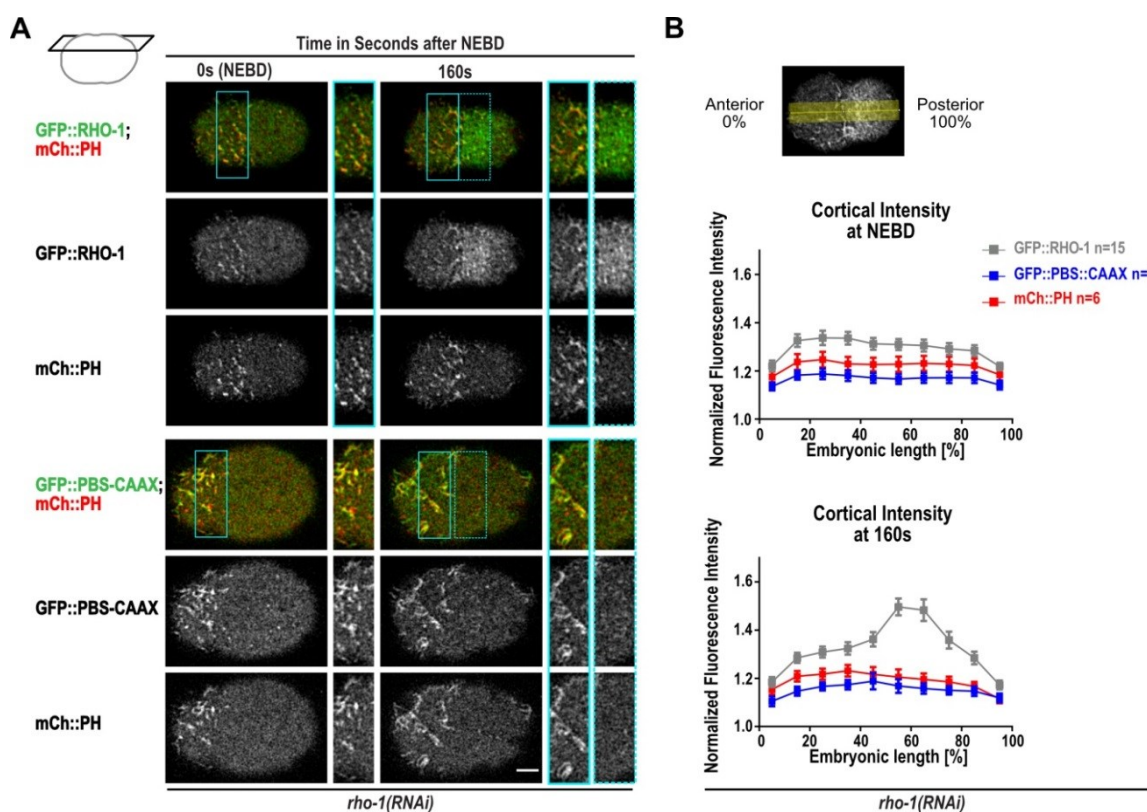


**Figure 29: The PBS and CAAX-motif are not sufficient to specifically accumulate RHO-1 at the equator. (A)** Representative cortical confocal time-lapse images showing one-cell embryos expressing GFP::RHO-1 and mCh::PH (top three rows) and GFP::BPS-CAAX and mCh::PH (bottom three rows) in the absence of endogenous RHO-1 at time points indicated. Insets highlight anterior PH- and GFP positive foci and the presence (GFP::RHO-1) or absence (GFP::PBS-CAAX) of GFP signal at the equatorial region. Time represents seconds after NEBD. Scale bar=5  $\mu$ m. **(B)** Line-scan analysis along embryonic length from anterior to posterior of cortical plane images for GFP::RHO-1 (gray; reproduced from control Figure 23 B), GFP::PBS-CAAX (blue) and mCh::PH (red) at indicated time points. Cortical fluorescence intensity was normalized to cytoplasmic intensity measured in a box at the anterior of central plane images. Error bars are SEM, n=number of embryos analyzed.

### 3.3.4 Does the actin cytoskeleton act as a physical barrier that restricts RhoA into a narrow zone at the equatorial membrane?

The actin cytoskeleton is a mesh-like structure that is present beneath- and anchored to the PM. In combination with myosin, the actin meshwork generates tension that supports the PM and determines cell shape. It was proposed and experimentally shown that the actin network in close proximity to the PM contributes to limited diffusion of lipids and proteins within the PM (Heinemann et al., 2013; Kusumi et al., 2005). Due to a compartmentalization of the PM by the actin mesh, lipids and proteins can only freely diffuse within compartments (Morone et al., 2006; Sheetz, 1983). During cytokinesis the density of linear F-actin at the equator increases since active RHO-1 activates formins,



which in turn nucleates F-actin. If F-actin at the equator limits RHO-1 diffusion within the PM by spatially restriction, this could represent a mechanism to maintain RHO-1 within a narrow zone. This hypothesis was tested by inhibiting cortical F-actin polymerization, which is induced by the two main nucleators Arp2/3 complex and formins (Chan et al., 2019; Davies et al., 2014). While formins were shown to be essential for cytokinesis (Severson et al., 2002; Watanabe et al., 2008), the Arp2/3 complex only changes kinetics of cytokinesis presumably by negatively regulating formin activity (Chan et al., 2019), which might be due to changes in the amount of free monomeric actin (Suarez et al., 2015; Rotty and Bear, 2015). Following these hypotheses, the absence of the Arp2/3 complex would induce higher F-actin density at the equator. If F-actin contributes to the restriction of RHO-1 into a narrow zone, higher densities of F-actin would result in changes of the RHO-1 zone accordingly. This hypothesis was tested by depleting the formin and the Arp2/3 complex and GFP::RHO-1 localization was followed by live-cell imaging.

#### **3.3.4.1 Equatorial RHO-1 zone formation is independent of linear and branched F-actin**

First, I addressed the question whether RHO-1 zone was altered in the absence of the two nucleators formin and Arp2/3 complex. In *C. elegans* the formin CYK-1 is the main nucleator required for cytokinesis that leads to polymerization of linear F-actin at the equatorial cortex activated by RHO-1. RNAi against CYK-1 was performed and GFP::RHO-1 localization was followed in one-cell embryos by spinning disk microscopy. Cortical images were line-scanned and GFP::RHO-1 intensity was measured along the anterior to posterior axes as described in 3.3.2.1. Live-cell imaging and line-scan analysis revealed that, in the absence of CYK-1, a GFP::RHO-1 zone is still formed at the equator 160 s after NEBD (Figure 30 A, C). CYK-1 knock-down was verified by using a strain expressing the actin marker LifeAct fused to RFP (BV70; received from Zhirong Bao). LifeAct is a small peptide (17 AAs) derived from a *S. cerevisiae* protein that marks F-actin and can be used for live-cell imaging (Riedl et al., 2008). Performing *cyk-1(RNAi)* in the strain expressing LifeAct::RFP showed the absence of an actin ring along the equator (Figure 30 B) and resulted in cytokinesis failure. In GFP::RHO-1 expressing *cyk-1(RNAi)* embryos, no ring ingression was observed and even 224 s after NEBD, when control embryos were already divided, GFP::RHO-1 intensity along the cortex was still present. The intensity profile for GFP::RHO-1 in *cyk-1(RNAi)* embryos, 224 s after NEBD showed similar intensities compared to control embryos at 160 s after NEBD. Intensities at 160 s

were reduced in *cyk-1(RNAi)* embryos compared to control, suggesting a delay in GFP::RHO-1 accumulation in the absence of CYK-1 (Figure 30 A, C).

Next, ARX-2 was depleted by RNAi, a component of the Arp2/3 complex in *C. elegans*, to analyze the influence of branched actin networks on RHO-1 zone formation. In the absence of ARX-2, GFP::RHO-1 still accumulated into a RHO-1 zone 160 s after NEBD, however ring ingression was delayed as previously described (Chan et al., 2019). The influence of ARX-2 depletion on F-actin was tested by performing RNAi in the strain expressing LifeAct::RFP, showing that F-actin structures are not altered at the equator (Figure 30 B). To test whether CYK-1 and ARX-2 have a synergistic effect on GFP::RHO-1 localization and RHO-1 zone formation, both proteins were co-depleted. The absence of both F-actin nucleators did not impair RHO-1 zone formation (Figure 30 A). In summary, I showed that F-actin polymerization nucleated by either the formin CYK-1 or the Arp2/3 complex is not required for RHO-1 zone formation, however there was a slight delay in GFP::RHO-1 accumulation at the equator in *cyk-1(RNAi)* embryos compared to control.

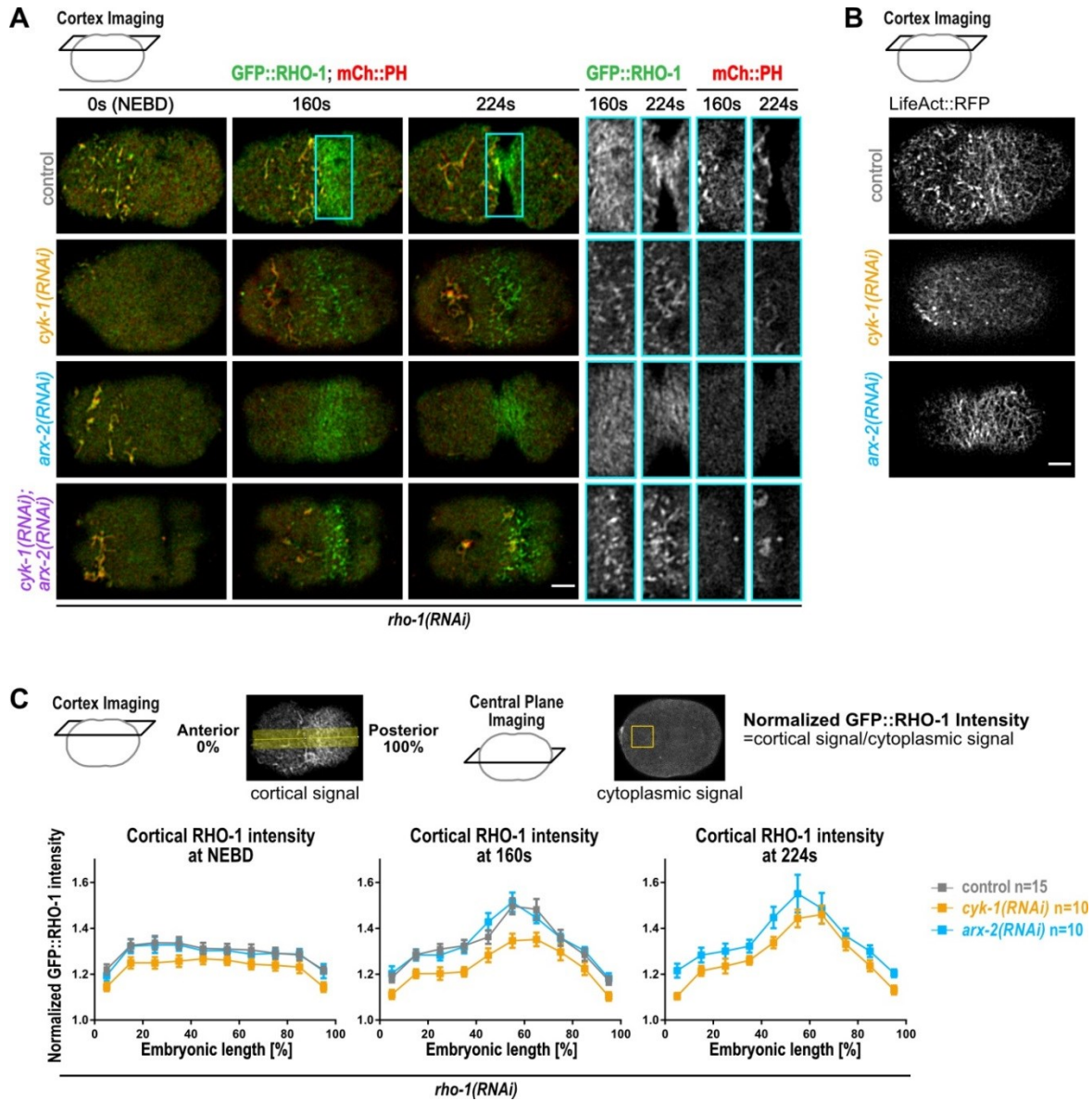


**Figure 30: Equatorial GFP::RHO-1 zone formation is independent of linear and branched F-actin.** (A) Representative cortical plane confocal time-lapse images of one-cell embryos expressing GFP::RHO-1 (green) and mCh::PH (red) after RNAi against indicated genes, at indicated time points. Time represents seconds after NEBD. Insets highlight equatorial region for GFP::RHO-1 and mCh::PH at 160 s and 224 s after NEBD. (B) Cortical plane confocal time-lapse images of embryos expressing LifeAct::RFP for control, *cyk-1(RNAi)* and *arx-2(RNAi)* 160 s after NEBD. (C) Line-scan analysis performed on cortical images of embryos, expressing GFP::RHO-1 and mCh::PH, after RNAi against indicated genes, at indicated time points. Line-scan analysis was performed from the anterior to the posterior and the signal was normalized to cytoplasmic signal of the central plane. Control is reproduced from Figure 23 B. Error bars are SEM, n=number of embryos analyzed. Scale bars=5  $\mu$ m.

### 3.3.4.2 Equatorial RHO-1 meshwork formation requires formin-induced F-actin polymerization

Live-cell imaging revealed that neither linear- nor branched F-actin was required for GFP::RHO-1 to form a RHO-1 zone at the equatorial membrane. Next, it was tested whether RHO-1 zone width was altered in *cyk-1(RNAi)* and *arx-2(RNAi)* embryos compared to control. RHO-1 zone width analysis was performed as described in 3.3.2.4 and illustrated in Figure 26 A. Zone width was analyzed when the ring was assembled for control at 160 s after NEBD. For *cyk-1(RNAi)* embryos ring ingression was inhibited and line-scan analysis revealed that in *cyk-1(RNAi)* embryos GFP::RHO-1 intensities increased over time (160 s to 224 s). Therefore, zone width was also measured 224 s after NEBD. While zone width in control embryos covered  $19 \pm 3\%$  of embryonic length, in *cyk-1(RNAi)* embryos RHO-1 zone was increased to  $30 \pm 9\%$  at 160 s after NEBD and covered  $26 \pm 11\%$  of embryonic length 224 s after NEBD (Figure 31 A). However, variances within the dataset of *cyk-1(RNAi)* embryos for both time points were more distinct compared to control, indicating a less organized localization of GFP::RHO-1 at the equator. In *arx-2(RNAi)* embryos RHO-1 zone formation was not changed, however ring ingression was slightly delayed. Therefore, in 7/10 embryos GFP::RHO-1 zone width could still be measured 224 s after NEBD. Zone width analysis at 160 s showed higher variances in *arx-2(RNAi)* embryos, however no significant increase in zone width compared to control ( $25 \pm 8\%$  and  $19 \pm 3\%$ , respectively). Over time, RHO-1 zone width in the absence of ARX-2 was less variable (at 224 s) and comparable to control 160 s after NEBD ( $22 \pm 5\%$  vs.  $19 \pm 3\%$ ), strengthening the hypothesis that the absence of ARX-2 does not alter RHO-1 organization during cytokinesis (Figure 31 A).

In control embryos, GFP::RHO-1 forms a dense meshwork of filamentous-like structures at the equator. Interestingly, live-cell imaging showed that GFP::RHO-1 foci, in the absence of CYK-1, no longer formed a dense meshwork but rather dot-like accumulations (Figure 30 A). These foci were quantified by performing structure analysis in Fiji and compared their perimeter and circularity. GFP::RHO-1 structures were segmented and only equatorial RHO-1 was considered for structure analysis (see section 3.3.2.4). I found that in the absence of CYK-1, GFP::RHO-1 foci showed a smaller perimeter and a higher circularity (Figure 31 B). In the absence of ARX-2, GFP::RHO-1 particles at the equator showed no differences in perimeter and circularity compared to foci detected in control embryos (Figure 31 B). These results suggest that formin-generated unbranched F-actin but

not branched F-actin is required for the formation of a dense meshwork of filamentous-like RHO-1 structures at the equatorial cortex during cytokinesis. Further these results indicate that an increase in F-actin density at the equator, due to loss of Arp2/3-induced branched actin networks, does not alter GFP::RHO-1 zone and meshwork formation.

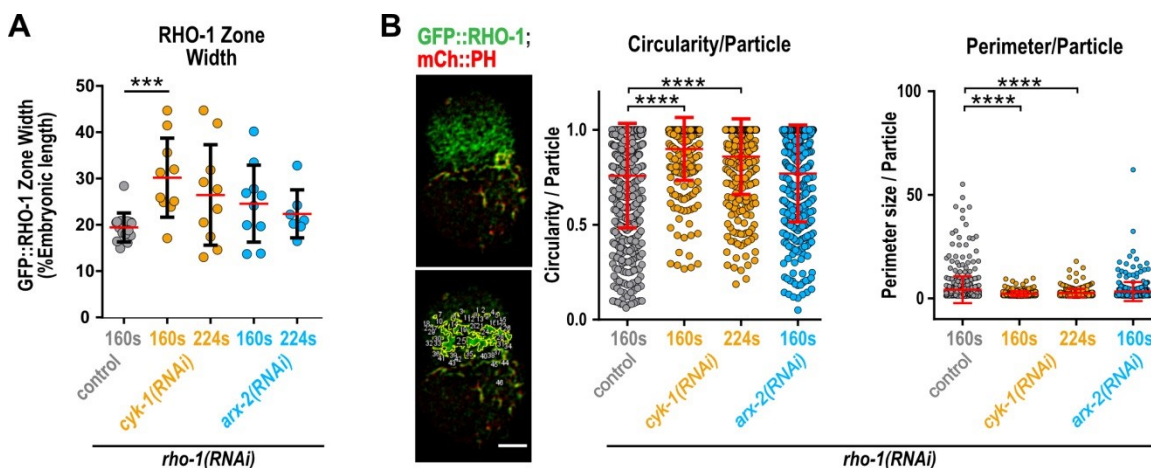


**Figure 31: Equatorial GFP::RHO-1 meshwork formation requires formin-induced F-actin polymerization.** (A) Zone width analysis was performed on cortical plane time-lapse images of embryos expressing GFP::RHO-1 for control (gray; n=15; reproduced from Figure 26 A), *cyk-1(RNAi)* (yellow; n=10) and *arx-2(RNAi)* (blue; n=10) embryos. Analysis was performed at 160 s after NEBD and in addition at 224 s after NEBD for *cyk-1(RNAi)* and *arx-2(RNAi)* (only 7/10 not ingressed) embryos. Error bars are SD. P-values were determined using Student's *t* test (\*\**P*<0.001). (B) Structure analysis was performed on cortical images segmented for GFP::RHO-1 particles that did not co-localize with mCh::PH foci. Mean cortical signal was subtracted (90%), 'Gaussian Blur Filter' and 'Unsharp Mask' was applied. Co-localizing GFP::RHO-1 and mCh::PH foci were eliminated by subtracting the red channel from the green channel. Remaining particles were analyzed for circularity and perimeter for control (gray; n=15; reproduced from Figure 26 B), *cyk-1(RNAi)* (yellow; n=10) and *arx-2(RNAi)* (blue; n=10) embryos using 'Particle Analyzer' in Fiji. Error bars are SD. P-values were determined using Mann-Whitney-U test (\*\*\*\**P*<0.0001).

### 3.3.4.3 Equatorial RHO-1 foci in *cyk-1(RNAi)* embryos represent active RHO-1

I showed that the formation of a dense GFP::RHO-1 meshwork at the equator was dependent on formin-induced F-actin polymerization. However, GFP::RHO-1 was still able to localize into an equatorial RHO-1 zone. Consequently, I addressed the question whether GFP::RHO-1 foci, in the absence of CYK-1, require RHO-1 activation by ECT-2. I tested this by two different approaches: (1) by co-depleting the formin (CYK-1) and the GEF (ECT-2) and following GFP::RHO-1 by live-cell imaging and (2) by depleting formin (CYK-1) in a strain expressing mNG-tagged anillin (ANI-1 in *C. elegans*) and following

its localization by live-cell imaging. Anillin binds multiple components of the contractile ring and is recruited to the equator by active RHO-1 (Maddox et al., 2005; Oegema et al., 2000; Straight et al., 2005). If mNG::ANI-1 still localizes to the equator in the absence of CYK-1, this would suggest that RHO-1 is active. If RHO-1 foci in the absence of CYK-1 represent inactive RHO-1, co-depletion of ECT-2 with CYK-1 should not affect their formation.

Performing *ect-2(RNAi);cyk-1(RNAi)* double RNAi experiments revealed that GFP::RHO-1 no longer localized into a RHO-1 zone (Figure 32 A), indicating that in *cyk-1(RNAi)* embryos GFP::RHO-1 foci depend on RHO-1 activation by ECT-2. This finding was further confirmed by the second experimental approach, where CYK-1 was depleted in a strain expressing mNG::ANI-1 and anillin was still found localized to the equator (Figure 32 B). In control embryos, anillin localizes to the equator accumulating into large clusters (Figure 32 B) as previously published (Tse et al., 2011). Interestingly, my preliminary data show, that in the absence of CYK-1 mNG::ANI-1 localization changed and appeared in rather smaller dot-like and linear structures at the equatorial cortex (Figure 32 B), comparable to GFP::RHO-1 in *cyk-1(RNAi)* embryos (Figure 30 A, Figure 32 A). However, since mNG::ANI-1 localization after *cyk-1(RNAi)* was only analyzed in 3 embryos, future work will require a quantitative comparison of the RHO-1 and ANI-1 structures by co-localization studies. Furthermore, since ANI-1 binds not only active RHO-1 but also F-actin and myosin via the N-terminus (Oegema et al., 2000; Field and Alberts, 1995; Straight et al., 2005), a shorter ANI-1 fragment solely including the RHO-1 binding domain (AH-PH (Tse et al., 2012)) should be used to confirm those preliminary observations.

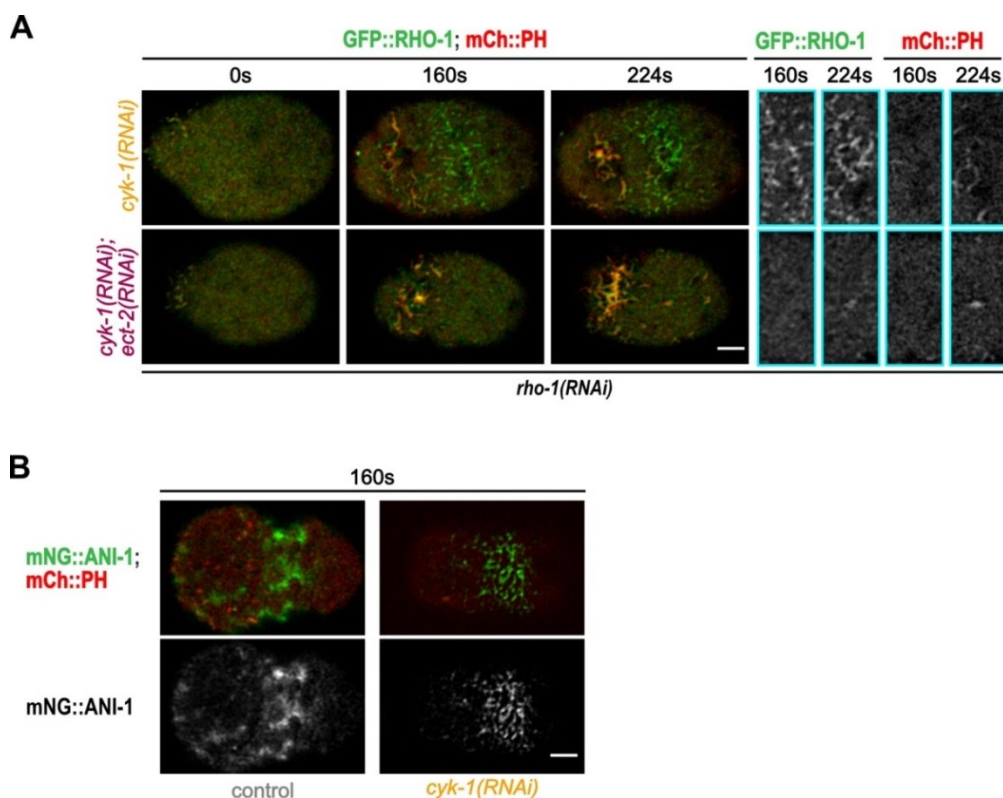


**Figure 32: Equatorial GFP::RHO-1 foci in *cyk-1(RNAi)* embryos represent active RHO-1.** (A) Representative cortical confocal time-lapse images of one-cell embryos expressing GFP::RHO-1 and mCh::PH after *cyk-1(RNAi)* (yellow; n=10) or *cyk-1(RNAi);ect-2(RNAi)* double (purple; n=6) for indicated time points. Time represents seconds after NEBD. Insets highlight equatorial region for GFP::RHO-1 and mCh::PH 160 s and 224 s after NEBD. (B) Representative cortical confocal time-lapse images of embryos expressing mNG::ANI-1 and mCh::PH, 160 s after NEBD, in the presence (control; gray; n=6) and after depletion of CYK-1 by RNAi (yellow; n=3). Scale bars=5  $\mu$ m.

### 3.3.4.4 Formation of GFP::RHO-1 filamentous foci at the equator is dependent on anillin

Anillin binds F-actin, myosin, RHO-1 and MgcRacGAP/CYK-4 and is therefore thought to act as a scaffold protein (Field and Alberts, 1995; Piekny and Glotzer, 2008; Straight et al., 2005). Anillin stabilizes the contractile ring in human and *Drosophila* cells (Somma et al., 2002; Oegema et al., 2000; Straight et al., 2005). In *C. elegans* however, it has been shown that the contractile ring in one-cell embryos can still ingress, even in the absence of anillin, yet leads to a symmetric ingression of the furrow (Maddox et al., 2007). A complex of anillin and MgcRacGAP (RacGAP50 in *Drosophila*) was described in *Drosophila* (Gregory et al., 2008; D'Avino et al., 2008), and another study in human cells proposed that anillin forms a complex with Ect2 (Frenette et al., 2012). If anillin indeed stabilizes the complex of Ect2-MgcRacGAP at the equatorial cortex, and this complex further activates

RhoA, then depleting anillin could result in the loss of RhoA from the PM. In addition, anillin was shown to promote RhoA activation by stabilizing and maintaining active RhoA at the cell equator by direct RhoA binding (Budnar et al., 2019; Piekny and Glotzer, 2008). To analyze the role of anillin in RHO-1 dynamics, ANI-1 was depleted by RNAi in the strain expressing GFP::RHO-1 and GFP::RHO-1 localization was followed by live-cell imaging.

Depletion of ANI-1 by RNAi in the strain expressing GFP::RHO-1, in the presence of endogenous RHO-1, showed no failure of first cell division (n=5) as described before (Maddox et al., 2007). However, co-depletion of endogenous RHO-1 together with ANI-1 in the strain expressing GFP::RHO-1, led to first division failure of the one-cell embryo and preliminary data (n=3) showed a reduction of the dense meshwork of GFP::RHO-1 at the equatorial membrane (Figure 33). Next, partial depletion of ANI-1 was performed with a condition where early embryos completed first division, however the dense meshwork of GFP::RHO-1 was still reduced (n=4). This suggested that indeed anillin might stabilize RHO-1 at the equator. Anillin could either be involved in direct RHO-1 activation by linking the complex of Ect2-MgcRacGAP with RHO-1 or by binding and stabilizing active RHO-1. However, the question arises why anillin depletion in the strain expressing GFP::RHO-1 leads to cytokinesis defects only when endogenous RHO-1 is depleted. One possibility is that the GFP-tag of RHO-1 affects the interaction of RHO-1 and anillin. If the strain expressing GFP::RHO-1 already shows impaired binding capacity for anillin, than further depletion of anillin by RNAi could enhance this effect. This would suggest that the interaction between anillin and RHO-1 is essential for successful cytokinesis also in *C. elegans* and that previous studies depleting ANI-1 by RNAi did not deplete the protein completely and thus remained some residual ANI-1 function.



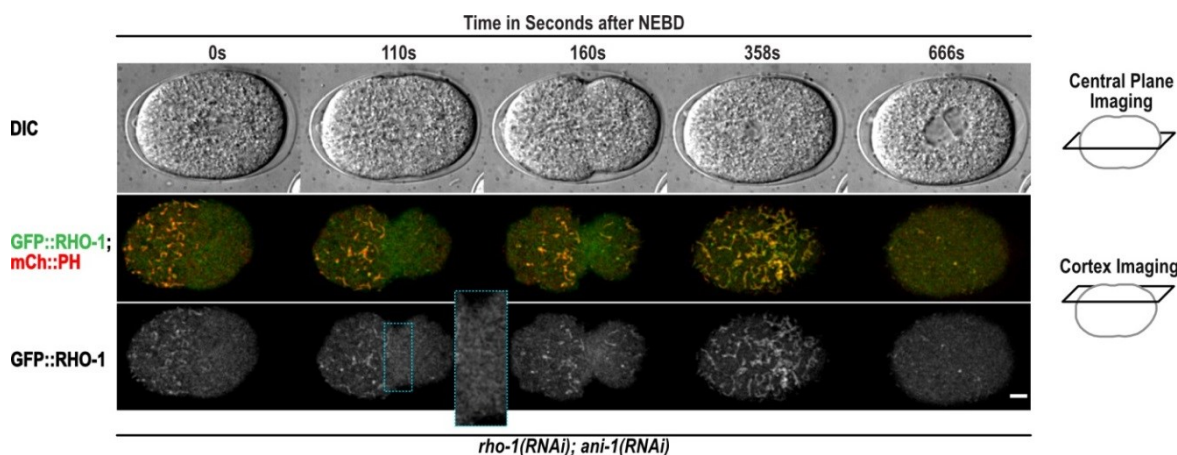


**Figure 33: Depletion of anillin reduces GFP::RHO-1 filamentous-like structures at the equator and embryos fail first division.** Representative one-cell embryo expressing GFP::RHO-1 and mCh::PH in the absence of endogenous RHO-1 and ANI-1. Central plane is shown for DIC (upper panel), cortical plane is shown as a merge for GFP::RHO-1 and mCh::PH (middle) and GFP::RHO-1 only (lower panel). One-cell embryos depleted of RHO-1 and ANI-1 (strong depletion) fail cytokinesis and RHO-1 meshwork formation is reduced at the equatorial membrane (n=3) as indicated by the inset (blue box, lower panel). Time represents seconds after NEBD. Scale bar=5  $\mu$ m.

### 3.3.4.5 Myosin II and ring constriction are not required for dense RHO-1 meshwork formation at the equator

In the absence of CYK-1 formin-induced F-actin, GFP::RHO-1 no longer formed filamentous-like structures at the equator and the contractile ring failed to ingress. In the absence of NMY-2, similar to the absence of CYK-1, ring ingression is inhibited resulting in cytokinesis failure (Maddox et al., 2005). If GFP::RHO-1 meshwork formation is a direct consequence of formin-induced F-actin polymerization, I would expect the GFP::RHO-1 meshwork still to be present in the absence of NMY-2. However, if meshwork formation is a consequence of F-actin dependent force formation or ring ingression, then the GFP::RHO-1 meshwork would be absent in NMY-2 depleted embryos. To test this, NMY-2 was knocked-down by RNAi and live-cell imaging of GFP::RHO-1, line-scan- and structure analysis were performed.

Depletion of NMY-2 resulted in first division failure as expected, however a GFP::RHO-1 zone was formed 160 s after NEBD comparable to control and the intensity increased over time (224 s) (Figure 34 A, B), suggesting that the contractile ring assembled but ring ingression was inhibited due to the absence of NMY-2. Next, structure analysis was performed and the perimeter and circularity of segmented foci were compared for control

and *nmy-2(RNAi)* embryos as described in 3.3.2.4. There was no difference detected for both characteristics in *nmy-2(RNAi)* in comparison to control embryos. This indicated, that indeed formin-induced F-actin polymerization was required for GFP::RHO-1 meshwork formation at the equatorial membrane and that this was not a consequence of failure in ring ingression. Further, these results showed that NMY-2 neither contributes to GFP::RHO-1 accumulation into a RHO-1 zone nor to the formation of a dense meshwork at the equatorial membrane.

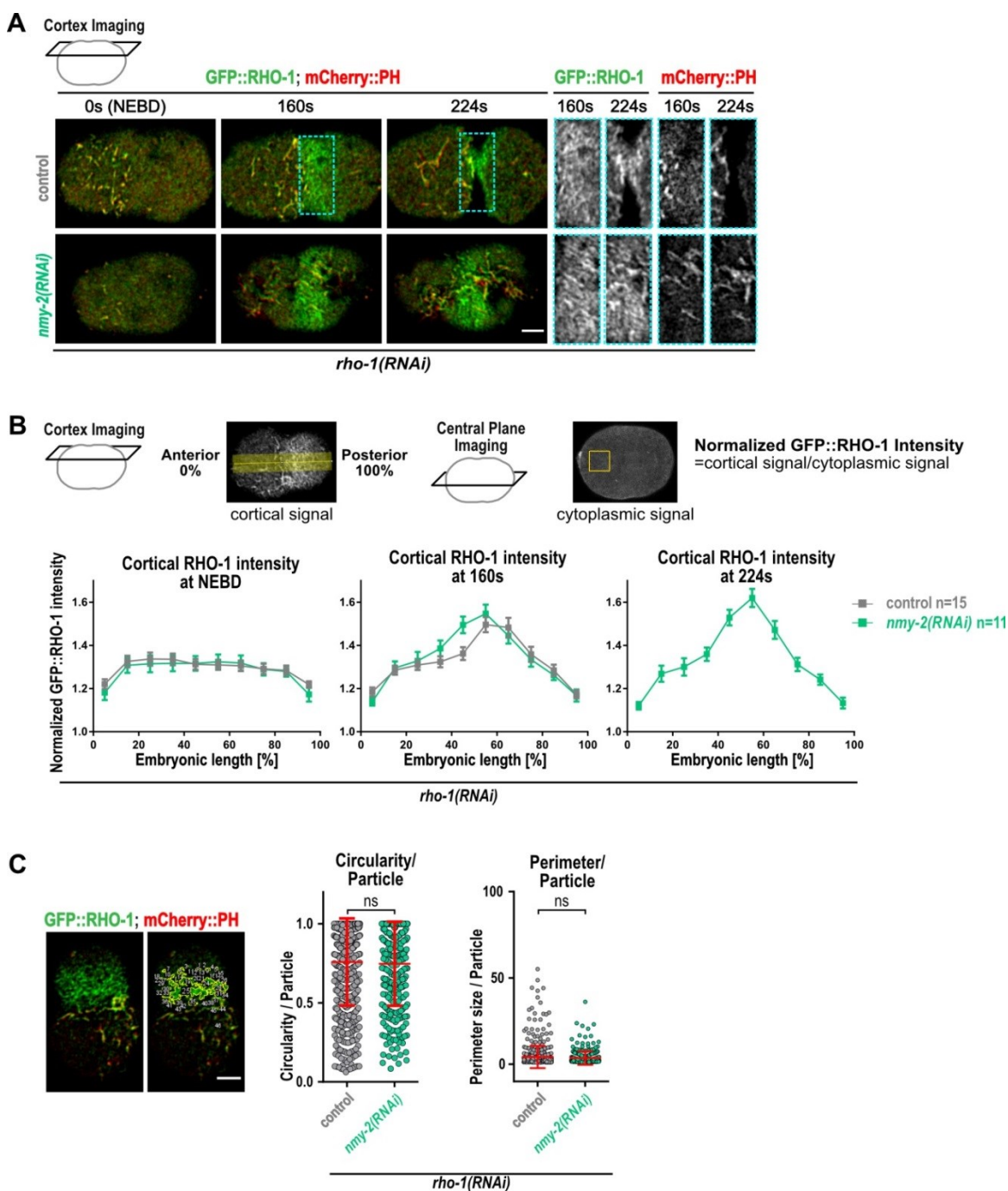


**Figure 34: Myosin II and ring constriction are not required for dense GFP::RHO-1 meshwork formation at the equator.** (A) Cortical confocal time-lapse images representing

embryos expressing GFP::RHO-1 and mCherry::PH in the presence (control; reproduced from Figure 30 A) and absence of NMY-2 at indicated time points relative to NEBD. Insets highlight equatorial region for GFP::RHO-1 and mCh::PH signal 160 s and 224 s after NEBD. **(B)** Line-scan analysis was performed at cortical images for control (gray) and *nmy-2(RNAi)* embryos (turquoise) at indicated time points. Cortical intensity was normalized to cytoplasmic signal determined from central plane images. Error bars are SEM, n=number of embryos analyzed. **(C)** Structure analysis was performed 160 s after NEBD on the same cortical images used in (B). Only PH-negative, active GFP::RHO-1 segmented particles were analyzed for circularity and perimeter using 'Particle Analyzer' in Fiji for control (gray; n=15; reproduced from Figure 23 B) and *nmy-2(RNAi)* (turquoise; n=11) embryos. Error bars are SD. P-values were determined by Mann-Whitney-U test (ns=not significant). Scale bars=5  $\mu$ m.

### **3.3.4.6 Are GFP::RHO-1 filamentous-like structures at the equatorial membrane a consequence of a dense F-actin meshwork?**

In the absence of the formin CYK-1, GFP::RHO-1 localized into dot-like clusters at the equatorial membrane that were ECT-2 dependent. ECT-2 activation of RHO-1 at the equatorial membrane leads to formin-induced F-actin polymerization and thus to a dense F-actin network at the equator. I tested the hypothesis, whether a dense mesh of F-actin could lead to the confinement of GFP::RHO-1 resulting in the observed filamentous-like structures. This was tested by two different approaches: (1) performing FRAP experiments to test whether RHO-1 mobility properties were changed relative to F-actin density and (2) by performing high-time resolution imaging to compare RHO-1 and F-actin dynamics.

#### **3.3.4.6.1 FRAP experiments to test whether F-actin restricts RHO-1 mobility at the equatorial cortex**

Protein dynamics can be followed by bleaching a defined region of interest and analyzing the recovery of the fluorescent signal, representing the mobility of the molecules. FRAP curves of membrane proteins consider three different types of mobility in the cell: (1) cytoplasmic diffusion, (2) lateral diffusion along the membrane and (3) exchange between the cytoplasm and the PM (Goehring et al., 2010) (Figure 35 A). FRAP experiments were performed at the cortex, therefore cytoplasmic diffusion was neglected. If RHO-1 was trapped by F-actin, reduced mobility would be expected at the cell equator where formin-induced F-actin density is high. To test this, recovery after photobleaching of a region within the RHO-1 zone (high F-actin density) was compared with a region outside the RHO-1 zone (low F-actin density) (Figure 35 B-D). The region outside the equatorial zone was bleached right after NEBD, at the anterior of the embryo, and the region within the equatorial zone was bleached once the RHO-1 zone was formed approximately 160 s

after NEBD. Comparison of the GFP::RHO-1 halftime of recovery ( $t_{1/2}$ ) for the two regions, showed slower recovery for higher F-actin density ( $3.5 \pm 0.76$  s) than for low F-actin density ( $2.05 \pm 0.26$  s) (Figure 35 D). This means that indeed the mobility of GFP::RHO-1 molecules within the RHO-1 zone is reduced, indicating that a dense F-actin mesh corals RHO-1 at the cell equator during cytokinesis. Thus, RHO-1 molecules are trapped within the F-actin network and the exchange with the cytoplasmic pool as well as by lateral diffusion along the PM is slowed down.

To specifically elucidate the influence on lateral diffusion within the PM, the bleached area at the anterior was analyzed by splitting it into two boxes; an outside and an inside box, as illustrated in Figure 35 E. In case of lateral diffusion, the recovery within the outside box would be faster compared to the inside box, indicating diffusion from the outside to the inside (Goehring et al., 2010). There was no difference in recovery curves for the outside and the inside box (Figure 35 E). This indicated, that with the settings used, the influence of lateral diffusion could not be distinguished from turnover of GFP::RHO-1 molecules travelling between the cytoplasm and the PM.

In summary, the experiments performed indicate that indeed a higher density of F-actin reduces GFP::RHO-1 mobility, resulting in slower recovery rates. However, whether F-actin influences RHO-1 lateral diffusion behavior within the PM could not be answered with these FRAP experiments and needs further investigation. First, the FRAP parameters need to be optimized to be able to distinguish between lateral diffusion and on/off rate for GFP::RHO-1 molecules within the anterior region. As a reference the PH marker can be used and experiments can be performed as previously shown by Goehring (Goehring et al., 2010). Once the correct parameters are found for the anterior region, the experiment should be performed at the equator, to test whether lateral diffusion is reduced by a dense F-actin mesh. Next, these results should be compared with lateral diffusion of GFP::RHO-1 within the RHO-1 zone of CYK-1 depleted embryos. If indeed F-actin restricts lateral diffusion of RHO-1, in the absence of CYK-1, lateral diffusion would be expected to be comparable to the anterior region with low formin-induced F-actin structures.

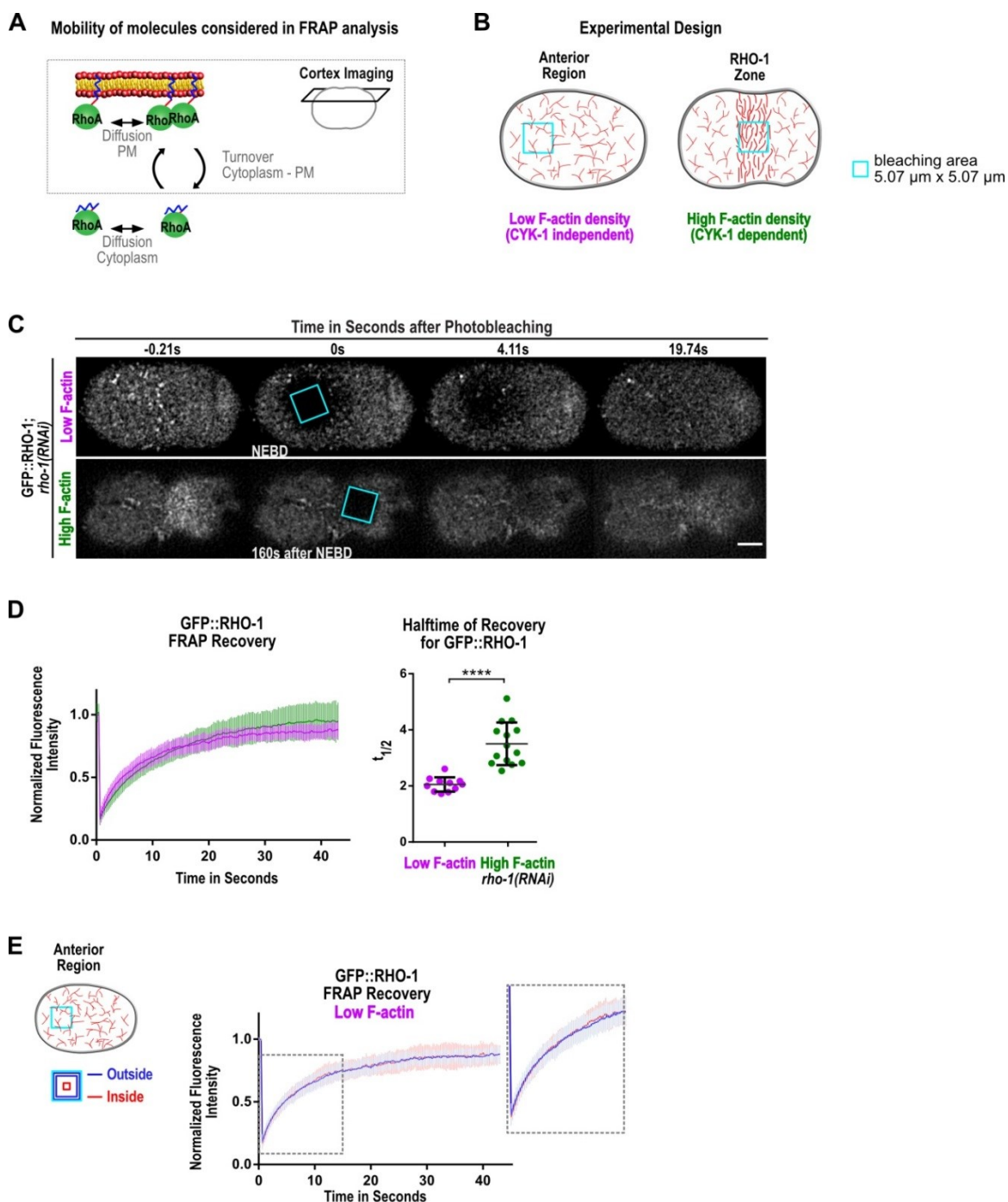


**Figure 35: FRAP experiments to test the influence of F-actin on GFP::RHO-1 mobility.** (A) Schematic showing mobility of molecules that contribute to the recovery of fluorescence in FRAP experiments: (1) Diffusion within the PM, (2) translocation from the cytoplasm to the PM and *vice versa* and (3) diffusion within the cytoplasm. (B) Schematic showing the experimental design to test the hypothesis, whether F-actin limits RHO-1 mobility at the equatorial cortex. Regions of low (anterior) and high (equator) F-actin density were bleached and analyzed. The low density region at the anterior was bleached right after NEBD; the high density region at the equator was bleached 160 s after NEBD, when a dense formin-induced F-actin mesh is present. (C) Representative cortical confocal FRAP time-lapse images of one-cell embryos expressing GFP::RHO-1 in the absence of endogenous RHO-1 for a region of low and high F-actin density as indicated. Time represents seconds relative to photobleaching (0 s). Bleaching area is shown in light blue. Scale bar=5  $\mu$ m. (D) FRAP recovery curves and halftime of recovery ( $t_{1/2}$ ) for GFP::RHO-1 for low (purple; pooled experiments from *rho-1(RNAi)* injected and non-injected

embryos as described in 2.2.14.8.1) and high (green; after *rho-1(RNAi)* injections) F-actin density regions. Error bars are SD. P-value was determined by Student's *t* test (\*\*\*\* $P < 0.0001$ ). **(E)** The anterior (low F-actin) bleaching area was analyzed by an outside (dark blue) and an inside box (red) as indicated ( $n=11$ ; pooled experiments from *rho-1(RNAi)* injected and non-injected embryos as described in 2.2.14.8.1). Inset highlights the first 15 s after photobleaching to compare recovery rates of the outside (blue curve) and the inside (red curve) box. There was no difference for the recovery curves detected, indicating that the contribution of on/off cycling vs. lateral diffusion of GFP::RHO-1 molecules could not be distinguished.

### **3.3.4.6.2 RHO-1 velocities are reduced at the equatorial cortex, a region of high F-actin density**

To further test the hypothesis that F-actin spatially restricts RHO-1 at the equatorial membrane, high-time resolution imaging of embryos expressing GFP::RHO-1 and LifeAct::RFP was performed. If F-actin corrals RHO-1 at the equatorial membrane, a reduced mobility of RHO-1 compared to a region with lower F-actin density would be expected (Figure 35 B). High-time resolution imaging was performed by acquiring an image every 2.75 s to follow RHO-1 and F-actin mobility. Dynamics were determined using PIV analysis, performed with the Fiji plugin 'PIV Analyzer' (Tseng and Duchemin, 2012). In brief, two consecutive time frame images were divided into the same sub-regions (interrogation windows) and cross-correlation was measured. This way, a vector field was generated providing information about displacement of objects within each sub-region. The magnitude of each vector represented the displacement or velocity measured for each position.

First, I tested whether RHO-1 and F-actin show different dynamics at the equator (high F-actin density) compared to an anterior region outside the RHO-1 zone (low F-actin density) (Figure 36 A). For each region (equator and anterior) six vectors were considered over a period of 15 time points, resulting in a total of 90 vectors analyzed per embryo (Figure 36 B, C). Velocity was categorized into six ranges of 10  $\mu\text{m}/\text{min}$  each, for a total range of 0-60  $\mu\text{m}/\text{min}$ . The analysis revealed, that GFP::RHO-1 and LifeAct::RFP showed similar velocity distributions. Interestingly, velocities at the equator (high F-actin density) were slower compared to the anterior region (low F-actin density). At the equator 80/90 GFP::RHO-1 vectors and 71/90 LifeAct::RFP vectors showed velocities between 0-10  $\mu\text{m}/\text{min}$ . At the anterior only 48/90 and 50/90 vectors had a velocity between 0-10  $\mu\text{m}/\text{min}$  for GFP::RHO-1 and LifeAct::RFP, respectively. The remaining categories ( $>10 \mu\text{m}/\text{min}$ ) showed two-fold higher numbers of vectors for the anterior- compared to the equatorial region. This result indicated that RHO-1 mobility is proportional to F-actin

density. Low F-actin density resulted in faster RHO-1 velocities at the anterior, while RHO-1 velocity at the equator, a region with higher F-actin accumulation, was reduced. This indicated that indeed the F-actin meshwork beneath the PM restricts RHO-1 mobility at the equator during cytokinesis.

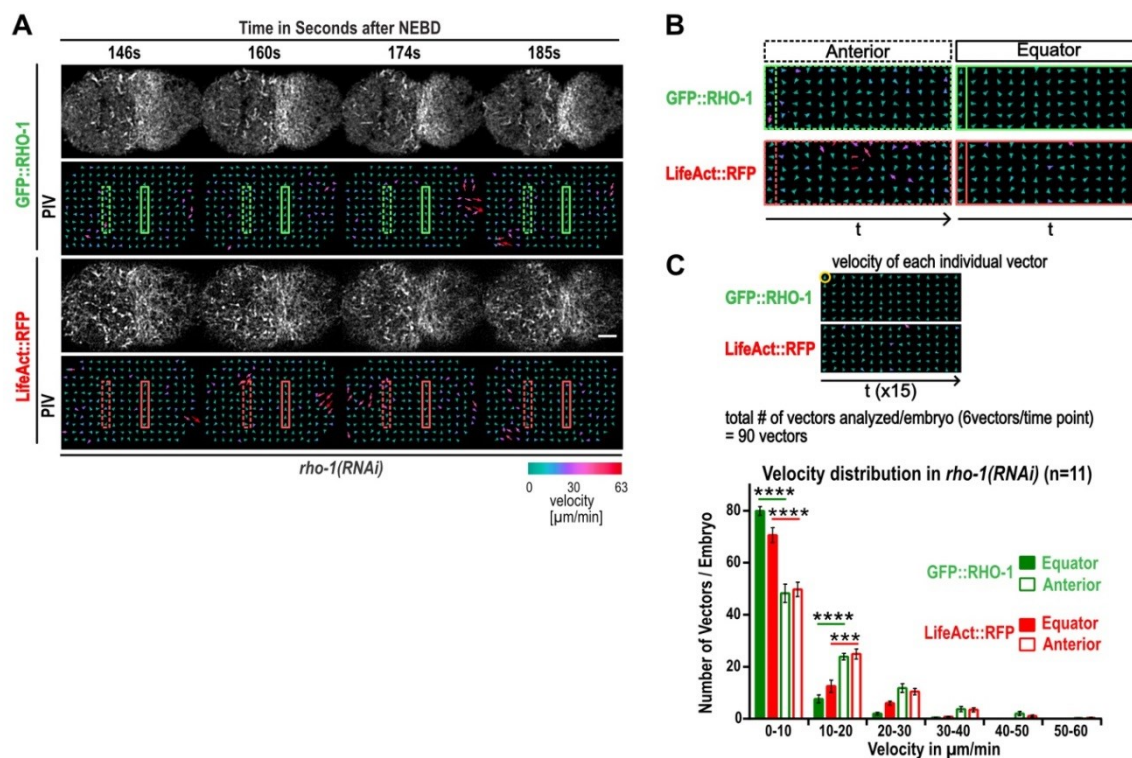


**Figure 36: GFP::RHO-1 and F-actin dynamics are reduced at the equatorial cortex.** (A) Representative cortical confocal high-time resolution images of a one-cell embryo expressing GFP::RHO-1 (green) and LifeAct::RFP (red) at indicated time points, relative to NEBD. PIV vector fields were generated using ‘PIV Analyzer’ in Fiji. For analysis two regions were used including six vectors each highlighted and shown for anterior (dashed box) and equator (solid box). Vectors are color-coded referring to velocity in μm/min as shown in the scale legend. (B) Kymographs for the anterior (dashed) and equatorial region (solid) for GFP::RHO-1 (green) and LifeAct::RFP (red) vector fields for 15 time points from 146 s to 185 s (time interval=2.75 s). (C) Schematic showing velocity distribution analysis. For each vector, within the anterior and equatorial region, the velocity was determined for GFP::RHO 1 (green) and LifeAct::RFP (red). For each region 6 vectors/embryo and time point were analyzed resulting in a total of 90 vectors/embryo, which is plotted against 6 velocity ranges of 10 μm/min each (total range of 0 μm/min-60 μm/min). Error bars are SEM; n=number of embryos analyzed. P-values were determined by Student’s *t* test (\*\*\*P<0.001, \*\*\*\*P<0.0001). Scale bar=5 μm.

Overall, velocity distribution of RHO-1 and F-actin were similar in both, the equatorial and anterior region. Next, the correlation of single vectors for GFP::RHO-1 and LifeAct::RFP was determined at the same positions and time points, to test whether RHO-1 and F-actin displacement: (1) occurred with similar velocity and (2) into similar direction. Velocity correlation was measured by Pearson’s Correlation Coefficient ( $\rho$ ) for all 90 vectors per

embryo (n=11). Individual correlation of the velocity of each vector pair (GFP::RHO-1 vs. LifeAct::RFP) is plotted in Figure 37 A for the anterior and equatorial region, showing only mild correlation between velocities of GFP::RHO-1 and LifeAct::RFP ( $\rho=0.19$ ). Similarly, the correlation between the directions of displacement was determined. Therefore, the angle between the vectors for GFP::RHO-1 and LifeAct::RFP was measured. Small angles represent movement into a similar direction, whereas angles close to  $180^\circ$  represent opposing movement. Mean % of vectors per embryo was plotted for angle ranges of  $30^\circ$ -intervals, within a total range of  $0$ - $180^\circ$ . More than one third of the population showed angles between  $0$ - $30^\circ$  at the equator, the remaining were distributed over other categories (Figure 37 B). At the anterior, angle distribution was more even, showing less % of vectors in the first category of  $0$ - $30^\circ$ , compared to the equatorial region ( $29.6 \pm 6.3\%$  and  $36.5 \pm 6.2\%$ , respectively). In summary, GFP::RHO-1 and LifeAct::RFP showed only mild correlation between the direction of movement and their velocities.

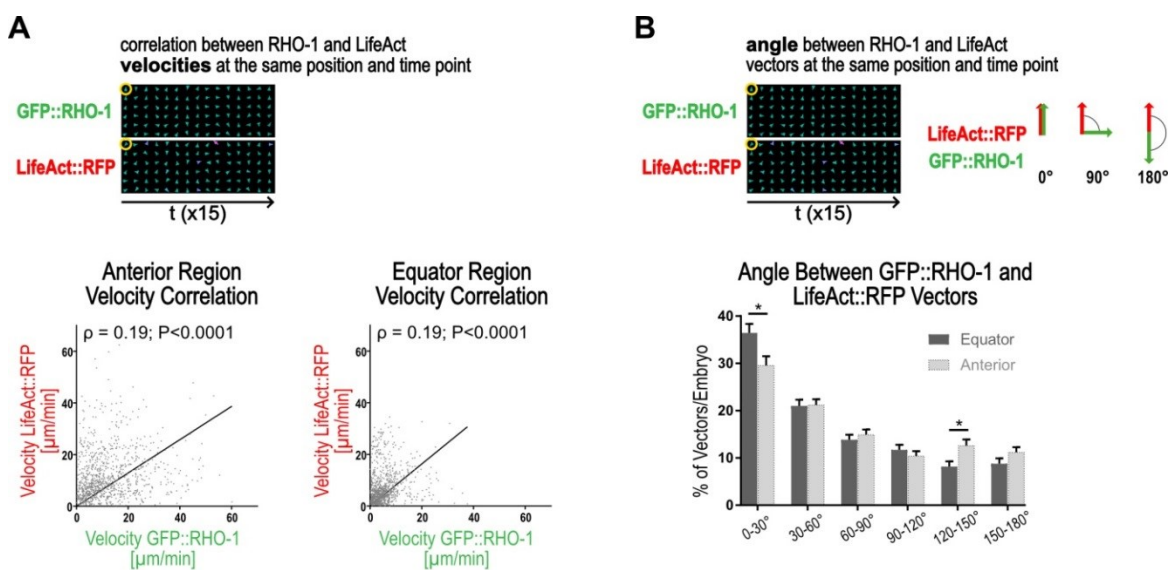


**Figure 37: Movement of GFP::RHO-1 and F-actin occur in similar directions with low correlation in velocity.** (A) Schematic representing velocity correlation analysis for GFP::RHO-1 and LifeAct::RFP, at the same position and time point, using PIV analysis of cortical high-time resolution images shown in Figure 36 A, B. The velocity of each vector at position  $x/y$  for GFP::RHO-1 (green) is compared to the velocity of the same position for LifeAct::RFP (red), for anterior and equator, for 15 time points. The correlation is plotted separately for both regions including all data points. Correlation was measured by Pearson's Correlation Coefficient ( $\rho$ ). P-values were determined by Student's  $t$  test. (B) Schematic representing correlation of angles between vectors for GFP::RHO-1 and LifeAct::RFP on the same dataset as described in (A). Small angles ( $0^\circ$ ) represent similar direction of movement whereas angles close to  $180^\circ$  represent opposite direction. For each position in  $x/y$  the angle between the vector for GFP::RHO-1 and LifeAct::RFP was determined and the mean % of vectors/embryo was plotted in ranges of  $30^\circ$  (for a total of  $0^\circ$  to  $180^\circ$ ). Error bars are SEM. P-values were determined using Student's  $t$  test (\* $P < 0.05$ ).



### 3.3.4.7 Reduced RHO-1 velocities at the equator are driven by formin-induced F-actin polymerization

PIV analysis revealed reduced velocities for GFP::RHO-1 at the equator, a region with high F-actin density, compared to an outside region with lower F-actin density. Reduced velocities at the equator indicate that RHO-1 mobility is restricted, which could be facilitated by the actin cytoskeleton following the hypothesis of the ‘membrane-skeleton picket fence model’ (Sheetz, 1983). To test whether formin-induced F-actin facilitates reduced velocities, high-time resolution imaging was performed in the absence of CYK-1, followed by PIV analysis and velocity distribution was determined for the anterior and equatorial region as described in 3.3.4.6.2. For control, the main population of GFP::RHO-1 vectors per embryo (80/90) showed reduced velocities of 0-10  $\mu\text{m}/\text{min}$  at the equatorial region compared to the anterior region (Figure 36). Interestingly in the absence of CYK-1, velocities at the equator were increased compared to control and there was no difference between velocities of vectors within the equatorial compared to the anterior region (Figure 38). This result indicated that indeed formin-induced F-actin at the equatorial cortex slows down RHO-1 dynamics, which could be facilitated by a corralling mechanism where RHO-1 is trapped by F-actin.

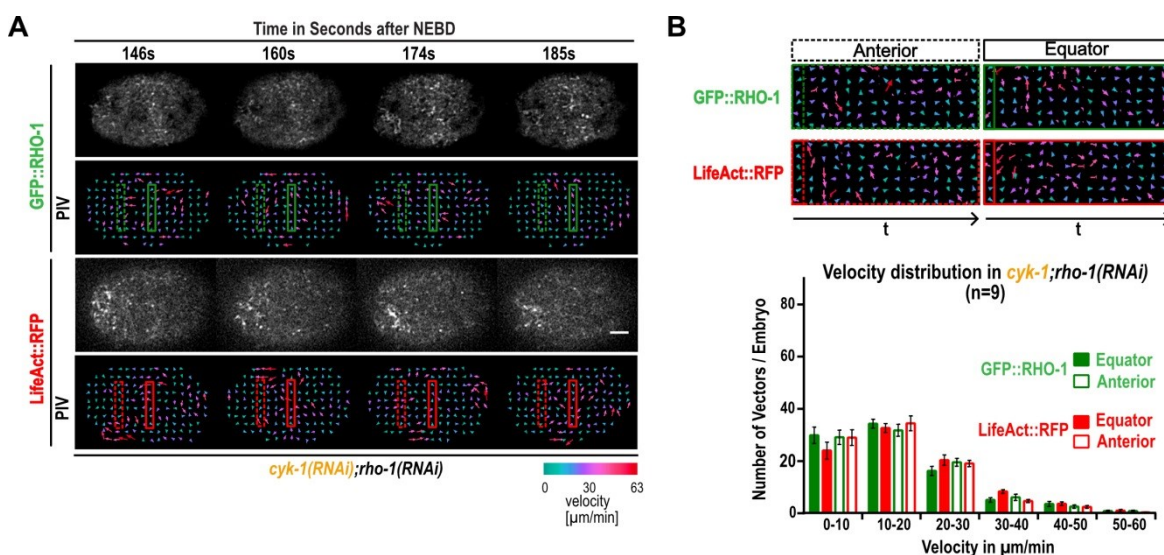


**Figure 38: Reduced GFP::RHO-1 velocity at the equator is dependent on formin-induced F-actin polymerization.** (A) Representative cortical confocal high-time resolution images of a one-cell embryo expressing GFP::RHO-1 and LifeAct::RFP, in the absence of CYK-1, at the indicated time points relative to NEBD. Vector fields were generated using ‘PIV Analyzer’ in Fiji. Anterior (dashed box) and equatorial (solid box) regions used for analysis are highlighted for GFP::RHO-1 (green) and LifeAct::RFP (red). Scale bar=5  $\mu\text{m}$ . (B) Kymographs of anterior (dashed) and equatorial (solid) regions for GFP::RHO-1 and LifeAct::RFP including 6 vectors each for 15 time points. 90 vectors/embryo were analyzed for their velocities (6 vectors/region for 15 time points) and mean number of vectors/embryo was plotted against velocity ranges of 10  $\mu\text{m}/\text{min}$  of a total range between 0  $\mu\text{m}/\text{min}$  to 60  $\mu\text{m}/\text{min}$  for GFP::RHO-1 (green) and

LifeAct::RFP (red) for the anterior and equatorial region. Error bars are SD; n=number of embryos analyzed.

### **3.3.4.8 Reduced RHO-1 velocities at the equator are independent of myosin II and ring constriction**

In the absence of CYK-1, embryos failed to form a contractile ring and consequently failed ring ingression and cytokinesis. To exclude the possibility that loss of contractility and constriction lead to the increase in GFP::RHO-1 mobility at the equator, live-cell imaging and PIV analysis was performed in one-cell embryos depleted of MNY-2 as described in 3.3.4.6.2. After depletion of NMY-2 by RNAi, GFP::RHO-1 and F-actin still localized into the equatorial band and thus formed the contractile ring without constriction (Figure 39 A). PIV analysis showed that, in the absence of NMY-2, velocity distribution was not altered between control and *nmy-2(RNAi)* embryos (Figure 36 C and Figure 39 B), strengthening the hypothesis that F-actin, and not ring ingression, slows down RHO-1 dynamics at the equator. Controversial to our finding that there is no difference in the velocity distribution for control and *nmy-2(RNAi)* embryos, it was shown that motor-dead myosin II reduces F-actin velocities in *C. elegans* one-cell embryos (Chan et al., 2018). However, this study differentiated lower velocities of 0-15  $\mu\text{m}/\text{min}$  in total. Therefore, I also split the smallest interval of 0-10  $\mu\text{m}/\text{min}$  in ranges of 2 and compared velocities of GFP::RHO-1 and LifeAct::RFP in control and *nmy-2(RNAi)* embryos. Indeed, F-actin flows were significantly reduced in the absence of NMY-2 at the equator and the anterior (Figure 39 C). However, GFP::RHO-1 velocity was only reduced at the anterior region after NMY-2 depletion.

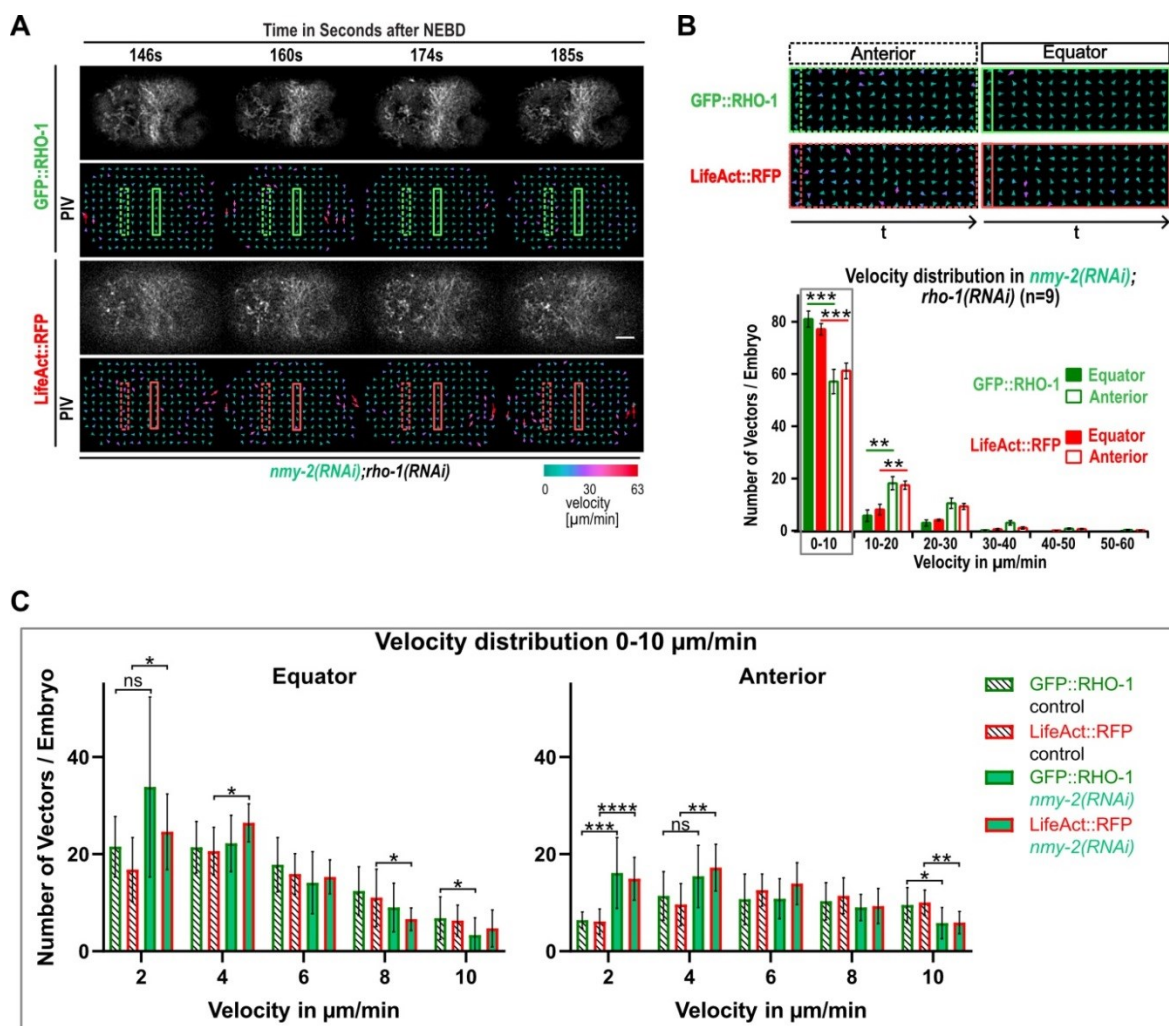


**Figure 39: Reduced GFP::RHO-1 velocity at the equator is independent of NMY-2 and ring constriction.** (A) Representative high-time cortical confocal images of a one-cell embryo expressing GFP::RHO-1 and LifeAct::RFP after NMY-2 RNAi at time points indicated. Time is represented in seconds after NEBD. PIV vector fields were generated using ‘PIV Analyzer’ in Fiji. Vectors are color-coded representing different velocities as indicated by the scale. Anterior (dashed boxes) and equatorial (solid boxes) highlight regions analyzed. Scale bar=5  $\mu\text{m}$ . (B) Kymographs of anterior and equatorial region highlighted in (A) for 15 time points (146 s-185 s; time interval 2.75 s). 90 vectors/embryo were analyzed for their velocities (6 vectors/region for 15 time points) and mean number of vectors/embryo was plotted against velocity ranges of 10  $\mu\text{m}/\text{min}$  of a total range between 0  $\mu\text{m}/\text{min}$  to 60  $\mu\text{m}/\text{min}$  for GFP::RHO-1 (green) and LifeAct::RFP (red) for the anterior and equatorial region. Error bars are SD; n=number of embryos analyzed. P-values were determined by Student’s *t* test (\*\* $P<0.01$ , \*\*\* $P<0.001$ ). (C) Higher magnification of the velocity distribution regarding 0-10  $\mu\text{m}/\text{min}$  for GFP::RHO-1 (green) and LifeAct::RFP (red) in control (black stripes; n=11; data from Figure 36) and *nmy-2(RNAi)* (turquoise; n=9) embryos at the equator and the anterior. Error bars are SD; P-values were determined by Student’s *t* test (ns=not significant; \* $P<0.05$ , \*\* $P<0.01$ , \*\*\* $P<0.001$ , \*\*\*\* $P<0.0001$ ).

### 3.3.4.9 Equatorial F-actin and RHO-1 partially co-localize

PIV analysis revealed similar velocity distributions for F-actin and RHO-1 at the equator as well as at an anterior region, indicating related movement along the PM. Next, I addressed the question whether similar velocities occur due to: (1) interaction of RHO-1 and F-actin or (2) F-actin confinement of RHO-1 into filamentous-like structures. If F-actin and RHO-1 show a direct interaction (or an indirect interaction via a linker protein), F-actin and RHO-1 co-localization would be expected at the equator. To test this, co-localization studies were performed in a strain expressing GFP::RHO-1 and LifeAct::RFP. As control a strain was used expressing LifeAct::RFP and the bona fide actin-binding protein plastin (PLST-1) fused to GFP (Ding et al., 2017). Previous work found that PLST-1 and F-actin co-localize with a Pearson's Coefficient of  $\rho=0.7$  (Ding et al., 2017). For co-localization analysis, confocal spinning disk time-lapse movies were used. Analysis was performed in Fiji at the time point of 160 s after NEBD. Filamentous-like structures were segmented. In brief, cytoplasmic mean signal was measured at the cortical plane and subsequently 90 % of the signal was subtracted for both LifeAct::RFP and GFP::RHO-1 channel. 'Gaussian Blur filter' and 'Unsharp Mask' were applied. Pearson's Coefficient was determined using the plugin 'Coloc2' in Fiji. Using this method, a correlation of  $\rho=0.6$  was determined for LifeAct::RFP and PLST-1::GFP, which is comparable to the correlation coefficient published (Ding et al., 2017). For GFP::RHO-1 and LifeAct::RFP the Pearson's correlation coefficient determined was  $\rho=0.35$ , suggesting only mild correlation (Figure 40). Therefore, RHO-1 and F-actin rather co-exist at the equator, indicating that F-actin confines RHO-1 not by interaction, but possibly by acting as a physical barrier. To test for specificity of the method, the F-actin channel was rotated 180° and the Pearson's Correlation Coefficient was determined again. For both, Plastin and RHO-1, F-actin randomization resulted in a Coefficient of  $\rho=0.1$ , indicating that the co-localization measured was specific. To test whether correlation of RHO-1 and F-actin is dependent on ring ingression, the same analysis was performed in the absence of NMY-2. There was no significant difference in the Pearson's Correlation Coefficient for RHO-1 and F-actin when NMY-2 was depleted by RNAi (Figure 40 B).

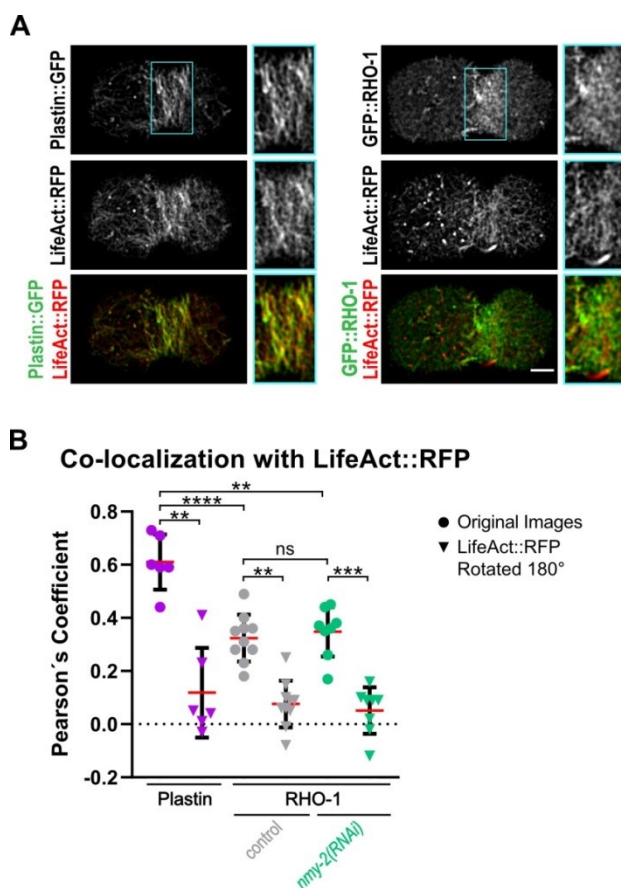


**Figure 40: Equatorial F-actin and GFP::RHO-1 only partially co-localize.** (A) Representative cortical confocal time-lapse images of a one-cell embryo expressing PLST-1::GFP (green) and LifeAct::RFP (red) (left) and a one-cell embryo expressing GFP::RHO-1 (green) and LifeAct::RFP (red) (right). Both embryos are shown 160 s after NEBD. Insets highlight the equatorial region, which was used for co-localization analysis in (B). Scale bar=5  $\mu\text{m}$ . (B) Co-localization was determined by Pearson's Coefficient, using 'Coloc2' in Fiji, for LifeAct::RFP with PLST-1::GFP (purple; n=6) or GFP::RHO-1. Random overlap was tested by rotating the F-actin channel 180° (triangles). Co-localization for RHO-1 and F-actin was tested for control (grey; n=10) and *nmy-2(RNAi)* (turquoise; n=8). Error bars are SD. P-values for GFP::RHO-1 were determined with Student's *t* test and for the remaining ones with Mann-Whitney-U test (ns=not significant, \*\*  $P < 0.01$ , \*\*\*  $P < 0.001$ , \*\*\*\*  $P < 0.0001$ ).

### 3.3.4.10 RHO-1 circumferentially aligns around the equatorial membrane following F-actin alignment

Co-localization studies revealed that F-actin and RHO-1 rather co-exist at the equatorial zone, indicating a rather indirect interaction of F-actin and RHO-1. This strengthens the hypothesis that RHO-1, localized to the PM, is confined by an F-actin mesh beneath the PM as proposed by the 'membrane-skeleton picket fence model' (Sheetz, 1983). F-actin circumferentially aligns around the cell equator and alignment promotes ring ingression (Spira and Cuylen, 2017; Henson et al., 2017; Reymann et al., 2016; Schroeder, 1968;

Fishkind and Wang, 1993). I found that also GFP::RHO-1 forms filamentous-like structures at the equatorial cortex. Consequently, I tested whether RHO-1 also aligns circumferentially around the cell equator in an anisotropic manner. High-time resolution live-cell images of embryos, co-expressing GFP::RHO-1 and LifeAct::RFP, were used and the direction of the observed filamentous-like structures at the equator was analyzed. Orientation of segmented equatorial structures was analyzed by the ‘directionality’ plugin provided in Fiji. Applying the method ‘local gradient orientation’ the plugin computes a histogram showing the amount of structures in respect to their direction. Orientation along the anterior posterior axes is represented by  $0^\circ$  whereas perpendicular alignment along the equator is represented by  $90^\circ$  (Figure 41 B). The results were plotted in a polar plot in R (<https://www.r-project.org>; R script was provided by Nikhil Mishra), where the amount of structures was plotted for given directions. Directions were ranging from  $0^\circ$ - $90^\circ$  and were subdivided into 45 bins. Therefore, random orientation was represented by 2.2 % as indicated in the polar plot by the blue arch (Figure 41 B). Directionality was determined for four different time points, between 97 s to 160 s after NEBD, in a defined region at the equator for LifeAct::RFP and GFP::RHO-1 from the same embryos (Figure 41 A). RHO-1 and F-actin structures were oriented in an isotropic manner 97 s and 119 s after NEBD when the contractile ring started to assemble. F-actin structures started to align along the equator 146 s after NEBD with increased mean frequencies for structures with directionality of  $70^\circ$ - $90^\circ$ . Interestingly, at the same time point GFP::RHO-1 still showed a random orientation with only slight tendency of alignment. Finally, 160 s after NEBD, LifeAct::RFP and GFP::RHO-1 were oriented in an anisotropic manner (Figure 41 B, C), indicating that also RHO-1 circumferentially aligns around the cell equator following F-actin alignment, strengthening the hypothesis of a corralling mechanism of F-actin towards RHO-1.

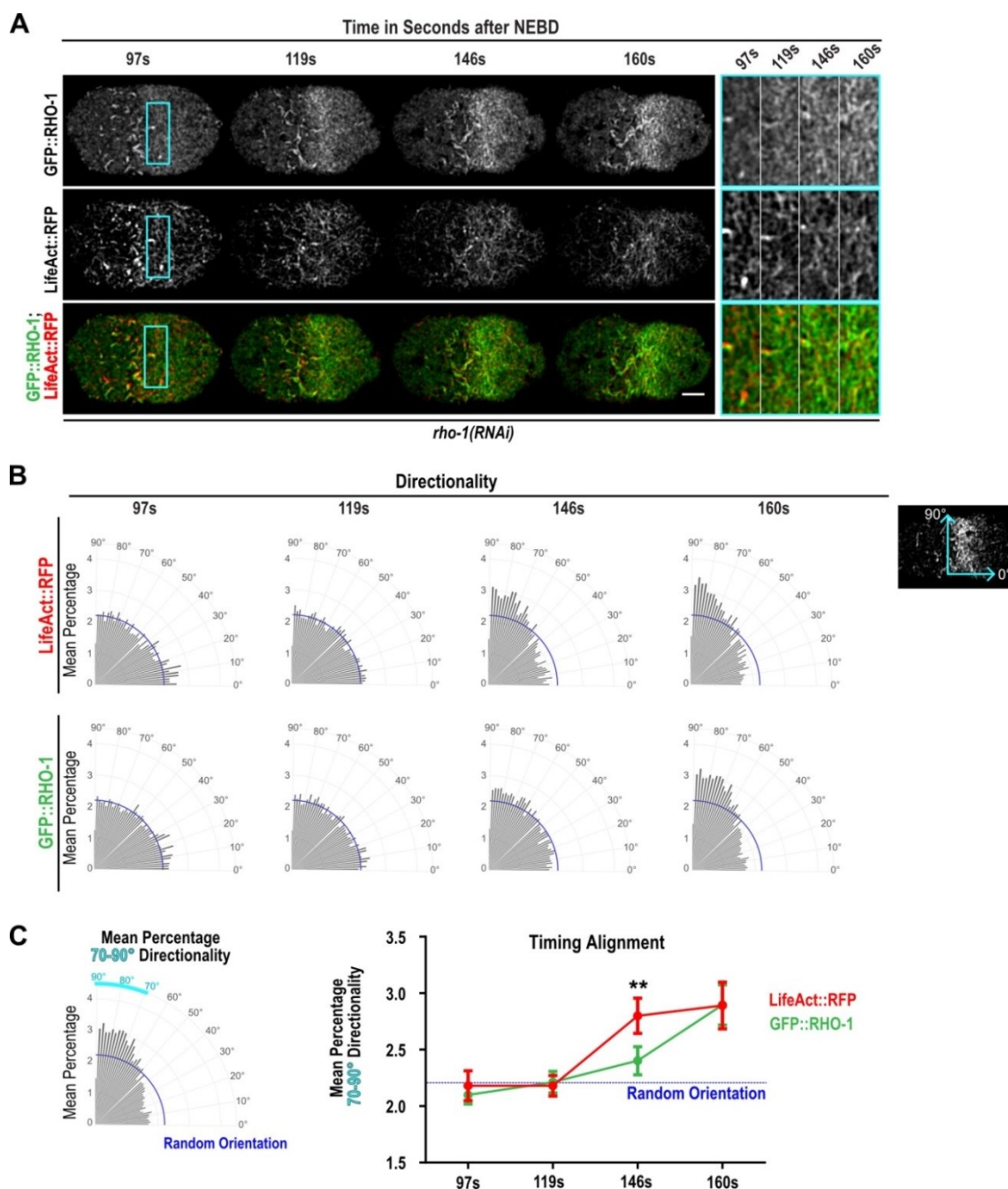


**Figure 41: GFP::RHO-1 circumferentially aligns around the equatorial cortex following F-actin alignment.** (A) Representative cortical high-time resolution images of a one-cell embryo expressing GFP::RHO-1 and LifeAct::RFP at indicated time points. Insets highlight the equatorial region that was used for directionality analysis. Scale bar=5  $\mu$ m. (B) Polar plots representing directionality of equatorial structures for LifeAct::RFP and GFP::RHO-1 at indicated time points (n=10 embryos). Data was generated using the 'directionality' plugin in Fiji. The dark blue arch represents random orientation at 2.2%. (C) Mean frequency of 70°-90° orientation was plotted over time, representing anisotropic alignment. Error bars are SEM. P-values were determined by Wilcoxon test (\*\*P<0.01). Time is seconds after NEBD.

## 4 Discussion

Cytokinesis is a complex process including several interconnected molecular mechanisms that control temporal and spatial regulation to ensure genetic inheritance into newly formed daughter cells (Green et al., 2012). This phenomenon in turn is crucial for life and therefore researchers put a lot of attention and effort into obtaining new insights in the field of cytokinesis in the last 40 to 50 years. While a lot of proteins and fundamental pathways involved in this process were identified, still many open questions remain (Eggert et al., 2006; Green et al., 2012; Pollard, 2017). The small GTPase RhoA was shown to be essential for cytokinesis (Kishi et al., 1993; Jantsch, 2000; Drechsel et al., 1997) and its local activation at the equator marks the position of furrow formation. The canonical model predicts that RhoA's activator Ect2, bound to centralspindlin, drives the local activation of RhoA by signals arising from the mitotic spindle (Yüce et al., 2005; Somers and Saint, 2003). RhoA is anchored to and is activated at the PM, and is thought to be able to diffuse within the PM. Considering a low intrinsic hydrolysis rate of PM-associated active RhoA (Zhang and Zheng, 1998a), RhoA would be assumed to diffuse away from the point of activation (Bement et al., 2006). However, what is observed during cytokinesis is a narrow zone of RhoA at the equatorial membrane (Bement and Benink, 2005; Piekny et al., 2005). Therefore, either diffusion of RhoA within the PM must be limited, and/or the inactivation of RhoA must be accelerated (Bement et al., 2006). How RhoA maintenance and restriction within a narrow zone is achieved during cytokinesis has remained elusive.

I addressed this question in the present work by testing the role of three putative mechanisms in contributing to narrow RhoA zone confinement: (1) increase of 'RhoA flux' by the GEF Ect2 and the GAPs (RGA-3 and RGA-4 in *C. elegans*), (2) interaction of RHO-1 with the lipids of the PM and (3) F-actin as a physical barrier beneath the PM.

### **Tools to visualize RHO-1 during cell division in *C. elegans***

RHO-1 is a small protein of 21.5 kDa and the addition of a fluorophore doubles its size. RhoA contains a phosphor-binding site, a switch one and a switch two region, which are all required for conformational changes to inactivate or activate the protein (Ihara et al., 1998). The addition of a fluorophore could lead to sterical hindrance, blocking effector binding sites or either of the regions required for RhoA regulation (Dvorsky and Ahmadian, 2004). To my knowledge, previous studies investigating RhoA dynamics were all performed in the presence of endogenous RhoA, and therefore the functionality of the



tagged RhoA could not be tested (Budnar et al., 2019; Michaelson et al., 2001; Abreu, 2014; Motegi and Sugimoto, 2006; Nakayama et al., 2009; Schonegg and Constantinescu, 2007; Yoshida et al., 2009). To obtain a fluorophore-tagged RHO-1 protein that is functional during cytokinesis in the one-cell embryo, I pursued multiple approaches. Tagging endogenous RHO-1 with a fluorophore by CRISPR/Cas9 led to sterile animals, consistent with previous findings where tagging RHO-1 impaired its function. However, I was able to establish a GFP::RHO-1 reporter using a genetic replacement system that was functional during the first cell division of the one-cell *C. elegans* embryo. However, this GFP::RHO-1 reporter impaired RHO-1 function during later embryonic development.

RhoA is not only required during cytokinesis, but also for other cellular and developmental processes. This could explain why embryos succeed during first divisions of the early embryo, however fail during later development. Alternatively, or in addition, the experimental setup could contribute to the observed finding. Depleting endogenous RHO-1 by RNAi is performed in the mother worm. The effect on the zygote is maternally inherited; therefore also maternal proteins are still present. Remaining maternal RHO-1 could support GFP::RHO-1 function in the one-cell embryo. Even though western blot analysis revealed that after *rho-1(RNAi)* endogenous RHO-1 levels were strongly reduced in worms expressing GFP::RHO-1, 15 % of analyzed control one-cell embryos completed cytokinesis after *rho-1(RNAi)*. This indicates that indeed some residual function of endogenous RHO-1 cannot be excluded.

RhoA was previously shown to localize into a narrow zone at the equator during cytokinesis in several organisms (Bement and Benink, 2005; Takaishi et al., 1995; Nishimura and Yonemura, 2006; Kamijo et al., 2006; Yüce et al., 2005; Yonemura and Hirao, 2004). Our GFP::RHO-1 reporter showed narrow RHO-1 zone formation at the equator during cytokinesis, and together with the functionality studies indicated physiological function and localization of RHO-1. The advantage of our reporter is that worms can be maintained in the presence of endogenous RHO-1, where they are fully viable. This was achieved by stably integrating transgenic RHO-1 into *C. elegans* genome, in addition to the endogenous locus. For experiments regarding RHO-1 dynamics studies, in the *C. elegans* one-cell embryo, endogenous RHO-1 can be depleted by RNAi injection and transgenic GFP::RHO-1 can be tracked, representing the first tool providing a functional GFP-tagged RHO-1 transgene for studies in the one-cell embryo.

Interestingly, GFP::RHO-1 was only visible at the equator in the absence of endogenous RHO-1, suggesting that the organism favored endogenous RHO-1 over the additional introduced GFP::RHO-1. This showed the importance of depleting endogenous RhoA, when using fluorescently-tagged exogenous RhoA reporters, which could explain the lack of RhoA localization to the equator for example in the study performed in 2001 by Michaelson (Michaelson et al., 2001).

Internally-tagged CDC42 was shown to be functional in *S. pombe* (Bendezú et al., 2015). The strategy was adopted also for RhoA in *X. laevis*, and the authors showed correct localization during wound repair and cytokinesis (Golding et al., 2019). However, functionality was only shown in the absence of endogenous RhoA for wound repair, but not for cytokinesis. In the present work, we adopted the internal-tagging approach (Bendezú et al., 2015), and used CRISPR/Cas9 to introduce sfGFP into *C. elegans* genome within the coding sequence of RHO-1. Consistent with the finding from Golding (Golding et al., 2019), also in *C. elegans* internally-tagged RHO-1 localized to the equatorial membrane during cytokinesis in heterozygous animals. However, homozygous animals were sterile, indicating that internally-tagged RHO-1 is not fully functional, yet sufficient for RHO-1 localization to the equator. In contrast, endogenous N- and C-terminal tagging of RHO-1 with mKate2 using CRISPR/Cas9 resulted in homozygous lethal animals and did not show any localization to the equator in heterozygous animals. This suggested that internal-tagging and/or the different fluorophore (sfGFP instead of mKate2) enables correct localization, yet compromises full functionality of RHO-1.

A published method to visualize RhoA *in vivo*, is the use of RhoA biosensors that are based on downstream effectors, only detecting active RhoA (Wagner and Glotzer, 2016; Bement and Benink, 2005; Piekny and Glotzer, 2008). Such biosensors consist of a RhoA binding site for anillin or rhotekin. While rhotekin fused to GFP was used in *X. laevis* (Bement and Benink, 2005), it was not applicable in *C. elegans* (Esther Zanin). The anillin-based biosensor (AH-PH) (Wagner and Glotzer, 2016; Piekny and Glotzer, 2008; Sun et al., 2015) contains not only the RhoA binding domain (RBD), but also two more C-terminal domains, C2 and PH. It was shown that the RBD, C2 and PH domain together show a synergistic effect of PM anchorage of anillin and that the individual domains were not sufficient to anchor anillin to the PM in human cells (Sun et al., 2015). The used AH-PH-biosensor spans about one third of anillin sequence (RBD, C2 and PH domain). The binding domain of anillin towards RhoA is not sufficient to be used as RhoA marker.

Thus, the AH-PH biosensor rather reflects anillin than active RhoA localization and therefore was not further analyzed in this thesis. Another advantage towards the RhoA biosensors is the fact that our GFP-tagged reporter represents a direct tool, which allows detecting inactive and active RHO-1.

In summary, as described in previous studies tagging RhoA with a fluorophore is not trivial (Yonemura and Hirao, 2004) and led to impaired function. However, we generated a tool, which is based on a genetic replacement system and can be used to study RHO-1 dynamics during cytokinesis in the one-cell *C. elegans* embryo.

### **Nanobody generation to follow active RhoA *in vivo***

One goal of this thesis was to generate a nanobody, a short peptide sequence, that specifically recognizes active RhoA, and that can be used for live-cell imaging by tagging with a fluorophore. In addition to our GFP::RHO-1 reporter, a nanobody against active RHO-1 would be advantageous to distinguish active from inactive RHO-1.

In collaboration with the company ChromoTek, we were able to isolate 12 sequence candidates showing specificity for *C. elegans* RHO-1-GDP and/or RHO-1-GTP *in vitro*. For 11 candidates the localization was analyzed in HeLa cells and for 3 candidates in *C. elegans*. However, for none of the candidates a specific PM localization was observed, suggesting that they do not bind RhoA/RHO-1 in living cells. The immune response in alpaca was induced by the *C. elegans* RHO-1 antigen. Even though human and *C. elegans* RhoA (and RHO-1) show 96 % similarity, the origin of the antigen could explain the lack of RhoA detection in HeLa cells using 11 of the sequences tested. Unfortunately, due to time restriction, I could only test three sequences in *C. elegans*, which showed no specificity for RHO-1 in the early *C. elegans* zygote in preliminary experiments. Due to time constraints, the transgenes were not stably integrated into the *C. elegans* genome but expressed from extrachromosomal arrays. Extrachromosomal arrays are often expressed highly variable in the different cell types and are also sometimes silenced. Thus, future work should express the nanobodies in *C. elegans* using the ubiquitous *pie-1* promoter and 3'UTR and stably integrate them into the genome by MosSCI method. In case, candidates show RHO-1-like localization pattern, one also has to demonstrate that endogenous RHO-1 is still fully functional during cell division and embryonic development. If RHO-1 function is compromised, one could change the promoter to optimize expression levels. As another future perspective the specificity of the received nanobodies should be characterized

*in vitro*. By performing pull-down assays, one has to test whether the nanobodies indeed preferentially bind GTP- but not GDP loaded RHO-1.

During my study, two other active RhoA nanobodies were established from a non-immune library (Moutel et al., 2016; Keller et al., 2019). In contrast, my approach was based on an immune library extracted from alpaca. In general an immune approach provides high affinity binders, however lower diversity compared to a non-immune library. The first sequence that was published, and was shown to be specific for active RhoA, could not be used as RhoA biosensor because it blocked RhoA function *in vivo* (Moutel et al., 2016). By screening the same library again, the authors found another RhoA-GTP specific nanobody, which was shown to not compete with the RBD binding domain (Keller et al., 2019). However, Keller and co-workers could not rule out the possibility of an influence of the chromobody on RhoA regulation, since GTP loaded levels were shown to be increased. Further, fusing the nanobody to a fluorophore did show recognition of PM-localized RhoA, however the signal to background ratio needs improvement to make the chromobody a usable tool. To overcome this problem, the authors used the nanobody sequence to build a Bioluminescence Resonance Energy Transfer (BRET)-biosensor that could be used as activation sensor (Keller et al., 2019). In summary, the nanobody sequences that were established cannot be used for my purpose, since the first sequence blocks RhoA function and the second established chromobody (1) might interfere with RhoA regulation and (2) cannot be used for live-cell dynamics studies due to low signal to background ratio. This further emphasizes to continue with the screening for the candidates that we generated together with the company ChromoTek.

### **GFP::RHO-1 is present in two distinct membrane associated pools during cell division**

Performing live-cell imaging of one-cell embryos expressing GFP::RHO-1 revealed that GFP::RHO-1 is present in two membrane pools during cytokinesis: (1) anterior patches and (2) an equatorial narrow zone of GFP::RHO-1, forming a dense meshwork of filamentous-like structures (Figure 42). To my knowledge, filamentous-like structures of endogenously regulated RHO-1, at the equatorial membrane, have not been described before. Several observations support the conclusion that their formation is not an artifact of the GFP-tag; (1) tagging RHO-1 with different fluorescent-tags (GFP, mCherry and sfGFP) and (2) introduction of the tags by different methods (MosSCI integration (N-terminal-tag) and CRISPR/Cas9 (internal-tag)) results in similar RHO-1 localization

patterns. In the future, it will be important to show that in control embryos endogenous RHO-1 localizes to filamentous-like structures by immunostainings.

While anterior patches showed co-localization with a membrane marker, there was no enrichment of the membrane marker visible at the equator. If the dense meshwork of GFP::RHO-1 was a consequence of ring ingression, I would have expected to see also an increase in the signal of the PM marker due to topological changes. However, there was no enriched signal of the PM marker, indicating that GFP::RHO-1 filamentous-like structures at the equator were formed independently of PM invagination effects. In contrast, patches at the anterior showed high co-localization with the membrane marker. Similar patches were described before for other Rho proteins including CDC-42 (Motegi and Sugimoto, 2006; Nakayama et al., 2009; Scholze et al., 2018). First, an interdependency of F-actin and PIP<sub>2</sub> structures was described (Motegi and Sugimoto, 2006). Later, these PM-localized structures were postulated to be filopodia-like structures, rather appearing as local enrichment due to membrane protrusions (Scholze et al., 2018). Thus, an enriched signal of proteins (such as RhoA, or Ect2), within these patches, represents PM-localized proteins that show an increase in signal as a consequence of membrane topology.

I further showed that membrane-targeting of RHO-1 by the two motifs, PBS and CAAX, are required for successful cytokinesis. In contrast to the (untagged) RHO-1 transgene, which rescued cytokinesis failure, (untagged) RHO-1 PM-targeting mutants did not. Further, in the absence of either of the two motifs, the PBS or CAAX, first cell division failed in the majority of embryos analyzed, indicating that PM anchorage of RHO-1 is a prerequisite for cytokinesis. The two motifs are sufficient to localize RHO-1 to the PM *per se*, which goes in line with previous findings (Michaelson et al., 2001). However, the PBS and CAAX together are not sufficient for equatorial enrichment during anaphase. I showed that only full-length GFP::RHO-1 is enriched at the cell equator in an ECT-2 dependent manner. These findings go in line with (1) the proposed model of local activation and recruitment of RhoA by Ect2, driven by cues from the mitotic spindle (Yüce et al., 2005; Somers and Saint, 2003) and (2) the hypothesis of PM-associated proteins forming filopodia-like structures at the anterior that rather reflect topological changes, due to membrane ruffling or protrusions (Scholze et al., 2018).

In summary, I hypothesize that RHO-1 is recruited to the PM in the one-cell embryo driven by the PBS and CAAX-motif. During cytokinesis the PBS and CAAX-motif are not sufficient to localize RHO-1 into a narrow zone at the equator; instead ECT-2 is required

for local recruitment and activation. Still, the two PM-targeting motifs, in addition to ECT-2 dependency, are a prerequisite for successful cytokinesis. In contrast, in *S. cerevisiae* the PBS of Rho1 is sufficient to localize Rho1 to the furrow site in the absence of the GEF (Yoshida et al., 2009). This further suggests that the interaction of RHO-1 with specific lipids in the PM does not contribute to the maintenance and confinement of RHO-1 into a narrow zone. However, an influence of lipids in regulating RHO-1 localization cannot be fully excluded, since the PBS and CAAX mutants did not localize to the PM.

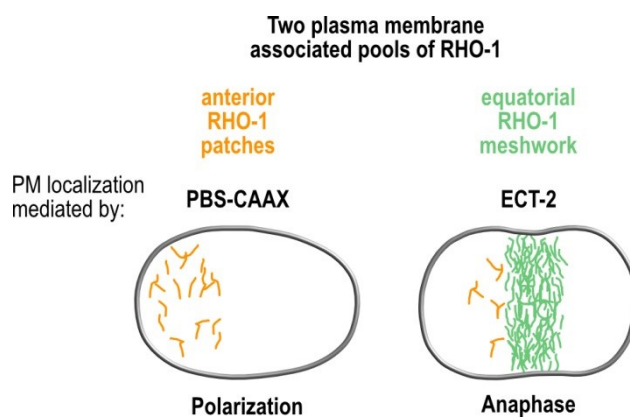


**Figure 42: GFP::RHO-1 is present in two distinct membrane associated pools during cell division.** During polarization and anaphase GFP::RHO-1 is present in anterior RHO-1 patches (orange) that co-localize with a membrane marker and that are independent of ECT-2. The localization to the PM is driven by the two PM-targeting motifs PBS and CAAX. During anaphase RHO-1 accumulates into filamentous-like structures (green) at the equatorial PM forming a dense RHO-1 meshwork.

### **RHO-1 zone width is restricted by an increased ‘RhoA flux’ mediated by the GAPs RGA-3 and RGA-4**

The ‘RhoA flux model’ was proposed by Bement and co-workers and describes a theoretical model of simultaneous activation and inactivation of RhoA by its regulators GEF and GAP (Bement et al., 2006). The accelerated inactivation by the GAP function was further proposed to contribute to the confinement of a narrow RhoA zone. A complex of Ect2 and MgcRacGAP was the basis for the ‘RhoA flux model’. The complex of Ect2 and MgcRacGAP in theory provides both properties for RhoA regulation: (1) activation by the GEF ECT-2 and (2) inactivation by the GAP MgcRacGAP. Therefore, complex formation of the two regulators could induce accelerated flux through the GTPase cycle. However, opposing findings were published concerning the function of MgcRacGAP (Canman et al., 2008; White and Glotzer, 2012). Therefore, MgcRacGAP is no longer

believed to be the GAP for RhoA during cytokinesis, but different proteins have been identified that inactivate RhoA during cytokinesis, namely MP-GAP in humans and RGA-3/4 in *C. elegans* (Zanin et al., 2013). In HeLa cells it was shown that MP-GAP depletion by RNAi only causes a wider RhoA zone in case the astral MTs are compromised (Zanin et al., 2013).

The two proteins RGA-3 and RGA-4 were shown to be the main GTPases for RHO-1 during cytokinesis in *C. elegans* (Zanin et al., 2013; Schmutz et al., 2007; Schonegg and Constantinescu, 2007). Therefore, RGA-3/4 are potential candidates to accelerate the ‘RhoA flux’, contributing to narrow RHO-1 zone maintenance. By depleting RGA-3/4 and following GFP::RHO-1 zone formation, I showed that RGA-3/4 indeed contributed to GFP::RHO-1 zone confinement, since a broader zone was observed in the absence of the two GAPs (Figure 43; *rga-3/4(RNAi)*). Further, GFP::RHO-1 zone formation was dependent on the GEF ECT-2, indicating that cycling between the active and inactive form of RHO-1 was required to form and confine a narrow zone as it was postulated by the ‘RhoA flux model’ (Figure 43) (Bement et al., 2006; Miller and Bement, 2009). In the future, those findings should be confirmed by analyzing the localization of (1) newly developed active RHO-1 sensors, (2) endogenous RHO-1 by immunostaining and (3) downstream targets of RHO-1 such as anillin and myosin.

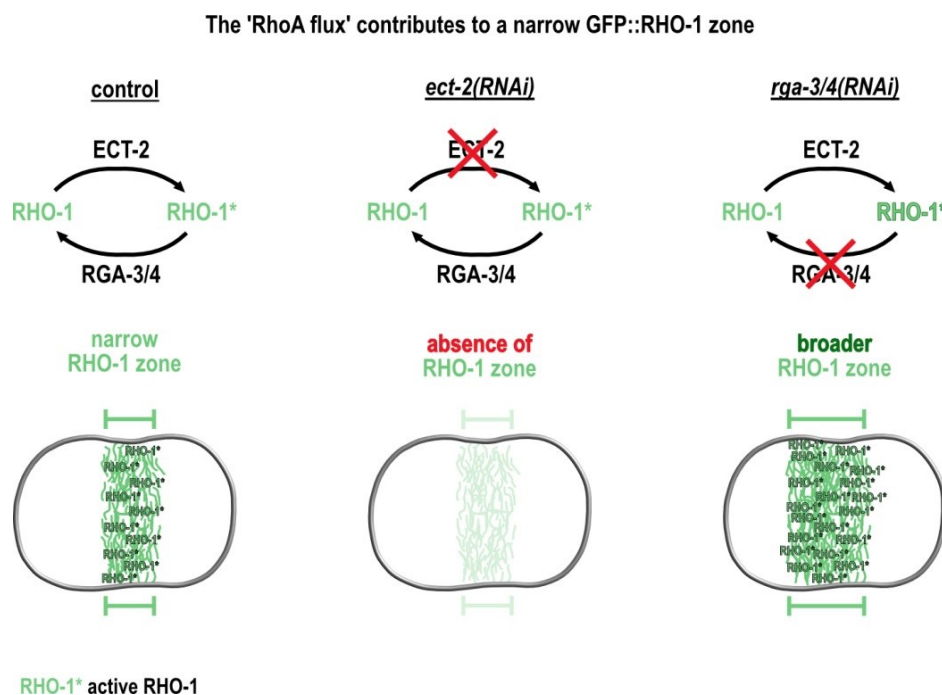


**Figure 43: The ‘RhoA flux’ contributes to a narrow GFP::RHO-1 zone.** In control embryos GFP::RHO-1 accumulates into a narrow zone at the equator. In *ect-2(RNAi)* embryos the GFP::RHO-1 zone is absent, indicating that equatorial GFP::RHO-1 is active. In *rga-3/4(RNAi)*

embryos the GFP::RHO-1 zone is broader, showing that inactivation of RHO-1 contributes to the restriction of a narrow RHO-1 zone.

The 'RhoA flux' contributes to the maintenance of an active narrow RHO-1 zone at the equatorial PM during cytokinesis. The canonical model predicts that activation and inactivation of RhoA, by the GEF and GAP, occurs at the PM. However, RhoA is also present in the cytoplasm and needs to be shuttled between the cytoplasm and the PM. Therefore, molecular mechanisms involved in trafficking RhoA to the PM and in sequestering RhoA from the PM potentially contribute to a narrow RhoA zone formation. RhoGDIs act as shuttles for small GTPases, mediating the translocation between the cytoplasm and the PM (Golding et al., 2019; Tnimov et al., 2012; Garcia, 2011). However, there is evidence that RhoGDIs are not the sole mechanism for small GTPases transport. Studies were performed, where RhoGDI-knock-out mice showed mild phenotypes and were viable (Togawa et al., 1999; Shibata et al., 2008). Further, in *S. cerevisiae* it was postulated that two different mechanisms can compensate for each other in terms of Cdc42 trafficking to the PM. Deletion of the RhoGDI did not show any growth phenotype in *S. cerevisiae* indicating that a second mechanism, which is based on vesicle transport, could mediate PM trafficking and compensate for lack of RhoGDI (Slaughter et al., 2009). It was shown that RhoGDI can bind inactive and active RhoA *in vitro* (Hart et al., 1992; Hancock and Hall, 1993; Tnimov et al., 2012), yet it is not known whether *in vivo* RhoGDI can sequester also active RhoA during cytokinesis. In *X. laevis* it was shown that RhoGDIs are able to bind inactive and active Cdc42 during wound repair, however active RhoA first needed to be inactivated before being removed from the PM by the RhoGDI (Golding et al., 2019). *C. elegans* harbors one RhoGDI named RHI-1. For the future it would be interesting to test, whether the RhoGDI, RHI-1, contributes to the formation and maintenance of the narrow RHO-1 zone during cytokinesis in *C. elegans*. If RHI-1 is an important independent regulator for RHO-1 in terms of trafficking to and off the PM, an effect in RHO-1 zone formation is expected in the absence of RHI-1 similar to the effect by GEF and GAPs depletion. If in *C. elegans* RHO-1 first needs to be inactivated by the GAPs, before being sequestered by the RhoGDI, as described for *X. laevis* during wound repair (Golding et al., 2019), then the contribution on RHO-1 zone formation and maintenance is expected to show a minor effect.



**Formin-induced F-actin at the equatorial cortex acts as a physical barrier beneath the PM that confines GFP::RHO-1 mobility**

Another possibility of RhoA zone restriction is a physical barrier that limits active RhoA mobility within the PM (Bement et al., 2006). The ‘membrane-skeleton picket fence model’ proposes that the actin cytoskeleton forms a meshwork beneath the PM that subdivides the membrane into compartments, where lateral diffusion of lipids and proteins within the PM is restricted, yet hop diffusion into an adjacent compartment is possible (Sheetz, 1983; Lee et al., 1993). While the actin cortex was shown to be present throughout the cell, F-actin density is increased at the equatorial region during cytokinesis compared to the poles (Green et al., 2012) (Figure 44). Considering F-actin as a physical barrier, higher density of F-actin would show stronger limitations of protein mobility compared to lower F-actin density regions. Consistent with this hypothesis, I found that GFP::RHO-1 mobility indeed was reduced at the equatorial cortex (region with high F-actin density) compared to a region outside the GFP::RHO-1 zone (region with low F-actin density) by performing high-time resolution imaging followed by PIV analysis. This finding was verified by FRAP experiments, showing that the recovery after photobleaching of GFP::RHO-1, within a region of low F-actin density was faster compared to a region of high F-actin density. This together indicated that the mobility of GFP::RHO-1 molecules within the RHO-1 zone at the equator is limited (Figure 44 A).

Increased F-actin polymerization is induced by RhoA at the equatorial cortex during cytokinesis (Watanabe et al., 2008; Piekny et al., 2005). To minimize F-actin mesh formation at the equator the formin CYK-1 was depleted. Reduced F-actin mesh increased GFP::RHO-1 mobility measured by PIV analysis, which was no longer distinguishable from GFP::RHO-1 mobility within an anterior region. This indicated that during cytokinesis a dense F-actin meshwork indeed restricts RHO-1 diffusion, which goes in line with the ‘membrane-skeleton picket fence’ model. Interestingly, and consistent with the loss of an F-actin mesh, also GFP::RHO-1 no longer formed a dense meshwork at the equatorial membrane in the absence of the formin CYK-1. Instead, formin depleted embryos showed rather dot-like clusters of GFP::RHO-1 at the equator, still forming an equatorial zone. This indicated that the formation of a RHO-1 zone *per se* is independent of F-actin as described before (Bement and Benink, 2005; Yüce et al., 2005), yet formin-induced F-actin contributed to the formation of filamentous-like structures (Figure 44 A’). GFP::RHO-1 clusters in *cyk-1(RNAi)* embryos also depend on RHO-1 activation, since they required ECT-2. Zone width analysis revealed a broader zone of

GFP::RHO-1, 160 s after NEBD, in *cyk-1(RNAi)* embryos compared to control and a more variable zone width, 224 s after NEBD, when intensity levels were similar to control (160 s after NEBD). Therefore, I am proposing that the equatorial F-actin mesh contributes to the formation of a defined RHO-1 zone by forming a scaffold that traps RHO-1 within the mesh. Trapped RHO-1 is limited in mobility and therefore is limited to diffuse away from the site of activation (Figure 44). For the future, it would be interesting to test RHO-1 zone width in the absence of both, CYK-1 and RGA-3/4. Depletion of either of the two, led to slight increase of the GFP::RHO-1 zone. Following the hypothesis that accelerated ‘RhoA flux’ is required to maintain a narrow RHO-1 zone and in addition the F-actin meshwork corrals RHO-1 at the equator, for the depletion of both, CYK-1 and RGA-3/4, a stronger broadening of the RHO-1 zone is expected. First, more active RHO-1 accumulates at the equator and second RHO-1 molecules are less restricted in its mobility. Therefore, RHO-1 is expected to diffuse along the PM, resulting in a wider RHO-1 zone.

I further tested the influence of the Arp2/3 complex that induces branched actin networks. In the absence of the Arp2/3 complex, GFP::RHO-1 meshwork formation was not altered at the equator suggesting that only formin-nucleated F-actin influences RHO-1 dynamics. Previous studies postulated an indirect effect of the Arp2/3 complex on cytokinesis via an increased activity of formin-mediated F-actin nucleation (Chan et al., 2019). In line with these experiments, Arp2/3 depletion slowed down ring ingression. Future work should analyze, in more detail, the changes in the F-actin mesh after Arp2/3 depletion. If the F-actin mesh is indeed denser, but RHO-1 dynamics do not change, it would suggest that there is a limit in how much RHO-1 dynamics can be altered by formin-nucleated F-actin.

In the absence of the formin CYK-1, GFP::RHO-1 appeared in dot-like foci at the equatorial membrane. These structures further showed higher mobility compared to the dense meshwork by PIV measurements, presumably due to limited F-actin present. The GFP::RHO-1 foci detected at the equator had the tendency to form clusters, and by following the individual foci over time clusters fused together. Cluster formation could be a consequence of protein oligomerization, or interaction with other cell cortex components. During polarization of the *C. elegans* embryo it was shown that, in the absence of the actin cytoskeleton, foci of myosin II and septins were formed (Michaux et al., 2018). Further, the absence of F-actin in *Drosophila* S2 anaphase cells resulted in foci containing anillin and RhoA (Hickson and O'Farrell, 2008). I showed that in the absence of formins, anillin was no longer forming clusters at the equator, as it was detected in control, but also formed

rather smaller and dot-like structures comparable to GFP::RHO-1 in *cyk-1(RNAi)* embryos. Further, in *ani-1(RNAi)* embryos the formation of GFP::RHO-1 filamentous-like foci was strongly reduced. Together this suggests that active RHO-1 is stabilized by anillin at the equatorial membrane by cluster formation, representing a mechanism of stable membrane association as previously described by Budnar *et al.* (Budnar *et al.*, 2019). RHO-1 clusters are then confined by the F-actin mesh, occurring in filamentous-like structures. In the future, co-localization studies are required to test whether RHO-1 and anillin indeed co-localize into clusters in the absence of formin. Further, it would be interesting to test whether in the absence of CYK-1 and ANI-1, GFP::RHO-1 clusters still accumulate into a RHO-1 zone at the equatorial membrane. If ANI-1 has a stabilizing and linking effect on RHO-1 and ECT-2 at the equator, no GFP::RHO-1 accumulation into clusters is expected in the absence of formin and anillin.

Co-localization analysis performed for GFP::RHO-1 and F-actin indicated rather a co-existence of the two proteins at the equator, than strong co-localization. RHO-1, as the activator for F-actin, does not seem to be physically attached to F-actin, but rather exists at the equator to induce contractile ring assembly. In line with the observation of the co-localization experiments, direct orientation- and mobility analysis revealed only moderate correlation. If RHO-1 and F-actin would be physically linked to each other, they would be expected to show higher co-localization (Ding *et al.*, 2017) and same displacement dynamics in PIV analysis, which was not observed. Together, these findings support the idea of a corralling mechanism, where RHO-1 and F-actin show an indirect interaction in terms of spatial restriction, which compresses RHO-1 into filamentous-like structures (Figure 44 A').

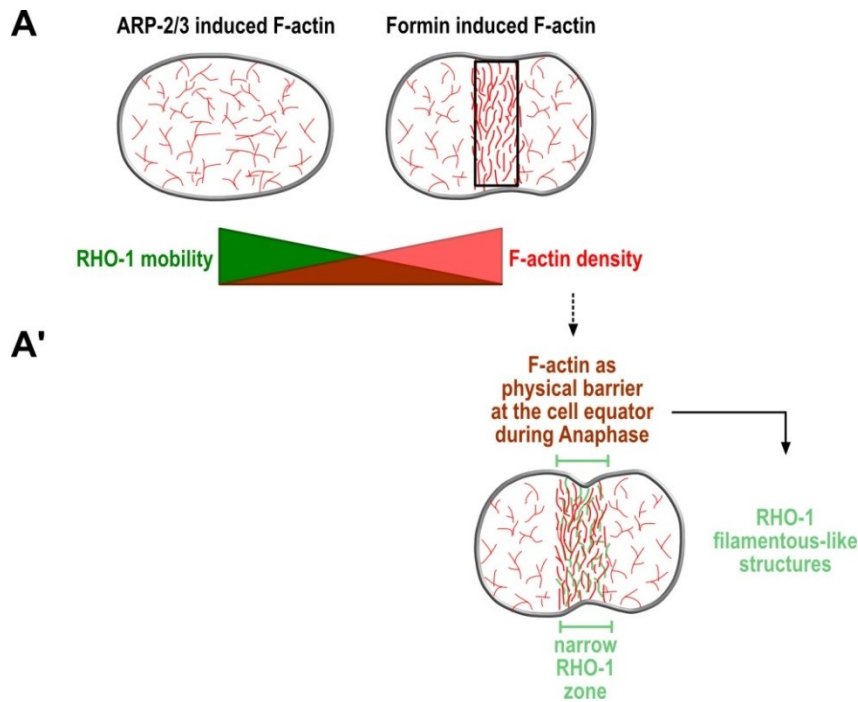


**Figure 44: During anaphase the dense F-actin mesh at the cell equator acts as a physical barrier that slows down GFP::RHO-1 mobility.** (A) PIV and FRAP analysis revealed that regions with higher F-actin density show reduced GFP::RHO-1 mobility, indicating that the dense formin-induced F-actin mesh at the equator contributes to narrow GFP::RHO-1 zone formation. (A') GFP::RHO-1 filamentous-like structures at the equatorial cortex are dependent on the formin (CYK-1)-induced F-actin meshwork.

F-actin and GFP::RHO-1 both align circumferentially around the cell equator during cytokinesis, which was shown by alignment assay. Alignment of F-actin was previously shown for cytokinesis (Spira and Cuylen, 2017; Henson et al., 2017; Reymann et al., 2016; Schroeder, 1968; Fishkind and Wang, 1993), however to my knowledge, it was not shown for RhoA before. Interestingly, GFP::RHO-1 alignment followed F-actin (Figure 45). This goes in line with my postulated hypothesis, where the increase of F-actin passively compresses GFP::RHO-1 into filamentous-like structures. The increase in F-actin density at the equator leads to spatial restriction, due to smaller compartment size, which could even result in immobile RHO-1 fractions.

The confinement of RhoA by F-actin could be a mechanism contributing to the restriction of RhoA into a narrow zone that is of importance for proper contraction and cytokinesis. For future studies it would be interesting to test whether, not only RHO-1 is confined within the F-actin mesh, but also RHO-1's regulators and downstream effectors. If RHO-1 is immobilized within the F-actin structure at the equator, this could be a possible mechanism of remaining active RHO-1 at a specific site, where it is needed to activate

downstream effectors. Indeed, the GAPs RGA-3/4 co-localize with F-actin (Michaux et al., 2018). RHO-1 mobility and turnover within the mesh might be slowed down due to trapping and lower accessibility, therefore supporting the activation of downstream effectors required for contractile ring formation and ingression. Trapped inactive RHO-1 could also be kept in place to be activated again by Ect2, representing a mechanism of faster reactivation and therefore continuous activation of effectors to build the contractile ring. This hypothesis of F-actin being involved in RhoA signaling during cytokinesis is further supported by previous findings, proposing the actin cortex to be involved in the regulation of immune receptor signaling (Mattila et al., 2016). Here, the actin cytoskeleton was described to be important for cluster formation of PM-associated proteins as well as for controlling protein interactions. The Ras GTPase was shown to assemble into nanoclusters within the membrane dependent on the actin cytoskeleton (Plowman et al., 2005). Further, RhoA was shown to be able to dimerize *in vitro* (Zhang and Zheng, 1998a) and light-induced RhoA oligomerization is sufficient to activate RhoA (Bugaj et al., 2013). Therefore, restricting RhoA within compartments of the F-actin mesh could represent a mechanism to mediate RhoA clustering at the equator, which in turn enhances RhoA signaling during cytokinesis. Cluster formation due to spatial confinement could facilitate the interaction of RhoA and its effectors/regulators by bringing them in close proximity. My results suggest that RhoA GTPase signaling is modulated by F-actin-mediated RhoA clustering, as it was shown to be true for a variety of signaling molecules (Goyette et al., 2019; Mattila et al., 2016).

To further support my proposed model, I am suggesting to perform genetic perturbation studies against F-actin binding proteins. If indeed the dense F-actin mesh defines GFP::RHO-1 localization into filamentous-like structures at the equatorial cortex, depletion of F-actin cross-linkers would loosen the actin mesh beneath the PM. Following my hypothesis, this should in turn lead to dispersed RhoA localization. Myosin, as one F-actin binding protein, was tested in the present work. GFP::RHO-1 zone formation and structure analysis revealed no changes when myosin was absent compared to control, yet increased GFP::RHO-1 accumulation occurred over time when ring ingression was blocked in *nmy-2(RNAi)* embryos. This indicated that NMY-2 does not contribute to the formation and maintenance of the narrow GFP::RHO-1 zone, however is indispensable for ring constriction.

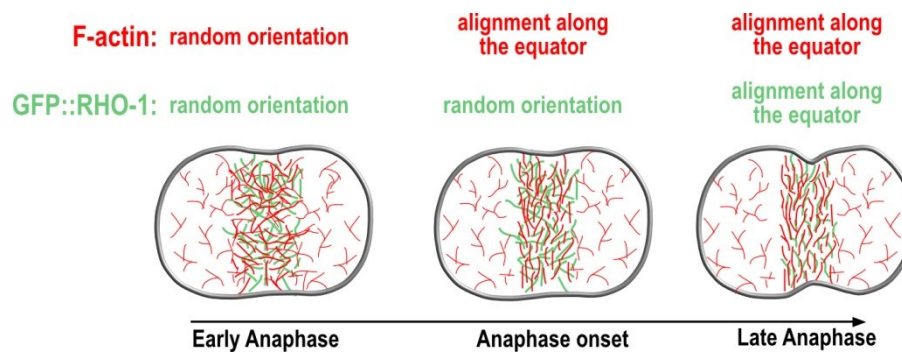


**Figure 45: During anaphase onset GFP::RHO-1 follows F-actin alignment along the equator.** In early anaphase both, F-actin and RHO-1, are randomly oriented at the equator. During anaphase onset F-actin first aligns around the cell equator, followed by RHO-1 alignment, indicating that F-actin acts as a scaffold for RHO-1 filamentous-like structures.

The actomyosin cortex beneath the PM is a dynamic structure that is modulated by signals from small Rho GTPases. In *C. elegans* early embryos (P0 and AB cells) contractile pulses were described that consist of several proteins of the RhoA pathway. Also RhoA activity was suggested to have oscillatory behavior in those cells (Michaux et al., 2018; Munro et al., 2004). Based on their study, the authors proposed that pulse formation is initiated by a positive feedback loop and terminated by a delayed F-actin and RGA-3/4 dependent negative feedback loop. Thereby, those two feedback loops generate locally active RhoA in contractility hubs (Michaux et al., 2018). Pulsed contractility is suggested to play a role in cell morphogenesis and makes the cortex an excitable medium, allowing fast reactions to internal and external stimuli. Whether this mechanism is also crucial for cytokinesis and whether such positive and negative feedback loops exist during cytokinesis is currently discussed (Michaud et al., 2021). Local activation of RhoA was shown to be driven by the GEF Ect2 during cytokinesis and activation of Ect2 by MgcRacGAP is regulated by Cdk1. The regulation by Cdk1 could be the trigger for such a positive feedback loop where Ect2 subsequently activates RhoA (Nishikawa et al., 2017; Bement et al., 2015). However, if this positive feedback would not be counteracted by another mechanism, RhoA could in principle spread along the entire PM. My data suggest that RHO-1 activation is counteracted by RGA-3/4 (Figure 46) and thus RGA-3/4 could also be part of a negative feedback during cytokinesis. Bement and Michaux postulated that increased F-actin at the equatorial cortex during cytokinesis could recruit the GAPs, and in turn lead to negative feedback on RHO-1 activity (Michaux et al., 2018; Bement et al., 2015). However, my data suggest that formin-nucleated F-actin contributes to the formation and maintenance of the dynamic equatorial narrow RHO-1 zone during cytokinesis (Figure 46). Thus in my

model, F-actin is not part of a negative feedback loop but would rather trap and thereby maintain active RhoA at the site of activation.

Further work will need to address whether the mechanisms that generate pulsed RhoA activities, for example during polarization of the *C. elegans* zygote (Michaux et al., 2018), are also applicable to cytokinesis. While isolated RHO-1/F-actin/RGA-3/4 contractility centers were shown during polarization, during cytokinesis contractility events happen within a dense ring structure. Identifying and characterizing the positive and negative feedback mechanisms during cytokinesis by analyzing the sequential assembly and disassembly of RhoA and its regulators will be an important task in the future.

In summary, the data presented in this thesis support evidence for two mechanisms contributing to the formation and maintenance of a narrow RHO-1 zone during cytokinesis: (1) ‘RhoA flux’-mediated restriction of RHO-1 and (2) an F-actin corralling mechanism towards RHO-1 (Figure 46).

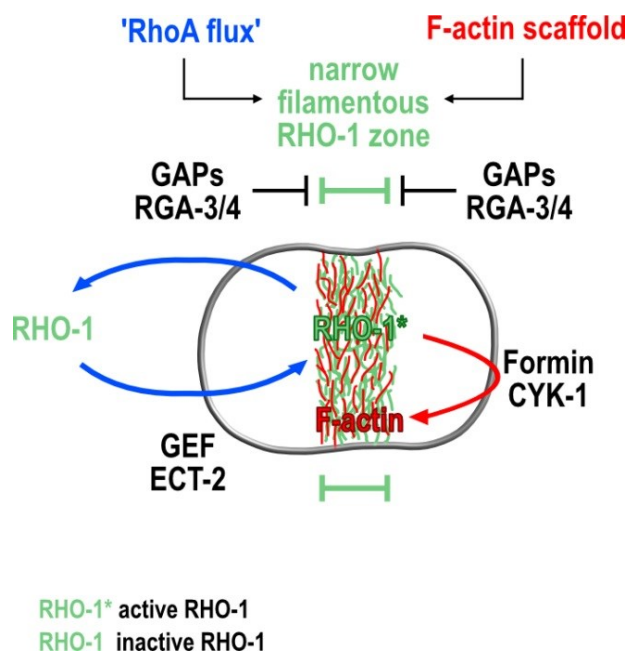


**Figure 46: Model of equatorial narrow RHO-1 zone formation and maintenance during cytokinesis.** RHO-1 is activated at the equator during cytokinesis by the GEF ECT-2. PM-associated active RHO-1 in turn activates formins. Formin-induced F-actin spatially restricts RHO-1 mobility leading to the formation of a dense RHO-1 meshwork of filamentous-like structures at the equator. During anaphase onset F-actin filaments align along the equatorial plane, followed by RHO-1 alignment. Increased ‘RhoA flux’, mediated by the GAPs RGA-3/4 (in *C. elegans*), contributes to a confined narrow zone of RHO-1.

## 5 References

- Abreu, M.T. 2014. Coordination of Rho family GTPase activities to orchestrate cytoskeleton responses during cell wound repair. *Curr Biol.* 24:144–155. doi:10.1016/j.cub.2013.11.048.
- Akhunzada, M.J., F. D'Autilia, and B. Chandramouli. 2019. Interplay between lipid lateral diffusion, dye concentration and membrane permeability unveiled by a combined spectroscopic and computational study of a model lipid bilayer. *Scientific Reports.* 9:1508. doi:10.1038/s41598-018-37814-x.
- Albertson, D.G., and J.N. Thomson. 1993. Segregation of holocentric chromosomes at meiosis in the nematode, *Caenorhabditis elegans*. *Chromosome Res.* 1:15–26. doi:10.1007/BF00710603.
- Audhya, A., F. Hyndman, I.X. McLeod, and A.S. Maddox. 2005. A complex containing the Sm protein CAR-1 and the RNA helicase CGH-1 is required for embryonic cytokinesis in *Caenorhabditis elegans*. *The Journal of cell biology.* 171:267–279. doi:10.1083/jcb.200506124.
- Basant, A., and M. Glotzer. 2018. Spatiotemporal regulation of RhoA during cytokinesis. *Curr Biol.* 28:R570–R580. doi:10.1016/j.cub.2018.03.045.
- Bement, W.M., M. Leda, A.M. Moe, A.M. Kita, and M.E. Larson. 2015. Activator–inhibitor coupling between Rho signalling and actin assembly makes the cell cortex an excitable medium. *Nature Cell Biology.* 17:1471–1483. doi:10.1038/ncb3251.
- Bement, W.M., A.L. Miller, and G. von Dassow. 2006. Rho GTPase activity zones and transient contractile arrays. *Bioessays.* 28:983–993. doi:10.1002/bies.20477.
- Bement, W.M., and H.A. Benink. 2005. A microtubule-dependent zone of active RhoA during cleavage plane specification. *The Journal of cell biology.* 170:91–101. doi:10.1083/jcb.200501131.
- Bendezú, F.O., V. Vincenzetti, D. Vavylonis, and R. Wyss. 2015. Spontaneous Cdc42 polarization independent of GDI-mediated extraction and actin-based trafficking. *PLoS Biol.* 13:e1002097. doi:10.1371/journal.pbio.1002097.



- Benink, H.A., and W.M. Bement. 2005. Concentric zones of active RhoA and Cdc42 around single cell wounds. *The Journal of cell biology*. 168:429–439. doi:10.1083/jcb.200411109.
- Billington, N., A. Wang, J. Mao, and R.S. Adelstein. 2013. Characterization of three full-length human nonmuscle myosin II paralogs. *J Biol Chem*. 288:33398–33410. doi:10.1074/jbc.M113.499848.
- Bishop, A., and A. Hall. 2000. Rho GTPases and their effector proteins. *Biochem J*. 348:241–255.
- Blanchoin, L., and R. Boujemaa. 2014. Actin dynamics, architecture, and mechanics in cell motility. *Physiological reviews*. 94:235–263. doi:10.1152/physrev.00018.2013.
- Bohnert, K.A., A.H. Willet, D.R. Kovar, and K.L. Gould. 2013. Formin-based control of the actin cytoskeleton during cytokinesis. *Biochemical Society Transactions*. 41:1750–1754. doi:10.1042/BST20130208.
- Bos, J.L., H. Rehmann, and A. Wittinghofer. 2007. GEFs and GAPs: critical elements in the control of small G proteins. *Cell*. 129:865–877. doi:10.1016/j.cell.2007.05.018.
- Bourne, H.R., D.A. Sanders, and F. McCormick. 1990. The GTPase superfamily: a conserved switch for diverse cell functions. *Nature*. 348:125–132. doi:10.1038/348125a0.
- Brenner, S. 1974. The genetics of *Caenorhabditis elegans*. *Genetics*. 77:71–94. doi:10.1093/genetics/77.1.71.
- Brito, C., and S. Sousa. 2020. Non-muscle myosin 2A (NM2A): structure, regulation and function. *Cells*. 9. doi:10.3390/cells9071590.
- Budirahardja, Y., and P. Gonczy. 2009. Coupling the cell cycle to development. *Development*. 136:2861–2872. doi:10.1242/dev.021931.
- Budnar, S., K.B. Husain, G.A. Gomez, and M. Naghibosadat. 2019. Anillin promotes cell contractility by cyclic resetting of RhoA residence kinetics. *Developmental cell*. 49:894–906.e12. doi:10.1016/j.devcel.2019.04.031.
- Bugaj, L.J., A.T. Choksi, C.K. Mesuda, and R.S. Kane. 2013. Optogenetic protein clustering and signaling activation in mammalian cells. *Nat Methods*. 10:249–252. doi:10.1038/nmeth.2360.

- Burkard, M.E., J. Maciejowski, and V. Rodriguez. 2009. Plk1 self-organization and priming phosphorylation of HsCYK-4 at the spindle midzone regulate the onset of division in human cells. *PLoS Biol.* 7:e1000111. doi:10.1371/journal.pbio.1000111.
- Canman, J.C., L. Lewellyn, K. Laband, and S.J. Smerdon. 2008. Inhibition of Rac by the GAP activity of centralspindlin is essential for cytokinesis. *Science.* 322:1543–1546. doi:10.1126/science.1163086.
- Carvalho, A., A. Desai, and K. Oegema. 2009. Structural memory in the contractile ring makes the duration of cytokinesis independent of cell size. *Cell.* 137:926–937. doi:10.1016/j.cell.2009.03.021.
- Castrillon, D.H., and S.A. Wasserman. 1994. Diaphanous is required for cytokinesis in *Drosophila* and shares domains of similarity with the products of the limb deformity gene. *Development.* 120:3367–3377. doi:10.1242/dev.120.12.3367.
- Chalamalasetty, R.B., S. Hümmer, E.A. Nigg, and H. Silljé. 2006. Influence of human Ect2 depletion and overexpression on cleavage furrow formation and abscission. *Journal of cell science.* 119:3008–3019. doi:10.1242/jcs.03032.
- Chalmers, A.D., P. Whitley, and A. Noatynska. 2012. Cell polarity and asymmetric cell division: the *C. elegans* early embryo. *Essays In Biochemistry.* 53:1–14. doi:10.1042/bse0530001.
- F.Y. Chan, J. Saramago, J. Leite, and A.M. Silva. 2018. Flow-independent accumulation of motor-competent non-muscle myosin II in the contractile ring is essential for cytokinesis. *bioRxiv.* 333286. doi:10.1101/333286.
- Chan, F.Y., A.M. Silva, and J. Saramago. 2019. The ARP2/3 complex prevents excessive formin activity during cytokinesis. *Molecular biology of the cell.* 30:96–107. doi:10.1091/mbc.E18-07-0471.
- Chircop, M. 2014. Rho GTPases as regulators of mitosis and cytokinesis in mammalian cells. *Small GTPases.* 5. doi:10.4161/sgtp.29770.
- Choy, E., V.K. Chiu, J. Silletti, M. Feoktistov, and T. Morimoto. 1999. Endomembrane trafficking of ras: the CAAX motif targets proteins to the ER and Golgi. *Cell.* 98:69–80. doi:10.1016/S0092-8674(00)80607-8.

- Clark, A.G., O. Wartlick, G. Salbreux, and E.K. Paluch. 2014. Stresses at the cell surface during animal cell morphogenesis. *Curr Biol.* 24:R484–R494. doi:10.1016/j.cub.2014.03.059.
- Clarke, S. 1992. Protein isoprenylation and methylation at carboxyl-terminal cysteine residues. *Annu Rev Biochem.* 61:355–386. doi:10.1146/annurev.bi.61.070192.002035.
- Corsi, A.K., B. Wightman, and M. Chalfie. 2015. A Transparent Window into Biology: A Primer on *Caenorhabditis elegans*. *Genetics.* 200:387–407. doi:10.1534/genetics.115.176099.
- D'Avino, P.P. 2009. How to scaffold the contractile ring for a safe cytokinesis—lessons from Anillin-related proteins. *Journal of cell science.* 122:1071–1079. doi:10.1242/jcs.034785.
- D'Avino, P.P., M.S. Savoian, and D.M. Glover. 2005. Cleavage furrow formation and ingression during animal cytokinesis: a microtubule legacy. *Journal of cell science.* 118:1549–1558. doi:10.1242/jcs.02335.
- D'Avino, P.P., T. Takeda, L. Capalbo, and W. Zhang. 2008. Interaction between Anillin and RacGAP50C connects the actomyosin contractile ring with spindle microtubules at the cell division site. *Journal of cell science.* 121:1151–1158. doi:10.1242/jcs.026716.
- D'Avino, P.P., and M.G. Giansanti. 2015. Cytokinesis in animal cells. *Cold Spring Harb Perspect Biol.* 7:a015834. doi:10.1101/cshperspect.a015834.
- Davidson, A.J., and W. Wood. 2016. Unravelling the actin cytoskeleton: a new competitive edge? *Trends in cell biology.* 26:569–576. doi:10.1016/j.tcb.2016.04.001.
- Davies, T., S.N. Jordan, V. Chand, J.A. Sees, and K. Laband. 2014. High-resolution temporal analysis reveals a functional timeline for the molecular regulation of cytokinesis. *Developmental cell.* 30:209–223. doi:10.1016/j.devcel.2014.05.009.
- Dechant, R., and M. Glotzer. 2003. Centrosome separation and central spindle assembly act in redundant pathways that regulate microtubule density and trigger cleavage furrow formation. *Developmental cell.* 4:333–344. doi:10.1016/s1534-5807(03)00057-1.
- DerMardirossian, C., and G.M. Bokoch. 2005. GDIs: central regulatory molecules in Rho GTPase activation. *Trends in cell biology.* 15:356–363. doi:10.1016/j.tcb.2005.05.001.

- Descovich, C.P., D.B. Cortes, S. Ryan, and J. Nash. 2018. Cross-linkers both drive and brake cytoskeletal remodeling and furrowing in cytokinesis. *Molecular biology of the cell*. 29:622–631. doi:10.1091/mbc.E17-06-0392.
- Dickinson, D.J., and B. Goldstein. 2016. CRISPR-based methods for *Caenorhabditis elegans* genome engineering. *Genetics*. 202:885–901. doi:10.1534/genetics.115.182162.
- Ding, W.Y., H.T. Ong, Y. Hara, and J. Wongsantichon. 2017. Plastin increases cortical connectivity to facilitate robust polarization and timely cytokinesis. *The Journal of cell biology*. 216:1371–1386. doi:10.1083/jcb.201603070.
- Drechsel, D.N., A.A. Hyman, A. Hall, and M. Glotzer. 1997. A requirement for Rho and Cdc42 during cytokinesis in *Xenopus* embryos. *Current biology*. 7:12. doi:10.1016/s0960-9822(06)00023-6.
- Dvorsky, R., and M.R. Ahmadian. 2004. Always look on the bright site of Rho: structural implications for a conserved intermolecular interface. *EMBO Rep*. 5:1130–1136. doi:10.1038/sj.embor.7400293.
- Edidin, M., S.C. Kuo, and M.P. Sheetz. 1991. Lateral movements of membrane glycoproteins restricted by dynamic cytoplasmic barriers. *Science*. 254:1379–1382. doi:10.1126/science.1835798.
- Eggert, U.S., T.J. Mitchison, and C.M. Field. 2006. Animal cytokinesis: from parts list to mechanisms. *Annu Rev Biochem*. 75:543–566. doi:10.1146/annurev.biochem.74.082803.133425.
- Emoto, K., H. Inadome, Y. Kanaho, and S. Narumiya. 2005. Local change in phospholipid composition at the cleavage furrow is essential for completion of cytokinesis. *J Biol Chem*. 280:37901–37907. doi:10.1074/jbc.M504282200.
- Ennomani, H., G. Letort, C. Guérin, J.L. Martiel, and W. Cao. 2016. Architecture and connectivity govern actin network contractility. *Curr Biol*. 26:616–626. doi:10.1016/j.cub.2015.12.069.
- Fay, D. 2006. Genetic mapping and manipulation: chapter 1--Introduction and basics. *WormBook*. 1–12. doi:10.1895/wormbook.1.90.1.

- Field, C.M., M. Coughlin, S. Doberstein, and T. Marty. 2005a. Characterization of anillin mutants reveals essential roles in septin localization and plasma membrane integrity. *Development*. 132:2849–2860. doi:10.1242/dev.01843.
- Field, C.M., and B.M. Alberts. 1995. Anillin, a contractile ring protein that cycles from the nucleus to the cell cortex. *The Journal of cell biology*. 131:165–178. doi:10.1083/jcb.131.1.165.
- Field, S.J., N. Madson, M.L. Kerr, and K. Galbraith. 2005b. PtdIns (4, 5) P2 functions at the cleavage furrow during cytokinesis. *Curr Biol*. 15:1407–1412. doi:10.1016/j.cub.2005.06.059.
- Fishkind, D.J., and Y. Wang. 1993. Orientation and three-dimensional organization of actin filaments in dividing cultured cells. *The Journal of cell biology*. 123:837–848. doi:10.1083/jcb.123.4.837.
- Flemming, W. 1882. *Zellsubstanz, Kern und Zelltheilung*. F.C.W. Vogel, Leipzig.
- Frenette, P., E. Haines, M. Loloyan, M. Kinal, and P. Pakarian. 2012. An anillin-Ect2 complex stabilizes central spindle microtubules at the cortex during cytokinesis. *PLoS One*. 7:e34888. doi:10.1371/journal.pone.0034888.
- Frøkjær, C. 2008. Single-copy insertion of transgenes in *Caenorhabditis elegans*. *Nat Genet*. 40:1375–1383. doi:10.1038/ng.248.
- Frøkjær, C. 2012. Improved Mos1-mediated transgenesis in *C. elegans*. *Nat Methods*. 9:117–118. doi:10.1038/nmeth.1865.
- Garcia, R. 2011. The “invisible hand”: regulation of RHO GTPases by RHOGDIs. *Nature reviews Molecular cell biology*. 12:493–504. doi:10.1038/nrm3153.
- Gibson, D.G., L. Young, R.Y. Chuang, and J.C. Venter. 2009. Enzymatic assembly of DNA molecules up to several hundred kilobases. *Nat Methods*. 6:343–345. doi:10.1038/nmeth.1318.
- Glotzer, M. 2004. Cleavage furrow positioning. *The Journal of cell biology*. 164:347–351. doi:10.1083/jcb.200310112.
- Glotzer, M. 2005. The molecular requirements for cytokinesis. *Science*. 307:1735–1739. doi:10.1126/science.1096896.

- Glotzer, M. 2009. The 3Ms of central spindle assembly: microtubules, motors and MAPs. *Nature reviews Molecular cell biology*. 10:9–20. doi:10.1038/nrm2609.
- Goehring, N.W., D. Chowdhury, A.A. Hyman, and S.W. Grill. 2010. FRAP analysis of membrane-associated proteins: lateral diffusion and membrane-cytoplasmic exchange. *Biophys J*. 99:2443–2452. doi:10.1016/j.bpj.2010.08.033.
- Golden, J.W., and D.L. Riddle. 1984. The *Caenorhabditis elegans* dauer larva: developmental effects of pheromone, food, and temperature. *Developmental biology*. 102:368–378. doi:10.1016/0012-1606(84)90201-x.
- Golding, A.E., I. Visco, P. Bieling, and W.M. Bement. 2019. Extraction of active RhoGTPases by RhoGDI regulates spatiotemporal patterning of RhoGTPases. *Elife*. 8. doi:10.7554/eLife.50471.
- Goldstein, B., and S.N. Hird. 1996. Specification of the anteroposterior axis in *Caenorhabditis elegans*. *Development*. 122:1467–1474. doi:10.1242/dev.122.5.1467.
- Goryachev, A.B., M. Leda, A.L. Miller, and G. von Dassow. 2016. How to make a static cytokinetic furrow out of traveling excitable waves. *Small GTPases*. 7:65–70. doi:10.1080/21541248.2016.1168505.
- Goyette, J., D.J. Nieves, Y. Ma, and K. Gaus. 2019. How does T cell receptor clustering impact on signal transduction? *Journal of cell science*. 132. doi:10.1242/jcs.226423.
- Graessl, M., J. Koch, A. Calderon, and D. Kamps. 2017. An excitable Rho GTPase signaling network generates dynamic subcellular contraction patterns. *The Journal of cell biology*. 216:4271–4285. doi:10.1083/jcb.201706052.
- Green, R.A., E. Paluch, and K. Oegema. 2012. Cytokinesis in animal cells. *Annual review of cell and developmental biology*. 28:29–58. doi:10.1146/annurev-cellbio-101011-155718.
- Gregory, S.L., S. Ebrahimi, J. Milverton, and W.M. Jones. 2008. Cell division requires a direct link between microtubule-bound RacGAP and Anillin in the contractile ring. *Curr Biol*. 18:25–29. doi:10.1016/j.cub.2007.11.050.
- Hall, A. 1998. Rho GTPases and the actin cytoskeleton. *Science*. 279:509–514. doi:10.1126/science.279.5350.509.
- Hall, D.H., and Z.F. Altun. 2009. Introduction. In *WormAtlas*.

- Hamers, C. 1993. Naturally occurring antibodies devoid of light chains. *Nature*. 363:446–448. doi:10.1038/363446a0.
- Hancock, J.F., and A. Hall. 1993. A novel role for RhoGDI as an inhibitor of GAP proteins. *The EMBO journal*. 12:1915–1921. doi:10.1002/j.1460-2075.1993.tb05840.x.
- Hart, M.J., Y. Maru, D. Leonard, O.N. Witte, and T. Evans. 1992. A GDP dissociation inhibitor that serves as a GTPase inhibitor for the Ras-like protein CDC42Hs. *Science*. 258:812–815. doi:10.1126/science.1439791.
- Heinemann, F., S.K. Vogel, and P. Schwillle. 2013. Lateral membrane diffusion modulated by a minimal actin cortex. *Biophys J*. 104:1465–1475. doi:10.1016/j.bpj.2013.02.042.
- Henson, J.H., C.E. Ditzler, and A. Germain. 2017. The ultrastructural organization of actin and myosin II filaments in the contractile ring: new support for an old model of cytokinesis. *Molecular biology of the cell*. 28:613–623. doi:10.1091/mbc.E16-06-0466.
- Hickson, G., and P.H. O'Farrell. 2008. Rho-dependent control of anillin behavior during cytokinesis. *The Journal of cell biology*. 180:285–294. doi:10.1083/jcb.200709005.
- Hirani, N., R. Illukkumbura, and T. Bland. 2019. Anterior-enriched filopodia create the appearance of asymmetric membrane microdomains in polarizing *C. elegans* zygotes. *Journal of cell science*. 132. doi:10.1242/jcs.230714.
- Hirsch, S.M., F. Edwards, and M. Shirasu. 2022. Functional midbody assembly in the absence of a central spindle. *The Journal of cell biology*. 221. doi:10.1083/jcb.202011085.
- Hodge, R.G., and A.J. Ridley. 2016. Regulating Rho GTPases and their regulators. *Nature reviews Molecular cell biology*. 17:496–510. doi:10.1038/nrm.2016.67.
- Hodgkin, J., H.R. Horvitz, and S. Brenner. 1979. Nondisjunction mutants of the nematode *Caenorhabditis elegans*. *Genetics*. 91:67–94. doi:10.1093/genetics/91.1.67.
- Hodgkin, J., and T. Doniach. 1997. Natural variation and copulatory plug formation in *Caenorhabditis elegans*. *Genetics*. 146:149–164. doi:10.1093/genetics/146.1.149.
- Hurley, J.H., and T. Meyer. 2001. Subcellular targeting by membrane lipids. *Current opinion in cell biology*. 13:146–152. doi:10.1016/s0955-0674(00)00191-5.

- Iglesias, P.A., and P.N. Devreotes. 2012. Biased excitable networks: how cells direct motion in response to gradients. *Current opinion in cell biology*. 24:245–253. doi:10.1016/j.ceb.2011.11.009.
- Ihara, K., S. Muraguchi, M. Kato, and T. Shimizu. 1998. Crystal structure of human RhoA in a dominantly active form complexed with a GTP analogue. *Journal of Biological Chemistry*. 273:9656–9666. doi:10.1074/jbc.273.16.9656.
- Jaffe, A.B., and A. Hall. 2005. Rho GTPases: biochemistry and biology. *Annual review of cell and developmental biology*. 21:247–269. doi:10.1146/annurev.cellbio.21.020604.150721.
- Janson, L.W., J. Kolega, and D.L. Taylor. 1991. Modulation of contraction by gelation/solution in a reconstituted motile model. *The Journal of cell biology*. 114:1005–1015. doi:10.1083/jcb.114.5.1005.
- Jantsch, V. 2000. CYK-4 a Rho family GTPase activating protein (GAP) required for central spindle formation and cytokinesis. *The Journal of cell biology*. 149:1391–1404. doi:10.1083/jcb.149.7.1391.
- Jordan, S.N., and J.C. Canman. 2012. Rho GTPases in animal cell cytokinesis: an occupation by the one percent. *Cytoskeleton (Hoboken)*. 69:919–930. doi:10.1002/cm.21071.
- Kachur, T.M., A. Audhya, and D.B. Pilgrim. 2008. UNC-45 is required for NMY-2 contractile function in early embryonic polarity establishment and germline cellularization in *C. elegans*. *Developmental biology*. 314:287–299. doi:10.1016/j.ydbio.2007.11.028.
- Kamijo, K., N. Ohara, M. Abe, and T. Uchimura. 2006. Dissecting the role of Rho-mediated signaling in contractile ring formation. *Molecular biology of the cell*. 17:43–55. doi:10.1091/mbc.e05-06-0569.
- Keller, L., N. Bery, C. Tardy, L. Ligat, G. Favre, and T.H. Rabbitts. 2019. Selection and Characterization of a Nanobody Biosensor of GTP-Bound RHO Activities. *Antibodies*. 8. doi:10.3390/antib8010008.
- Kimura, K., M. Ito, M. Amano, K. Chihara, and Y. Fukata. 1996. Regulation of myosin phosphatase by Rho and Rho-associated kinase (Rho-kinase). *Science*. 273:245–248. doi:10.1126/science.273.5272.245.



- Kishi, K., T. Sasaki, S. Kuroda, T. Itoh, and Y. Takai. 1993. Regulation of cytoplasmic division of *Xenopus* embryo by rho p21 and its inhibitory GDP/GTP exchange protein (rho GDI). *The Journal of cell biology*. 120:1187–1195. doi:10.1083/jcb.120.5.1187.
- Konstantinidis, D.G., K.M. Giger, and M. Risinger. 2015. Cytokinesis failure in RhoA-deficient mouse erythroblasts involves actomyosin and midbody dysregulation and triggers p53 activation. *Blood*. 126:1473–1482. doi:10.1182/blood-2014-12-616169.
- Kotýnková, K., K.C. Su, S.C. West, and M. Petronczki. 2016. Plasma membrane association but not midzone recruitment of RhoGEF ECT2 is essential for cytokinesis. *Cell reports*. 17:2672–2686. doi:10.1016/j.celrep.2016.11.029.
- Kusumi, A., C. Nakada, and K. Ritchie. 2005. Paradigm shift of the plasma membrane concept from the two-dimensional continuum fluid to the partitioned fluid: high-speed single-molecule tracking of membrane molecules. *Annu Rev Biophys Biomol Struct*. 34:351–378. doi:10.1146/annurev.biophys.34.040204.144637.
- Kusumi, A., Y. Sako, and M. Yamamoto. 1993. Confined lateral diffusion of membrane receptors as studied by single particle tracking (nanovid microscopy). Effects of calcium-induced differentiation in cultured epithelial cells. *Biophys J*. 65:2021–2040. doi:10.1016/S0006-3495(93)81253-0.
- Lacroix, B., and A.S. Maddox. 2012. Cytokinesis, ploidy and aneuploidy. *J Pathol*. 226:338–351. doi:10.1002/path.3013.
- Lee, G.M., F. Zhang, A. Ishihara, and C.L. McNeil. 1993. Unconfined lateral diffusion and an estimate of pericellular matrix viscosity revealed by measuring the mobility of gold-tagged lipids. *The Journal of cell biology*. 120:25–35. doi:10.1083/jcb.120.1.25.
- Leite, J., A.F. Sobral, A.M. Silva, and A.X. Carvalho. 2019. Network contractility during cytokinesis—from molecular to global views. *Biomolecules*. 9. doi:10.3390/biom9050194.
- Li, Y., and E. Munro. 2021. Filament-guided filament assembly provides structural memory of filament alignment during cytokinesis. *Developmental cell*. 56:2486–2500.e6. doi:10.1016/j.devcel.2021.08.009.
- Longenecker, K., P. Read, S.K. Lin, and A.P. Somlyo. 2003. Structure of a constitutively activated RhoA mutant (Q63L) at 1.55 Å resolution. *Acta Crystallogr D Biol Crystallogr*. 59:876–880. doi:10.1107/s0907444903005390.

- Mabuchi, I., and M. Okuno. 1977. The effect of myosin antibody on the division of starfish blastomeres. *The Journal of cell biology*. 74:251–263. doi:10.1083/jcb.74.1.251.
- Maddox, A.S., B. Habermann, A. Desai, and K. Oegema. 2005. Distinct roles for two C. elegans anillins in the gonad and early embryo. *Development*. 132:2837–2848. doi:10.1242/dev.01828.
- Maddox, A.S., L. Lewellyn, A. Desai, and K. Oegema. 2007. Anillin and the septins promote asymmetric ingression of the cytokinetic furrow. *Developmental cell*. 12:827–835. doi:10.1016/j.devcel.2007.02.018.
- Mangal, S., J. Sacher, T. Kim, D.S. Osório, F. Motegi, A.X. Carvalho, K. Oegema and E. Zanin. 2018. TPXL-1 activates Aurora A to clear contractile ring components from the polar cortex during cytokinesis. *The Journal of cell biology*. 217:837–848. doi:10.1083/jcb.201706021.
- Marsland, D., and J.V. Landau. 1954. The mechanisms of cytokinesis: Temperature-pressure studies on the cortical gel system in various marine eggs. *J Exp Zool*. 125:507–539.
- Matsumura, F. 2005. Regulation of myosin II during cytokinesis in higher eukaryotes. *Trends in cell biology*. 15:371–377. doi:10.1016/j.tcb.2005.05.004.
- Matsumura, F., Y. Yamakita, and S. Yamashiro. 2011. Myosin light chain kinases and phosphatase in mitosis and cytokinesis. *Arch Biochem Biophys*. 510:76–82. doi:10.1016/j.abb.2011.03.002.
- Mattila, P.K., F.D. Batista, and B. Treanor. 2016. Dynamics of the actin cytoskeleton mediates receptor cross talk: An emerging concept in tuning receptor signaling. *The Journal of cell biology*. 212:267–280. doi:10.1083/jcb.201504137.
- Maupin, P., and T.D. Pollard. 1986. Arrangement of actin filaments and myosin-like filaments in the contractile ring and of actin-like filaments in the mitotic spindle of dividing HeLa cells. *J Ultrastruct Mol Struct Res*. 94:92–103. doi:10.1016/0889-1605(86)90055-8.
- Mavrakis, M., and Y. Azou. 2014. Septins promote F-actin ring formation by crosslinking actin filaments into curved bundles. *Nature Cell Biology*. 16:322–334. doi:10.1038/ncb2921.

- McCullagh, M., and M.G. Saunders. 2014. Unraveling the mystery of ATP hydrolysis in actin filaments. *J Am Chem Soc.* 136:13053–13058. doi:10.1021/ja507169f.
- Mello, C.C., J.M. Kramer, and D. Stinchcomb. 1991. Efficient gene transfer in *C. elegans*: extrachromosomal maintenance and integration of transforming sequences. *The EMBO journal.* 10:3959–3970. doi:10.1002/j.1460-2075.1991.tb04966.x.
- Menant, A., and R.E. Karess. 2012. Inducing “cytokinesis” without mitosis in unfertilized *Drosophila* eggs. *Cell Cycle.* 11:2856–2863. doi:10.4161/cc.21190.
- Mendel, G. Versuche über Pflanzen-Hybriden. Verhandlungen des naturforschenden Vereins in Brünn IV, 3–47 (1866).
- Michaelson, D., J. Silletti, and G. Murphy. 2001. Differential localization of Rho GTPases in live cells regulation by hypervariable regions and RhoGDI binding. *The Journal of cell biology.* 152:111–126. doi:10.1083/jcb.152.1.111.
- Michaud, A., Z.T. Swider, J. Landino, M. Leda, and A.L. Miller. 2021. Cortical excitability and cell division. *Curr Biol.* 31:R553–R559. doi:10.1016/j.cub.2021.02.053.
- Michaux, J.B., F.B. Robin, and W.M. McFadden. 2018. Excitable RhoA dynamics drive pulsed contractions in the early *C. elegans* embryo. *The Journal of cell biology.* 217:4230–4252. doi:10.1083/jcb.201806161.
- Mierzwa, B., and D.W. Gerlich. 2014. Cytokinetic abscission: molecular mechanisms and temporal control. *Developmental cell.* 31:525–538. doi:10.1016/j.devcel.2014.11.006.
- Mikeladze, T. 2012. Analysis of centriole elimination during *C. elegans* oogenesis. *Development.* 139:1670–1679. doi:10.1242/dev.075440.
- Miki, H., and T. Takenawa. 2003. Regulation of actin dynamics by WASP family proteins. *J Biochem.* 134:309–313. doi:10.1093/jb/mvg146.
- Miller, A.L. 2011. The contractile ring. *Curr Biol.* 21:R976–8. doi:10.1016/j.cub.2011.10.044.
- Miller, A.L., and W.M. Bement. 2009. Regulation of cytokinesis by Rho GTPase flux. *Nature Cell Biology.* 11:71–77. doi:10.1038/ncb1814.

- Minoshima, Y., T. Kawashima, K. Hirose, and Y. Tonozuka. 2003. Phosphorylation by aurora B converts MgcRacGAP to a RhoGAP during cytokinesis. *Developmental cell*. 4:549–560. doi:10.1016/s1534-5807(03)00089-3.
- Mishima, M. 2016. Centralspindlin in Rappaport's cleavage signaling. *Seminars in cell & developmental biology*. 53:45–56. doi:10.1016/j.semcd.2016.03.006.
- Moon, S.Y., and Y. Zheng. 2003. Rho GTPase-activating proteins in cell regulation. *Trends in cell biology*. 13:13–22. doi:10.1016/s0962-8924(02)00004-1.
- Morone, N., T. Fujiwara, K. Murase, and R.S. Kasai. 2006. Three-dimensional reconstruction of the membrane skeleton at the plasma membrane interface by electron tomography. *The Journal of cell biology*. 174:851–862. doi:10.1083/jcb.200606007.
- Motegi, F., N.V. Velarde, F. Piano, and A. Sugimoto. 2006. Two phases of astral microtubule activity during cytokinesis in *C. elegans* embryos. *Developmental cell*. 10:509–520. doi:10.1016/j.devcel.2006.03.001.
- Motegi, F., and A. Sugimoto. 2006. Sequential functioning of the ECT-2 RhoGEF, RHO-1 and CDC-42 establishes cell polarity in *Caenorhabditis elegans* embryos. *Nature Cell Biology*. 8:978–985. doi:10.1038/ncb1459.
- Moutel, S., N. Bery, V. Bernard, L. Keller, and E. Lemesre. 2016. NaLi-H1: A universal synthetic library of humanized nanobodies providing highly functional antibodies and intrabodies. *Elife*. 5. doi:10.7554/eLife.16228.
- Munro, E., J. Nance, and J.R. Priess. 2004. Cortical flows powered by asymmetrical contraction transport PAR proteins to establish and maintain anterior-posterior polarity in the early *C. elegans* embryo. *Developmental cell*. 7:413–424. doi:10.1016/j.devcel.2004.08.001.
- Musacchio, A., and A. Desai. 2017. A molecular view of kinetochore assembly and function. *Biology (Basel)*. 6. doi:10.3390/biology6010005.
- Nakayama, Y., J.M. Shivas, D.S. Poole, and J.M. Squirrell. 2009. Dynamin participates in the maintenance of anterior polarity in the *Caenorhabditis elegans* embryo. *Developmental cell*. 16:889–900. doi:10.1016/j.devcel.2009.04.009.

- Neef, R., R. Kopajtich, X. Li, and E.A. Nigg. 2007. Choice of Plk1 docking partners during mitosis and cytokinesis is controlled by the activation state of Cdk1. *Nature Cell Biology*. 9:436–444. doi:10.1038/ncb1557.
- Niiya, F., X. Xie, K.S. Lee, H. Inoue, and T. Miki. 2005. Inhibition of cyclin-dependent kinase 1 induces cytokinesis without chromosome segregation in an ECT2 and MgcRacGAP-dependent manner. *J Biol Chem*. 280:36502–36509. doi:10.1074/jbc.M508007200.
- Nishikawa, M., S.R. Naganathan, F. Jülicher, and S.W. Grill. 2017. Controlling contractile instabilities in the actomyosin cortex. *Elife*. 6. doi:10.7554/eLife.19595.
- Nishimura, Y., and S. Yonemura. 2006. Centralspindlin regulates ECT2 and RhoA accumulation at the equatorial cortex during cytokinesis. *Journal of cell science*. 119:104–114. doi:10.1242/jcs.02737.
- Oegema, K., M.S. Savoian, and T.J. Mitchison. 2000. Functional analysis of a human homologue of the *Drosophila* actin binding protein anillin suggests a role in cytokinesis. *The Journal of cell biology*. 150:539–552. doi:10.1083/jcb.150.3.539.
- Oegema, K., and T. Hyman. 2006. Cell division. *WormBook*. 1–40. doi:10.1895/wormbook.1.72.1.
- Osório, D.S., F.Y. Chan, J. Saramago, and J. Leite. 2019. Crosslinking activity of non-muscle myosin II is not sufficient for embryonic cytokinesis in *C. elegans*. *Development*. 146. doi:10.1242/dev.179150.
- Otomo, T., C. Otomo, D.R. Tomchick, and M. Machius. 2005. Structural basis of Rho GTPase-mediated activation of the formin mDia1. *Mol Cell*. 18:273–281. doi:10.1016/j.molcel.2005.04.002.
- Petronczki, M., M. Glotzer, N. Kraut, and J.M. Peters. 2007. Polo-like kinase 1 triggers the initiation of cytokinesis in human cells by promoting recruitment of the RhoGEF Ect2 to the central spindle. *Developmental cell*. 12:713–725. doi:10.1016/j.devcel.2007.03.013.
- Piekny, A., M. Werner, and M. Glotzer. 2005. Cytokinesis: welcome to the Rho zone. *Trends in cell biology*. 15:651–658. doi:10.1016/j.tcb.2005.10.006.
- Piekny, A.J., and M. Glotzer. 2008. Anillin is a scaffold protein that links RhoA, actin, and myosin during cytokinesis. *Curr Biol*. 18:30–36. doi:10.1016/j.cub.2007.11.068.

- Piekny, A.J., and A.S. Maddox. 2010. The myriad roles of Anillin during cytokinesis. *Seminars in cell & developmental biology*. 21:881–891. doi:10.1016/j.semcdb.2010.08.002.
- Pines, J. 2011. Cubism and the cell cycle: the many faces of the APC/C. *Nature reviews Molecular cell biology*. 12:427–438. doi:10.1038/nrm3132.
- Pinto, I.M., B. Rubinstein, and R. Li. 2013. Force to divide: structural and mechanical requirements for actomyosin ring contraction. *Biophys J*. 105:547–554. doi:10.1016/j.bpj.2013.06.033.
- Plowman, S.J., C. Muncke, and R.G. Parton. 2005. H-ras, K-ras, and inner plasma membrane raft proteins operate in nanoclusters with differential dependence on the actin cytoskeleton. *Proc Natl Acad Sci U S A*. 102:15500–15505. doi:10.1073/pnas.0504114102.
- Pollard, T.D. 1976. The role of actin in the temperature-dependent gelation and contraction of extracts of *Acanthamoeba*. *The Journal of cell biology*. 68:579–601. doi:10.1083/jcb.68.3.579.
- Pollard, T.D. 2017. Nine unanswered questions about cytokinesis. *The Journal of cell biology*. 216:3007–3016. doi:10.1083/jcb.201612068.
- Pollard, T.D., and J.A. Cooper. 2009. Actin, a central player in cell shape and movement. *Science*. 326:1208–1212. doi:10.1126/science.1175862.
- Pollard, T.D., and B. O'Shaughnessy. 2019. Molecular mechanism of cytokinesis. *Annu Rev Biochem*. 88:661–689. doi:10.1146/annurev-biochem-062917-012530.
- Poteryaev, D., J.M. Squirrell, and J.M. Campbell. 2005. Involvement of the Actin Cytoskeleton and Homotypic Membrane Fusion in ER Dynamics in *Caenorhabditis elegans*. *Molecular biology of the cell*. 16:2139–2153. doi:10.1091/mbc.e04-08-0726.
- Priya, R., G.A. Gomez, and S. Budnar. 2017. Bistable front dynamics in a contractile medium: Travelling wave fronts and cortical advection define stable zones of RhoA signaling at epithelial adherens junctions. *PLoS Comput Biol*. 13:e1005411. doi:10.1371/journal.pcbi.1005411.
- Prokopenko, S.N., A. Brumby, and L. O'Keefe. 1999. A putative exchange factor for Rho1 GTPase is required for initiation of cytokinesis in *Drosophila*. *Genes & development*. 13:2301–2314. doi:10.1101/gad.13.17.2301.

- Rappaport, R. 1961. Experiments concerning the cleavage stimulus in sand dollar eggs. *J Exp Zool.* 148:81–89. doi:10.1002/jez.1401480107.
- Rappaport, R. 1985. Repeated furrow formation from a single mitotic apparatus in cylindrical sand dollar eggs. *J Exp Zool.* 234:167–171. doi:https://doi.org/10.1002/jez.1402340120.
- Reymann, A.C., F. Staniscia, A. Erzberger, and G. Salbreux. 2016. Cortical flow aligns actin filaments to form a furrow. *Elife.* 5. doi:10.7554/eLife.17807.
- Riedl, J., A.H. Crevenna, K. Kessenbrock, and J.H. Yu. 2008. Lifeact: a versatile marker to visualize F-actin. *Nat Methods.* 5:605–607. doi:10.1038/nmeth.1220.
- Ritchie, K., R. Iino, T. Fujiwara, and K. Murase. 2003. The fence and picket structure of the plasma membrane of live cells as revealed by single molecule techniques. *Mol Membr Biol.* 20:13–18. doi:10.1080/0968768021000055698.
- Rodríguez, S. 2021. Rho GTPases in Skeletal Muscle Development and Homeostasis. *Cells.* 10. doi:10.3390/cells10112984.
- Rossman, K.L., C.J. Der, and J. Sondek. 2005. GEF means go: turning on RHO GTPases with guanine nucleotide-exchange factors. *Nature reviews Molecular cell biology.* 6:167–180. doi:10.1038/nrm1587.
- Rothbauer, U., K. Zolghadr, S. Tillib, and D. Nowak. 2006. Targeting and tracing antigens in live cells with fluorescent nanobodies. *Nat Methods.* 3:887–889. doi:10.1038/nmeth953.
- Rotty, J.D., and J.E. Bear. 2015. Competition and collaboration between different actin assembly pathways allows for homeostatic control of the actin cytoskeleton. *Bioarchitecture.* 5:27–34. doi:10.1080/19490992.2015.1090670.
- Saffman, P.G., and M. Delbrück. 1975. Brownian motion in biological membranes. *Proc Natl Acad Sci U S A.* 72:3111–3113. doi:10.1073/pnas.72.8.3111.
- Sako, Y., and A. Kusumi. 1994. Compartmentalized structure of the plasma membrane for receptor movements as revealed by a nanometer-level motion analysis. *The Journal of cell biology.* 125:1251–1264. doi:10.1083/jcb.125.6.1251.

- Sandquist, J.C., A.M. Kita, and W.M. Bement. 2011. And the dead shall rise: actin and myosin return to the spindle. *Developmental cell*. 21:410–419. doi:10.1016/j.devcel.2011.07.018.
- Saxton, M.J. 1995. Single-particle tracking: effects of corrals. *Biophys J*. 69:389–398. doi:10.1016/S0006-3495(95)79911-8.
- Schindelin, J., and I. Arganda. 2012. Fiji: an open-source platform for biological-image analysis. *Nat Methods*. 9:676–682. doi:10.1038/nmeth.2019.
- Schmidthals, K., J. Helma, and K. Zolghadr. 2010. Novel antibody derivatives for proteome and high-content analysis. *Anal Bioanal Chem*. 397:3203–3208. doi:10.1007/s00216-010-3657-0.
- Schmutz, C., J. Stevens, and A. Spang. 2007. Functions of the novel RhoGAP proteins RGA-3 and RGA-4 in the germ line and in the early embryo of *C. elegans*. *Development*. 134:3495–3505. doi:10.1242/dev.000802.
- Scholze, M.J., K.S. Barbieux, and A. De Simone. 2018. PI (4, 5) P2 forms dynamic cortical structures and directs actin distribution as well as polarity in *C. elegans* embryos. *Development*. 145. doi:10.1242/dev.164988.
- Schonegg, S., and A.T. Constantinescu. 2007. The Rho GTPase-activating proteins RGA-3 and RGA-4 are required to set the initial size of PAR domains in *Caenorhabditis elegans* one-cell embryos. *Proc Natl Acad Sci U S A*. 104:14976–14981. doi:10.1073/pnas.0706941104.
- Schroeder, T.E. 1968. Cytokinesis: filaments in the cleavage furrow. *Experimental cell research*. 53:272–276. doi:10.1016/0014-4827(68)90373-x.
- Schroeder, T.E. 1972. The contractile ring: II. Determining its brief existence, volumetric changes, and vital role in cleaving *Arbacia* eggs. *The Journal of cell biology*. 53:419–434. doi:10.1083/jcb.53.2.419.
- Schroeder, T.E. 1975. Dynamics of the contractile ring. *Soc Gen Physiol Ser*. 30:305–334.
- Schwayer, C., M. Sikora, J. Slovakova, and R. Kardos. 2016. Actin rings of power. *Developmental cell*. 37:493–506. doi:10.1016/j.devcel.2016.05.024.



- Segal, D., A. Zaritsky, E.D. Schejter, and B.Z. Shilo. 2018. Feedback inhibition of actin on Rho mediates content release from large secretory vesicles. *The Journal of cell biology*. 217:1815–1826. doi:10.1083/jcb.201711006.
- Severson, A.F., D.L. Baillie, and B. Bowerman. 2002. A Formin Homology protein and a profilin are required for cytokinesis and Arp2/3-independent assembly of cortical microfilaments in *C. elegans*. *Current biology*. 12:2066–75. doi:10.1016/s0960-9822(02)01355-6.
- Sheetz, M.P. 1983. Membrane skeletal dynamics: role in modulation of red cell deformability, mobility of transmembrane proteins, and shape. *Semin Hematol*. 20:175–188.
- Sheetz, M.P. 1993. Glycoprotein motility and dynamic domains in fluid plasma membranes. *Annu Rev Biophys Biomol Struct*. 22:417–431. doi:10.1146/annurev.bb.22.060193.002221.
- Sheetz, M.P., M. Schindler, and D.E. Koppel. 1980. Lateral mobility of integral membrane proteins is increased in spherocytic erythrocytes. *Nature*. 285:510–511. doi:10.1038/285510a0.
- Shibata, S., M. Nagase, S. Yoshida, and W. Kawarazaki. 2008. Modification of mineralocorticoid receptor function by Rac1 GTPase: implication in proteinuric kidney disease. *Nat Med*. 14:1370–1376. doi:10.1038/nm.1879.
- Singer, S.J. 2004. Some early history of membrane molecular biology. *Annual Review of Physiology*. 66:1–27. doi:10.1146/annurev.physiol.66.032902.131835.
- Singer, S.J., and G.L. Nicolson. 1972. The fluid mosaic model of the structure of cell membranes. *Science*. 175:720–731. doi:10.1126/science.175.4023.720.
- Slaughter, B.D., A. Das, J.W. Schwartz, B. Rubinstein, and R. Li. 2009. Dual modes of cdc42 recycling fine-tune polarized morphogenesis. *Developmental cell*. 17:823–835. doi:10.1016/j.devcel.2009.10.022.
- Soderling, S.H., and J.D. Scott. 2006. WAVE signalling: from biochemistry to biology. *Biochemical Society Transactions*. 34:73–76. doi:10.1042/BST0340073.

- Somers, W.G., and R. Saint. 2003. A RhoGEF and Rho family GTPase-activating protein complex links the contractile ring to cortical microtubules at the onset of cytokinesis. *Developmental cell*. 4:29–39. doi:10.1016/s1534-5807(02)00402-1.
- Somma, M.P., B. Fasulo, and G. Cenci. 2002. Molecular Dissection of Cytokinesis by RNA Interference in *Drosophila* Cultured Cells. *Molecular biology of the cell*. 13:2448–2460. doi:10.1091/mbc.01-12-0589.
- Spira, F., and S. Cuylen. 2017. Cytokinesis in vertebrate cells initiates by contraction of an equatorial actomyosin network composed of randomly oriented filaments. *Elife*. 6. doi:10.7554/eLife.30867.
- Stiernagle, T. 2006. Maintenance of *C. elegans*. *WormBook*. 1. doi:10.1895/wormbook.1.101.1.
- Straight, A.F., C.M. Field, and T.J. Mitchison. 2005. Anillin binds nonmuscle myosin II and regulates the contractile ring. *Molecular biology of the cell*. 16:193–201. doi:10.1091/mbc.e04-08-0758.
- Su, K.C., T. Takaki, and M. Petronczki. 2011. Targeting of the RhoGEF Ect2 to the equatorial membrane controls cleavage furrow formation during cytokinesis. *Developmental cell*. 21:1104–1115. doi:10.1016/j.devcel.2011.11.003.
- Suarez, C., R.T. Carroll, T.A. Burke, and J.R. Christensen. 2015. Profilin regulates F-actin network homeostasis by favoring formin over Arp2/3 complex. *Developmental cell*. 32:43–53. doi:10.1016/j.devcel.2014.10.027.
- Subauste, M.C., M. Von Herrath, and V. Benard. 2000. Rho family proteins modulate rapid apoptosis induced by cytotoxic T lymphocytes and Fas. *Journal of Biological Chemistry*. 275:9725–9733. doi:10.1074/jbc.275.13.9725.
- Sun, L., R. Guan, I.J. Lee, Y. Liu, M. Chen, J. Wang, and J.Q. Wu. 2015. Mechanistic insights into the anchorage of the contractile ring by anillin and Mid1. *Developmental cell*. 33:413–426. doi:10.1016/j.devcel.2015.03.003.
- Swan, K.A., A.F. Severson, J.C. Carter, and P.R. Martin. 1998. *cyk-1*: a *C. elegans* FH gene required for a late step in embryonic cytokinesis. *Journal of cell science*. 111:2017–2027. doi:10.1242/jcs.111.14.2017.

- Sönnichsen, B., L.B. Koski, A. Walsh, and P. Marschall. 2005. Full-genome RNAi profiling of early embryogenesis in *Caenorhabditis elegans*. *Nature*. 434:462–469. doi:10.1038/nature03353.
- Takaishi, K., T. Sasaki, T. Kameyama, and S. Tsukita. 1995. Translocation of activated Rho from the cytoplasm to membrane ruffling area, cell-cell adhesion sites and cleavage furrows. *Oncogene*. 11:39–48.
- Tcherkezian, J., and N. Lamarche-Vane. 2007. Current knowledge of the large RhoGAP family of proteins. *Biol Cell*. 99:67–86. doi:10.1042/BC20060086.
- Tnimov, Z., Z. Guo, Y. Gambin, and U. Nguyen. 2012. Quantitative analysis of prenylated RhoA interaction with its chaperone, RhoGDI. *J Biol Chem*. 287:26549–26562. doi:10.1074/jbc.M112.371294.
- Togawa, A., J. Miyoshi, H. Ishizaki, M. Tanaka, and A. Takakura. 1999. Progressive impairment of kidneys and reproductive organs in mice lacking Rho GDI $\alpha$ . *Oncogene*. 18:5373–5380. doi:10.1038/sj.onc.1202921.
- Tse, Y.C., A. Piekny, and M. Glotzer. 2011. Anillin promotes astral microtubule-directed cortical myosin polarization. *Molecular biology of the cell*. 22:3165–3175. doi:10.1091/mbc.E11-05-0399.
- Tse, Y.C., M. Werner, and K.M. Longhini. 2012. RhoA activation during polarization and cytokinesis of the early *Caenorhabditis elegans* embryo is differentially dependent on NOP-1 and CYK-4. *Molecular biology of the cell*. 23:4020–4031. doi:10.1091/mbc.E12-04-0268.
- Tseng, Q., and E. Duchemin. 2012. Spatial organization of the extracellular matrix regulates cell–cell junction positioning. *Proc Natl Acad Sci U S A*. 109:1506–1511. doi:10.1073/pnas.1106377109.
- Turek, M., I. Lewandrowski, and H. Bringmann. 2013. An AP2 transcription factor is required for a sleep-active neuron to induce sleep-like quiescence in *C. elegans*. *Curr Biol*. 23:2215–2223. doi:10.1016/j.cub.2013.09.028.
- Uzbekov, R., and C. Prigent. 2022. A journey through time on the discovery of cell cycle regulation. *Cells*. 11. doi:10.3390/cells11040704.

- Van Unen, J., N.R. Reinhard, T. Yin, Y.I. Wu, and M. Postma. 2015. Plasma membrane restricted RhoGEF activity is sufficient for RhoA-mediated actin polymerization. *Scientific Reports*. 5:14693. doi:10.1038/srep14693.
- Verbrugghe, K., and J.G. White. 2004. SPD-1 is required for the formation of the spindle midzone but is not essential for the completion of cytokinesis in *C. elegans* embryos. *Curr Biol*. 14:1755–1760. doi:10.1016/j.cub.2004.09.055.
- Vereb, G., J. Szöllösi, J. Matko, and P. Nagy. 2003. Dynamic, yet structured: the cell membrane three decades after the Singer–Nicolson model. *Proc Natl Acad Sci U S A*. 100:8053–8058. doi:10.1073/pnas.1332550100.
- Vicker, M.G. 2000. Reaction–diffusion waves of actin filament polymerization/depolymerization in *Dictyostelium* pseudopodium extension and cell locomotion. *Biophys Chem*. 84:87–98. doi:10.1016/s0301-4622(99)00146-5.
- Wagner, E., and M. Glotzer. 2016. Local RhoA activation induces cytokinetic furrows independent of spindle position and cell cycle stage. *The Journal of cell biology*. 213:641–649. doi:10.1083/jcb.201603025.
- Watanabe, S., Y. Ando, and S. Yasuda. 2008. mDia2 induces the actin scaffold for the contractile ring and stabilizes its position during cytokinesis in NIH 3T3 cells. *Molecular biology of the cell*. 19:2328–2338. doi:10.1091/mbc.e07-10-1086.
- White, E.A., and M. Glotzer. 2012. Centralspindlin: at the heart of cytokinesis. *Cytoskeleton (Hoboken)*. 69:882–892. doi:10.1002/cm.21065.
- White, J.G., and G.G. Borisy. 1983. On the mechanisms of cytokinesis in animal cells. *Journal of Theoretical Biology*. 101:289–316. doi:10.1016/0022-5193(83)90342-9.
- Yonemura, S., and K. Hirao. 2004. Rho localization in cells and tissues. *Experimental cell research*. 295:300–314. doi:10.1016/j.yexcr.2004.01.005.
- Yoshida, S., S. Bartolini, and D. Pellman. 2009. Mechanisms for concentrating Rho1 during cytokinesis. *Genes & development*. 23:810–823. doi:10.1101/gad.1785209.
- Yüce, Ö., A. Piekny, and M. Glotzer. 2005. An ECT2–centralspindlin complex regulates the localization and function of RhoA. *The Journal of cell biology*. 170:571–582. doi:10.1083/jcb.200501097.

- Zanin, E., A. Desai, I. Poser, Y. Toyoda, and C. Andree. 2013. A conserved RhoGAP limits M phase contractility and coordinates with microtubule asters to confine RhoA during cytokinesis. *Developmental cell*. 26:496–510. doi:10.1016/j.devcel.2013.08.005.
- Zeiser, E., and C. Frøkjær. 2011. MosSCI and gateway compatible plasmid toolkit for constitutive and inducible expression of transgenes in the *C. elegans* germline. *PLoS One*. 6:e20082. doi:10.1371/journal.pone.0020082.
- Zhang, B., Y. Gao, S.Y. Moon, Y. Zhang, and Y. Zheng. 2001. Oligomerization of Rac1 gtpase mediated by the carboxyl-terminal polybasic domain. *Journal of Biological Chemistry*. 276:8958–8967. doi:10.1074/jbc.M008720200.
- Zhang, B., and Y. Zheng. 1998a. Negative regulation of Rho family GTPases Cdc42 and Rac2 by homodimer formation. *Journal of Biological Chemistry*. 273:25728–25733. doi:10.1074/jbc.273.40.25728.
- Zhang, B., and Y. Zheng. 1998b. Regulation of RhoA GTP hydrolysis by the GTPase-activating proteins p190, p50RhoGAP, Bcr, and 3BP-1. *Biochemistry*. 37:5249–5257. doi:10.1021/bi9718447.
- Zhao, W., and G. Fang. 2005. MgcRacGAP controls the assembly of the contractile ring and the initiation of cytokinesis. *Proc Natl Acad Sci U S A*. 102:13158–13163. doi:10.1073/pnas.0504145102.
- Zumdieck, A., K. Kruse, H. Bringmann, and A.A. Hyman. 2007. Stress generation and filament turnover during actin ring constriction. *PLoS One*. 2:e696. doi:10.1371/journal.pone.0000696.
- van Oostende Triplet, C., M.J. Garcia, and H.H. Bik. 2014. Anillin interacts with microtubules and is part of the astral pathway that defines cortical domains. *Journal of cell science*. 127:3699–3710. doi:10.1242/jcs.147504.

## 6 Appendix

### 6.1 Semi-automated macros used for image processing of cortical plane live-cell microscopy images.

For representation purposes throughout this work, all cortical plane live-cell microscopy images were processed in Fiji by semi-automated macros shown in Appendix 1 and Appendix 2. The two channels green (488 nm laser-line) and red (561 nm laser-line) were processed separately. For merged image representation, the two channels were merged after individual image processing.

#### Green channel (488 nm laser line)

```

1
2
3 output = getDirectory("Choose a Directory");
4 imageName = getTitle();
5
6
7 waitForUser("make a selection in cytoplasm");
8
9 //subtract cytoplasmic signal and apply filters (1.Gaussian Blur, 2.Unsharp Mask)
10
11 {
12     for (i=1; i<=nSlices; i++) {
13         setSlice(i);
14         getStatistics(area, mean);
15         normMean = mean-(mean/100*20);
16         print(normMean);
17         run("Select None");
18         run("Subtract...", "value="+normMean);
19         run("Gaussian Blur...", "sigma=1");
20         run("Unsharp Mask...", "radius=2 mask=0.60");
21         run("Restore Selection");
22     }
23 }
24
25
26 run("Select None");
27 setMinAndMax(0, 850);
28 run("Grays");
29 saveAs("tiff", output + imageName + "_Filters");
30

```

**Appendix 1: Semi-automated macro for image processing in Fiji of cortical images acquired with the 488 nm laser-line.** First, 80 % of cytoplasmic signal was subtracted, followed by applying ‘Gaussian Blur’ and ‘Unsharp Mask’ filters. Subsequently all images were scaled in the same manner, by setting the ‘Min and Max’ to 0 and 850.

**Red channel (561 nm laser line)**

```

1
2
3 output = getDirectory("Choose a Directory");
4 imageName = getTitle();
5
6
7 waitForUser("make a selection in cytoplasm");
8
9 //subtract cytoplasmic signal and apply filters (1.Gaussian Blur, 2.Unsharp Mask)
10
11 {
12     for (i=1; i<=nSlices; i++) {
13         setSlice(i);
14         getStatistics(area, mean);
15         normMean = mean-(mean/100*10);
16         print(normMean);
17         run("Select None");
18         run("Subtract...", "value="+normMean);
19         run("Gaussian Blur...", "sigma=1");
20         run("Unsharp Mask...", "radius=2 mask=0.60");
21         run("Restore Selection");
22     }
23 }
24 }
25
26 run("Select None");
27 setMinAndMax(0, 400);
28 run("Grays");
29 saveAs("tiff", output + imageName + "_Filters");
30

```

**Appendix 2: Semi-automated macro for image processing in Fiji of cortical images acquired with the 561 nm laser-line.** First, 90 % of cytoplasmic signal was subtracted, followed by applying ‘Gaussian Blur’ and ‘Unsharp Mask’ filters. Subsequently all images were scaled in the same manner, by setting the ‘Min and Max’ to 0 and 400.

## Acknowledgement

Diese Dissertation wurde an der Ludwig-Maximilians-Universität München, an der Fakultät für Biologie, im Bereich Zell- und Entwicklungsbiologie, unter der Leitung von Prof. Dr. Esther Zanin angefertigt.

Gerne möchte ich die Gelegenheit nutzen und mich an dieser Stelle bei all denen bedanken, die mich auf meinem Weg begleitet und unterstützt haben.

Einen besonderen Dank richte ich an Prof. Dr. Esther Zanin, die es mir ermöglicht hat diese Dissertation anzufertigen. Ich bedanke mich für die sehr gute Arbeitsatmosphäre und Unterstützung mit vielen ideenreichen Ratschlägen.

Vielen Dank an die Mitglieder meines Thesis Advisory Committees (TAC), Frau Prof. Dr. Claudia Veigel und Prof. Dr. Aymelt Itzen, die mich während meiner Arbeit begleitet haben. Danke für die spannenden und anregenden Diskussionen. Insbesondere bedanke ich mich an dieser Stelle bei Herrn Prof. Dr. Aymelt Itzen für die Expertise und die Unterstützung bei der Proteinaufreinigung, in Form einer Exkursion in seinem Labor an der Technischen Universität München. Ich bedanke mich bei dem netten Team des Itzen Labors, besonders bei Frau Dr. Sophie Vieweg, für die tatkräftige Unterstützung und Hilfsbereitschaft.

Ich bedanke mich bei Dr. Hartmann Harz für die technische Unterstützung bei allen Angelegenheiten rund um das Imaging.

Vielen Dank an Frau Dr. Tamara Mikeladze-Dvali und ihre Gruppe für die Inspirationen und konstruktive Kritik aus unseren wöchentlichen Treffen sowie die gute gemeinschaftliche Atmosphäre im Labor. Ich bedanke mich bei allen Mitgliedern des Zanin, Mikeladze-Dvali, Conradt, Lambie und Wagener Labors für die gute Zusammenarbeit, die wertvollen Anregungen sowie die gemeinsamen Freizeitaktivitäten.

Ein besonderes Dankeschön für die tolle gemeinsame Zeit richte ich an meine Kollegen und Kolleginnen Dr. Kristina Buchner, Dr. Sriyash Mangal, Dr. Sandra Schneid und Friederike Wolff aus dem Zanin Labor. Danke, dass ihr mir immer mit einem offenen Ohr zur Seite standet. Ein herzliches Dankeschön an Sandra für das Korrekturlesen meiner Dissertation und an alle Studenten, die mich bei der experimentellen Arbeit unterstützt haben.



Vielen Dank an die Koordinatorinnen der Graduate School Life Science Munich (LSM) sowie an alle Mitglieder der LSM, denen ich in diesem spannenden Lebensabschnitt begegnet bin und mit denen ich einen Teil des Weges zusammen beschreiten durfte.

Ganz besonders möchte ich mich bei meinen Eltern, Martina und Deltlef Sacher, bedanken. Vielen herzlichen Dank für die uneingeschränkte und liebevolle Unterstützung. Danke an meine Eltern und Schwiegereltern, für die vielen schönen Oma- und Opa-Stunden mit Jakob, die es mir ermöglicht haben als berufstätige Mutter meine Dissertation zu Ende zu schreiben.

Ich danke meinem Ehemann, Benedikt Bellessem, und meinem Sohn, Jakob Bellessem, einfach dafür, dass es euch gibt und ihr immer für mich da seid. Danke Benny für deine unermüdliche Geduld, deine Rücksichtnahme und die Motivation auch in schwierigen Phasen.

## Curriculum Vitae

Jennifer Leonie Bellessem (née Sacher)

### EDUCATION

- 02/2015 – 01/2020 PhD at the Department of Cell- and Developmental Biology (AG Zanin), Ludwig-Maximilians-University Munich. “Temporal and spatial organisation of RhoA during cytokinesis” Graduate School of Life Science Munich
- 04/2012 – 03/2014 Master of Science (M.Sc.) „Biotechnology/Molecular Biotechnology“, Technical University Aachen (RWTH). “Influence of anisotropic surface structures on the haemocompatibility of polycarbonate-urethane“, Institute of Applied Medical Engineering, Helmholtz-Institute Aachen
- 09/2007 – 03/2011 Bachelor of Science (B.Sc.) „Biotechnology/Bioinformatics“, University of Applied Sciences Emden/Leer. “Analysis of the mitotic cell division after UVA irradiation using cell biological and microscopic methods“, Institute of Molecular Biology and Biochemistry II, University Medical Center Düsseldorf
- 07/1998 – 05/2006 Theodor – Fliedner – Gymnasium Düsseldorf, Abitur

### RESEARCH EXPERIENCE

- 11/2012 – 02/2013 Internship at the Institute of Pathology, University Medical Center Aachen, “Generation and characterization of stable Secernin-1 knockdown clones of the prostate carcinoma cell line PC3”:
- 01/2012 – 02/2012 Internship at the University of Calgary (Department of Biological Sciences) Canada, “Identification of uncultured CO & CH<sub>4</sub> oxidizing organisms from geothermal springs”:
- 03/2009 – 06/2009 Student assistant at the University of Applied Sciences Emden/Leer, research project „Modelling of a CO<sub>2</sub>-washer“:
- 10/2008 – 06/2009 Student assistant at the University of Applied Sciences Emden/Leer, tutor for natural sciences and technology:

### PUBLICATIONS

S. Mangal, **J. Sacher**, T. Kim, D.S. Osório, F. Motegi, A.X. Carvalho, K. Oegema and E. Zanin. 2018. TPXL-1 activates Aurora A to clear contractile ring components from the polar cortex during cytokinesis. *The Journal of cell biology*. 217:837–848. doi:10.1083/jcb.201706021.

M. Lebedev, FY. Chan, A. Lochner, **J. Bellessem**, DS. Osório, E. Rackles, T. Mikeladze-Dvali, AX. Carvalho, E. Zanin. Anillin forms linear structures and facilitates furrow ingression after septin and formin depletion. *Cell Rep*. 2023 Sep 26;42(9):113076. doi: 10.1016/j.celrep.2023.113076. Epub 2023 Sep 3. PMID: 37665665; PMCID: PMC10548094.